THE OUTERMOST HII REGIONS OF NEARBY GALAXIES

by

Jessica K. Werk

A dissertation submitted in partial fulfillment
of the requirements for the degree of
Doctor of Philosophy
(Astronomy and Astrophysics)
in The University of Michigan
2010

Doctoral Committee:

Professor Mario L. Mateo, Co-Chair
Associate Professor Mary E. Putman, Co-Chair, Columbia University
Professor Fred C. Adams
Professor Lee W. Hartmann
Associate Professor Marion S. Oey
Professor Gerhardt R. Meurer, University of Western Australia

To Mom and Dad,

for all your love and encouragement while I was taking up space.

ACKNOWLEDGMENTS

I owe a deep debt of gratitude to a long list of individuals, institutions, and substances that have seen me through the last six years of graduate school.

My first undergraduate advisor in Astronomy, Kathryn Johnston, was also my first Astronomy Professor. She piqued my interest in the subject from day one with her enthusiasm and knowledge. I don't doubt that I would be studying something far less interesting if it weren't for her.

John Salzer, my next and last undergraduate advisor, not only taught me so much about observing and organization, but also is responsible for convincing me to go on in Astronomy. Were it not for John, I'd probably be making a lot more money right now doing something totally mind-numbing and soul-crushing.

And Laura Chomiuk, a fellow Wesleyan Astronomy Alumnus, has been there for me through everything − problem sets and personal heartbreak alike. To know her as a friend, goat-lover, and scientist has meant so much to me over the last 10 years, that confining my gratitude to these couple sentences just seems wrong.

I was born academically in the Astronomy Department of Wesleyan University. I have only fond memories of the place and people that comprised it during those Golden Years.

And if I was born academically at Wesleyan, then I learned to walk in the University of Michigan Astronomy Department, a truly wonderful, engaged, and supportive community of scientists, students, and staff. Sarah Lloyd in the main office managed to be so kind while doing some of the most thankless work, and I thank her deeply for answering all my mundane questions ranging from health insurance to travel reimbursement to "detachment" issues with a smile. I hold all the graduate students who overlapped with me in such high regard, and can't wait to see them at

future conferences and to cite their papers, and to perhaps work with them. And of course, specifically, to Sarah Ragan, Janet Colucci, Laura Ingleby, Jen Blum, Becky Stanek, Matt Walker, Jeffrey Fogel, Tom Brink, Scott Cameron, Ajay Tannirkulam, Eli Rykoff, and Jun Ji, a huge thank you, for everything, but mostly for keeping me sane. Sarah and Janet get another whole line to themselves here, because, well, they're just so awesome. All of the professors in the Department were excellent to me, and taught me so much both inside and outside of the classroom. In particular, Sally Oey, who continues to involve me in her group meetings, has been so supportive during my move to Columbia University, a pleasure to work with, and a great mentor. Nuria Calvet often went above and beyond her role of graduate student mentor, and is a big part of the reason why I'm not currently suffering from wisdom tooth pain. And all of my dissertation committee members have offered me valuable insight over the last few years for which I am grateful. I am grateful to Mario Mateo in particular, who took over as my local committee chair and thesis advisor in the aftermath of my "detachment, " and who has offered sound scientific advice, always, during my time at the University of Michigan.

The Astronomy Department at Columbia University has been most hospitable during my two-year stay as a Non-Degree-Seeking Visiting Scholar. Everyone, from faculty to staff to students, has been welcoming. In particular, Mildred Garcia and Trudy Reyes made sure my somewhat complicated status didn't get in the way of health insurance and stipend. Jennifer Donovan-Meyer, Stephanie Tonnesen, and Sarah Tuttle have been true friends during these thesis-writing days, almost making it fun. Jana Grcevich, another Michigan transplant, is one of the smartest, most wonderful people I have ever met, and I am so glad to have worked with her. Joshua Peek inspires me everyday with his enthusiasm for astronomy and new, exciting ideas. And Jacqueline van Gorkom never ceases to impress me with her boundless energy for astronomy, effortless insight, and continued kindness.

The research presented in this Thesis has made extensive use of the NASA/IPAC Extragalactic Database (NED) which is operated by the Jet Propulsion Laboratory, California Institute of Technology, under contract with the National Aeronautics and

Outside of the astronomical community, my family and friends were endlessly supportive and genuinely curious about my research, a real boon during the requisite soul-searching that accompanies the decision to become an academic. And Nicholas Ranallo put up with more than his share of random but impassioned exclamations about astrophysical processes on Saturday afternoons – I can't wait until our Saturday afternoons are once again filled with the HP and GD instead. Not soon enough...

Gerhardt Meurer has managed to teach me so much, though we've never been in the same place for more than one week. His scientific advice, moral support, and guidance over the last six years have been invaluable to me. Any thanks I could offer here would be totally inadequate.

And everyday, I feel fortunate beyond words to be working with Mary Putman. I just hope that someday I can be half as insightful, thoughtful, and brilliant as she is. Without a doubt, she is exactly the sort of astronomer I aspire to be.

PREFACE

This work presented here relies upon the data from no fewer than 10 observing runs on various telescopes – the MDM 2.4-m, Magellan Baade 6.5-m, Gemini-North 8-m, VLA, *HST* – discussions with scientists at 9 astronomical conferences, and collaborative efforts with astronomers all over the world. I am indebted to so many of them for insightful suggestions and comments on this work in various forms – paper drafts, power-point presentations, and conference posters. Emma Ryan-Weber, Robert Kennicutt, Janice Lee, Diedre Hunter, Bill Vacca, David Thilker, Daniel Hanish, Ken Freeman, Andrey Kravtsov, Mederic Boquien, Joel Bregman, Nate Bastien, Rupali Chandar, Hans Zinneker, Carolina Kehrig, Joss Bland-Hawthorn, Carsten Weidner, Ron Allen, Xavier Prochaska, Barry Madore, Alan Dressler, Liese van Zee, Kevin Croxall, Eric Keto, Iraklis Konstantopoulos, Jay Strader, David Schiminovich, all those mentioned in the Acknowledgments, and more have all contributed a great deal in helping me interpret the results of this thesis.

Chapters 2, 3, and 4 of this thesis, though slightly modified from their original versions, were published previously in both *The Astronomical Journal* and *The Astrophysical Journal*. They are reproduced here (altered slightly to fit the thesis format) with permission from the AAS. The full citation for each article is:

Chapter 2 - Werk, J. K., Putman, M. E., Meurer, G. R., Ryan-Weber, E. V., Kehrig, C., Thilker, D. A., Bland-Hawthorn, J., Drinkwater, M. J., Kennicutt, R. C., Wong, O. I., Freeman, K. C., Oey, M. S., Dopita, M. A.; Doyle, M. T., Ferguson, H. C., Hanish, D. J., Heckman, T. M., Kilborn, V. A., Kim, J. H., Knezek, P. M.; Koribalski, B., Meyer, M., Smith, R. C., Zwaan, M. A. "Outlying HII Regions in HI-Selected Galaxies." 2010, AJ, 139, 279

Chapter 3 - Werk, J. K., Putman, M. E., Meurer, G. R., Oey, M. S., Ryan-

Weber, E. V., Kennicutt, R. C., & Freeman, K. C. "Isolated OB Associations in Stripped HI Gas Clouds." 2008, ApJ, 678, 888

Chapter 4 - Werk, J. K., Putman, M. E., Meurer, G. R., Thilker, D. A., Allen, R. J., Bland-Hawthorn, J., Kravtsov, A., & Freeman, K. "The Metal-enriched Outer Disk of NGC 2915." 2010, ApJ, 715, 656

CONTENTS

LIST OF FIGURES

LIST OF TABLES

ABSTRACT

The outlying HII regions of nearby galaxies provide a unique opportunity to probe the star-formation history, evolution, and origin of the gas in the outskirts of galaxies. Following a systematic search of a sample of "normal" gas-rich galaxies derived from the NOAO Survey for Ionization in Neutral Gas Galaxies (SINGG), and a separate sample of interacting, disturbed, or extended HI-disk galaxies (HI Rogues), I have catalogued and confirmed over 75 outlying HII regions located far beyond the main optical components of galaxies ($r > r_{25}$). In this thesis, I use outlying HII regions to address several fundamental questions about the nature of star formation in the low-density gas outside of galaxies. In particular, I determine the frequency with which outlying HII regions occur in gas-rich galaxies, the properties of their resolved, underlying stellar populations, and the oxygen abundances of the outermost, low-density gas in which they form. First, I use a self-developed automated algorithm to search for HII regions beyond projected optical radii in an unbiased sample of gas-rich galaxies. I find the overall frequency of outlying HII regions in the SINGG sample of gas-rich galaxies is 8 - 11% when I correct for background emission-line galaxy contamination ($\sim 75\%$ of emission-line point sources). I study the resolved stellar populations of several of these outlying HII regions using broadband *HST* ACS/HRC images. To the resolution and faintness limits of the *HST* images, outlying OB associations have the same stellar populations as Galactic OB associations, and appear to be dissolving on rapid timescales. Finally, I present optical emission-line spectra for outlying HII regions in the extended and/or disturbed neutral gas surrounding 14 nearby star-forming, gas-rich galaxies with a wide range of morphologies. The result that the outer-galaxy gas is consistently enriched to the same level as the inner-galaxy gas has implications for the physical origin of the mass-metallicity relation for gas-

rich dwarf galaxies, as well as the chemical evolution that takes place within galaxies over their lifetimes. This work represents significant progress for understanding star formation in low-density conditions and its role in galaxy evolution.

CHAPTER 1

Introduction

In the 85 years since Hubble determined that spiral and elliptical "nebulae" were indeed "habitants of space beyond" (Hubble, 1925), the study of galaxy formation and evolution has progressed immeasurably. A wealth of information from decades of multi-wavelength observations and, more recently, hydrodynamical simulations has shaped the currently-accepted basic view of galaxy formation: a scale-free gravitational clustering and hierarchical merging of dark matter halos coupled with gas accretion from the intergalactic medium (IGM), and subsequent collapse of the gas (White & Rees, 1978). However, there are still numerous holes in our understanding of how galaxies acquire their gas from the IGM in the first place, how they process it and ultimately regulate star formation, and how and to what extent they return their gas to the IGM.

Star formation is the primary visible outcome of the gas accretion that initially forms galaxies. How it relates to the integrated properties of galaxies and their interstellar media is a fundamental question that underlies much of extragalactic astrophysics. This thesis specifically hones in on star formation in the low-density, far-outskirts of galaxies, as traced by HII regions – ionized nebulae enclosing a single generation of stars with at least one star massive and hot enough to ionize hydrogen ($M > 15$ $M_\odot$). So called "outlying HII regions" are traditionally thought to defy standard star formation relations, contain atypical stellar populations, and form from pristine, unenriched gas. Determining their true nature, frequency, and environment is important for characterizing star formation demographics in general. Furthermore, it can lead to a comprehensive picture how low-density, isolated star formation is first triggered and subsequently regulated.

This Chapter introduces some of the broad topics in extragalactic star formation to which this study of outlying HII regions is relevant. First, in Section 1.1, I provide an overview of the global star-formation law for galaxies. I build on this discussion in Section 1.1.1 by describing recent work that addresses whether this relation holds on spatially-resolved scales, and in low-density environments. After pointing out that outlying HII regions are potentially quite useful in this regard, I review some of the previous discoveries of star formation in the outskirts of galaxies in Section 1.1.2. Then, Section 1.2 focuses on clustered star formation and methods that can be used to derive the intrinsic properties of the stellar populations that power HII regions. Additionally, I describe some of the very recent work that suggests outlying star clusters may obey a top-light stellar initial mass function. In Section 1.3, I point out that HII regions can be used to determine gas-phase metal abundances, which are useful for constructing abundance gradients across galaxies and understanding global relations between galaxy mass and metallicity. Finally, in Section 1.4, I outline the questions answered and topics covered by this thesis.

1.1 Making Stars out of Gas in Galaxies

On galaxy-wide scales, the most recent star formation is located along spiral arms in the form of HII regions, and occasionally appears as a strong, visible burst in the galaxy nucleus (Kennicutt, 1983). It has long been observed that the morphologies and masses of galaxies are intrinsically related to their star formation activity (Tinsley, 1968). Where "early-type" elliptical galaxies generally form few new stars, "late-type" spirals are teeming with young stars, and interacting, disturbed galaxies have the highest level of star formation activity. Quantitative measurements of the rate at which a galaxy is forming its stars (the star formation rate, SFR) are possible by observing light that is sensitive to the youngest stars: UV radiation that originates primarily in young massive stars (OB stars), Balmer photon fluxes that are essentially the re-emission of the UV photons that ionize surrounding hydrogen atoms ($H\alpha$, traditionally), and the infrared continuum where dust-reprocessed UV radiation emerges (Kennicutt, 1998a). Such measurements have confirmed the strong

dependence of the star formation rate on galaxy morphology (a.k.a. Hubble type) and mass, albeit with a large scatter.

Efforts to get at the physical underpinning of the star formation rate began with Thackeray (1948), who proposed that "the development of a star may be more or less controlled by the properties of the space or nebula which surrounds it." Schmidt (1959) built upon this very idea, and hypothesized that the star formation rate of a galaxy varies as a power law with the density of its interstellar gas. In the last 20 years, Schmidt's prediction has been borne out by an abundance of observational evidence indicating a very tight correlation between the observed star formation rate surface density and the gas surface density on disk-averaged scales in nearby, star-forming galaxies. This correlation is commonly referred to as the global star formation law of galaxies, or Schmidt law (Kennicutt, 1989, 1998b). It is such that a single power law over 5 orders of magnitude (Figure 1.1) successfully describes this connection between a galaxy's gas supply and the efficiency with which the gas gets converted into stars – independently of galaxies' other properties. The star formation law is typically parameterized as $\Sigma_{SFR} = A\Sigma_{gas}^N$, where Σ_{SFR} is in units of $M_\odot$ yr^{-1}, Σ_{gas} in units of $M_\odot$ pc^{-2}, N = 1.4$\pm$0.15, and A $\sim 2.5 \times 10^{-4}$. Despite the overwhelming success of this law at describing the global behavior of star formation in galaxies with varying densities of gas, the underlying physics remain poorly understood.

The numerous possible physical explanations for this tight correlation highlights this lack of understanding. As neutral hydrogen synthesis maps have revealed that the gas disks of galaxies often extend beyond their active star-forming disks, there is at least qualitative evidence for some "critical gas density" below which star formation ceases. The Toomre local gravitational stability parameter (Toomre, 1964) for differentially rotating disks offers one possible explanation for why star formation proceeds where the gas density lies above some "threshold density" (Skillman, 1987; Kennicutt, 1989, 1998b; Martin & Kennicutt, 2001). Yet, this simple gravitational stability criterion picture cannot completely explain the relation, particularly for low-mass and irregular galaxies with rising rotation curves (Thornley & Wilson, 1995; Hunter et al., 1998). Furthermore, there is an ongoing argument as to whether these gravita-
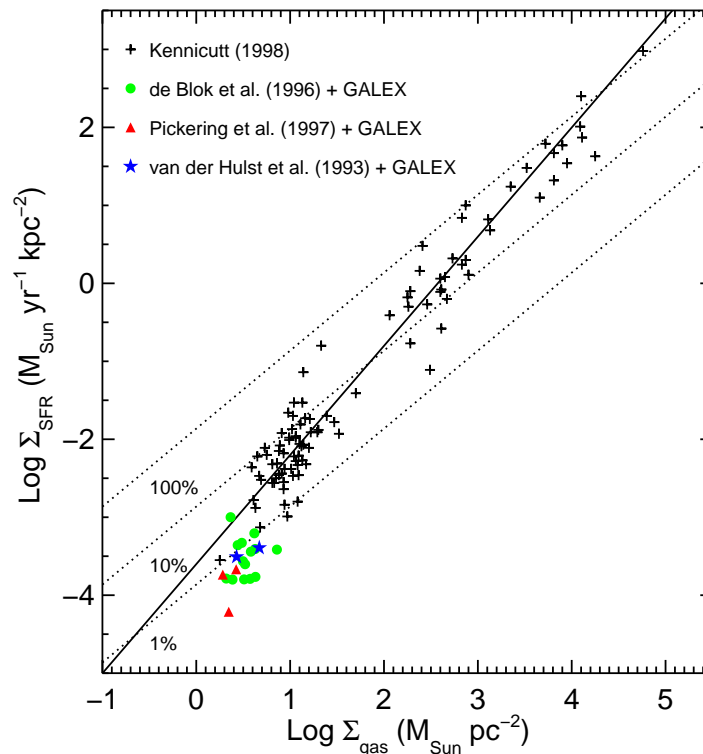
Figure 1.1. Global Star Formation Law. From Wyder et al. (2009), the star formation rate surface density as a function of the total hydrogen (neutral + molecular) gas surface density. The star-formation law (black crosses + solid line; Kennicutt 1998) is generally thought to be a single power law of the form $\Sigma_{SFR} = A\Sigma_{gas}^N$ where N = 1.4±0.15. New data in the low-density regime (compiled from various references and studied in Wyder et al. 2009) may show a downturn at low densities.

tional instabilities are predominantly global, potentially formed by large-scale flows (Heitsch & Hartmann, 2008), or regulated locally by supersonic turbulence, and/or cloud-cloud collisions (Krumholz & McKee, 2005; Tasker & Tan, 2009). Additionally, there are a multitude of alternative non-gravitational explanations for how a gas cloud originally becomes unstable to collapse, including: the onset of thermal instability at threshold radii in the form of a gas phase transition (Schaye, 2004), magnetic regulation (Shu et al., 2007; Mac Low, 2009), and self-regulation from supernova-generated turbulence (Silk, 1997). All of these models have varying degrees of success at reproducing the observed global relation, underscoring how difficult it is to determine the dominant process(es). In this regard, more observations that cover a broad range of physical conditions and scales are essential.

1.1.1 The Spatially-Resolved and Low-Density Star Formation Laws

Understanding the physical origin of the global star formation law, and the scales and densities over which it holds is of fundamental importance not only to the study of star formation, but also galaxy evolution. Cosmologists often use the empirical star formation law in their star-formation prescriptions to reproduce the observed galaxy luminosity function, for instance (Kay et al., 2002). There are two primary observational approaches to increase our knowledge of what is driving the dependence of the star formation rate on the global gas density: the first is to take a spatially-resolved approach instead of using disk-integrated measurements that wipe out local variations in gas and SFR densities (Kennicutt et al., 2007; Bigiel et al., 2008), and the second is to study the SFR-gas density relation in extreme environments.

The first method has seen key advances in the last few years with results from *Spitzer* and GALEX, combined with high-resolution CO and HI maps. Kennicutt et al. (2007) shows that in M51, down to scales of individual star-forming regions, the global star formation law originates from a local relationship between the CO-inferred molecular gas surface density and the SFR density. At sub-kpc scales using GALEX UV SFRs, Bigiel et al. (2008) finds a departure from the N=1.4 Schmidt law, with N=1.0. Their interpretation is that stars are forming in giant molecular clouds with uniform properties and an efficiency that varies as a function of galactocentric radius. Both of these studies find that, on local scales, the SFR does not correlate with the neutral gas, and both provide important advancements in terms of what theoretical models must account for.

Star formation in the so called "low-density regime" (Bigiel et al., 2008; Wyder et al., 2009), below the typical gas-density "thresholds" for star formation ($3-10$ $M_\odot$ pc^{-2}; Martin & Kennicutt 2001) holds significant promise to further our knowledge of how star formation proceeds in galaxies. Since these thresholds arise naturally from the form of the star-formation law, it goes hand-in-hand that at low gas densities, the star formation rate power law begins to break down (Skillman, 1987; Kennicutt, 1998b). Lelièvre & Roy (2000) observed a steepening of the power-law, with N = 2.9, in the low density gas outside of NGC 628 (see next Section). With a study of 19

low-surface-brightness galaxies, Wyder et al. (2009) find a similar downturn in the Schmidt law at gas densities less than 10 $M_\odot pc^{-2}$. They additionally find this result to be consistent with the predictions of Krumholz & McKee (2005) that claim there is a downturn because star formation occurs in supersonically turbulent molecular clouds in which the local gravitational potential energy exceeds the turbulent energy (causing collapse), and the molecular gas fraction declines with decreasing total gas density. Work in this low-density regime is still in the early stages, and additional studies of these environments are essential.

1.1.2 Star Formation in the Outskirts of Galaxies

The first detailed examination of star formation in the low-density gas beyond optical radii was that of Ferguson et al. (1998b), who obtained deep, wide-field Hα images of 20 face-on spiral galaxies to find the outermost HII regions. In three of these face-on spirals, NGC 628, NGC 1058, and NGC 6946, they found isolated HII regions organized in faint spiral arms extending into the "extreme outer limits" of all three galaxies. Lelièvre & Roy (2000) discusses the properties of the outlying HII regions of NGC 628 presented by Ferguson et al. (1998b). In total, there are 137 HII regions detected beyond the optical radius of NGC 628 at which the surface brightness drops below 25 mag/sq. $''$ ($R_{25} = 15.7$ kpc). They lie up to 27 kpc from the galaxy's center, and having average ionizing luminosities fainter by 2 orders of magnitude than HII regions within the optical star forming disk (10^{37} ergs s^{-1} vs 10^{39} ergs s^{-2}). Figure 1.2 shows a portion of the Hα continuum-subtracted image of NGC 628, where Hα emission (red) traces the HII regions, and the broadband R-band light (blue) traces the integrated, underlying population of stars. It is apparent in this image that although star formation persists at large radii, it is generally fainter and sparser.

In a discussion of gravitational instability criteria for star formation, Martin & Kennicutt (2001) hypothesize that the occasional presence of isolated HII regions beyond "critical" gas densities for star formation results from local, random density perturbations that generate supercritical pockets of gas beyond typical threshold radii. The true physical trigger for star formation at large radii still remains un-
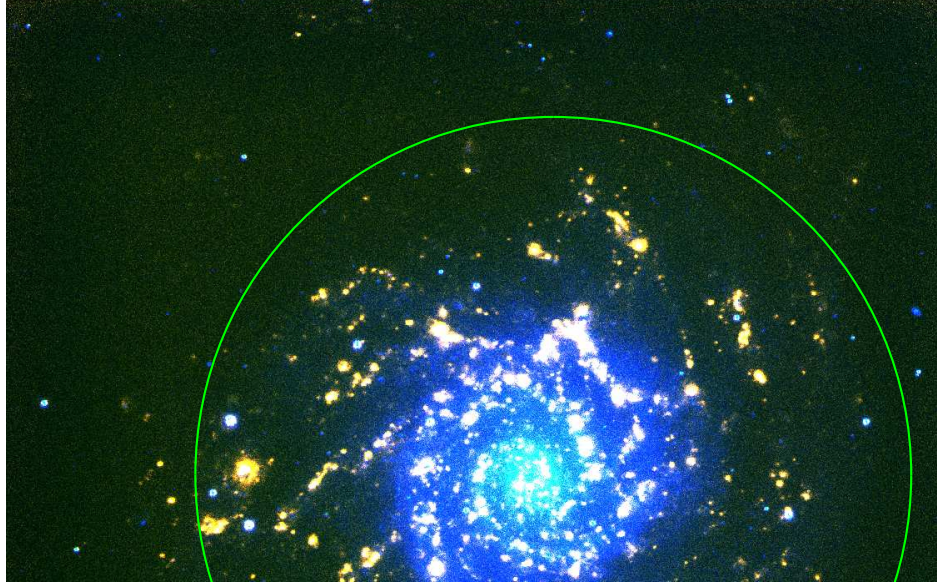
Figure 1.2. The outlying HII Regions in NGC 628. A color Hα and R-band image of the galaxy NGC 628 obtained from the ancillary data of the Spitzer Infrared Nearby Galaxies Survey (SINGS; Kennicutt et al. 2003) that highlights the star formation that persists beyond optical radii. The green circle marks the optical radius of the galaxy, R_{25}.

der debate, and the topic of outlying star formation (often going by such names as isolated, intergalactic, or intracluster HII regions) continues to gain attention in the scientific literature (Boquien et al., 2007; Walter et al., 2006; Oosterloo et al., 2004; Ryan-Weber et al., 2004; Cortese et al., 2004; Sakai et al., 2002; Gerhard et al., 2002; Arnaboldi et al., 2002).

Most of the attention paid to outlying star formation in the last few years has come on the heels of GALEX results that find FUV-bright extensions of optical disks out to large galactocentric radii (XUV disks) in 30% of nearby spiral galaxies (Thilker et al., 2007). M83, a prominent example of XUV star formation (Thilker et al., 2005), is shown in Figure 1.3. The GALEX FUV radiation follows primarily O and B stars, unlike Hα which represents the ionizing radiation of O stars (Meurer et al., 2009). Because of a general lack of multiwavelength, high-resolution, and spectroscopic data at large galactocentric radii, these UV-studies have generated more questions than answers about star formation in the outskirts of galaxies, including: To what extent does Hα emission at large radii tell a story consistent with that of the UV radiation (Goddard et al., 2010)? Is the star formation at large radii simply an extension of
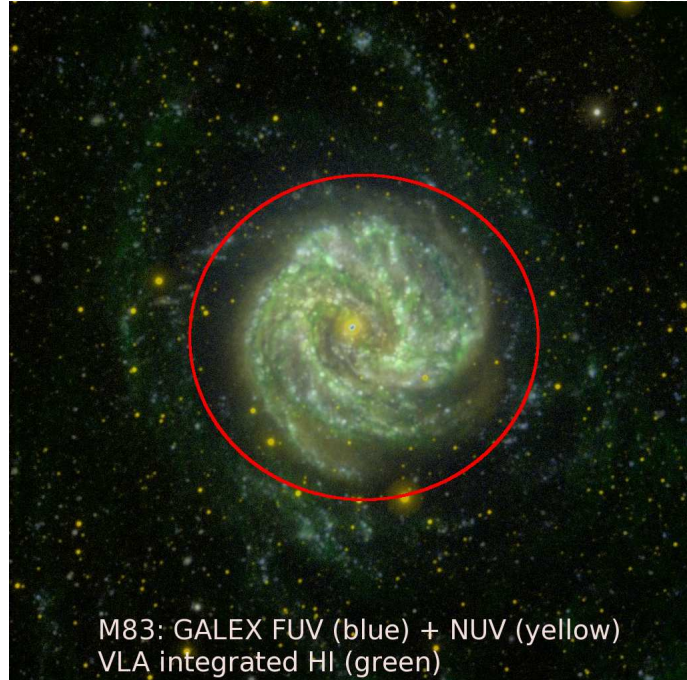
Figure 1.3. Extended Star Formation in M83. GALEX two color image (FUV = blue, NUV = yellow) of M83 overlaid with the VLA HI data (transparent green) from The HI Nearby Galaxies Survey (THINGS; Walter et al. 2008). The XUV disk is visible beyond the red circle, which marks the optical radius for M83.

the inner-galaxy star formation? And, what can the star formation history and the metal content of the gas at large radii tell us about galaxy formation, evolution, and fundamental observed scaling relations? These uncertainties, in part, are due to a lack of information about the underlying stellar populations.

1.2 The Stellar Populations of HII Regions

Star formation in our Galaxy and others generally appears to be organized hierarchically: from spiral arms, to giant complexes, to OB associations, to star clusters, to subgroups within star clusters (Blaauw, 1964; Efremov et al., 1987; Efremov, 1995; Bastian et al., 2005). Figure 1.4 shows an example of the distribution of stars and HII regions in a *Hubble Heritage* color-composite image of a section of one spiral arm in M51 (Mutchler et al., 2005). This hierarchical structure may ultimately dictate the subsequent evolution of star clusters themselves, often viewed as a fundamental unit of star formation (Elmegreen & Hunter, 2010). The intrinsic properties of star

clusters and their stellar populations have been discussed since the early 20th century (Blaauw, 1964). For this reason, there are numerous ways to classify them: by age, by stellar density, by internal kinematics, by mass, and by environment (Lada & Lada, 2003). Here, we discuss the stellar populations of HII regions, which are, by definition, clouds of ionized gas illuminated by a star or stellar cluster containing stars massive enough to emit Lyman continuum photons (E > 13.6 eV). The stars that power HII regions traditionally reside in OB associations – loose, gravitationally-unbound groupings of young stars and clusters of stars (Age <10 Myr) that produce ionizing radiation.

Figure 1.4. Hierarchical star formation in M51 seen in the ACS Hubble Heritage color-composite image. There are four bands represented in this color image: F435W (B, blue), F555W (V, green), F814W (I, orange-red), along with F658N (Hα, diffuse bright, pink-red). This image shows just a portion of one spiral arm in M51, in which there are bright stellar complexes composed of clusters of stars, some of which correspond to HII regions as evidenced by their Hα emission. The hierarchical star formation in M51 has been explored by Bastian et al. (2005). This image is approximately 4.5 × 3.5 kpc, with one resolution element in the image corresponding to 4.6 pc.

1.2.1 Integrated Properties of OB Associations

HII regions and their parent OB Associations are a readily visible tracer of star formation in galaxies, and correlating their fundamental properties with galactic environment is potentially useful for understanding the processes that govern star formation. Observed HII regions have a wide range of ionizing luminosities (generally determined from the recombination Balmer series emission line Hα), $\sim 10^{36}$ - $10^{39.5}$ ergs s^{-1}, corresponding to underlying parent OB associations with an equal range of stellar populations. For example, HII regions like the nearby Orion nebula are ionized by only a few O stars, whereas the most luminous HII regions, like 30 Doradus, are ionized by hundreds of O stars (Hillenbrand, 1997). Furthermore, as mentioned in Section 1.1, the distribution and total number of HII regions (and thus their SFRs) in galaxies varies according to galaxy Hubble type. Perhaps it is then somewhat surprising that galactic environment, at least thus far investigated for spiral galaxies, seems to have very little impact on the stellar populations of the OB associations powering HII regions within nearby spiral galaxies (Bresolin et al., 1998). Systematic trends in the star-formation activity along the Hubble sequence (Kennicutt, 1998a) are simply due to differences in total number of ionizing stars and the number of HII regions per unit area (Bresolin & Kennicutt, 1997). These results that the intrinsic properties of HII regions are universal across a wide range of spiral galaxies hint that the star formation process is rather robust and uniform; however more galactic environments should be investigated.

A caveat to the universality mentioned above is that in all but the most nearby galaxies, there is not adequate resolution to count and obtain spectral types for individual stars in an OB association. In these instances, one must rely on integrated light measurements and stellar population synthesis models to deduce their intrinsic properties like mass, stellar density, and age. The basic method of stellar population synthesis has been around since the late 1960s (Tinsley, 1968). Essentially, it involves the summation of individual stellar "templates" (derived from a grid of stellar evolution tracks that give effective temperatures and bolometric luminosities for various stellar masses as a function of time, and converted to broadband luminosity

using stellar atmosphere models or spectral libraries), weighted by some assumed initial mass distribution of the stars, to ultimately obtain the luminosities, colors, and spectra of a single-generation stellar population (of some assumed metallicity) as a function of its age (Bruzual A. & Charlot, 1993; Leitherer et al., 1999). Then, in theory, if one can measure the broadband luminosity of a star cluster in several different broadband filters, one can determine its age, mass, and integrated stellar spectrum. Evolutionary synthesis models also allow one to go from an Hα luminosity to the number of ionizing O stars that are present within an unresolved HII region.

There are, however, well-known degeneracies in evolutionary synthesis models, especially at young ages (like OB associations) and low luminosities. For instance, it has been shown that for low-mass young star clusters, e. g. with luminosities $M_V <$ -10.0, there are not enough stars to sample the full range of stellar initial masses in a typical power-law initial mass function (IMF) with an exponent of -2.35 (Salpeter, 1955), upper mass limit of 100 $M_\odot$, and lower mass limit of 0.5 $M_\odot$ (Cerviño & Luridiana, 2004). These stochastic effects lead to a great deal of uncertainty in the derived properties of a star cluster. There are additional uncertainties in the assumed "universal" power-law form of the stellar IMF, including the range of stellar masses over which it applies. Indeed, questions as to whether there is a broadly-varying upper mass limit to the IMF, dependent on environment, metallicity and/or cluster properties, have been proposed since the introduction of the functional form of the IMF by Salpeter (1955). This topic is quite rich, owing to the profound influence the distribution of initial stellar masses has on the observed properties of clusters, and the insights into the star formation process such a distribution can provide.

1.2.2   Distribution of Masses in Outlying OB Associations

A great many global trends for galaxies (e.g. mass-metallicity relation for low-mass galaxies (Köppen et al., 2007), increasing SFRs for later type galaxies (van den Bergh, 1976)) can be explained by a variable stellar IMF, in lieu of some other physical explanation (Bastian et al., 2010). However, directly observing departures in the power-law form of the IMF, and the appropriate stellar mass range over which functional forms

apply, are complicated by incomplete statistics, observational selection effects, uncertainties in extinction, and more. Because of the different ranges of stellar masses probed by direct measurements of UV radiation ($M_* > 3\ M_\odot$) and Hα emission ($M_* > 15\ M_\odot$), there has been a recent focus on Hα/UV ratios over a range of galaxy luminosities and surface brightnesses (generally a proxy for galaxy mass) as a useful way to constrain the upper end of the stellar IMF on galaxy-wide scales. From these studies, there has emerged a global trend (seen in Figure 1.5) in which the Hα/UV flux ratio systematically decreases with galaxy luminosity, surface-brightness, and total SFR (Meurer et al., 2009; Lee et al., 2009; Hunter et al., 2010). This trend cannot easily be explained by uncertainties in the evolutionary synthesis models, dust-attenuation, incomplete sampling of the stellar IMF, leakage of ionizing photons, or varying star formation histories. There are then strong implications that this trend is a signature of a lower upper mass limit to the stellar IMF (and/or a different slope) in galaxies with less-efficient star formation (Meurer et al., 2009). However, some combination of several of the uncertainties listed above, could, in theory, also be responsible (Lee et al., 2009).
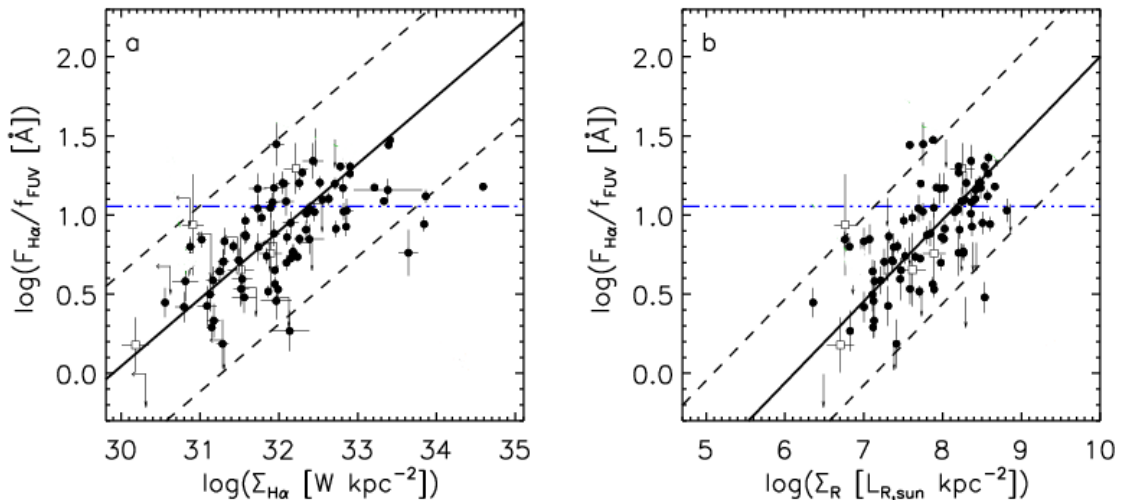
Figure 1.5. The Hα/UV flux ratio vs. galaxy Hα (left) and R-band (right) surface brightness for nearby, star-forming galaxies. The linear-least-squares fit to the data is shown as a solid, black line, while the constant Hα/UV ratio predicted from evolutionary synthesis models with a fully-populated traditional Salpeter IMF is shown as a blue dashed-dotted line. These plots are reproduced from figure 3 of Meurer et al. (2009).

The semi-empirical integrated galactic initial mass function (IGIMF) of Weidner & Kroupa (2005) that employs a dependence of the the maximum mass of a star that can form in a cluster and the cluster total mass predicts the decline of the Hα/UV flux ratio with total galaxy mass and SFR (Pflamm-Altenburg et al., 2009). In this formulation of the galaxy-wide IMF (essentially a top-light IMF, when compared with traditional Salpeter power-law forms), a star cluster is represented by an IMF with an M_{up} (the most massive star in the star cluster) that decreases in value for lower and lower mass clusters. The physical basis for such a dependence has been recently proposed by Krumholz et al. (2010). In their adaptive mesh refinement radiation-hydrodynamic simulations, the feedback from stellar radiation in initially high surface density gas clouds is more effectively trapped, which results in a low-level of fragmentation such that massive stars (in binary systems) form. Conversely, the feedback from stellar radiation in initially low surface density gas clouds can more easily escape, which results in a high-level of fragmentation such that it produces many low mass stars, putting only a small fraction of the gas cloud initial mass into the most massive star. It follows then that the low surface density clouds produce the low-mass star clusters that would have top-light IMFs.

As outlying HII regions are systematically fainter than their inner-galaxy counterparts (Lelièvre & Roy, 2000), and UV radiation is more widespread than Hα emission at large radii (Thilker et al., 2007), the outer regions of galaxies are prime testing grounds for potential variations in the upper mass limit to the IMF. Several initial studies in this regard indicate that the faintness and sparseness of outlying HII regions is consistent with a size-of-sample statistical effect rather than a top-light IMF (Zaritsky & Christlein, 2007; Goddard et al., 2010). Yet, there have been no conclusive studies to date of a spatially resolved, source-by-source comparison of Hα and UV light for nearby galaxies, nor of the resolved stellar populations at large galactocentric radii.

1.3 HII Regions as Tracers of Gas-Phase Metallicity

Spectroscopic studies of HII regions are integral to the study of star formation in galaxies. At the low electron densities typical of HII regions ($n_e < 10^4$ cm^{-3}), forbidden emission lines, such as [OIII] $\lambda\lambda$4959, 5007 and [OII] $\lambda\lambda$3727, are characteristic features of HII region emission-line spectra, along with the radiative recombination lines of the hydrogen Balmer and Paschen series (e.g. Hα). Because the strength of every emission line from every element present in the HII region depends on its chemical abundance in the nascent ISM gas, HII regions are valuable metallicity indicators (Osterbrock, 1989). As such, they trace the star formation history of the gas (the vast majority of elements heavier than He are fused within stars) and act as chemical tags that can aid in determining the origin of the gas.

A direct measurement of the HII region's oxygen abundance from the oxygen emission lines present in its spectrum requires a measurement of the temperature-sensitive line ratio [OIII] $\lambda\lambda$4959, 5007/λ4363 (Osterbrock, 1989). Yet, the critical emission line [OIII] λ4363 is often too weak to be detected, especially in low-temperature and high-metallicity gas. However, there are numerous calibrations between emission lines of greater intensity that trace the gas metal abundance with reasonable success. One in particular, R_{23} = ([OII] λ3727 + [OIII] $\lambda\lambda$4959, 5007) / Hβ (Pagel et al., 1979), seems to follow the direct oxygen abundance well, because of the stellar mass-temperature-metallicity relation which naturally produces a softening (low-excitation) of stellar spectra with increasing metallicity (McGaugh, 1991).

The effect of self-enrichment (metals ejected into the HII region via strong winds from Wolf-Rayet stars) on the measured gas metal abundances in HII regions has been a topic of discussion since the early 1990's. If winds from massive stars significantly enrich HII regions on timescales shorter than 10^7 years, then the usefulness of HII regions as local ISM metal abundance indicators and tracers of the gas star-formation history may be limited. However, there is no convincing evidence that HII regions are significantly polluted by massive star ejecta, as indicated by the low dispersion in O/H abundances across galaxies (Kennicutt & Garnett, 1996; Kobulnicky, 1999) and

that HII region oxygen abundances follow stellar abundances quite well (Bresolin, 2010). The most likely physical explanation as to why not is that the ejecta are in the hot phase of the ISM (T = 10^6 - 10^7 K) while the HII region gas is at a cooler phase (T < 10^4 K), and the metals cannot mix efficiently through diffusion because of these differences in temperature and density (Tenorio-Tagle, 1996). A recent study by Wofford (2009) models self-enrichment of metal-poor HII regions and confirms that the maximum oxygen abundance enhancement from the winds of Wolf-Rayet stars would be only 0.025 dex, unobservable by current methods. Therefore, we can reasonably assume that HII regions are reliable indicators of the true metal abundance of the gas in their vicinity.

1.3.1 The Chemical Evolution of the Outermost Gas

The practice of determining chemical abundance gradients using HII region emission-line spectra was initiated by Searle (1971), who inferred a declining Galactic O/H abundance gradient from the observed increase in HII region excitation and temperature with radius (with [OIII]λ4959,λ5007 /[OII] λ3727 and [OIII]/Hβ ratios). Shields & Tinsley (1976) confirmed the anti-correlation between T_{eff} and metallicity, and attributed the radial gradients to a metallicity dependent upper mass limit for star formation such that $M_{upper} \propto Z^{-1/2}$, a scaling theoretically determined by Kahn (1974) who model massive star formation with a radiation "cocoon." Since then, numerous detailed studies have confirmed the overall trend for the decrease in oxygen abundance with galactocentric radii (e.g. Oey & Kennicutt 1993; Zaritsky 1994; Bresolin et al. 1999; Kennicutt et al. 2003 in a large number of spiral (barred + unbarred) and irregular star-forming galaxies, although the underlying physical cause is still a subject of debate. The radial oxygen abundance gradients of nearby spiral galaxies range from -0.03 dex/kpc^{-1} to -0.15 dex/kpc^{-1} (Zaritsky et al., 1994).

Potential causes for the observed gradients could be a radial variation of the star formation rate via a local star formation law and threshold density for star formation (Phillipps & Edmunds, 1991), an "inside-out" model of galaxy formation such that the inner galaxy disk forms first though gas infall (Fu et al., 2009) coupled

with the radial dependence of star-formation activity, or star-formation in "viscous" disks (Zaritsky, 1992; Ferguson & Clarke, 2001). In the last explanation, Zaritsky (1992) notes that the single scale-length exponential surface luminosity profiles of galaxies arise naturally in star-forming, viscous disks (Lin & Pringle, 1987; Sommer-Larsen & Yoshii, 1990), and demonstrates that this same effect successfully reproduces radial abundance gradients in non-interacting, unbarred spiral galaxies as well. In this model, the abundance gradient flattens at the knee of the rotation curve of the galaxy. Although the results of Bresolin et al. (2009) for the flat abundance gradient in the outer disk of M83 might confirm this predicted trend, it is not generally accepted that abundance gradients flatten at large radii due to a dearth of data at these large distances (van Zee et al., 1998). There is a further lack of abundance gradient observational data for both dwarf galaxies (Croxall et al., 2009) and irregular, disturbed, or interacting galaxies (Rupke et al., 2010).

1.3.2   The Mass-Metallicity Relation for Galaxies

There is a fundamental, global relation between galaxy mass and metallicity in the sense that lower mass galaxies have lower overall heavy-element content. Larson (1974) first predicted that the average stellar metal abundance in a galaxy would depend on its mass owing to more significant gas loss from the energy supplied by supernovae in lower-mass galaxies. His notion turned out to fit well with observations of nebular oxygen abundances of irregular galaxies several years later by Lequeux et al. (1979), and has become known as the mass-metallicity relation for galaxies in the 36 years since (Skillman et al., 1989; Tremonti et al., 2004). We show the strong correlation between galaxy B-band luminosity (a proxy for stellar mass) and metal content in Figure 1.6. This relation is often parameterized in terms of effective yields and and total (gas + stellar) mass to elucidate its origin, where effective yield measures how much a galaxy's metallicity deviates from its "closed-box" value, given a certain gas mass fraction (see Chapter 4 for details). Systematically low effective yields of dwarf galaxies have been taken as evidence that low mass galaxies have evolved less as "closed-boxes" than their more massive counterparts (Tremonti et al.,

2004).
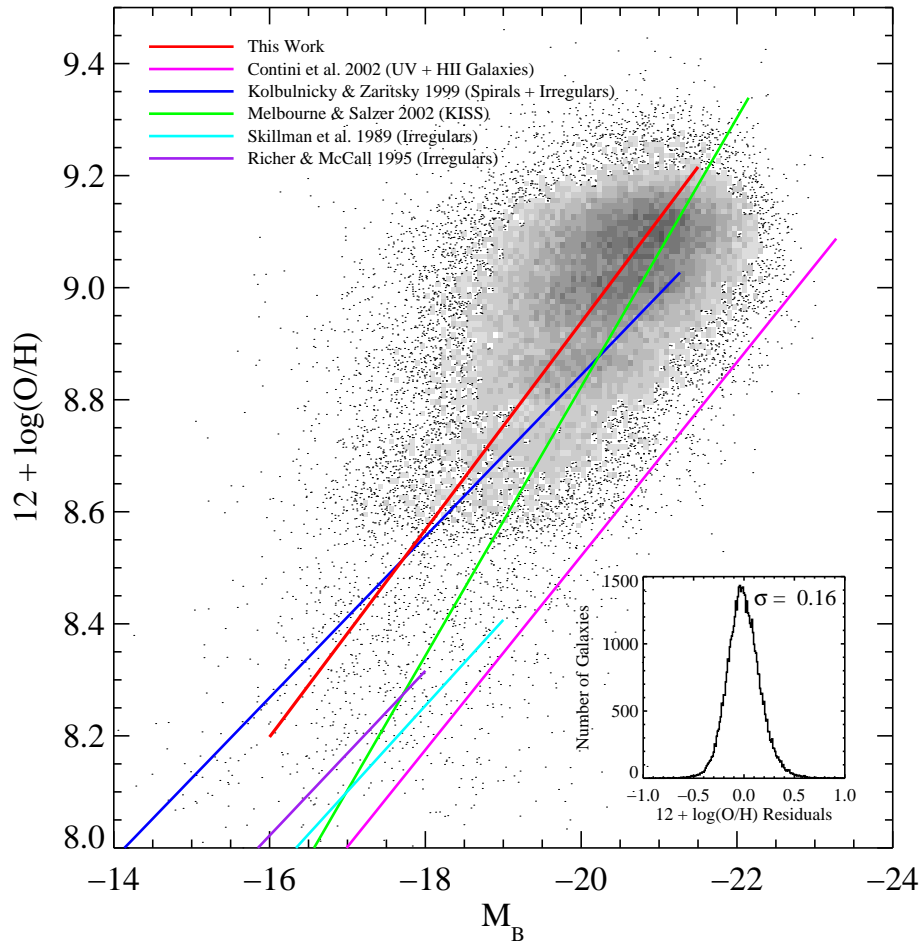
Figure 1.6. The luminosity-metallicity relation for 35,000 SDSS galaxies, as 12 + Log (O/H) vs. B-band absolute magnitude. This plot is reproduced from figure 4 of Tremonti et al. (2004). Several other derived relations are overplotted atop the best-fit line of Tremonti et al. (2004) (red), yet their values of 12 + Log(O/H) were obtained using various different methods. Much of the scatter is due to the large errors in the oxygen abundances.

Although supernova-driven metal expulsion is the most popular and classic explanation for the low effective yields of dwarf galaxies (Larson, 1974; Tremonti et al., 2004), there are several issues that complicate the picture. Dalcanton (2007) shows, for instance, that metal loss itself does not have a strong dependence on galaxy mass, and that any subsequent star formation following an episode of mass loss quickly pushes the effective yield up to its closed-box value. In the calculations presented by Dalcanton (2007), low star formation efficiencies in gas-rich dwarfs be-

tween episodes of mass-loss are what keep their effective yields low. Dilution by infalling low-metallicity gas may also play some role, but alone cannot explain the mass-metallicity relation (Dalcanton, 2007). An explanation offered by Tassis et al. (2008) is that the metals are not expelled via supernova-driven winds, but rather efficiently mixed via gravitational processes into the hot halo gas, where they are unobservable by standard ground-based methods. Coupled with low star formation efficiencies of low-mass, gas-rich dwarfs, Tassis et al. (2008) can reproduce the observed mass-metallicity relation without including winds from supernova in their model. And finally, if low-mass galaxies preferentially do not make as many O-type stars as more massive galaxies, as in the IGIMF theory, then their effective yields will appear to be low (Köppen et al., 2007). One big unknown in gas-rich dwarfs is the metal content of the gas that extends beyond their central star forming optical bodies (Garnett, 2002). Such measurements might help to untangle the chemodynamical processes that set the mass-metallicity relation.

1.4   In This Thesis...

Outlying HII regions act as the single thread that unites all of the topics discussed in the previous sections. A systematic, in-depth study of their nature has the potential to shed light on several vital questions that persist in the continuing efforts to understand star formation in galaxies:

- How frequently does massive star formation, as indicated by Hα emission, occur beyond the main optical bodies of gas-rich galaxies? The answer to this question may help us to understand the trigger of star formation and the form of the star-formation law in low-density gas. Comparing this frequency to that of outlying UV-bright star clusters may provide evidence for or against a varying stellar IMF at large radii.

- Do OB associations at large projected radii carry a clear imprint of the environment in which they form? Determining the ages and masses of the stars that form outside of spiral arms is essential for understanding the formation

and evolution of clusters as a function of their local environment.

- Do the declining radial metallicity gradients observed for nearby, star-forming galaxies continue to decline at large radii? The shape of the metallicity gradient over a wide range of galactic radii will inform our limited understanding of global metal dispersal in galaxies.

- What can the metal abundance in the outermost gas of galaxies tell us about the processes that govern the mass-metallicity relation? These measurements will help us to distinguish between potential underlying causes such as supernova-driven metal expulsion, the infall of pristine gas, and metal-mixing.

In this thesis, I address the above questions about star formation in the mostly-gaseous, far outskirts of galaxies by examining the detailed properties of a population of outlying HII regions. Following long-standing astrophysical techniques dating back to the 1950s (the review of Shields 1990 contains a comprehensive list of references), I use these HII regions as laboratories for understanding massive star formation, star clustering, and chemical feedback processes, and attempt to place my results into the larger context of galaxy evolution and fundamental scaling relations.

1.4.1 The Frequency and Nature of Outlying HII Regions

Chapter 2 addresses the frequency of outlying HII regions in gas-rich galaxies, and how it compares to the frequency of XUV disks in nearby spiral galaxies. It is the first study to perform a systematic search for outlying HII regions in an unbiased sample of gas-rich galaxies. Previous work on the subject of outlying HII regions tends to focus on individual systems and very nearby (D < 15 Mpc), face-on spiral galaxies. Instead, I report the frequency of outlying HII regions in the Survey for Ionization in Gas Rich Galaxies (SINGG; Meurer et al. 2006) selected via a set of uniform criteria applied to the survey data using a self-developed automated algorithm. SINGG provides Hα and continuum R-band imaging of galaxies that sample the full HI mass spectrum probed by the HI-Parkes All Sky Survey (HIPASS; Barnes et al. 2001). Because SINGG selects galaxies based on their HI content, its data are not prone

to many of the optical and infrared selection effects that bias the local view of star formation demographics. The resultant sample contains star-forming galaxies of all morphologies (Meurer et al., 2006), and can recover the SFR density of the local universe (Hanish et al., 2006).

1.4.2 The Underlying Stellar Populations of Outlying HII Regions

Even if HII regions within nearby galaxies exhibit similar stellar populations across a range of morphological types, there is still some question as to whether the outermost HII regions in galaxies, often far beyond the influence of spiral density waves and located in the low-density gas at the outskirts, have the same properties as typical extragalactic and Galactic HII regions. I address that very question in Chapter 3, by examining deep *HST* ACS High-Resolution Channel (HRC) images of 3 outlying OB associations and comparing their stellar populations to those typical of Galactic and extragalactic HII regions. I also comment on their likelihood for survival in the context that the vast majority of star clusters are disrupted on timescales of 10 Myr independent of their initial masses (Fall et al., 2005; Chandar et al., 2010). Since the stellar masses of these intrinsically faint outer HII regions are below 10^4 M$_\odot$, I consider the effects of failing to completely sample the full range of stellar initial masses along a typical Salpeter IMF as well.

1.4.3 The Metal Abundances of Outlying HII Regions

In Chapter 4 we report the first oxygen abundance gradient that reaches significantly beyond optical radii in dwarf galaxies in the very gas-rich star-forming dwarf galaxy NGC 2915. We use outlying HII regions located in the extended gas disk of this galaxy to make strong-line oxygen abundance measurements, and find that the outer HII regions are just as metal-enriched as those in the optical interior of the galaxy. This result has implications on the dwarf galaxy mass-metallicity relation and on the distribution of metals throughout extended gas disks. In Chapter 5 we explore the oxygen abundance gradients out to large galactocentric radii in 13 additional gas-rich systems having a wide range of optical and gaseous morphologies, all of which

have outlying HII regions. These measurements, for the first time, convincingly show flat abundance gradients at large radii in a wide variety of systems, and have broad implications for galaxy chemodynamical evolution.

CHAPTER 2

The Frequency and Nature of Outlying HII Regions in HI-Selected Galaxies

2.1 Introduction

Several recent studies of spiral galaxies with extended UV (XUV) disks (Thilker et al., 2005; Gil de Paz et al., 2005) have indicated that the spatial extent of star formation in outer disks is underestimated by looking for HII regions alone (via Hα imaging), as Hα emission tends to be even less widespread than predicted by typical stellar population synthesis models that incorporate a power-law IMF with a slope of $\alpha \sim 2.35$. The reasons for this relative lack of Hα emission at large galactocentric radii could be many, including but not limited to stochastic fluctuations in the IMF at low stellar luminosities (Boissier et al., 2006), a top-light IMF in the remotest reaches of galaxies (Meurer et al., 2009), or a large fraction of escaping ionizing photons from the less dense outer-galactic regions (see Introduction). The extent of this underestimation, specifically at large projected galactocentric distances, remains unquantified, as no comprehensive systematic study of Hα emission in the outer reaches of galaxies has yet emerged.

Here, we fill that gap in our knowledge of star formation in the outskirts of galaxies by returning to Hα imaging to search for outlying HII regions. As a star formation tracer that is sensitive to only the highest mass stars, Hα provides an important complement to the recent GALEX results. We perform an automated search to find outlying compact sources of net line emission using the imaging data from the Survey for Ionization in Neutral Gas Galaxies (SINGG; Meurer et al 2006; hereafter M06). The large angular area outside the optical radius of galaxies in each 14.7´ SINGG field

presents the opportunity to search for outlying HII regions at large radii and perform a blind search for background emission-line sources. We initially refer to both types of sources as "ELdots" for their appearance as emission line dots in the images. In all cases, ELdots exhibit strong emission lines in the SINGG narrowband filter, and are point sources well outside the broadband optical emission of nearby galaxies (r>2 × r_{25}). ELdots can be outlying Hα-emitting HII regions at a similar velocity to the HIPASS source galaxy or background galaxies emitting a different line ([OIII], [OII], or Hβ) that is redshifted into the narrow filter passband used for the observations. To distinguish between these options, we present follow-up spectroscopy and deep archival GALEX images for a subsample of ELdots.

In this study, we are primarily interested in the Hα-emitting ELdots, although we tabulate the properties of the background galaxies as well. We call Hα-emitting ELdots "outlying HII regions." They are distinct from the central galactic star formation, and more sparse, yet they often lie in extended neutral gas and/or an extended UV component associated with the galaxy. Outlying HII regions (abbreviated outer-HIIs) provide a unique laboratory to understand star formation under relatively extreme conditions (e.g. low neutral gas column density, weak galaxy potential), and may shed light on the full extent of stellar disks (Bland-Hawthorn et al., 2005; Irwin et al., 2005).

The chapter proceeds as follows: in Section 2.2, we describe the SINGG sample; in Section 2.3, we describe our ELdot sample selection; in Section 2.4, we present spectroscopic observations of a subsample of ELdots; in Section 2.5 we examine the ELdots in deep GALEX images, where available from the archives; in Section 2.6, we discuss the properties of our ELdot sample; in Section 2.7, we discuss extended star formation in SINGG; and in Section 2.8 we summarize and present the key findings of this study.

2.2 SINGG data

We searched for ELdots in the SINGG Release 1 (SR1) imaging data presented by M06. A full description of the sample, observations, and data reduction techniques

used by SINGG is presented by M06. Here we summarize the most relevant facts and refer the interested reader to M06 for details. The SINGG sample was selected from the HI Parkes All-Sky Survey (HIPASS; Barnes et al. 2001) purely on the basis of HI mass and recessional velocity. SR1 consists of observations of 93 HIPASS targets, which contain a total of 111 emission line galaxies. We refer to the HIPASS targets/SINGG fields as JXXXX-YY, where XXXX is RA in hours and minutes and YY is declination in degrees. In the text, we refer to the galaxy(ies) contained in the field with their common optical names (e.g. NGC 1512). For reference, table 6 of M06 contains the common optical name for each HIPASS target.

The SINGG images obtained with the CTIO 1.5m telescope have a field of view of $14.7'$ and typically consisted of three dithered images with a combined exposure time of 1800s in a narrow band filter (band pass widths $\sim 30-75\text{Å}$) to isolate the redshifted Hα emission, and 360s exposures in the R band for the continuum. Following standard CCD image processing, a net Hα image was created from differencing the combined images in each filter after a suitable convolution to match point spread functions. Observations of spectro-photometric standards were used to flux calibrate the data. The median seeing was $1.6''$ while the median 5σ limiting Hα flux for a point source is $2.6 \times 10^{-16}\,\text{erg}\,\text{cm}^{-2}\,\text{s}^{-1}$. The median Hubble flow distance of the entire SINGG sample is 18.5 Mpc, corresponding to a median FOV of 79 kpc. Foreground Galactic dust extinction was removed using the reddening maps of Schlegel et al. (1998). All magnitudes are in the AB magnitude system.

The discovery of outer-HIIs in SINGG was initially presented by Ryan-Weber et al. (2004; hereafter RW04), who performed a by-eye search of the SR1 data for ELdots. This work represents a continuation of RW04, with the addition of an automated search algorithm developed specifically to pick out ELdots, follow-up spectroscopy, and comparison with existing deep UV GALEX data. The initial sample presented in RW04 is augmented extensively by our more systematic search and fluxes are updated to include the more recent calibration presented in M06.

2.3 Sample of ELdots

2.3.1 Selection Criteria

We approached our sample selection with the goal of finding HII regions in the outskirts of galaxies or the IGM. We have automated the search for ELdots in an IDL program written specifically for the purpose of finding compact, high equivalent width sources at distances greater than $2 \times r_{25}$ from the nearest SINGG galaxy. The program incorporates SExtractor (Bertin & Arnouts, 1996) for object detection and photometry, and includes the following steps:

- The object detection threshold used by the SExtractor requires that at least three adjacent pixels have counts 3.0σ above the image background level. We use 32 deblending sub-thresholds, with a minimum contrast parameter of 0.005, assuring the detection of small, unresolved objects. We determine magnitude zero-points from the SINGG image photometry described in M06. Since SExtractor is run on sky-subtracted narrow-band and continuum images, we perform no additional background subtraction. Minor sky gradients in a few of the SINGG images amount to variations at the 0.1σ level in the worst cases, and employing a background subtraction in these cases makes virtually no difference in the final sextractor object catalogs.

- To limit the number of spurious detections in the automatically-produced candidate list, we include only those objects which lie in areas of the SINGG images composed of at least two exposures. Usually this amounts to rejecting approximately 100 pixel-wide strips on each edge of the image.

- To keep cosmic rays, hot pixels, and larger angular sized galaxies out of our final sample of ELdots, we implement two cuts in FWHM, calculated individually for each frame. The FWHM size of the object must be greater than 1 pixel and less than the mean image FWHM + 3σ. We show an example of this criterion, and the distribution of object FWHM sizes in the SINGG field J0409-56, in Figure 2.1a. The mean FWHM of objects in the SINGG images is typically

25

(a)

(b)
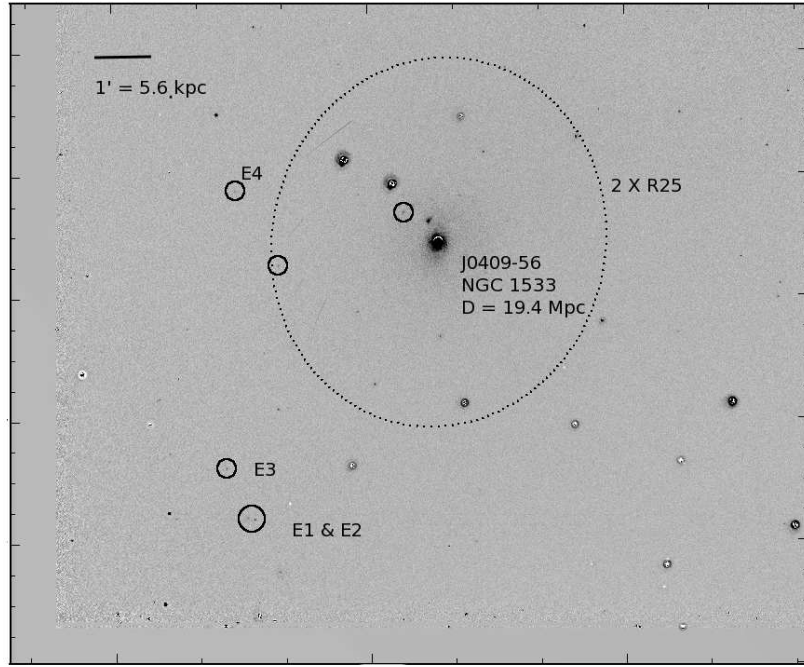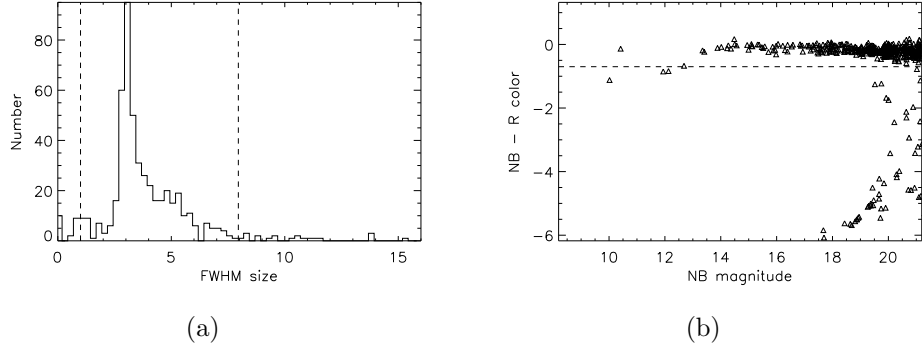
(c)

Figure 2.1. ELdot selection criteria. (a): The distribution of objects' FWHM sizes (in pixels) in the same field, J0409-56, as determined by SExtractor. Dashed vertical lines show the minimum and maximum size thresholds for an object to be classified as an ELdot. (b): The distribution of objects' raw SExtractor NB−R colors in the SINGG field J0409-56. The dashed line represents the color limit of -0.7. ELdots are selected to have colors less than this value. The diagonal line of objects below the color limit represents those objects which have no R-band emission, and are all given the same default upper-limit R-band magnitude. (c): Continuum-subtracted Hα image of J0409-56, with the ELdots circled and labeled. The dotted line represents the $2 \times r_{25}$ elliptical isophote determined from the SINGG R-band image. The two circled sources within $2 \times r_{25}$ are ultimately rejected by the finder, despite meeting size and color criteria. We give the angular and equivalent physical scale in the top left corner. The projected galactocentric distances of the ELdots in this field range from 19 kpc (E4) to 31 kpc (E1 and E2).

near 4 pixels ($\sim 1.6''$ at the pixel scale of SINGG) while the standard deviation (σ) of this size distribution ranges between 1.5 and 2 pixels. Thus, objects with angular sizes greater than $\sim 4''$ ($8-10$ pixels) are eliminated from the sample of ELdots. This maximum angular size represents a broad range of physical sizes when we consider the range of distance spanned by the SINGG sample. The minimum and maximum distances of SINGG targets, roughly 4 Mpc and 70 Mpc, yields maximum HII region sizes of 80 pc to 1400 pc, respectively. We discuss this size selection effect, along with other caveats related to the SINGG ELdots in Section 2.3.3.

- To ensure we include only those objects with real emission lines and little or no continuum emission, we use a NB$-$R (NB= narrow band; R= R band) color cut of -0.7. This cut in color roughly corresponds to a cut in equivalent width of 20 Å. Depending on the filter transmission curve, it can be as low as 5 Å and as high as 35 Å. Figure 2.1b plots the raw NB$-$R color versus NB magnitude for all of the objects meeting the above criteria in the field J0409-56, and shows this color limit.

- The program uses the surface-brightness profiles of each SINGG galaxy in an image, and rejects any object that lies within two times the $\mu_R = 25$ mag arcsec^{-2} elliptical isophote of any of the potential host galaxies in the image. r_{25} is a standard galactocentric distance that generally denotes the full extent of a galaxy's optical disk. Traditionally, it is defined in the B-band. Here, we use $2 \times r_{25}$ in the R-band as a threshold to distinguish between HII regions in the disk and those outside the optical disk. Using values tabulated by the NASA Extragalactic Database (NED), we find the B-band r_{25} values for the SINGG galaxies (where available) range between 1.5 and 2.2 $\times r_{25}$ in the R-band, with an average at 1.9 $\times r_{25}$ in the R-band. We show an example of our $2 \times r_{25}$ (R-band) surface-brightness cut for J0409-56 in Figure 2.1c. A dotted line marks the selection ellipse, and the circled objects represent objects detected by the finder that meet color and size criteria. Two of the six circled objects lie within

$2\times r_{25}$, and are therefore ultimately rejected by the automated ELdot finder.

- Finally, we examine the objects that meet the above criteria in 100×100 pixel ($43" \times 43"$) image cut-outs produced by the program. This step is used to reject the few remaining cosmic rays, or other spurious edge objects.

2.3.2 Sample Overview

Our final sample of ELdots from 93 SINGG images includes 96 compact emission-line sources with line fluxes ranging from 1.07×10^{-16} to 4.16×10^{-15} ergs s^{-1} cm^{-2}. 50 of the 93 SINGG systems probed contain at least one ELdot, sampling the full myriad of SINGG systems, from strongly interacting groups to quiescent spiral galaxies. However, 4 SINGG systems cover such a large angle that little or none of the image area for $r/r_{25} = 2$ -3 is covered, and so we exclude those systems from any statistical analysis. In total, we cover a search area of 4.0 deg^2. Because the narrow band filters used by M06 vary by over a factor of 2 in bandwidth, a more relevant quantity is the volume in terms of Å deg^2, which we determine by multiplying the area beyond $2\times r/r_{25}$ in each field by the full width at half maximum transmission of the filter as tabulated in M06. This calculation yields a total apparent surveyed volume of 165 Å deg^2.

Table 2.1 lists all SINGG ELdots (named by the HIPASS target and ELdot number) and their positions, EWs, distance in r/r_{25} from the host SINGG galaxy, Hα fluxes, R$-$band magnitudes and their errors, information about spectroscopic follow up (see next section) and host galaxy morphologies (see below). We find 24 ELdots in the SINGG field J0403-43, and tabulate the properties of those ELdots separately in Table 2.2. We performed circular aperture photometry on each ELdot using the IDL routine APER, and have accounted for photometric calibration errors (see SR1), and sky and continuum subtraction errors in the listed flux errors. The error due to the pixel to pixel variance of the sky is the largest contributor. Eleven ELdots have no R-band emission above our detection limit of 3σ times the continuum sky variance, and so the values in the table for the R-band magnitudes are upper limits, denoted by a ">".

Column 10 of Table 2.1 contains a morphological type defined as follows: Solitary (solo) signifies that this SINGG galaxy has no known companions and is free from morphological disturbances in SINGG Hα and continuum images, HI synthesis maps (where available), and digital sky survey images; Companion (comp) indicates a known companion or newly discovered SINGG companion for the galaxy, but no visible disturbance in galaxy structure seen in the previously mentioned set of images; Interacting (int) are systems that are clearly disturbed in either optical or HI synthesis images or both, with or without a discernible nearby companion. The motivation for this classification scheme is twofold. First, we wanted to include information from available neutral hydrogen synthesis maps, which often show disturbance when none is visible optically. Second, we wanted to account for galaxies that have nearby companions, a relevant consideration in the context of ELdots, potential companions themselves. Since the SINGG sample was initially selected based on HI mass, there are very few early-type galaxies within it, so the traditional morphological classification scheme (spiral vs. elliptical) is largely irrelevant. The distribution of morphologies for the 89 SINGG primary galaxies searched for ELdots is as follows: 62 appear to be solitary, undisturbed systems; 17 systems are distinctly disturbed or interacting; and 10 systems have known companions but show no signs of interaction or disturbance. For reference, the 39 systems that do not contain ELdots (and therefore are not tabulated in Table 2.1) have the following morphologies: 31 are solitary systems, 4 have companions, and 4 are interacting.

2.3.3 Selection Effects

Here, we discuss some of the biases inherent in our sample selection method. Because we define ELdots in a purely observational sense (point sources of high net emission in the SINGG narrow bandpass) we are subject to distance-related selection effects. The size selection effect, mentioned above, is such that point sources in the most distant SINGG systems could be well-resolved into dwarf galaxies were they considerably more nearby. For instance, if an ELdot in the most distant SINGG system actually has a physical size of ~ 540 pc (the limit set by the seeing; $1.6''$ at 70 Mpc), it would

Designation	RA	dec	EW	r/r$_{25}$	F$_{line}$	m$_R$	Run ID	Line	Morph
(1)	(2)	(3)	(4)	(5)	(6)	(7)	(8)	(9)	(10)
J0005-28:E1	00 05 19.0	-28 10 24	103	15.9	2.74±0.23	22.44±0.168	Nov05	[OII]	int
J0019-22:E1	00 19 10.5	-22 41 25	263	2.5	3.97±0.37	23.06±0.265	.....	....	solo
J0019-22:E2	00 19 11.1	-22 38 35	299	2.7	3.90±0.37	>23.21	.....	....	””
J0031-22:E1	00 31 12.4	-22 53 20	30	16.6	2.64±0.39	21.17±0.058	.....	....	solo
J0031-22:E2	00 31 34.2	-22 49 13	27	14.2	2.12±0.39	21.27±0.063	.....	....	””
J0039-14:E1	00 39 00.2	-14 13 09	58	3.9	3.16±0.25	21.67±0.088	.....	....	int
J0039-14:E2	00 39 19.1	-14 08 04	53	4.9	4.21±0.27	21.26±0.063	.....	....	””
J0156-68:E1	01 55 36.8	-69 03 08	42	25.9	2.85±0.33	21.43±0.071	.....	....	solo
J0209-10a:E1	02 09 16.2	-10 13 10	148	6.6	9.34±1.16	21.48±0.095	.....	....	int
J0209-10a:E2	02 09 27.6	-10 07 16	456	8.4	8.14±1.15	>22.85	Sep02	Hα	””
J0209-10a:E3	02 09 37.6	-10 05 35	191	10.9	5.00±1.12	22.43±0.212	Nov05	Hα	””
J0221-05:E1	02 21 49.5	-05 27 41	241	3.5	4.47±0.88	22.82±0.221	.....	....	int
J0221-05:E2	02 21 41.2	-05 26 29	90	3.7	3.60±0.87	21.99±0.110	Nov05	[OIII]	””
J0221-05:E3	02 21 29.7	-05 23 50	80	5.3	4.93±0.88	21.52±0.074	.....	....	””
J0223-04:E1	02 23 50.7	-04 37 55	630	2.4	9.62±0.68	23.03±0.247	.....	....	solo
J0223-04:E2	02 23 53.0	-04 37 28	213	2.2	6.30±0.62	22.31±0.136	.....	....	””
J0223-04:E3	02 23 54.3	-04 37 05	387	2.3	9.15±0.67	22.55±0.166	.....	....	””
J0224-24:E1	02 25 21.8	-24 51 59	84	6.2	3.69±0.63	21.87±0.087	.....	....	int
J0256-54:E1	02 56 38.6	-54 40 35	59	3.8	2.71±0.91	21.86±0.112	.....	....	solo
J0256-54:E2	02 57 17.3	-54 39 16	27	8.1	1.80±0.91	21.47±0.081	.....	....	””
J0256-54:E3	02 56 31.3	-54 31 35	54	5.2	2.94±0.92	21.67±0.096	.....	....	””
J0317-22:E1	03 17 10.3	-22 54 18	331	2.2	3.70±0.64	>23.35	Nov05	Hα	comp
J0317-22:E2	03 16 59.3	-22 49 39	132	2.3	2.44±0.64	22.81±0.194	Nov05	[OIII]	””
J0320-52:E1	03 19 49.2	-52 05 24	206	8.7	7.22±0.40	22.14±0.124	.....	....	solo
J0322-04:E1	03 23 12.0	-04 15 16	332	8.5	12.0±0.58	22.09±0.110	Oct03	[OIII]	solo
J0322-04:E2	03 22 54.3	-04 12 58	91	3.6	6.06±0.44	21.43±0.064	.....	....	””
J0322-04:E3	03 22 50.2	-04 10 02	74	2.7	5.40±0.43	21.32±0.058	.....	....	””
J0322-04:E4	03 22 53.1	-04 09 26	64	3.7	2.01±0.39	22.24±0.126	.....	....	””
J0341-01:E1	03 41 30.5	-01 58 09	54	8.9	2.31±0.25	21.91±0.084	.....	....	solo
J0348-39:E1	03 48 22.3	-39 27 03	121	4.3	3.57±1.20	22.32±0.205	.....	....	solo
J0351-38:E1	03 51 55.1	-38 29 22	70	6.2	2.97±0.36	21.94±0.105	.....	....	solo
J0355-42:E1	03 55 59.1	-42 23 03	206	2.2	2.89±0.45	>23.14	.....	....	int
J0359-45:E1	03 58 47.9	-45 47 08	43	8.0	1.84±0.73	21.95±0.118	.....	....	comp
J0409-56:E1	04 10 13.6	-56 11 37	677	3.7	1.05±0.63	>23.02	Sep02	Hα	int
J0409-56:E2	04 10 14.4	-56 11 35	456	3.7	7.07±0.57	>23.02	Sep02	Hα	””
J0409-56:E3	04 10 16.8	-56 10 46	412	3.4	6.39±0.57	>23.02	IMACS	Hα	””
J0409-56:E4	04 10 15.6	-56 06 14	318	2.1	4.93±0.56	>23.02	Sep02	Hα	””
J0441-02:E1	04 41 12.9	-02 53 46	176	2.4	3.60±0.54	22.73±0.265	Dec06	[OIII]	solo
J0457-42:E1	04 56 38.9	-42 43 26	16	12.5	1.25±0.33	21.30±0.064	.....	....	solo
J0459-26:E1	05 00 16.4	-25 59 12	374	2.6	9.16±1.23	22.53±0.250	Nov05	[OIII]	solo
J0503-63:E1	05 03 24.9	-63 42 59	87	2.7	7.74±0.81	21.11±0.072	.....	....	comp
J0504-16:E1	05 04 28.0	-16 35 55	430	2.6	12.0±1.08	22.36±0.162	.....	....	int
J0506-31:E1	05 05 57.7	-31 55 05	28	5.0	2.28±0.48	21.23±0.061	Dec06	[OIII]	solo
J0507-16:E1	05 07 42.5	-16 21 43	102	2.4	2.47±0.84	22.53±0.169	Nov05	[OIII]	solo
J0507-37:E1	05 07 29.8	-37 23 24	182	3.2	18.2±0.90	21.00±0.055	Oct03	[OIII]	solo
J0510-31:E1	05 11 08.7	-31 42 51	108	6.3	1.37±0.34	>23.25	.....	....	solo
J0510-31:E2	05 11 15.6	-31 41 17	187	5.8	2.67±0.35	23.11±0.272	.....	....	””
J0512-32:E1	05 11 28.1	-32 55 41	133	5.0	10.3±1.13	21.28±0.075	Oct03	[OIII]	solo
J0943-09:E1	09 43 42.5	-10 00 55	342	7.1	5.79±0.61	22.91±0.245	May06	[OIII]	solo
J1002-05:E1	10 02 46.9	-05 55 01	28	5.9	7.15±0.47	19.99±0.028	May06	star	solo
J1018-17:E1	10 18 06.9	-18 00 04	123	9.3	3.94±0.79	22.22±0.142	.....	....	solo
J1051-19:E1	10 25 17.3	-20 03 28	138	11.0	6.23±0.56	21.85±0.094	May06	[OIII]	solo
J1051-19:E2	10 25 14.7	-20 03 09	49	11.1	1.23±0.51	22.49±0.162	Dec06	Hβ	””
J1054-18:E1	10 54 25.4	-18 09 17	161	6.5	12.7±0.59	21.24±0.046	.....	....	comp
J1109-23:E1	11 10 06.1	-23 42 13	22	2.2	1.07±0.90	21.81±0.090	May06	[OIII]	solo
J1131-02:E1	11 31 23.1	-02 23 15	80	5.3	2.95±0.66	22.07±0.133	May06	[OIII]	comp
J1131-02:E2	11 31 40.4	-02 16 45	79	2.8	2.86±0.66	22.09±0.136	May06	[OIII]	””
J1341-29:E1	13 41 53.0	-29 58 25	105	2.8	4.77±1.18	21.86±0.159	May06	[OIII]	int
J2009-61:E1	20 08 43.1	-61 57 26	112	15.2	3.19±0.57	22.37±0.168	May06	[OIII]	solo
J2052-69:E1	20 52 59.3	-69 12 26	149	4.5	2.96±0.50	>22.76	May06	[OIII]	solo
J2102-16:E1	21 02 19.4	-16 50 11	103	2.1	3.61±0.36	22.14±0.150	Oct03	Hβ	solo
J2149-60:E1	21 48 55.7	-60 39 52	29	2.7	1.39±0.47	21.80±0.095	May06	[OIII]	int
J2202-20:E1	22 03 04.1	-20 45 48	82	2.4	2.33±0.32	22.36±0.144	May06	Hα	comp
J2202-20:E2	22 02 44.3	-20 43 09	88	4.7	1.79±0.31	22.72±0.196	.....	....	””
J2214-66:E1	22 15 49.0	-66 44 30	71	4.3	2.23±0.47	>22.26	.....	....	solo
J2217-42:E1	22 16 59.0	-42 45 59	81	5.7	2.80±0.99	22.15±0.119	.....	....	solo
J2220-46:E1	22 21 18.6	-46 09 31	56	4.0	5.24±0.69	21.09±0.060	Nov05	[OIII]	solo
J2234-04:E1	22 34 39.6	-04 35 53	253	13.9	15.1±0.65	21.57±0.095	Nov05	[OIII]	solo
J2257-41:E1	22 57 51.2	-42 50 57	114	6.2	1.77±0.65	23.03±0.259	.....	....	solo
J2336-37:E1	23 35 50.4	-37 59 17	39	4.6	1.72±0.64	21.91±0.111	.....	....	comp
J2336-37:E2	23 36 29.4	-37 58 54	46	2.3	1.33±0.64	22.35±0.162	.....	....	””
J2352-52:E1	23 51 51.3	-52 34 33	33	5.4	4.44±0.38	20.69±0.042	HST04	bkgdgal	int

Table 2.1. Properties of ELdots found in SINGG images. Column descriptions [units]: (1) Source name. (2) Source Right Ascension [J2000 hms] (3) Source declination [J2000 dms]. (4) Equivalent Width [Å] (5) Number of times beyond the 25th magnitude elliptical isophote the source lies (6) Emission-line flux of the source measured from SINGG image [10^{-16} ergs s^{-1} cm^{-2}] (7) R-band continuum magnitude measured from SINGG image [AB mags] (8) Observing run identification for spectroscopic follow-up, if applicable. HST04 is imaging with the high resolution channel, and in the case of J2352-52, revealed an obvious background galaxy. Exposure times and HST run information are given in Werk et al. (2008). (9) The emission-line spectroscopically confirmed to fall within the SINGG narrow-band. Hα indicates star-formation associated with the SINGG galaxy (outer-HII); [OIII] falling within the Hα bandpass indicates a source redshift of approximately 0.3; [OII] indicates a redshift of 0.76; and Hβ indicates a redshift of ∼ 0.4; (10) morphological classification described in Section 2.3.

30

be rejected in a system more nearby than ~ 30 Mpc since its angular size would be larger than the maximum angular size in the most nearby SINGG systems (see FWHM selection criterion, above). In practice, however, we do not see this sort of rejection. In each image there are usually between 10 and 20 objects with sizes greater than our maximum threshold, and they are invariably galaxies with no Hα emission (this cut is applied before the NB$-$R color cut) and the SINGG galaxies themselves (sometimes detected as multiple sources with SExtractor). These objects would be subsequently rejected after implementing either the equivalent width criteria (in the case of galaxies with no Hα) or the criterion that they be outside $2\times$r/r$_{25}$ of the SINGG galaxy (in the case of the SINGG galaxies themselves).

It is possible that a small-sized, nearby (d < 30 Mpc) SINGG galaxy with Hα emission could be detected as an ELdot if it were located instead in the upper distance range ($30-70$ Mpc) of the HIPASS targets. By examining all of the nearby galaxies in SR1 (62 galaxies with d < 30 Mpc), we identify only two SINGG galaxies (primary HIPASS targets) that meet all the ELdot criteria except that they fall beyond the maximum angular size threshold: ESO358- G060 (FCC302; J0345-35) and ESO444-G084 (J1337-28). These are nearby dwarf galaxies with very low R-band surface brightnesses that contain compact, luminous HII Regions. ESO358-G060 is an edge-on, LSB member of the Fornax Group (Drinkwater et al., 2001) with a distance of ~ 20 Mpc (Mould et al., 2000). The physical size of its central HII region is 850 pc, and at 70 Mpc, it would appear as a point source, with little or no underlying continuum emission. ESO444-G084 is a compact dwarf irregular galaxy that lies at a distance of 4.6 Mpc (TRGB; Karachentsev et al. 2002) and is only 380 kpc from M83. The physical size of the luminous HII regions in this galaxy, taken together, is approximately 600 pc, roughly the size of SINGG point sources at 70 Mpc. These two galaxies are potentially illustrative of the types of sources we find in the most distant systems.

Another distance-related caveat for the sample is that SINGG is a magnitude-limited survey. As such, the faintest HII regions in the most nearby systems would not be detected in the most distant systems. We would, however, be able to detect the

ionizing flux from a single O7V star (roughly 10^{37} ergs s^{-1}; faint end of extragalactic HII region luminosity distributions; see Oey et al. 2003) at distances up to about 30 Mpc. At the most distant SINGG target with d~ 70Mpc, the limiting Hα luminosity is roughly 10^{38} ergs s^{-1}.

With both the magnitude and size selection effects, 30 Mpc marks an approximate distance beyond which the sample is no longer sensitive to single-star-dominated, faint HII regions, and Hα point sources potentially correspond to small dwarf galaxies. Outer-HIIs more distant than 30 Mpc (complexes of HII regions, dwarf galaxies) are therefore distinct from those that lie in more nearby systems (typical galactic OB associations). We will return to this distance limit in our discussion (Section 2.7), where we consider a more physically homogeneous sample of outer-HIIs that, in both luminosity and size, look like typical galactic HII regions.

2.4   Spectroscopic Follow-Up

ELdots, while generally having large equivalent widths in the SINGG narrow band filters, may not be Hα emitters at the velocity of the SINGG galaxy. Other strong nebular emission lines ([OIII], Hβ, or [OII]) may be responsible for the comparatively high narrow-band flux if the redshifted emission line falls into the Hα filter bandpass used to observe the target SINGG galaxy. Therefore, we used spectroscopy to determine which ELdots are Hα emitters at the redshift of the target galaxy and which are background sources emitting another line in the narrow bandpass. We undertook follow-up long-slit spectroscopy at multiple telescopes, sometimes as a telescope's primary program, other times as back-up observations during non-photometric conditions. We obtained follow-up spectra for 33 of the ELdots, and found background galaxies to comprise the majority of the sample. Since outer-HIIs at the redshift of the SINGG galaxy are our primary interest for this work, we chose to discontinue spectroscopic follow-up for the entire sample.[1]   In this section we present follow-

---

[1]Lessons Learned from Follow-up Spectroscopy: Because most ELdots are optically very faint in R-band continuum images, the object acquisition process for follow-up spectroscopy was quite difficult, and generally required blind offsets from nearby bright stars. Ultimately, we found multi-slit masks to be the most efficient way of getting spectra for these faint objects, however applying

up spectroscopy for roughly half of the SR1 systems containing ELdots, and in the next section, present a more efficient photometric method for distinguishing between background galaxies and outer-HIIs.

Observations carried out in September 2002 and October 2003 were presented in RW04, and represent spectra taken with the Double Beam Spectrograph on the RSAA 2.3 m telescope. Subsequent runs in November 2005, May 2006, and December 2006 took place at Las Campanas Observatory on the Baade 6.5 m telescope with the Inamori Magellan Areal Camera and Spectrograph (IMACS). The long-slit spectra obtained during these runs used the 300 l/mm grating and the f/4 camera, resulting in a dispersion of 0.74 $\mathring{A}$ pixel^{-1} and a spectral range of 3650 - 9740 $\mathring{A}$. Exposure times varied between 900 and 2000 seconds, depending upon the flux of the ELdot observed. Absolute flux calibration was not paramount to our goal of getting the ELdot's velocity. We spectroscopically confirm eight ELdots to be Hα emitters at comparable velocities to their apparent host galaxies. Five of these outer-HIIs were presented in RW04. Figure 2.2 shows the reduced and calibrated spectra for three newly confirmed outer-HIIs: J0317-22:E1, J0209-10a:E3, and J2202-20:E1, with the results discussed below. For reference, the bold, horizontal lines span the FWHM of the observed HIPASS HI profiles for the SINGG host galaxies, and are placed in wavelength space at the expected velocity of the Hα emission line.

- In the spectrum of J0317-22:E1, we have detected Hβ, [OIII] λ 4959 $\mathring{A}$ and 5007$\mathring{A}$, Hα and [NII] λ 6548$\mathring{A}$ and λ 6583 $\mathring{A}$. The recession velocity measured from the Hα emission line is $\sim$ 4700 km/s ($\lambda = 6664$ $\mathring{A}$), quite a bit offset from the HI velocity of the host galaxy (ESO 481-G017) at $\sim$ 3920 km/s (spanning $\sim$ 3850 km/s to $\sim$ 4000 km/s). HI synthesis maps recently obtained with the VLA show a small HI cloud at the velocity of the ELdot, but no direct gaseous

---

this method to the entire SINGG sample is not only costly, but a poor use of slit mask space (can hold thousands of slits in a single field) considering the presence of only 1-2 ELdots per field. Furthermore, the majority of the ELdots in SINGG are background galaxies. GALEX data is important for understanding the full context of the outer-galaxy star formation, but it also emerges as a useful tool for distinguishing between background galaxies and outer-HIIs (see Section 2.5). We recommend using follow-up spectroscopy for confirmation of local star formation only in truly ambiguous cases for which there are no GALEX data available.
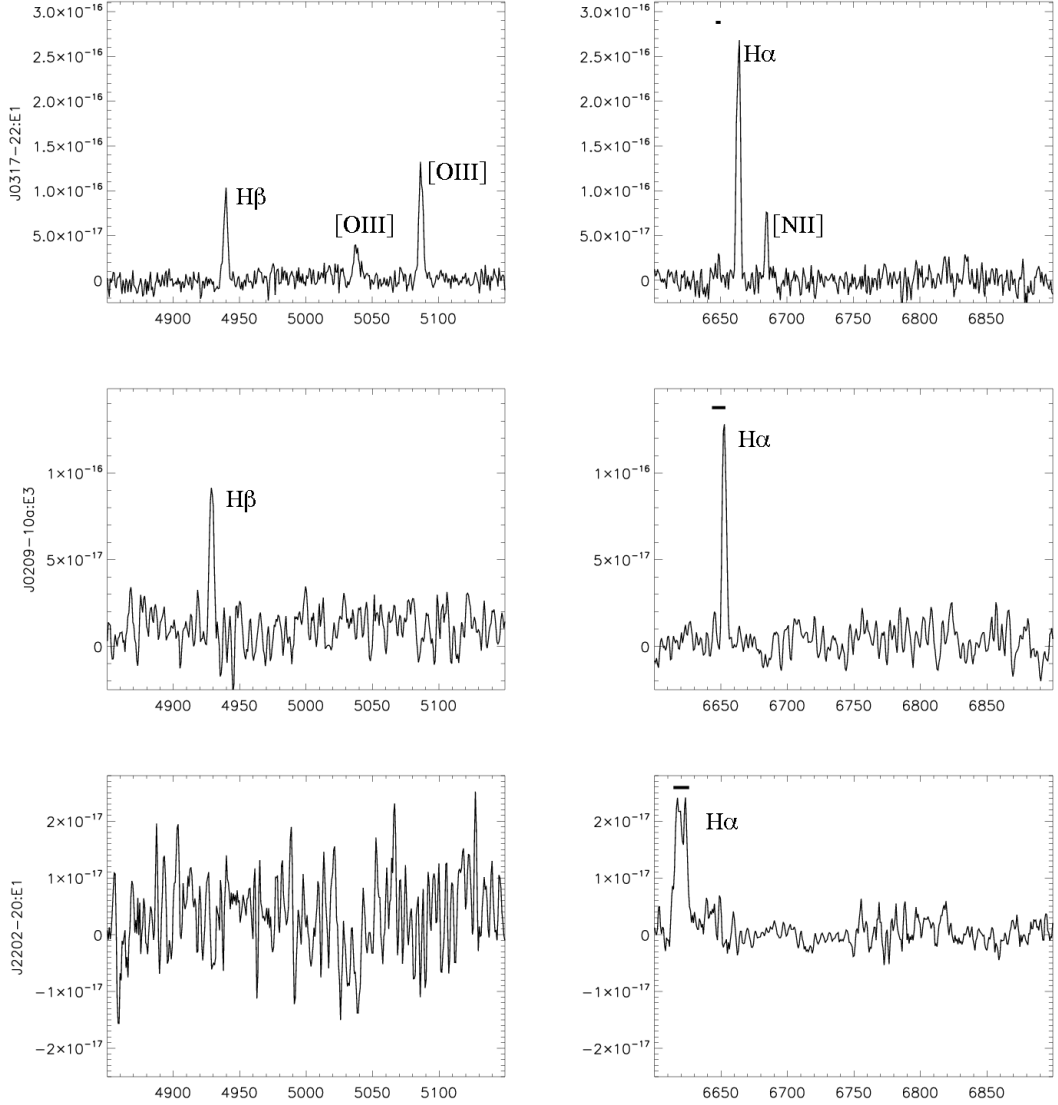
Figure 2.2. Follow-up spectra of three ELdots classified as outer-HIIs. Bold horizontal lines span the FWHM of the 21cm line profiles for each HIPASS target, and are placed at the expected velocity of the Hα emission line. Top: emission-line spectrum of J0317-22:E1 showing [OIII] and Hβ emission lines in the blue, and Hα and [NII] in the red. The Hα emission of the ELdot is offset from the potential host galaxy by about 20Å, or 700 km/s. Middle: Spectrum of J0209-10a:E3 showing two emission lines, best fit by Hβ and Hα. Bottom: Single-line spectrum of J2202-20:E1 showing coincidence of the main emission line with the HI profile.

connection to the main galaxy (Santiago-Figueroa et al., 2009). We show the SINGG image of this system, along with the location of two ELdots in the field in Figure 2.3. We obtained follow-up spectroscopy for J0317-22:E2 as well, and multiple lines confirmed it is a background emitter at z∼ 0.3.

- The spectrum of J0209-10a:E3 reveals only two emission lines, Hβ and Hα, and is the second outer-HII in the J0209-10a system (HCG 16). The recession velocity from the Hα emission line is 4160 km/s ($\lambda = 6653$ Å), comparable to that of the SINGG host galaxies, measured from the HI profile, at ~ 3900 km/s. We show the SINGG image of this system, with the two spectroscopically-confirmed outer-HIIs circled and labeled in Figure 2.4. As it lies south of the image area shown in Figure 2.4, we do not show the location of J0209-10a:E1, for which we did not obtain a spectrum.

- Finally, we detect only one emission line for J2202-20:E1, but consider it very likely to be Hα. The recession velocity measured from the emission line at 6620 Å, 2660 km/s, matches the HI velocity of the host galaxy (NGC 7184), 2620 km/s, very well. Furthermore, the ELdot is located on the major axis of the optical disk, on the northeasterly receding edge (van der Kruit & Freeman, 1986), and could easily be an isolated extension of a spiral arm (see Figure 2.5). In addition to J2202-20:E1, we show the location of J2202-20:E2 in Figure 2.5. We did not obtain a follow-up spectrum for this ELdot.

Two other ELdots were presented by RW04 for which we now have additional information. We detected multiple emission lines of the ELdot J0409-56:E3 using an IMACS multi-slit mask, confirming its association with SINGG galaxy NGC 1533, but will present its spectrum, along with others, in a forthcoming study on outer-HII region metallicities. The ELdot J2352-52:E1, initially presented as a single-line detection in RW04, appears to be a red background galaxy in HST High Resolution Channel images. These *HST* ACS/HRC observations were carried out in October 2004 in three filters: F250W (5910 s); F555W (2796 s); and F814W (2908 s). For more information on data reduction, see Werk et al. (2008). We show the F814W
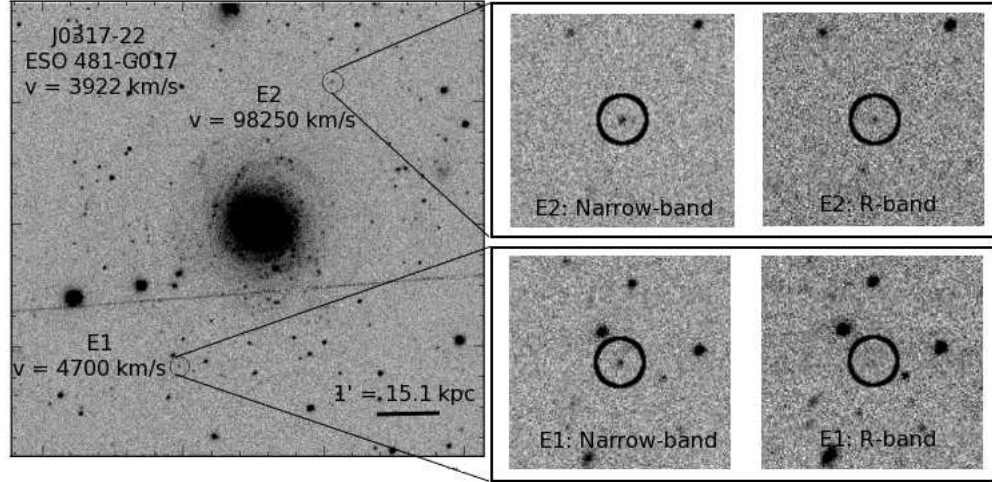
Figure 2.3. SINGG Hα image of the field J0317-22 (ESO 481-G017), with its two ELdots circled and labeled. On the right, close-up views of the ELdots in both narrow-band and R-band filters. Follow-up spectra have confirmed that E1 is an outer-HII, at roughly the same distance as the SINGG galaxy, while E2 is an [OIII] emitter at a redshift of 0.3.
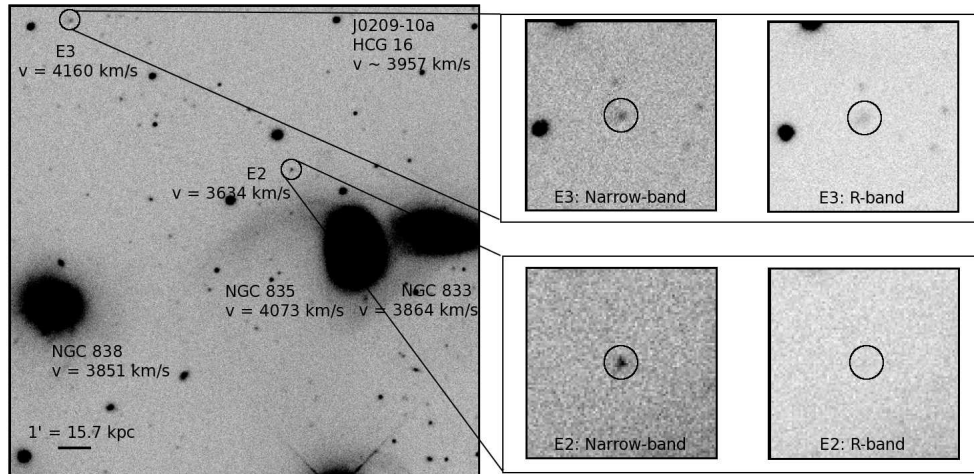
Figure 2.4. SINGG Hα image of the field J0209-10a (HCG 16), with its two ELdots circled and labeled. On the right, close-up views of the ELdots in both narrow-band and R-band filters. J0209-10a:E1 is not shown in the image, as it is considerably further south (off the image area shown) than E2 and E3. Follow-up spectra have confirmed that both E2 and E3 are outer-HIIs, at roughly the same distance as the compact group.
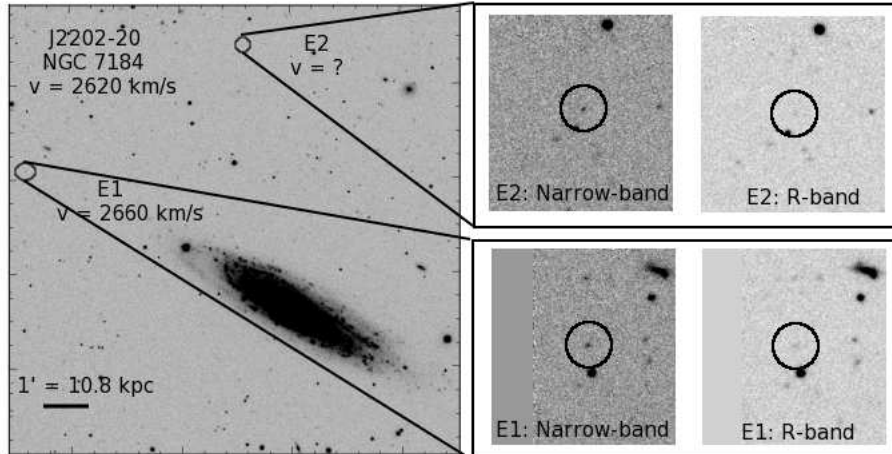
Figure 2.5. SINGG Hα image of the field J2202-20 (NGC 7184), with its two ELdots circled and labeled. Same as Figure 2.3, we show close-up views of the ELdots in both narrow-band and R-band filters on the right. In this case, a follow-up spectrum of E1, combined with HI data of van der Kruit & Freeman (1986) strongly indicates that E1 is an outer-HII, at roughly the same distance as the SINGG galaxy. We do not have spectroscopic follow-up data for E2.

image in Figure 2.6 that reveals J2352-52:E1 to be a background galaxy with spiral structure and ongoing star formation. We do not present the individual spectra of the 23 spectroscopically-confirmed background emitters and one foreground M star in this Chapter. 20 of these background emitters are emission line galaxies at z∼ 0.3, 2 are Hβ-emitters at z∼ 0.4, and 1 is an [OII]-emitter at z∼ 0.8.

2.5 Comparison with deep GALEX data

While Hα emission typically signifies the presence of O stars with $M_\star \geq 20M_\odot$, UV emission traces stellar light from both O and B stars with $M_\star \geq 3M_\odot$. Therefore, deep GALEX images of the outer-HIIs can help provide a more detailed picture of the star formation occurring at large galactocentric distances. In turn, the Hα images of the XUV disks provide an important constraint on the youngest, most massive stellar populations at large radii. Recent results have shown that extended UV (XUV) emission (beyond optical) is relatively common in gas-rich nearby galaxies imaged with GALEX (Thilker et al., 2007). This star formation at large galactocentric radii and how it compares to that within the main optical body is a key part in assembling a complete picture of the star formation process on galactic scales.

37
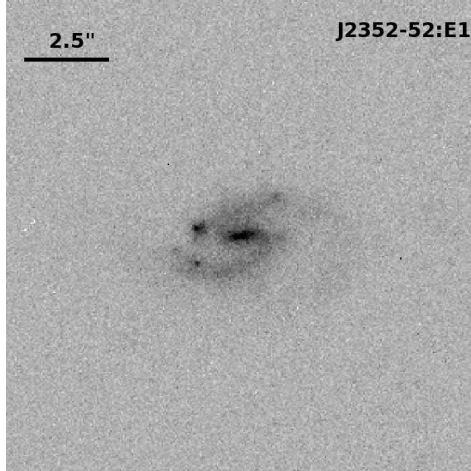
Figure 2.6. HST HRC image of the ELdot in the HIPASS target J2352-52. This image, in the F814W bandpass, reveals that J2352-52:E1 is a background galaxy with spiral structure. RW04 detected only one emission line in this object's long-slit sprectrum, and therefore could not confirm its nature. Considering the angular size of the galaxy (2.5"), the emission line could be either Hβ at z$\sim$ 0.4 or [OIII] at z$\sim$ 0.3, making its diameter either 16 kpc or 20 kpc.

We searched the Multimission Archive at Space Telescope Science Institute (MAST) for GALEX images of ELdots with exposure times longer than $\sim$ 1000 seconds. We did this with two primary goals in mind: first, UV images of outer-HIIs broaden our understanding of their environment and outer-disk star formation in general; second, UV images of ELdots may reveal a method for distinguishing outer-HIIs from background galaxies that is less observationally expensive than follow-up spectroscopy. 16 of the SINGG fields containing ELdots have long-exposure GALEX data available from the MAST archive. Most were obtained through various GALEX Guest Investigator (GI) programs, while a few were part of the Nearby Galaxy Survey (NGS) or the Medium Imaging Survey (MIS). Some of the galaxies are also part of the Survey of Ultraviolet emission in Neutral Gas Galaxies (SUNGG), a sub-sample of SINGG targets imaged by GALEX as part of a Cycle 1 Legacy Survey. 14 of the 16 SINGG fields, along with GALEX program IDs and exposure times are given in Table 2.3. The two SINGG fields we do not include in this table are J0459-26 and J0403-43. J0459-26 is excluded because the background ELdot in this field is detected in neither the FUV nor the NUV GALEX images, although it does have long-exposure GI and MIS GALEX data available. J0403-43 is excluded because the large number of

ELdots in this system justifies a separate table (Table 2.2). We do not detect J0005-28:E1 or J0403-43:E19 in their FUV deep GALEX images but include the magnitudes for these objects as upper limits based on the background of the GALEX image (3σ detection thresholds). The FUV bandpass of GALEX has an effective wavelength of 1516 Å, and the NUV GALEX bandpass has an effective wavelength of 2267 Å.

2.5.1   GALEX Morphology and Outlying HII Regions

A number of studies that examine the relation between UV and Hα emission in the outer parts of galaxies claim a deficiency of massive, young O stars (e.g. Gil de Paz et al. 2005; Meurer et al. 2009). This deficiency is still under debate, and could be due to stochastic effects in a low star formation efficiency environment, a different stellar or cluster initial mass function at larger radii, or could also be a product of the lack of a uniform, high-quality Hα dataset. Whatever the case, it is important to examine the connection between outer-HIIs and XUV emission. As we have seen, there are certainly HII regions present in the outer parts of galaxies, and whether or not they are part of a larger population of extended star formation is quite relevant to answering some of the questions raised in recent studies regarding their paucity. Here, we examine the UV morphologies of four SINGG systems with outer-HIIs. Compared to the SINGG images, the GALEX images have a psf that is 3 times as broad ($4.5''$ versus $1.5''$), so their quality appears sightly degraded. Nonetheless, in these four cases, we see evidence that outer-HIIs are indeed part of a more extended population of UV-bright clusters.

In this section, we refer to the XUV morphological types presented by Thilker et al. (2007). XUV disks display two typical morphologies that Thilker et al. (2007) classifies as either Type 1 or Type 2. Type 1 objects are classified as having clustered UV-bright/optically faint sources in their outer parts, while Type 2 objects have blue FUV$-$NIR colors and XUV emission organized in a large disk structure. Type 1 XUV galaxies are often found in interacting systems, and a truncation radius for the star formation is not well-defined. Conversely, Type 2 disks have an obvious end to their outer-disk star formation, which is happening in a LSB disk lacking a significant

older stellar population. It is possible for a galaxy to be a mixed-type as well, in that it matches both sets of criteria.

We show the color GALEX image of NGC1533 (HIPASS target J0409-56) that contains 4 outer-HIIs in Figure 2.7. The visible gray cloudiness surrounding NGC 1533 in Figure 2.7 traces the HI distribution at roughly 1.5×10^{20} cm^{-2}, and is based on ATCA HI contours previously presented by Ryan-Weber et al. (2003a). The SE portion of the HI cloud appears to contain a population of blue, clustered sources. While the Hα emission in this area is limited to the outer-HIIs, the UV emission is more prevalent, and indicates ongoing star formation outside UV and optical threshold contours. NGC 1533 is a Type 1 XUV galaxy, with bright UV-emission complexes outside the anticipated location of the star formation threshold. The optical extent (r_{25}) of NGC 1533 is only 10 kpc, based on the distance to NGC 1533 (19.4 Mpc; DeGraaff et al. 2007). The XUV emission extends to greater than 30 kpc, filling the extended HI structures surrounding NGC 1533.

Three other systems with ELdots exhibit Type 1 XUV emission: MCG-04-02-0003 (HIPASS target J0019-22), the NGC 1512/10 interacting pair (HIPASS target J0403-43), and NGC 1487 (HIPASS target J0355-42). We present both SINGG (Hα and R-band) and GALEX (NUV and FUV) color images of these systems in Figures 2.8 - 2.10 for comparisons of the Hα and UV emission. In MCG-04-02-0003 (see Figure 2.8, the two ELdots lie at the edges of a Type 1 XUV disk that is completely invisible in the R-band, just barely discernable in Hα, and very bright in the FUV. Combined with their blue FUV$-$NUV colors (see next section), the environment of the ELdots in this system indicates that they are indeed outer-HIIs associated with MCG-04-02-0003. In Figure 2.9 (the NGC 1512/10 system; left panel), the ELdots stand out as Hα (red) point sources arranged in an extended spiral structure. On the right-hand panel of Figure 2.9, we see that NGC 1512 has a large Type 1 XUV disk (r > 30 kpc), that extends beyond the edges of the SINGG image. Its properties are presented fully in Thilker et al. (2007) and also discussed extensively by Koribalski & Lopez-Sanchez (2009). We conclude that the vast majority of ELdots in this system are outer-HIIs, given both their abundance in the SINGG image and their location

J0409-56
NGC 1533

1' = 5.6 kpc

E4

E3

E1, E2
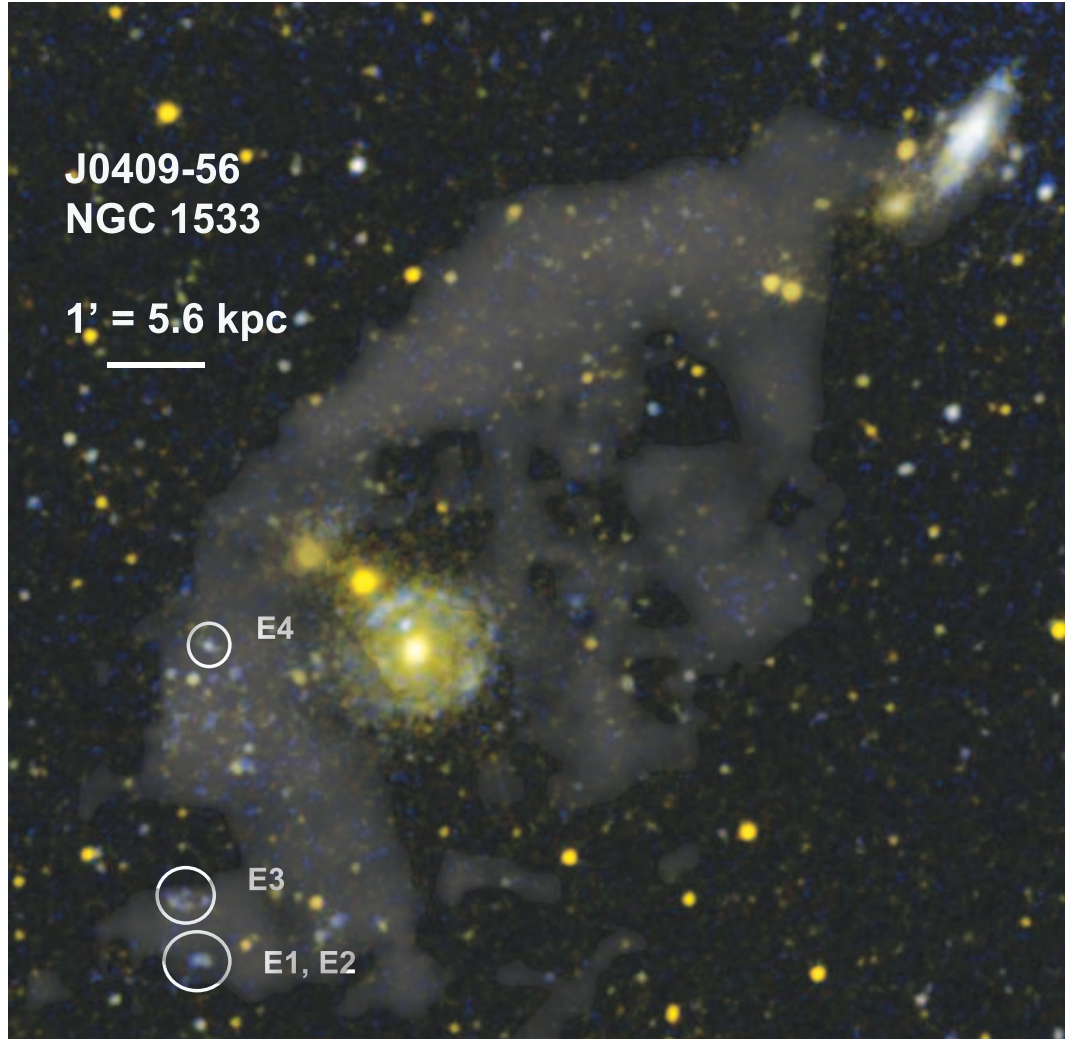
Figure 2.7. GALEX two-color FUV and NUV image of the HIPASS target J0409-56, with its four ELdots circled and labeled. FUV is in blue and NUV is in yellow. The clouded area shown marks the location of an HI column density of at least 1.5×10^{20} cm^{-2} from an ATCA 21-cm synthesis map. We show the physical scale in the top left corner of the image.

in a large and bright Type 1 XUV disk. And finally, in Figure 2.10, the single ELdot in this system lies in a larger stellar complex with a blue FUV−NUV color that is part of the Type 1 XUV emission associated with NGC 1487. Again, given its blue color and surroundings of FUV-bright stellar complexes, we consider this ELdot to be an outer-HII.
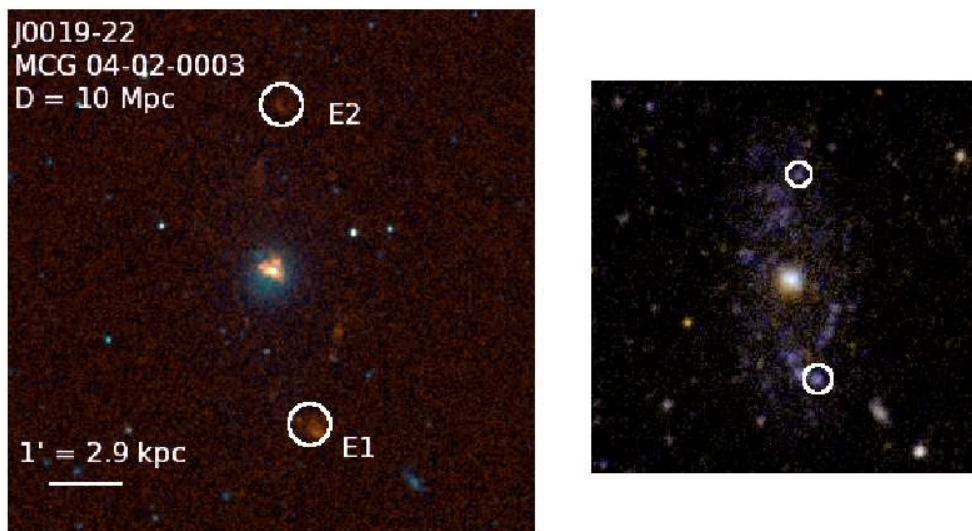
Figure 2.8. GALEX/SINGG images of J0019-22. Left: SINGG color image (Hα = red, R-band = blue) of the field J0019-22 containing the galaxy MCG-04-02-0003, with its two ELdots circled and labeled. Right: GALEX two-color FUV (blue) and NUV (yellow) image of the same galaxy. The ELdots are associated with two of the many clusters bright in the FUV that lie in an extended disk around the main galaxy.

2.5.2 UV and Optical Photometry

Using deep GALEX archival data, we examine potential differences in UV flux and color between background galaxy ELdots and outer-HIIs. Through position-matching, we find the ELdots in the GALEX images and source catalogs, and list their Galactic foreground reddening-corrected (Schlegel et al., 1998) FUV magnitudes and FUV-NUV colors in Tables 2.2 and 2.3. The photometric measurements come from combined, flux calibrated, background-subtracted images taken from the GALEX pipeline (Morrissey et al., 2007). We have separated the ELdots in Table 2.3 by the status of their spectroscopic confirmation. In Table 2.2, we have placed horizontal lines delineating the multiple ELdots detected as single UV-complexes in the GALEX image due to the lower resolution of the GALEX images compared to the SINGG images (4.5″ versus 1.5″; see Figure 2.9).

The median FUV−NUV color of the seven background galaxies is 0.20, while three spectroscopically confirmed outer-HIIs have bluer UV colors, from 0.03 to -0.79.
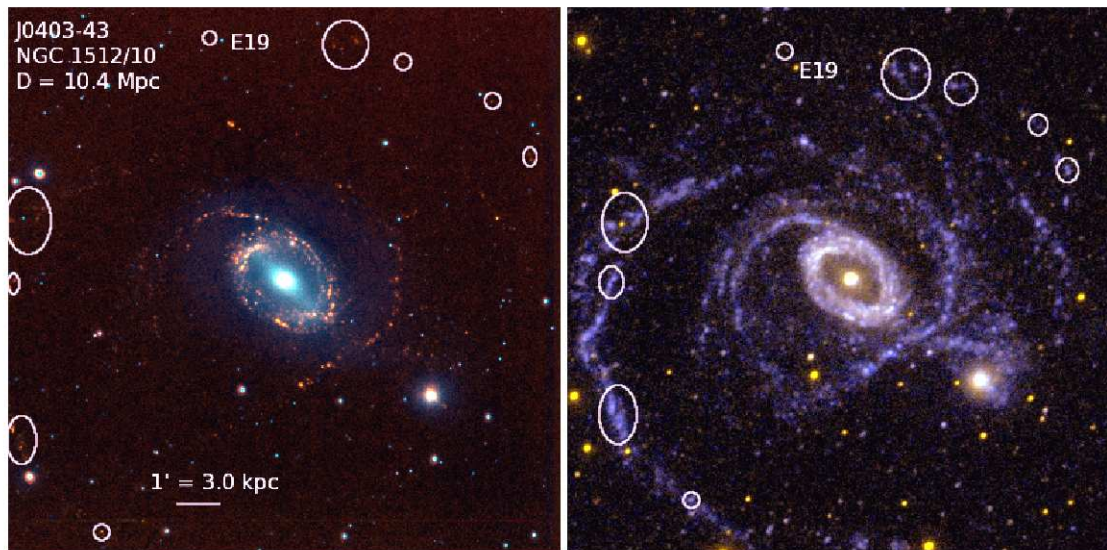
Figure 2.9. GALEX/SINGG images of J0403-13. Left : SINGG color image of J0403-43 (NGC 1512/10 system), with Hα in red and R-band in blue. The 24 ELdots of this system are circled. Right: GALEX color image of the same system with FUV in blue and NUV in yellow. As noted in the text and Table 2.2, the lower resolution of the GALEX images sometimes results in multiple SINGG ELdots detected as a single UV-complex. We see this effect for many of the ELdots in this field. We have labeled J0403-43:E19 in both images to show that there is no FUV emission associated with this ELdot, a likely background galaxy.

Designation	RA	dec	EW	r/r$_{25}$	F$_{Line}$	m$_R$	FUV	FUV−NUV
(1)	(2)	(3)	(4)	(5)	(6)	(7)	(8)	(9)
J0403-43:E1	04 04 20.9	-43 27 36.4	349	2.8	16.7±0.86	21.80±0.108	20.90±0.07	-0.06±0.14
J0403-43:E2	04 04 21.1	-43 27 36.6	389	2.8	14.5±0.80	22.08±0.137	.....	....
J0403-43:E3	04 04 32.8	-43 25 21.1	507	2.8	29.3±1.24	21.60±0.091	19.24±0.06	-0.22±0.10
J0403-43:E4	04 04 32.9	-43 25 25.0	175	2.8	8.06±0.67	21.84±0.112	.....	....
J0403-43:E5	04 04 34.0	-43 24 53.1	518	2.8	41.5±1.65	21.24±0.068	18.89±0.06	-0.16±0.10
J0403-43:E6	04 04 34.0	-43 24 57.0	555	2.8	25.5±1.12	21.85±0.112	.....	....
J0403-43:E7	04 04 33.9	-43 24 49.5	182	2.8	12.2±0.75	21.44±0.080	.....	....
J0403-43:E8	04 04 34.4	-43 21 05.2	493	2.4	23.4±1.05	21.81±0.109	19.67±0.07	-0.12±0.11
J0403-43:E9	04 04 34.5	-43 21 08.2	534	2.4	17.0±0.87	22.24±0.157	.....	....
J0403-43:E10	04 04 33.6	-43 20 56.0	215	2.4	12.9±0.77	21.56±0.088	.....	....
J0403-43:E11	04 04 34.0	-43 19 56.1	591	2.4	13.9±0.79	22.57±0.207	20.24±0.07	-0.22±0.12
J0403-43:E12	04 04 33.9	-43 19 49.9	387	2.4	5.86±0.64	>23.05	.....	....
J0403-43:E13	04 04 34.3	-43 19 20.6	202	2.5	7.27±0.66	22.11±0.141	19.93±0.07	-0.04±0.11
J0403-43:E14	04 04 30.3	-43 19 16.7	425	2.2	7.39±0.66	22.90±0.272	19.83±0.07	-0.07±0.11
J0403-43:E15	04 04 29.5	-43 19 01.1	221	2.2	10.1±0.71	21.85±0.113	.....	....
J0403-43:E16	04 03 18.1	-43 17 42.7	271	2.5	6.90±0.65	22.49±0.193	21.37±0.07	-0.17± 0.13
J0403-43:E17	04 03 18.4	-43 17 33.6	241	2.5	7.71±0.66	22.24±0.157	21.35± 0.07	-0.25 ±0.14
J0403-43:E18	04 03 23.8	-43 16 10.1	713	2.5	10.8±0.72	>23.05	22.90± 0.12	-0.58±0.30
J0403-43:E19	04 04 05.0	-43 14 27.9	188	2.2	4.37±0.62	22.59±0.210	24.23±0.54	0.56 ±0.66
J0403-43:E20	04 03 43.9	-43 14 32.5	587	2.2	8.89±0.68	>23.05	20.54±0.07	-0.01 ±0.11
J0403-43:E21	04 03 36.6	-43 15 07.3	360	2.2	5.46±0.63	>23.05	20.97±0.07	-0.11 ±0.14
J0403-43:E22	04 03 47.0	-43 14 28.3	420	2.2	6.38±0.64	>23.05	21.81±0.08	-0.14 ±0.16
J0403-43:E23	04 03 45.8	-43 14 46.3	887	2.1	13.4±0.78	>23.05	22.52±0.09	-0.34 ±0.21
J0403-43:E24	04 03 46.9	-43 14 41.8	415	2.1	10.1±0.71	22.54±0.202	21.71±0.08	-0.12 ±0.15

Table 2.2. Properties of ELdots found in J0403-43. Column descriptions [units]: (1) Source name. (2) Source Right Ascension [J2000 hms] (3) Source declination [J2000 dms]. (4) Equivalent Width (5) Number of times beyond the 25th magnitude elliptical isophote the source lies (6) Emission-line flux of the source measured from SINGG image [10^{-16} ergs s^{-1} cm^{-2}] (7) R-band magnitude [AB mags] (8) GALEX FUV magnitude (AB magnitude) of the source closest to the SINGG ELdot corrected for Galactic extinction (9) FUV - NUV color. Pertaining to columns 8 and 9: due to resolution discrepancies between SINGG images (1.5") and GALEX images (4.5") multiple ELdots are detected as single sources in the GALEX images. We have delineated affected sources by the horizontal lines in the table. The GALEX image for J0403-43 comes from the Nearby Galaxy Atlas (NGA), and has FUV and NUV exposure times of 2370 seconds.

Eldots with Spectra	Line	GI Program/Image ID	FUV Exptime	NUV Exptime	FUV	FUV−NUV
(1)	(2)	(3)	(4)	(5)	(6)	(7)
J0005-28:E1	[OII]	GI1_009016_HPJ0005m28*	1608	1608	>23.62	0.51±0.45
J0221-05:E2	[OIII]	XMMLSS_03_Meurer*	25915.7	3907	22.56±0.11	0.33±0.24
J0409-56:E1/2	Hα	GI3_087004_NGC1533	1520	3152	20.74±0.08	-0.14±0.13
J0409-56:E3	Hα	”	”	”	22.67±0.14	0.03±0.28
J0409-56:E4	Hα	”	”	”	22.35±0.12	-0.79±0.37
J0506-31:E1	[OIII]	NGA_NGC1800_000*1	1695	1695	23.38±0.13	-0.30±0.34
J0507-37:E1	[OIII]	GI2_121004_LGG127*	2155	2155	22.26±0.13	0.49±0.22
J0512-32:E1	[OIII]	GI1_047029_UGCA106*	1637	4476	22.14±0.12	0.05±0.23
J2149-60:E1	[OIII]	GI1_009095_NGC7125 *	1687	2664	22.55±0.15	-0.55±0.46
J2352-52:E1	[OIII]	GI1_047112_ESO149_G003	1565	1624	22.75±0.15	0.90±0.21
ELdots without Spectra						
J0019-22:E1	.....	GI1_047003_MCG_04_02_003*	3448	1664	20.37±0.07	0.18±0.11
J0019-22:E2	.....	”	”	”	21.33±0.08	0.10±0.17
J0031-22:E1	.....	GI1_009007_HPJ0031m22*	1608	1608	22.01± 0.05	0.28± 0.07
J0031-22:E2	.....	”	”	”	22.97±0.05	0.64±0.07
J0221-05:E1	.....	XMMLSS_03_Meurer*	25915.7	3907	23.65±0.21	0.55±0.44
J0221-05:E3	.....	”	”	”	23.19±0.16	0.63±0.31
J0224-24:E1	.....	GI1_009115_NGC0922*	2285	2285	22.53±0.12	0.27±0.24
J0320-52:E1	.....	MIS2DFR_38632_0859	1855	1855	22.39±0.11	-0.40±0.26
J0355-42:E1	.....	GI1_047022_NGC1487*	1696	1696	22.55±0.11	-0.32±0.28
J0359-45:E1	.....	GI1_047023_HorDwarf *	3116	1510	23.57±0.24	0.66±0.37

Table 2.3. GALEX UV Properties of ELdots. Column descriptions: (1) Source name. (2) The emission-line spectroscopically confirmed to fall within the SINGG narrow-band, if available. Hα indicates star-formation associated with the SINGG galaxy; [OIII] falling within the Hα bandpass indicates a source redshift of approximately 0.3; and [OII] indicates a redshift of 0.76. (3) The GALEX Guest Investigator program identification that provided the GALEX images. An asterisk indicates that the field is part of the SUNGG sample. (4) and (5) NUV and FUV exposure times (6) Apparent FUV magnitude (in AB mags) of the source at the position of the ELdot. In one case, J0409-56:E1 & 2, two separate ELdots appear as a single source, due to the larger PSF of the GALEX images (4.6″) compared to the SINGG Hα images (∼ 1.5 ″) (7) FUV - NUV colors (in AB mags) of the ELdots.
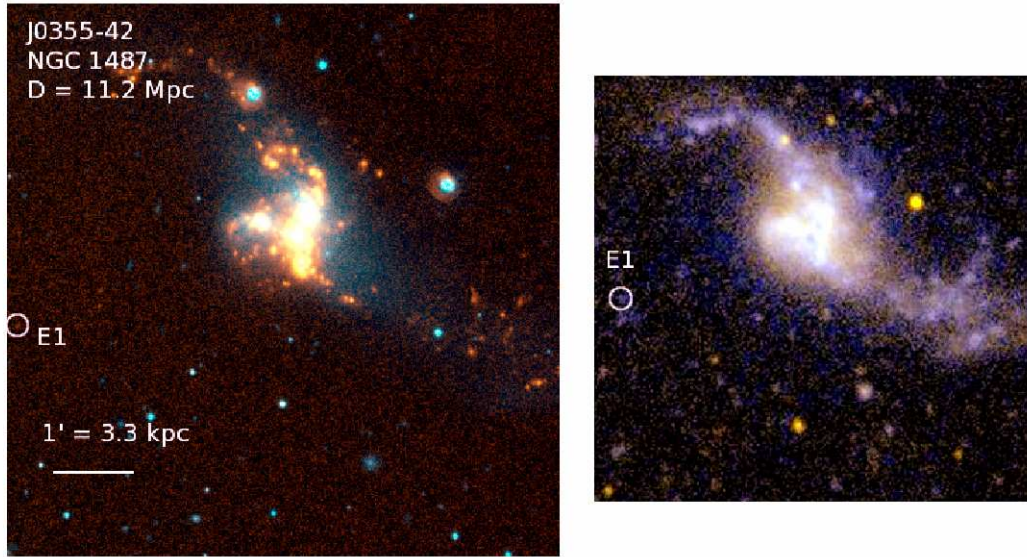
Figure 2.10. GALEX/SINGG images of J0355-42. Right: SINGG color image of J0355-42 (NGC 1487), with Hα in red and R-band in blue. Left: GALEX color image of the same field of view as the SINGG image on the left. On the GALEX panel, blue shows FUV while yellow shows NUV. The ELdot in this field is circled on the left-hand side of each image.

When we include the large number of outer-HIIs in J0403-43, the two in J0019-22, and the one in J0355-42, the color separation is more pronounced. All of the outer-HIIs in J0403-43 have FUV−NUV colors well below zero, except for J0403-43:E19, which has fairly red FUV−NUV color of 0.56. The two outer-HIIs in J0019-22 have moderately blue colors of 0.18 and 0.10, while the outer-HII in J0355-42 has a color of -0.32.

Although the outer-HIIs have blue FUV−NUV colors, a blue FUV−NUV color does not necessarily indicate an ELdot is an outer HII. Three of the seven background galaxy ELdots, J0512-32:E1, J0506-31:E1 and J2149-60:E1 have quite blue colors (FUV−NUV = 0.05, -0.30, and -0.55, respectively). On the other hand, a red FUV−NUV color (> 0.25) appears to positively indicate a background source. The reddest outer-HII has a FUV−NUV color of 0.18, and the vast majority (∼ 90%) of outer-HIIs have FUV−NUV colors < 0. Of the ten ELdots with UV photometry but without spectra, six have red colors consistent with background sources. Furthermore, the red ELdot, J0403-43:E19, may be a background galaxy in a field
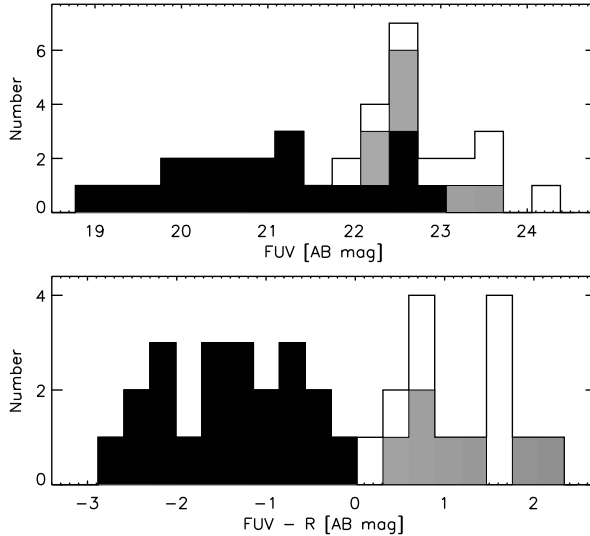
Figure 2.11. ELdot photometric properties. Two histograms showing the SINGG and GALEX photometric properties of all SINGG ELdots having both datasets available. In both panels, the black represents outer-HIIs, the gray represents background galaxies, and the clear area represents the ELdots that have not yet been confirmed to be either. Top: The distribution of GALEX FUV magnitudes. Bottom: The distribution of GALEX FUV−R colors.

replete with outer HIIs, especially since it is not located in one of the well-defined spiral arms of NGC1512/10 (see Figure 2.9) and its narrow-band line emission and equivalent width are the lowest of the J0403-43 ELdots (see next section). We do not include this ELdot in our sample of outer-HIIs.

The two histograms in Figure 2.11 show the distribution of GALEX FUV magnitudes (top panel) and FUV−R colors (bottom panel) of the ELdots in the SINGG fields for which deep GALEX images are available. The outer-HIIs (black histogram) have the brightest FUV magnitudes and the bluest FUV−R colors, while the background galaxies and ELdots without spectroscopic follow-up (gray and clear histograms, respectively) are faintest in FUV and reddest in FUV−R. The distribution of FUV−R is distinctly bimodal for the two primary types of ELdots. The outer-HIIs stand out as having very blue FUV−R colors, due to their faint continua and bright FUV emission.

Figure 2.12 shows two plots that display the separation of background galaxies and outer-HIIs in FUV and optical color-color space. On the top panel, we plot the FUV−NUV color versus the FUV−R color, and on the bottom panel we show the
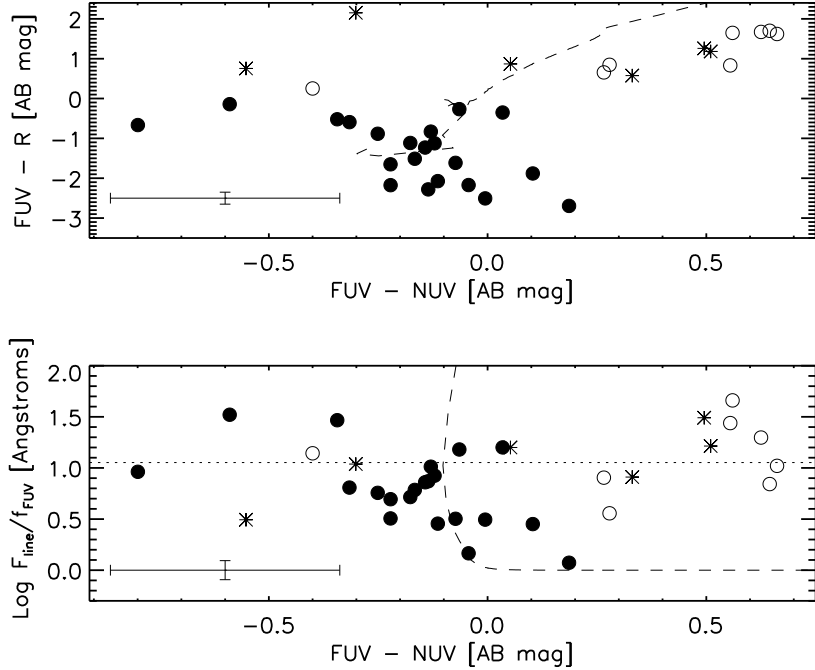
Figure 2.12. SINGG and GALEX color-color plots of the ELdots having both datasets available. Filled circles mark outer-HIIs, open circles mark ELdots without follow-up, and the asterisks show the background galaxies. The dashed lines show the tracks for a single-burst stellar population with M_{up}= 100 $M_\odot$ and solar metallicity generated by Starburst99 for reference. On both plots, we show the mean error for each quantity in the lower left-hand corner. Top: FUV−NUV versus FUV− R in AB magnitudes Bottom: FUV−NUV versus SINGG line flux divided by the GALEX FUV flux density, in units of Å. The dotted, straight line represents a fiducial value of $F_{H\alpha}/f_{FUV}$, for which stars form at a constant rate with $M_{up} = 100$ in a Salpeter IMF.

FUV−NUV color versus the ratio of the SINGG narrow-band flux (F_{line} in units of ergs s^{-1} cm^{-2}) divided by the GALEX FUV flux density (f_{FUV} in units of ergs s^{-1} cm^{-2} $\mathring{A}^{-1}$) that has units of Å. The dashed lines on both panels show the color evolution of a single-burst stellar population with a Salpeter IMF ($M_{up} = 100$ $M_\odot$) and solar metallicity. We note that this model cannot accurately represent the stellar populations of the outer-HIIs, as their total masses range between 200 - 2000 $M_\odot$, significantly less stellar mass than is required to fully populate the stellar IMF (Werk et al., 2008). At these masses, stochastic effects dominate the results, and the models become degenerate. We show the Starburst99 tracks simply for reference in comparison with the numerous other works that do so.

Most of the background galaxies (asterisks) have redder FUV−NUV colors than

outer-HIIs, in addition to their redder FUV−R colors, seen in the top panel of Figure 2.12. On the bottom panel, outer-HIIs have both lower F_{line}/f_{FUV}, on average, and bluer FUV − NUV colors. Both of these figures show that, given the distinction between outer-HIIs and background galaxies in color space, most of the remaining ELdots in our sample from the bottom half of Table 2.3 are likely to be background ELdots.

For reference, the dotted line on the bottom panel of Figure 2.12 marks the expected value of $F_{H\alpha}/f_{FUV}$ for a stellar population continuously forming stars that obeys a Salpeter IMF with $M_{up} = 100$ $M_\odot$. All but four of the outer-HIIs lie below this line. A recent study by Meurer et al. (2009) challenges the notion of a universal IMF using integrated Hα and UV emission measurements for a sample of ~ 100 SINGG and SUNGG galaxies. Along this line, the low F_{line}/f_{FUV} ratios of outer-HIIs in conjunction with their relative paucity in comparison with the multitude of GALEX XUV clusters may also be suggestive of a truncated IMF. Detailed calculations of expected F_{line}/f_{FUV} and the fraction of Hα-emitting clusters in XUV disks for various star formation histories and stellar IMFs could further support or reject this claim for outer disk star formation.

2.6   Properties of the Sample

We show the distribution of ELdot equivalent widths, line fluxes, R Band magnitudes, and r/r$_{25}$ values in Figures 2.13 and 2.14. To indicate our source identification, we use a nested shading scheme in Figure 2.13. The clear, outer histogram shows all ELdots in this study, light gray indicates those ELdots we have identified as background galaxies and outer-HIIs via follow-up data (GALEX imaging and optical spectroscopy), and black, the innermost histogram, specifically shows only outer-HIIs. Thus, the visible clear area corresponds to ELdots with no follow-up data, and the visible light gray area indicates background galaxies.

To calculate the narrow-band emission's equivalent width in Å, we divide the flux of the ELdot in the continuum subtracted, net Hα image by its flux density in the R band. Seen in the top panel of Figure 2.13, the ELdots span a range in EWs

49
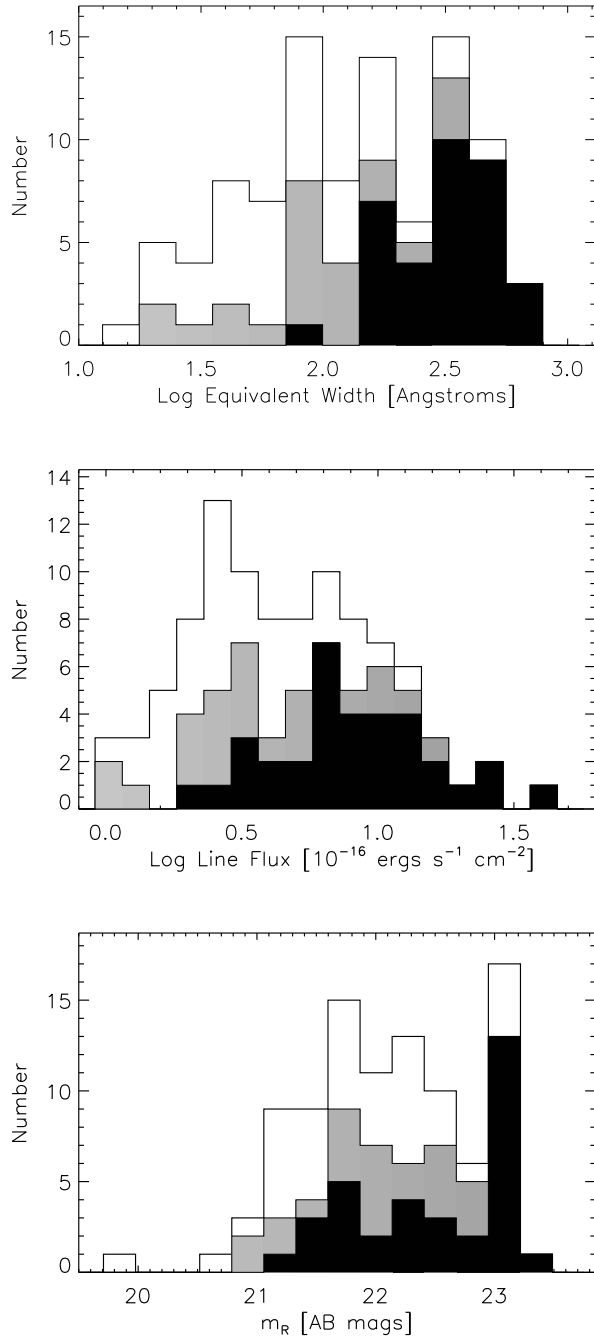
Figure 2.13. SINGG properties of ELdots. Top: Histogram showing the distribution of equivalent widths for the line detected in the SINGG bandpass for all ELdots (clear), for ELdots with follow-up data (gray; background galaxies plus outer-HIIs) and for outer-HIIs (black). Middle: Histogram showing the distribution of ELdot line fluxes in the SINGG narrow-band filter (Hα flux, if at the velocity of the target galaxy) with the same shading scheme as above. Bottom: Histogram showing the distribution of SINGG R Band magnitudes for the ELdots, again with the same shading scheme.

from the cut for our sample selection at approximately 20 Å to 900 Å. Beyond 150 Å, the majority of ELdots are Hα emitting outer-HIIs with EW's that extend out to a maximum value of 900 Å. The median values of the EW's are 160 Å for the entire sample of ELdots and 412 Å for the outer-HIIs. A simple two-sided KS-test on the distributions of EWs shows a 5% probability that all outer-HIIs are derived from the overall distribution, and a 59% probability for all background galaxies and outer-HIIs. Therefore, outer-HIIs tend to have higher EWs than the entire sample of ELdots and known background galaxies.

The distribution of line fluxes in log space is shown in the middle panel of Figure 2.13. The majority of the ELdots have line fluxes less than 1×10^{-15} ergs s^{-1} cm^{-2}. The median values are 4.93×10^{-16} ergs s^{-1} cm^{-2} (entire sample) and 8.9×10^{-16} ergs s^{-1} cm^{-2} (outer-HIIs). The limiting Hα luminosity of a point source at the median distance of the SINGG sample is 10^{37} ergs s^{-1}, or $\sim 1.0 \times 10^{-16}$ ergs s^{-1} cm^{-2}, roughly the ionizing output of a single O7V star (Martins et al., 2005). Outer-HIIs tend to have slightly higher line fluxes than the full sample of ELdots.

The distribution of R band magnitudes shown in the bottom panel of Figure 2.13 has a more narrow distribution than the line fluxes based on our strict color cut of NB$-$R = -0.7 and the detection limit of the survey. The mean R band magnitude is 22.15 for the entire sample and 22.48 for the outer-HIIs. Outer-HIIs comprise the majority of sources at the faint end of this distribution. A two-sided KS-test on the distributions of R band magnitudes gives a 39% probability that background galaxies and outer-HIIs are drawn from the full sample and only a 5% probability that outer-HIIs are. Both fainter R band magnitudes and higher line fluxes contribute to the tendency of outer-HIIs to have higher EWs than the entire sample of ELdots.

A full understanding of the locations of the ELdots in the SINGG images requires a calculation of the finder search area as a function of r/r$_{25}$. The top panel of Figure 2.14 shows the total area in elliptical annuli of the 93 SINGG images at given r/r$_{25}$. We calculated this value by summing the area in each elliptical annulus of a given r/r$_{25}$ for every SINGG image. Most SINGG images do not extend beyond 17 r/r$_{25}$, and the majority of the area in each image lies within 5 r/r$_{25}$. This histogram is

helpful for understanding those shown in the two lower panels of Figure 2.14, the distribution of r/r$_{25}$ values for the ELdots. Our shading scheme for Figure 2.14 differs from the nested shading scheme of Figure 2.13. The middle panel of Figure 2.14 shows the distributions of all SINGG ELdots *minus* the outer-HIIs (clear) and all background galaxies (light gray). These distributions roughly follow that of the search area, indicating that background galaxies (which comprise most of the SINGG ELdot sample) are distributed randomly in the SINGG fields. The majority of ELdots are found within $5 \times$ r/r$_{25}$, because that is where the majority of the search area lies. On the bottom panel of Figure 2.13, we show the distribution of r/r$_{25}$ values for the outer-HIIs. This histogram includes the 23 outer-HIIs of J0403-43 all within the first bin, and thus is heavily biased for that system. Nonetheless, outer-HIIs appear more likely to be found closer to a host galaxy than background galaxies. A two-sided KS test indicates a 98% probability that background galaxies and the full sample of ELdots come from the same distribution, while the probability is 24% that the outer-HIIs come from the same distribution.

2.7   Discussion of Outer-HIIs

The outlying HII regions discussed here are not of a uniform nature, nor are they found in a set of uniform systems. Some are OB associations, isolated in the far outskirts of galaxies, others are part of extended UV disks, and others may be dwarf satellite companions to host SINGG galaxies. Furthermore, outer-HIIs are found in systems that span a large range of HI mass probed by SINGG (M06), from Log M$_{HI}$ = 8.25 (J0019-22) to 10.31 (J0209-10a). What links all of the outer-HIIs together is that they represent new stars forming in the absence of a significant, if any, underlying stellar population. As we have discussed, part of the variety in the outer-HIIs arises because of the range of distances probed by the SINGG survey, from 4 Mpc to 70 Mpc. Thus, compact objects roughly the angular size of the SINGG PSF of 1.6$''$ will span a range of physical sizes between 30 and 500 parsecs, as discussed in Section 2.3.3. Those physical sizes correspond to compact star clusters in the most nearby cases, to small dwarf galaxies in the most distant systems. Conversions of Hα fluxes
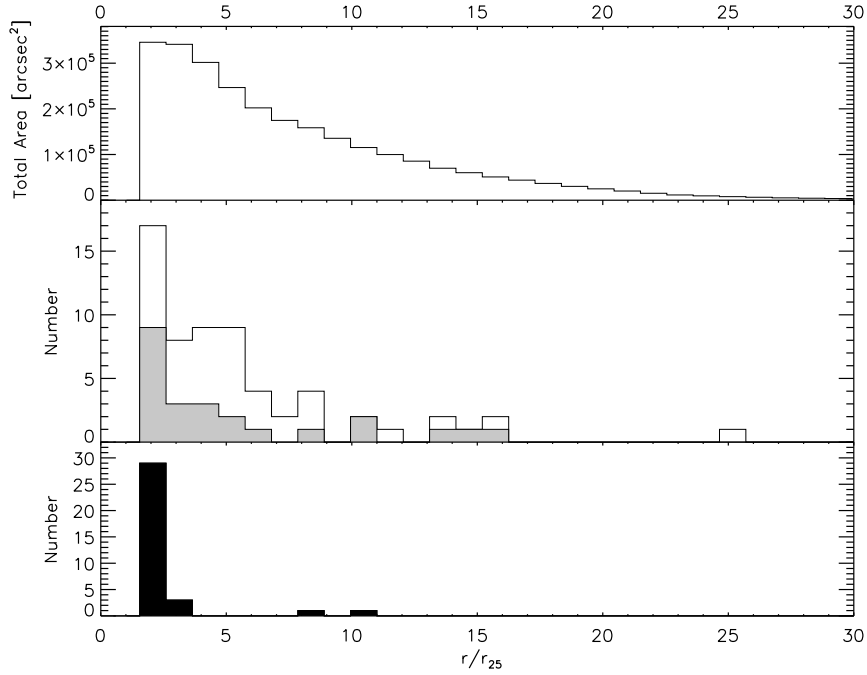
Figure 2.14. Histograms showing finder search area as a function of r/r$_{25}$. Top: The total area in square arcseconds probed in elliptical annuli at given r/r$_{25}$ for all 93 SR1 fields. Middle: the distribution of r/r$_{25}$ values for all SINGG ELdots minus outer-HIIs (clear) and background galaxy ELdots (gray). Bottom: the distribution of r/r$_{25}$ values for SINGG outer-HIIs.

to Hα luminosities use distances listed in table 6 of M06, except for NGC 1533 (J0409-56) which has a distance of 19.4 Mpc determined by Barber DeGraaff et al. (2007). For conversions to an equivalent number of O9V stars, we use Q$_o$ = 7.33 × 10^{11} L$_{H\alpha}$ s^{-1} (Osterbrock, 1989) and the ionizing photon output of a single O9V star to be 10$^{47.90}$ s^{-1} (Martins et al., 2005). The seven SINGG systems containing outer-HIIs are presented below in order of SINGG target galaxy distance:

1. **J0019-22:** The two outer-HIIs are young star clusters or OB associations located in a Type 1 XUV disk around the host dwarf galaxy, MCG 04-02-003. A distance of 10 Mpc gives maximum physical diameters of the HII regions of 70 pc, roughly in line with those of the resolved stellar clusters associated with the outer-HIIs outside of NGC 1533 and similar in size to Galactic OB associations (Werk et al., 2008). The environment of these outer-HIIs however, is distinct from that of NGC 1533 in that they seem to fit in a faint, organized disk. The

outer-HIIs lie at projected galactocentric distances of roughly 5 kpc, on the edges of the XUV disk.The Hα luminosities of the two outer-HIIs are similar, roughly $10^{36.6}$ ergs s^{-1}, the equivalent of about 4 O9V stars. J0019-22 is a solitary galaxy, though it is slightly peculiar in that it possesses a star-forming compact core and an optically very faint but FUV-bright XUV disk. We note that this galaxy is the only solitary SINGG galaxy that contains outer-HIIs based on our morphological classification system.

2. **J0403-43:** The numerous outer-HIIs associated with the NGC 1512/10 pair are organized in outer spiral features that align quite well with the XUV GALEX complexes. A distance of 10.4 Mpc (Gil de Paz et al., 2007) gives a maximum physical diameter for these outer-HIIs of 75 pc, again, in line with typical Galactic OB associations. Projected galactocentric distances of the outer-HIIs range from 15 - 20 kpc, while the FUV-bright spiral arms extend beyond the SINGG image, to greater than 30 kpc in projected distance from the center of NGC 1512. The Hα luminosities span a rather broad range, between $10^{36.9}$ and $10^{37.9}$ ergs s^{-1}, representing anywhere between 5 and 50 O9V stars. The NGC 1512/10 pair is a nearby interacting galaxy pair with an Type 1 XUV disk (see Thilker et al. 2007).

3. **J0355-42:** Here, we see a single outer-HII that is part of the extended, young star formation triggered by a violent galaxy collision that formed the galaxy NGC 1487 (Mengel et al., 2008). The Hα emission is coming from the tip of a much larger FUV-bright stellar complex at the outskirts of NGC 1487, roughly 13 kpc in projection from the system's center. In the GALEX image shown in Figure 2.10, we can see that this complex may be part of a faint arm-like structure extending from the central, optically bright part of NGC 1487. There are two additional high-EW point sources along this faint structure (seen in the SINGG Hα image, also with FUV counterparts), though they lie within $2 \times$ r/r$_{25}$. The physical size ($\sim$ 80 pc at D = 11.2 Mpc) and Hα luminosity ($10^{36.7}$ ergs s^{-1}) of the outer-HII are again consistent with that of a typical OB

association.

4. **J0409-56:** The 4 outer-HIIs outside NGC 1533 lie in a ring of HI gas and are powered by young, low-mass OB associations revealed by *HST* HRC images presented in Werk et al. (2008). Hα luminosities between $10^{37.4}$ and $10^{37.7}$ ergs s^{-1} correspond to emission from 20 -40 O9V stars. The GALEX image of the system (Figure 2.7) shows that these OB associations are part of recent extended star formation as traced by its Type 1 XUV emission, represented by a number of FUV-bright stellar complexes in the southeast part of the HI ring. The overdensity of FUV sources here fits well with the picture presented by Werk et al. (2008) that included a number of blue field objects that did not show any Hα emission. The HI ring is connected to a companion galaxy in the upper-right of Figure 2.7 (see Ryan-Weber et al. (2003a) for more details), and we therefore classify NGC 1533 as interacting.

5. **J2202-20:** The outer-HII near the edge-on spiral galaxy NGC 7184 is an Hα-emitting knot in an extension of the galaxy's optical disk (see Figure 2.5). The galaxy's distance of 37 Mpc gives the outer-HII a maximum physical FWHM size of 270 pc, comparable to the star-forming complexes present in the XUV disks of the GALEX sample (Thilker et al., 2007). This outer-HII lies on the northeast tip the rotating HI-disk of NGC 7184. Its Hα luminosity, $10^{37.6}$ ergs s^{-1}, is equivalent to that from 35 O9V stars. While NGC 7184 is the dominant galaxy in the J2202$-$20 field, there is a dwarf galaxy to the south east which is also a line emitter as identified by M06. It is not clear whether these two galaxies are interacting, and so we have designated this system as one with a companion.

6. **J0317-22:** The outer-HII may be a dwarf galaxy near the spiral ESO481-G017 given its large velocity offset from the main galaxy and their distance of 52 Mpc, which places the maximum size of the outer-HII at nearly 400 pc. The projected distance from the galaxy center to the outer-HII is 43 kpc. The Hα luminosity is considerably higher than more nearby outer-HIIs ($10^{38.1}$ ergs

s^{-1}) and is equivalent to 125 O9V stars. High-resolution HI observations of the system arepresented by Santiago-Figueroa et al. (2009), and show ESO481-G017 to have several companions.

7. **J0209-10a:** The two outer-HIIs lie in the intracluster medium of Hickson Compact Group (HCG) 16. Because this system lies at a distance of 54 Mpc, these two outer-HIIs are probably not simply single isolated star clusters, but could be complexes of young star clusters or emerging dwarf galaxies. As with J0317-22:E1, the Hα luminosities of the two outer-HIIs range from $10^{38.2}$ and $10^{38.5}$ ergs s^{-1}, which translates to hundreds of O9V stars. The outer-HIIs lie in a large extension of HI gas stripped from the galaxies in the group (Verdes-Montenegro et al., 2001) due to the ongoing interaction in HCG 16.

Examples in the existing scientific literature of objects similar to the outer-HIIs presented here tend to showcase interacting systems and galaxy groups as the locations for outer-galaxy or intracluster star formation (Boquien et al., 2007; Walter et al., 2006; Oosterloo et al., 2004; Cortese et al., 2004; Sakai et al., 2002; Gerhard et al., 2002; Arnaboldi et al., 2002). Furthermore, the incidence of Type-1 XUV disks in GALEX is shown to correlate with galaxy interactions (Thilker et al., 2007). We can confirm that outer-HIIs tend to be found in interacting systems or systems with companions. Six of the seven systems presented here exhibit such a nature. In contrast, the majority of the SR1 systems (and systems containing background galaxy ELdots) are solitary. Additionally, the SINGG fields containing outer-HIIs that have available long-exposure GALEX data (J0409-56, J0019-22, J0403-43, and J0355-42) show that outer-HIIs are strongly related to extended UV emission, each associated with Type 1 XUV morphologies. In these cases, the Hα emission traces only the youngest, most massive clusters among a more extensive population of star clusters in the low density outskirts of galaxies. We will examine the connection between outer-HIIs and XUV emission in a future paper. Of particular interest is a calculation of the number of expected Hα-emitting massive O stars at large galactocentric radii given the luminosity of the XUV disk and assuming a Salpeter stellar IMF.

We can estimate the frequency of outer-HIIs in gas-rich galaxies with our results. Of the 33 systems for which we have follow-up data (optical spectra: 26 systems; GALEX deep images: 7 additional systems), seven contain outer-HIIs, or $\sim 20\%$. There are 17 distinct systems with ELdots for which we have no spectroscopic or GALEX follow-up data. On the whole, the ELdots in these systems have lower equivalent widths and brighter R-band magnitudes than the outer-HIIs (see Figure 2.13). If, at most, $\sim 20\%$ of these 17 systems lacking follow-up contain outer-HIIs, then we would expect, at most, 3 more systems with outer-HIIs. For the overall frequency of outer-HIIs in the entire SR1 sample, we include the additional 39 systems in which there are no finder-detected ELdots. The frequency of star formation beyond $2 \times r_{25}$ in an unbiased sample of 89 gas-rich systems spanning a wide range of morphologies and masses is therefore between 8 and 11% (7 - 10 systems).

As noted in Section 2.3.3, outer-HIIs with distances beyond 30 Mpc likely represent emission from multiple HII regions, and perhaps potential dwarf galaxies. Comparatively, the outer-HIIs with distances less than 30 Mpc are more similar in size and luminosity to HII regions powered by single OB associations, and are seen to be part of extended UV emission associated with the host galaxy. As there is much recent interest in the latter type of outer-HII, we additionally calculate the frequency of outer-HIIs in SINGG galaxies with D < 30 Mpc (62 of 89 SR1 systems). A total of 32 of these systems contain ELdots, though only 22 have follow up data (optical spectra: 16 systems; GALEX deep images: 6 additional systems). 4 of these 22 systems contain outer-HIIs, or $\sim 20\%$. Similar to the calculation performed above, we then expect, at most, 2 of the additional 10 systems with ELdots but without follow-up data to contain outer-HIIs. Thus, the frequency of outer-HIIs in our distance-limited sample is between 6 and 10% (4 - 6 systems).

2.8 Summary and Conclusions

ELdots are emission-line point sources ("dots") well outside the main optical R-band emission of a galaxy, defined as $2 \times r_{25}$ in this work. Using an automated finder, we catalogue a total of 96 ELdots in 50 of 89 SINGG systems. We classify ELdots as

either outlying HII regions (outer-HIIs) or background galaxies by spectroscopy and GALEX morphology and colors. This study highlights four key results:

- Follow-up GALEX data, combined with SINGG photometric properties, can help distinguish between outer-HIIs and background galaxy ELdots, nearly eliminating the need for spectroscopic follow-up. The distribution of ELdot FUV−R colors is bimodal, revealing that outer-HIIs are considerably bluer than higher-redshift emission-line background galaxies. The very blue outer-HII colors are due primarily to the extremely low R-band emission from these objects, indicating new stars forming where there is little or no underlying older stellar population. Outer-HIIs also tend to have higher emission-line EWs than background galaxy ELdots and are likely to be found closer to a potential host galaxy than the background galaxies, which are uniformly distributed across the SINGG search area.

- Through our systematic search of a sample of gas-rich galaxies, we have confirmed that massive star formation in the far outskirts of galaxies tends to be associated with galaxy interactions and nearby companions. This result agrees with other recent findings of star formation outside the main optical bodies of galaxies.

- In the cases where long-exposure GALEX data is available, we find that outer-HIIs appear to be associated with XUV emission, specifically of Type-1 morphology.

- We find that the frequency of massive star formation in the far outskirts of galaxies, as traced by Hα emission in the full SR1 sample, is between 8 and 11%. Outer-HII regions in this full sample span a wide range of Hα luminosities, from $10^{36.6}$ ergs s^{-1} to $10^{38.5}$ ergs s^{-1}, and have physical sizes from 70 pc to 500 pc, representing OB associations ionized by a few O stars in the most nearby systems, and dwarf galaxies with hundreds of O stars in the most distant systems. When we isolate our sample of outer-HIIs to a nearby sample with D

< 30 Mpc, we can compare our frequency statistics more directly with those of XUV galaxies. These outer-HIIs are more homogeneous in nature, similar in size and luminosity to Galactic OB associations. Where Thilker et al. (2007) find XUV emission to be present in $\sim 30\%$ of spiral galaxies in the local universe, we find the frequency of outlying HII regions in gas-rich galaxies more nearby than 30 Mpc to be between 6 and 10%.

CHAPTER 3

NGC 1533 Case Study: Isolated OB Associations in Stripped H I Gas Clouds

3.1 Introduction

Studying resolved stellar populations in the low-density outskirts of galaxies can tell us to what extent the processes that govern star formation depend upon galactic environment. Toward this end, we present an *HST* study of three outlying H II regions that lie in the low-density HI-ring surrounding the galaxy NGC 1533. Ryan-Weber et al. (2004) originally discovered these H II regions (and two others) by-eye in the continuum-subtracted narrow-band image of NGC 1533 taken by the Survey for Ionization in Neutral Gas Galaxies (SINGG, Meurer et al. 2006). These outlying HII regions were also presented in the previous Chapter. For consistency with Ryan-Weber et al. (2004), we refer to them as regions 1, 2, and 5.

The peculiar ring-like distribution of HI around NGC 1533 as seen in Figure 3.1 (and figure 2 of Ryan-Weber et al. 2004 with higher H I cut-off levels) may be the result of an interaction with the nearby dwarf galaxy seen in the NW corner, IC2038 (with the SINGG identification J0409-56:S2). No obvious optical counterpart to the disturbed HI appears in either the DSS image or the SINGG image. The velocities of the three spectroscopically confirmed regions coincide well with the HI gas, which is bound to NGC 1533 (Ryan-Weber et al., 2004). The projected radius from the center of NGC 1533 to the outlying H II regions ranges from 19 kpc (region 5) to 31 kpc (regions 1 and 2), up to four times the R-band 25th magnitude isophotal radius of NGC 1533. Table 3.1 summarizes the properties of the three H II regions presented in Ryan-Weber et al. (2004) and imaged here. It gives the regions' positions,
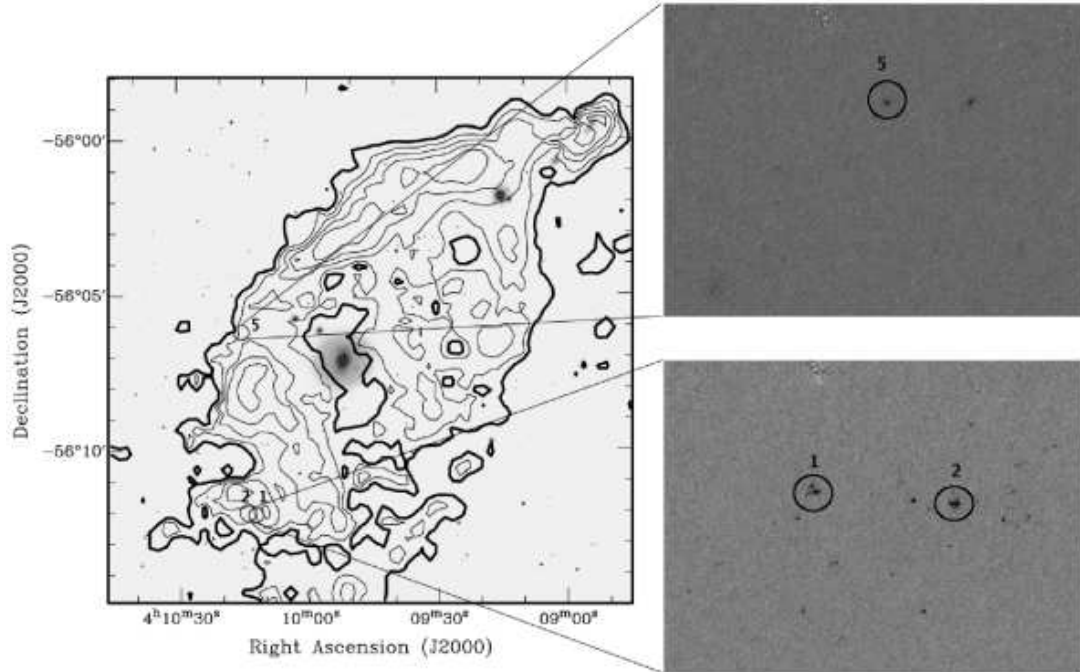
Figure 3.1. The Hα SINGG image of NGC 1533 overlaid with Australia Telescope Compact Array (ATCA) HI contours. The image is marked with the locations of the individual spectroscopically confirmed H II regions studied here. The HRC detection images are shown to the right of the SINGG image. The ATCA HI contours are 1.0 (in bold; 3σ), 1.5, 2.0, 2.5, and 3.0 $\times 10^{20}$ cm^{-2} and have a resolution of ~ 1 arcminute. There is no detectable H I emission on the optical core of NGC 1533.

projected radii from NGC 1533, velocities determined from their Hα emission lines, Hα luminosities, and H I columns at each region's position. Note that the values in our Table 3.1 differ from those presented in Ryan-Weber et al. (2004) because of the recent revision in the measurement of the distance to NGC 1533 using images taken in parallel to those discussed here (see Barber DeGraaff et al. 2007).

HII Region	RA	dec	r_{proj}	v	Log $L_{H\alpha}$	N_{HI}
(1)	(2)	(3)	(4)	(5)	(6)	(7)
1	04 10 13.7	-56 11 37.5	31	846 ± 50	37.67 ± 0.26	2.4
2	04 10 14.5	-56 11 35.9	31	831 ± 50	37.50 ± 0.26	2.4
5	04 10 15.7	-56 06 16.2	19	901 ± 50	37.35 ± 0.26	1.5

Table 3.1. Properties of NGC 1533's outlying HII regions. Summary of properties originally presented in Ryan-Weber et al. (2004): Positions are given in J2000 coordinates, with RA in hours, minutes, and seconds, and Declination in degrees, arcminutes, and arcseconds. (4) the projected separation in kiloparsecs to the optical center of NGC 1533. These numbers differ from those presented in Ryan-Weber et al. (2004) because we use the most recent measurement of the distance to NGC 1533, 19.4 Mpc (Barber DeGraaff et al., 2007).(5) velocities in km/s as measured from the Hα emission line in longslit spectra. (6) Log Hα luminosities in ergs s^{-1} as measured in SINGG Hα images. (7) The H I column densities (in 10^{20}cm^{-2}) are measured from ATCA maps, at the position of each H II region. NGC 1533 has a heliocentric velocity measured by HIPASS to be 785 km s^{-1}.

In this chapter, we present *Hubble Space Telescope* Advanced Camera for Surveys/ High Resolution Channel (ACS/HRC) images and photometry of the three spectroscopically-confirmed outlying H II regions associated with NGC 1533. These observations enable us to resolve the star-forming regions, identify their ionizing sources, and carry out an in-depth study of their stellar populations. In combination with the HST data, we make use of an ATCA H I synthesis map of NGC 1533 (Ryan-Weber et al., 2003b) to help constrain some of the details of the formation and evolution of the outlying H II regions.

Outlying H II regions are often found forming in relatively low column density H I gas. There is no H I detected to a limit of 2×10^{19} cm^{-2} at the location of the H II region near NGC 4388 (Oosterloo & van Gorkom, 2005), and the H I surface density in the vicinity of the three confirmed systems, regions numbered 1, 2, and 5 in Figure 3.1 is $1.5 - 2.5 \times 10^{20}$ cm^{-2} (Ryan-Weber et al., 2004). Furthermore, the H I peaks in the neutral gas ring surrounding NGC 1533 and in the stripped material around NGC 4388 do not exhibit any detectable level of star formation. These observations offer further support for the lack of correlation between star formation rate densities and H I surface densities on local scales found by Kennicutt et al. (2007), unlike what is seen on global galactic scales. The overall kinematics of the gas in the region of the outlying H II regions may provide clues as to the trigger of the star formation and the potential growth of the stellar associations into a tidal dwarf galaxy.

Independent of the gaseous properties of cluster environments, star-cluster "in-

fant mortality" suggests that the isolated, young star clusters presented here may be short-lived (Rafelski & Zaritsky, 2005; Fall et al., 2005; Chandar et al., 2006). Will supernova and mass loss in these clusters remove enough interstellar matter to leave the stars freely expanding, resulting in the clusters' rapid dissolution? Studies of the Antennae galaxies (Fall et al., 2005; Chandar et al., 2006) and the Small Magellanic Cloud (Rafelski & Zaritsky, 2005) purport that over half of clusters formed dissolve less than 10 Myr after their formation independent of their initial masses. However, a recent study by Gieles et al. (2007) concludes that there is little or no "infant mortality" for ages beyond 10-20 Myrs in the Small Magellanic Cloud, and de Grijs & Goodwin (2007) find less than 30% of young (< 20 Myrs) SMC clusters undergo "infant mortality." Generally, studies of this kind require a statistical sample of clusters. Instead, resolving a few star clusters in an isolated environment in a period during which they may be actively dissolving offers a different approach to examining their fates.

The photometric properties of the underlying stars in these outlying H II regions can help to answer some of the questions surrounding their formation and evolution. Previous studies have used stellar population synthesis models and evolutionary tracks to infer cluster ages and masses. For example, Whitmore et al. (1999) identify 3 distinct populations of star clusters in and around NGC 4038/4039 (Antennae Galaxy) using their integrated photometric properties. Gerhard et al. (2002) determine the mass and age of an isolated H II region in the Virgo Cluster from its measured Hα and V band luminosities. Thus far, studies of these sorts of objects have focused on what the star clusters' integrated light reveals about their formation histories, and have been unable to resolve the clusters into individual stars or stellar components. With the discovery of more and more young, faint clusters in tidal tails of merging galaxies, intracluster space and the intergalactic medium, there arises a need for information about the nature of the forming stars. Yet, there is an unavoidable, inherent uncertainty in the properties of lower mass clusters derived from models that assume a fully populated IMF (Cerviño & Luridiana, 2004). Resolving the star clusters presents an opportunity to examine their populations in greater detail.

We organize this Chapter as follows: Section 3.2 contains a description of our observations and measurements; Section 3.3 presents the results and model comparisons; Section 3.4.1 explores comparisons between these outlying H II regions and other extragalactic and Galactic young stellar populations; in Sections 3.4.2 and 3.4.3, we discuss the gas properties in the vicinity of the outlying H II regions and examine the likely fates of the stellar associations; and Section 3.5 briefly summarizes our results. The Appendix contains the new calculation of the conversion factor between the ionizing luminosity and the total number of main sequence O stars contained within an H II region following the methodology of Vacca (1994).

3.2 Observations and Measurements

3.2.1 HST Observations

HST ACS/HRC observations were carried out in October 2004. The targets were observed in three filters: F250W (5808 s); F555W (2860 s); and F814W (2892 s), covering a wide wavelength range chosen to sample the shape of the ultraviolet to optical SED. Throughout this Chapter, we will refer to the F250W filter as UV, F555W as V, and F814W as I in the interest of brevity and simplicity. Each orbit was split into two exposures separated by a small dither, resulting in 5σ limiting AB magnitudes of 28.0 in UV, 28.9 in V, and 29.0 in I. The images were processed with the CALACS calibration pipeline in order to remove the instrumental signature, and then combined using the *Apsis* pipeline (Blakeslee et al., 2003) resulting in cleaned and combined single images in each filter at each pointing at the optimal pixel scale of ACS/HRC, $0\farcs025$ pixel^{-1}. We create a detection image by summing the images in the three filters. Due to the paucity of known point sources in our HRC images, we measured the PSF from HRC images taken in the same cycle and in the same filters of the center of 47 Tuc, using at least 50 stars per image. The point sources in each image have an average Gaussian FWHM of 2.6 pixels, independent of the 3 filters investigated. At the adopted distance to NGC 1533, assumed to be 19.4 Mpc (Barber DeGraaff et al., 2007), this FWHM corresponds to a physical size of 6.1 pc.

Figure 3.1 shows the ACS/HRC detection images of the OB associations powering the isolated H II regions along with their locations in the R-band continuum SINGG image of NGC 1533 (Meurer et al., 2006); we show the H I distribution (Ryan-Weber et al., 2003b) with contours. The half-light radii of associations 1, 2, and 5 are 7.9, 9.0, and 6.2 pixels respectively, corresponding to physical sizes of 18.5, 21.1, and 14.5 pc. At a distance of 19.4 Mpc, 1 arcsecond corresponds to 94 parsecs. Three to nine clumps, most close in size to the image PSF, comprise each association. While multiple sources bright in UV and V surround associations 1 and 2, no such objects appear within the same proximity to association 5.

3.2.2 Source Detection and Definitions

We catalogued the sources in our images by applying the SExtractor code (Bertin & Arnouts, 1996), as implemented in the *Apsis* pipeline, to the relevant detection images. We eliminated spurious sources (e.g. single pixel detections, image edge artifacts) and objects detected in only one band by inspecting the SExtractor detections by-eye. Because the bulk of the following analysis requires color measurements, single-band detections (4 sources) are not of particular usefulness to us, though they may indeed be real. Of the initial 30 sources identified by SExtractor in the image containing associations 1 and 2, we include 19 in this analysis. Of the initial 36 sources identified by SExtractor in the image containing association 5, 11 appeared to be genuine detections, including one single-band detection (F814W) of an obvious background galaxy. Figure 3.1 shows the HRC detection images containing the labelled isolated associations. SExtractor split association 1 into three separate objects, and detected associations 2 and 5 as single objects. Further examination revealed each association to be composed of multiple clumps insufficiently deblended by SExtractor. Within the associations, we separated the components using IRAF contour plots with levels of 2σ, 4σ, 6σ and 8σ, defining an individual component as having at least two contours, corresponding to at least 4σ above the background. These criteria resulted in six components in association 1, nine components in association 2, and three components in association 5 (see Figure 3.2). Finally, using the
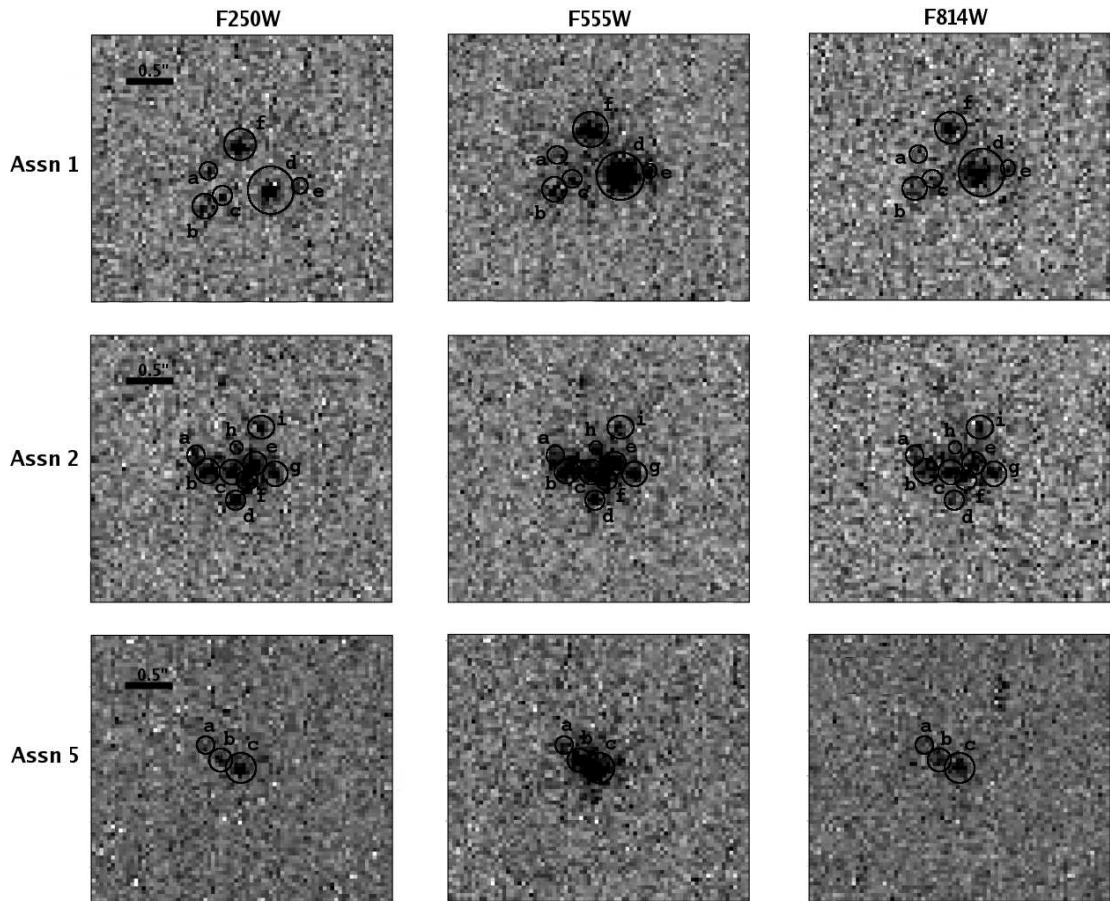
Figure 3.2. Cut-out images in each HRC filter of the three isolated associations and their components (which we refer to as "clumps"), circled and labeled. The image scale is shown in the top left corner. F250W is a UV bandpass, while F555W and F814W closely correspond to V and I bands, respectively. We present a detailed description of source detection and definition in Section 3.2.2.

66

IRAF task IMEXAM, we fitted Gaussian distributions to all field objects and clumps in order to determine their FWHMs.

There are three main types of objects to which we will refer throughout this Chapter: the stellar associations powering the total H II regions ($\equiv$associations), the components of the associations ($\equiv$clumps), and the field sources in the vicinity of the associations ($\equiv$ field objects). Furthermore, we assume that all of the extended and red field objects in the vicinity of the associations are background galaxies (see Section 3.2.4 and Table 3.4), and thus exclude them from most of this analysis. We address background galaxy contamination of the rest of the field objects in Section 3.2.4. The images of the objects included in this study are presented in Figures 3.1 - 3.4. Figure 3.1 gives an idea of the environment containing the outlying associations. All three lie in a low column density H I ring, with projected radii 19 - 31 kpc from the nucleus of NGC 1533. Figure 3.2 displays close-ups of the clumps in the three bands, UV (left column), V (center column), and I (right column), circled and labeled. The letters in the images correspond to the names in Table 3.2. Figure 3.3 shows the two HRC fields (in the three combined filters), with labels next to each object. Finally, Figure 3.4 shows three-color image close-ups of the associations, clumps, and field objects in the two sets of HRC images. In these color close-ups, blue, green, and red represent the UV, V, and I bands, respectively.

Assn (1)	(2)	F_λ (F250W) (3)	V−I (4)	UV−V (5)	m_V (6)	M_V (7)	FWHM (8)
1	Total	8.13 ± 0.78	$-0.12^{+.10}_{-.10}$	$-0.21^{+.11}_{-.12}$	$23.38^{+.04}_{-.04}$	-8.06	61
	a	0.24 ± 0.04	$-0.69^{+.45}_{-.52}$	$-0.86^{+.25}_{-.30}$	$27.85^{+.17}_{-.20}$	-3.59	3.39
	b	0.52 ± 0.07	$-0.22^{+.18}_{-.21}$	$-0.48^{+.16}_{-.18}$	$26.64^{+.09}_{-.10}$	-4.80	4.91
	c	0.18 ± 0.04	$-0.33^{+.27}_{-.35}$	$-0.18^{+.27}_{-.34}$	$27.51^{+.13}_{-.15}$	-3.93	5.48
	d	2.17 ± 0.14	$-0.46^{+.05}_{-.05}$	$0.33^{+.07}_{-.07}$	$24.27^{+.02}_{-.02}$	-7.17	9.40
	e	0.21 ± 0.04	$-0.37^{+.20}_{-.23}$	$0.07^{+.22}_{-.27}$	$27.06^{+.09}_{-.10}$	-4.38	4.00
	f	1.95 ± 0.09	$-0.45^{+.10}_{-.10}$	$-0.66^{+.06}_{-.06}$	$25.38^{+.04}_{-.04}$	-6.06	4.98
	DLC	2.63 ± 0.78	$-0.25^{+.19}_{-.22}$	$0.33^{+.29}_{-.39}$	$24.04^{+.09}_{-.10}$	-7.40	–
2	Total	11.2 ± 0.77	$0.08^{+.09}_{-.10}$	$-0.67^{+.08}_{-.09}$	$23.51^{+.04}_{-.05}$	-7.99	67
	a	0.26 ± 0.04	$-0.02^{+.22}_{-.27}$	$-0.54^{+.21}_{-.24}$	$27.47^{+.12}_{-.14}$	-3.97	4.44
	b	1.18 ± 0.07	$-0.31^{+.09}_{-.10}$	$-0.47^{+.07}_{-.08}$	$25.73^{+.04}_{-.04}$	-5.71	9.66
	c	1.40 ± 0.07	$-0.16^{+.08}_{-.09}$	$-0.67^{+.06}_{-.07}$	$25.75^{+.04}_{-.04}$	-5.69	8.67
	d	0.62 ± 0.05	$-0.86^{+.23}_{-.28}$	$-0.83^{+.11}_{-.12}$	$26.80^{+.07}_{-.08}$	-4.64	5.31
	e	1.25 ± 0.07	$-0.25^{+.09}_{-.10}$	$-0.62^{+.07}_{-.08}$	$25.82^{+.04}_{-.05}$	-5.62	9.60
	f	0.93 ± 0.05	$-0.45^{+.11}_{-.12}$	$-0.74^{+.08}_{-.08}$	$26.27^{+.05}_{-.05}$	-5.17	< 4.70
	g	0.85 ± 0.07	$-0.17^{+.13}_{-.15}$	$-0.64^{+.10}_{-.11}$	$26.26^{+.06}_{-.07}$	-5.18	4.83
	h	0.17 ± 0.04	$-0.09^{+.23}_{-.28}$	$-0.11^{+.27}_{-.34}$	$27.47^{+.12}_{-.13}$	-3.97	< 4.70
	i	0.58 ± 0.07	$0.19^{+.20}_{-.23}$	$-1.03^{+.17}_{-.18}$	$27.06^{+.12}_{-.13}$	-4.38	5.03
	DLC	3.96 ± 0.77	$0.17^{+.17}_{-.19}$	$-0.26^{+.20}_{-.24}$	$24.19^{+.10}_{-.11}$	-7.25	–
5	Total	3.51 ± 0.66	$-0.22^{+.15}_{-.17}$	$0.02^{+.20}_{-.23}$	$24.06^{+.06}_{-.06}$	-7.38	40
	a	0.15 ± 0.05	$0.46^{+.29}_{-.36}$	$-0.55^{+.36}_{-.48}$	$28.05^{+.20}_{-.25}$	-3.39	4.46
	b	0.61 ± 0.07	$-0.45^{+.12}_{-.13}$	$0.02^{+.13}_{-.15}$	$25.96^{+.05}_{-.06}$	-5.48	< 4.70
	c	1.57 ± 0.10	$-0.54^{+.10}_{-.11}$	$-0.33^{+.08}_{-.08}$	$25.28^{+.04}_{-.04}$	-6.16	9.54
	DLC	1.33 ± 0.66	$-0.54^{+.25}_{-.32}$	$0.74^{+.44}_{-.75}$	$24.37^{+.10}_{-.11}$	-7.07	–

Table 3.2. Photometry results and sizes for isolated associations and their components. (1) Association (2) Component identifier (3) The flux in the F250W bandpass times 10^{-18} ergs s^{-1} cm^{-2} Å^{-1} (4) V−I colors have been transformed to Vega Magnitudes in the standard Johnson-Cousins filter system using the prescription of Sirianni et al. (2005). V band magnitudes are technically in units of Vega magnitudes, although magnitude systems converge in the V band, making the given values roughly correct for the AB magnitude system as well. (5) The UV−V colors are left in AB magnitudes, as there is no calibration for the conversion of the F250W filter to Vega magnitudes. (6) Apparent V−band magnitudes were corrected for nebular emission ([OIII]$\lambda\lambda4959,5007$). (7) Absolute V−band magnitudes were calculated using a distance modulus of 31.44. (8) FWHM size in pc.
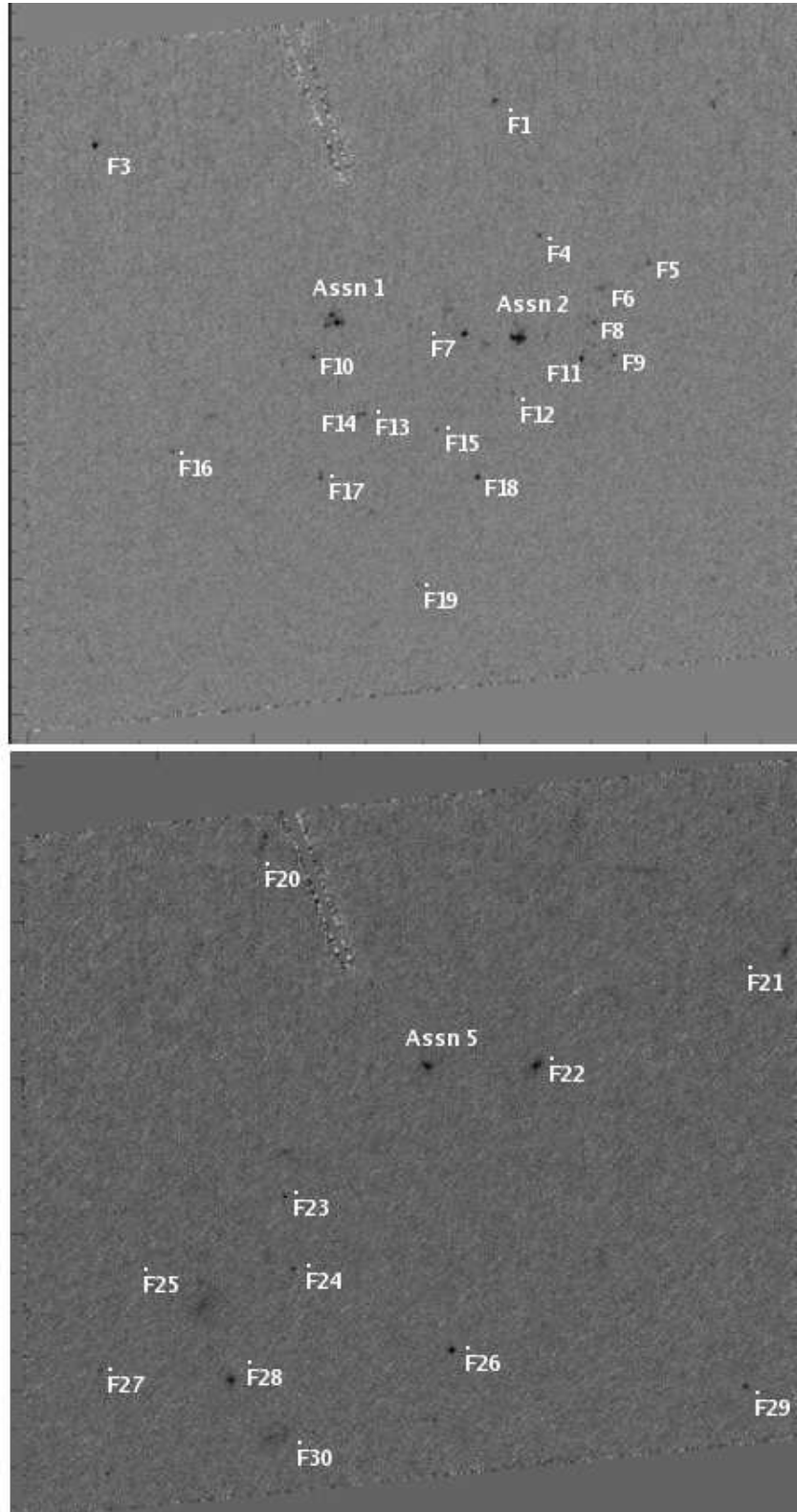
Figure 3.3. HRC detection images show the full fields containing the isolated stellar associations 1, 2, and 5. The 30 detected field objects are labeled according to their names in subsequent tables.
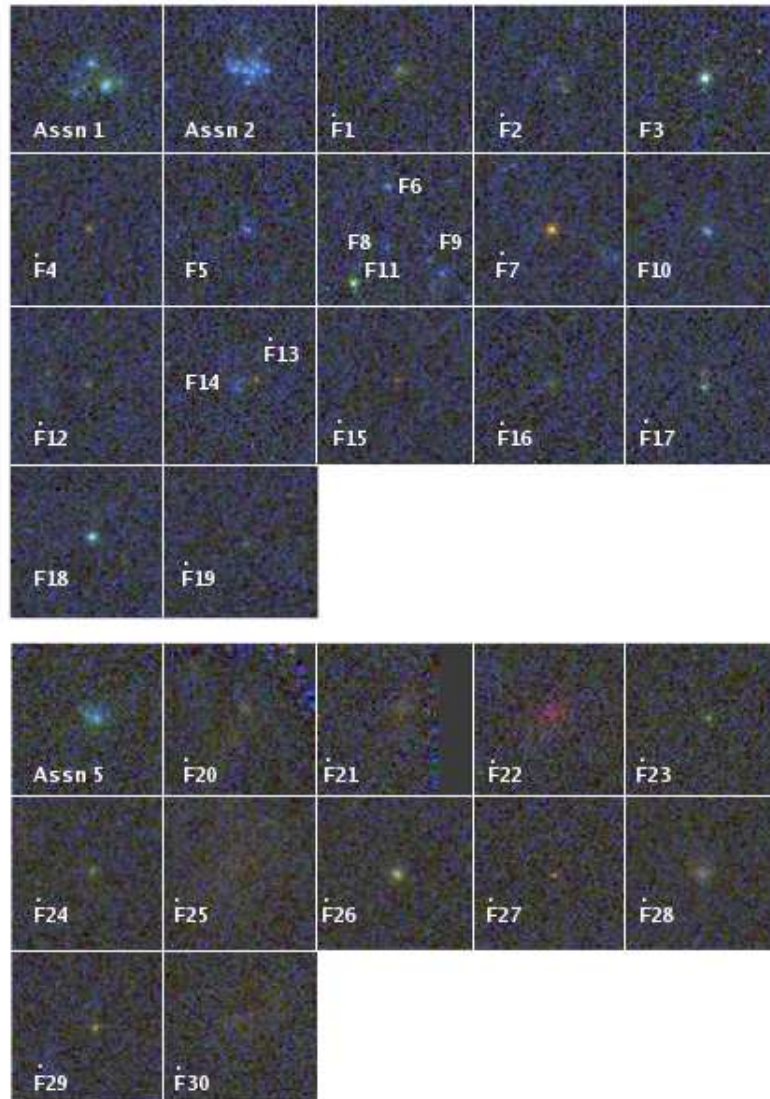
Figure 3.4. Three-color HRC images of associations and field objects. Here, blue, green and red represent UV (F250W), V (F555W), and I (F814W), respectively. The objects are labeled with names corresponding to those given in subsequent tables.

70

3.2.3 Aperture Photometry

We performed circular aperture photometry on each source using the IDL routine APER. Aperture sizes for each association and field object were determined by examining where the curve of growth (in flux vs. aperture radius) began to flatten, whereas aperture sizes for the clumps were determined by eye. For each association and field object, sky annuli were positioned approximately 1 arcsecond away from each of the objects' centers. Because the clumps are so closely spaced in the image, we subtracted the sky measurement outside the corresponding association as a best estimate. As evidenced by Figure 3.2, the circular apertures containing the clumps do not account for all the light in the association. We chose the aperture sizes to contain the maximum amount of emission while not overlapping with other apertures. By masking out the apertures containing the clumps, and running APER on what remained, we determined fluxes for the diffuse light components (DLC) of each association. This component simply represents the light losses resultant from the small apertures, and thus may not be genuine diffuse emission. Thus, the DLC is essentially the difference between the total association flux, and the sum of the fluxes of the individual clumps.

A correction for foreground extinction, based on the Schlegel et al. (1998) extinction maps, (foreground E(B-V) = 0.016), was applied according to the parameterization of Cardelli et al. (1989), including the update for the near-UV given by O'Donnell (1994). Given the location of the isolated associations far outside the optically luminous area of NGC 1533, we excluded any correction for the internal extinction. Additionally, fluxes for the associations were corrected for the strong emission lines [O Roman3]$\lambda\lambda 4959, 5007$ present in the F555W bandpass. We used the STSDAS package SYNPHOT to simulate photometry using an actual spectrum of association 1 (to be presented in a future paper) both with and without the nebular emission lines. The procedure for this correction is as follows: (1) We measured the Hα flux for all three H II regions in the NGC1533 SINGG narrow-band, continuum-subtracted image; (2) We measured the Hα emission line flux in the spectrum of association 1; (3) We divide quantity (1) by quantity (2) for each association to obtain a flux

correction factor for each individual association; (4) Using SYNPHOT, we measure the total flux of association 1's spectrum contained in the F555W bandpass; (5) We subtract the emission lines in this area of spectrum, and remeasure the total flux in the same area with SYNPHOT; (6) We subtract (5) from (4) to get an uncalibrated flux of just the emission lines in the F555W bandpass; (7) Finally, we calibrate and scale the total nebular emission-line flux from (6) by the individual correction factor determined in (3).

These emission-line corrections were 0.26, 0.17, and 0.27 AB magnitudes ($17\% - 28\%$ of the total flux) for associations 1, 2 and 5, respectively. We note that these emission line corrections assume that the flux ratios of Hα to [O III] emission lines are the same for each association. The error due to potential reasonable variations in these line ratios is negligible when compared to the total corrections. Furthermore, this correction has the effect that the associations are redder in V-I after correction than one would expect based on the V-I colors of the individual clumps, which were not corrected for nebular emission due to the limited ($\sim$1.5 arcsecond) resolution of the SINGG Hα images.

Finally, for comparison with population synthesis models and previous work, we transformed the ST magnitudes to the Vega magnitude system, and the filters to the standard Johnson-Cousins system following the method outlined by Sirianni et al. (2005) for both the F555W and F814W data. Because magnitude systems converge in the V band, and because the F555W filter is quite similar to the Johnson-Cousins V band, its transformation produces virtually no change. Furthermore, the F250W filter has no Johnson-Cousins counterpart, and it is impractical to convert AB magnitudes to Vega magnitudes in this part of the spectrum. Throughout this Chapter, we will quote V-I colors in terms of Vega magnitudes in the standard Johnson-Cousins filters. This magnitude system allows for the greatest ease in comparing our results with both previous work and existing population synthesis models. However, UV-V and UV-I colors and UV magnitudes will remain in the HRC filter bandpasses and in AB magnitudes. The faintness of the clumps and field objects combined with considerable pixel-pixel noise in the read noise limit produces errors in the photometry as high

as 0.25 magnitudes. The resulting Vega magnitudes are presented in tables 3.2, 3.3, and 3.4 as well as the V-I and UV-V colors, along with the measured FWHM of each source.

3.2.4 Source Properties and Contamination by Background Galaxies

Our sample of field objects and clumps totals 48 individual sources altogether, 34 of which are located in the 3 kpc × 3 kpc field around associations 1 and 2. We estimate that the associations span 40 - 75 parsecs in their full visible extent, similar to large Milky Way stellar associations. Figure 3.3 gives the location of all objects identified in the two HRC images, with the field containing associations 1 and 2 on the top frame, and that of association 5 on the bottom frame. Of the 48 individual sources, only 17 are resolved. 9 of the 11 field objects in the association 5 field are well-resolved extended sources. The V-I colors of the clumps range from -0.7 to 0.2 in V-I, and those of the field sources range from -0.9 to 1.8. If all the sources were at the same distance as NGC 1533, the absolute V-band magnitudes range from -3.4 to -7.3.

Almost certainly, some of the field objects in the HRC images represent distant background galaxies. From Hubble Deep Field galaxy number densities, we expect 1-2 × 10^5 galaxies per square degree in WFPC2, corresponding to a limiting I-band magnitude of 25-26 (Casertano et al., 2000). Field galaxy number densities are lower in the far-UV, roughly 3×10^4 galaxies per square degree to a limiting AB magnitude of 26.5 (Teplitz et al., 2006). Considering these number densities, we would then expect 5-10 red background galaxies to appear in our $29'' \times 26''$ field of view, and 0-1 galaxies with emission in the UV. We detect and analyze 11 objects in the vicinity of association 5, none of which appear in the UV images, and the majority of which appear quite red in V-I. Of the 11 objects in the vicinity of association 5, six are very obviously extended or elliptical red sources, with V-I colors (Vega magnitudes) between 0.7 and 1.8 (as previously mentioned, one object is detected only in F814W). Three of the remaining five compact sources have V-I colors in a similarly red range, while two exhibit fairly blue V-I colors, 0.04 and 0.19. The lack of UV emission

from these sources combined with the number being consistent with our prediction for background galaxy detections leads us to classify all 11 as background emitters.

We detect and analyze 19 objects in the vicinity of associations 1 and 2. In contrast to the association 5 field objects, many of these field objects appear bright in UV and V, suggesting that the star formation in the SE part of NGC 1533's H I ring extends beyond the initially detected isolated H II regions. Furthermore, most of the surrounding blue field objects lie clustered within 500 parsecs of the nearest association (1 or 2), while the likely background galaxies are spread more evenly throughout the image. While we cannot say for certain which of the field objects around associations 1 and 2 are background galaxies, we can predict that the 10 sources not detected in F250W, 5 of which have V-I colors greater than 1.0, are more likely to be distant background galaxies. These sources also appear to be more extended. Moreover, this number of sources is consistent with the prediction based on the background galaxy density of deep WFPC2 images.

We do note, however, that we are unable to distinguish extended likely background galaxies from potentially old ($\sim$ 1 Gyr), extended open clusters, which can have V-I colors up to 1.4 and absolute magnitudes ranging from -1 to -5.1 in the V band (Lata et al., 2002). Nor can we differentiate unresolved likely background galaxies from globular clusters, which have V-I colors ranging from 0.85 to 2.65, and absolute V-band magnitudes from -1.5 to -9.5 (Harris, 1996). Still, such old, extended open clusters are rare in the Milky Way (e.g. Lata et al. 2002; Lada & Lada 2003), and globular clusters tend to lie closer to the galaxy center (within $\sim$ 20 kpc) than the star formation seen here (Harris, 1996), although a few are as far as 100 kpc from Galactic center. Still another possibility remains that some of these objects could represent isolated red supergiants.

Tables 3.3 and 3.4 present the photometric properties and optical sizes for all detected field objects. In these tables, we have identified those field objects which are the best candidates for distant background galaxies (extended, red, and/or no UV-emission) as $\dot{F}$, and those blue field objects which are most likely to be associated with the ongoing star-formation around NGC 1533 as F. Figure 3.3 shows three-color

ID	RA	dec	F_λ (F250W)	V−I	UV−V	m_V	M_V	FWHM
(1)	(2)	(3)	(4)	(5)	(6)	(7)	(8)	(9)
$\dot{\mathrm{F}}1$	04 10 14.54	-56 11 44.84	–	$0.05^{+.23}_{-.26}$	–	$25.52^{+.14}_{-.16}$	-5.92	11.38
$\dot{\mathrm{F}}2$	04 10 15.51	-56 11 43.35	–	$1.38^{+.32}_{-.43}$	–	$26.63^{+.28}_{-.39}$	-4.81	7.81
F3	04 10 12.73	-56 11 45.58	1.36 ± 0.14	$-0.23^{+.04}_{-.04}$	$1.17^{+.19}_{-.23}$	$23.92^{+.03}_{-.03}$	-7.52	5.91
$\dot{\mathrm{F}}4$	04 10 14.64	-56 11 39.58	–	$1.01^{+.17}_{-.19}$	–	$26.55^{+.14}_{-.16}$	-4.89	7.88
F5	04 10 15.10	-56 11 37.89	1.02 ± 0.13	$-0.40^{+.34}_{-.45}$	$-0.95^{+.20}_{-.23}$	$26.35^{+.15}_{-.17}$	-5.09	5.60
F6	04 10 14.82	-56 11 36.00	0.90 ± 0.14	$-0.61^{+.36}_{-.51}$	$-0.74^{+.22}_{-.25}$	$26.27^{+.15}_{-.17}$	-5.17	5.95
$\dot{\mathrm{F}}7$	04 10 14.24	-56 11 36.35	–	$2.03^{+.10}_{-.11}$	–	$25.24^{+.10}_{-.11}$	-6.20	6.02
F8	04 10 14.80	-56 11 35.18	0.56 ± 0.11	–	$-1.07^{+.25}_{-.30}$	$27.12^{+.17}_{-.20}$	-4.32	3.97
F9	04 10 14.89	-56 11 34.69	0.75 ± 0.13	$0.34^{+.21}_{-.25}$	$-0.67^{+.23}_{-.26}$	$26.41^{+.15}_{-.17}$	-5.03	5.62
F10	04 10 13.55	-56 11 36.42	1.59 ± 0.14	$-0.27^{+.18}_{-.21}$	$-0.86^{+.13}_{-.14}$	$25.78^{+.09}_{-.10}$	-5.66	7.15
F11	04 10 14.74	-56 11 34.77	0.35 ± 0.14	$-0.10^{+.07}_{-.08}$	$2.04^{+.36}_{-.55}$	$24.56^{+.04}_{-.04}$	-6.88	5.48
$\dot{\mathrm{F}}12$	04 10 14.41	-56 11 33.89	–	$0.79^{+.24}_{-.30}$	–	$26.95^{+.20}_{-.25}$	-4.49	5.34
$\dot{\mathrm{F}}13$	04 10 13.74	-56 11 34.02	–	$1.49^{+.27}_{-.34}$	–	$26.94^{+.25}_{-.32}$	-4.50	5.64
F14	04 10 13.70	-56 11 33.91	0.68 ± 0.17	$-0.89^{+.52}_{-.93}$	$-0.44^{+.31}_{-.39}$	$26.28^{+.19}_{-.23}$	-5.16	4.66
$\dot{\mathrm{F}}15$	04 10 14.05	-56 11 32.99	–	$1.36^{+.27}_{-.34}$	–	$27.28^{+.25}_{-.32}$	-4.16	5.60
$\dot{\mathrm{F}}16$	04 10 12.86	-56 11 33.76	–	$0.67^{+.29}_{-.36}$	–	$26.61^{+.24}_{-.30}$	-4.83	8.02
$\dot{\mathrm{F}}17$	04 10 13.49	-56 11 31.89	–	$-0.32^{+.20}_{-.24}$	–	$25.77^{+.09}_{-.10}$	-5.67	5.19
F18	04 10 14.19	-56 11 30.99	2.41 ± 0.16	$-0.27^{+.08}_{-.09}$	$-0.19^{+.08}_{-.09}$	$24.66^{+.04}_{-.04}$	-6.78	5.62
$\dot{\mathrm{F}}19$	04 10 13.85	-56 11 27.36	–	$-0.01^{+.27}_{-.33}$	–	$26.92^{+.16}_{-.19}$	-4.52	5.78

Table 3.3. Photometry results and sizes for field objects near associations 1 and 2. (1) Field identifier (2) and (3) RA, dec (J2000) positions in hms, and dms (4) The flux in the F250W bandpass times 10^{-18} ergs s^{-1} cm^{-2} Å^{-1} (5) V−I colors have been transformed to Vega Magnitudes (see Table 3.2 (6) The UV−V colors in AB magnitudes (7) Apparent V−band magnitudes, corrected for nebular emission ([OIII]$\lambda\lambda4959,5007$). (8) Absolute V−band magnitudes were calculated using a distance modulus of 31.44. (9) FWHM size in pc.

(RGB) images of the field objects and background galaxies. The top panel shows the field objects surrounding associations 1 and 2, and the bottom panel displays the field objects of association 5. The labels on each image correspond to the names listed in tables 3.3 and 3.4("Assn" for the association; "F" for field object, and "Ḟ" for likely background galaxy). We do include all of these objects in the subsequent analysis for completeness' sake (except where their red colors push them outside of adopted plotting ranges), and we urge the reader to consider the 10 "dotted" objects in Table 3.3 and the 11 objects in Table 3.4 (also identified in the figures) as potential background galaxies.

In Figures 3.5 and 3.6, we compare the individual sources' absolute magnitudes and V-I and UV-V colors with those of single star MK spectral types and a 50 M$_\odot$ instantaneous-burst Starburst99 population (see 3.1). In order to plot MK spectral types in M$_V$ versus UV-V, we converted their U-band absolute Vega magnitudes to the F250W filter in AB magnitudes using the SYNPHOT. To arrive at Starburst99

ID	RA	dec	V−I	m_V	FWHM
(1)	(2)	(3)	(4)	(5)	(6)
Ḟ20	04 10 16.52	-56 06 24.07	$1.22^{+.28}_{-.36}$	$25.27^{+.25}_{-.33}$	14.68
Ḟ21	04 10 16.86	-56 06 04.30	$1.71^{+.22}_{-.28}$	$25.64^{+.21}_{-.27}$	15.47
Ḟ22	04 10 16.00	-56 06 11.62	$-$	$-$	17.48
Ḟ23	04 10 15.06	-56 06 18.80	$0.04^{+.16}_{-.18}$	$26.00^{+.09}_{-.10}$	6.95
Ḟ24	04 10 14.77	-56 06 17.57	$0.19^{+.16}_{-.18}$	$25.99^{+.11}_{-.12}$	9.99
Ḟ25	04 10 14.48	-56 06 20.22	$1.56^{+.21}_{-.25}$	$24.30^{+.19}_{-.23}$	24.73
Ḟ26	04 10 14.66	-56 06 10.95	$0.85^{+.07}_{-.09}$	$24.80^{+.06}_{-.07}$	9.91
Ḟ27	04 10 14.04	-56 06 23.07	$2.25^{+.28}_{-.38}$	$27.14^{+.27}_{-.37}$	5.89
Ḟ28	04 10 14.20	-56 06 18.31	$0.71^{+.11}_{-.11}$	$24.81^{+.08}_{-.08}$	17.90
Ḟ29	04 10 14.02	-56 06 16.17	$1.34^{+.13}_{-.13}$	$26.09^{+.11}_{-.12}$	6.36
Ḟ30	04 10 14.96	-56 06 00.15	$1.79^{+.32}_{-.43}$	$24.83^{+.30}_{-.42}$	24.97

Table 3.4. Photometry results and sizes for field objects near Association 5. (1) Field identifier (2) and (3) RA, dec (J2000) positions in hms, and dms (4) V−I colors have been transformed to Vega Magnitudes (see Table 3.2 (5) Apparent V−band magnitudes, corrected for nebular emission ([OIII]$\lambda\lambda$4959,5007). (6) Absolute V−band magnitudes were calculated using a distance modulus of 31.44. (7) FWHM size in pc for straightforward comparison with clumps and other field objects. We do not detect Ḟ22 in any filter other than F814W, although we consider it a real source, with an I band magnitude of 23.14 (Vega magnitudes).

UV-V colors we calculated the F250W AB magnitude using the output synthetic spectrum along with SYNPHOT. In many cases, the colors and absolute magnitudes of the objects are well-matched by single O or B stars. This similarity does not prove that field objects and clumps are single stars, but that O and B stars dominate the radiation output in many cases. In other cases, the expected magnitude-color evolution of a Starburst99 population (run for an instantaneous burst Salpeter IMF with $\alpha = 2.35$, $M_{up} = 100$, $M_{low} = 0.5$, Padova group isochrones, and Z$= 0.4 Z_\odot$) with an initial mass of 50 M$_\odot$ matches the data. We note that a 50 M$_\odot$ population with a 100 M$_\odot$ upper mass limit is unphysical, and results in fractional stars. We have simply used an initial starburst mass of 50 M$_\odot$ to appropriately scale the absolute magnitude and illustrate a degeneracy. The colors are unaffected by the mass of the initial starburst. We discuss the implications of fractional stars and stochastic IMFs in section 3.3.3. For completeness, we have included the bluest (in V-I) background galaxy candidates in Figure 3.5, using NGC 1533's distance modulus to calculate their absolute magnitudes. The reddest candidates do not lie within the ascribed color range.
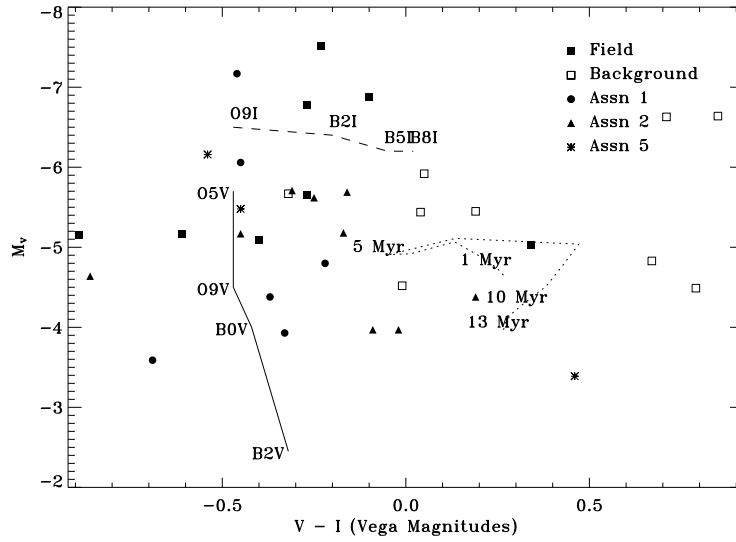
Figure 3.5. Color-magnitude diagram for the blue field objects and clumps, with V-I in Vega magnitudes. The dashed and solid lines shown are calibrations of MK spectral types from Schmidt-Kaler (1982). The dotted line represents the V-I color evolution of a Starburst99 50 $M_\odot$ population with Z= $0.4Z_\odot$. The population synthesis model was run for an instantaneous burst Salpeter IMF ($\alpha = 2.35$, $M_{up} = 100$, $M_{low} = 0.5$), and employs Padova group isochrones.
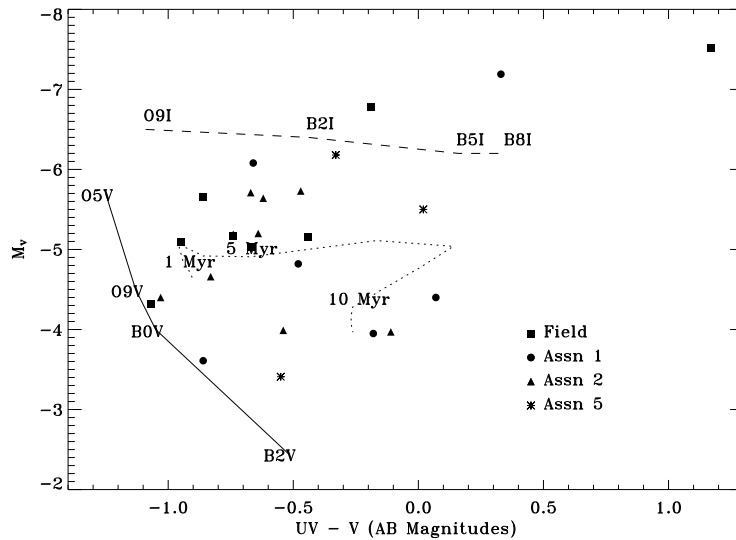
Figure 3.6. Color-magnitude diagram for the field objects and clumps, with UV-V in AB magnitudes. The dashed and solid lines shown are calibrations of MK spectral types from Schmidt-Kaler (1982). The dotted line represents the UV-V color evolution of the same Starburst99 population shown in Figure 3.5.

77

3.3 Stellar Populations of Associations

Ideally, stellar population synthesis models, along with integrated colors and luminosities, can provide a solution for the masses and ages of the stars populating the clusters. These models aim to account for most of the known stellar evolutionary processes, and integrate over various sets of assumed initial conditions. In the following analysis, we describe two approaches we took in an effort to constrain the stellar populations of the isolated associations. We compare the associations' colors and luminosities to output from Starburst99 models (Leitherer et al., 1999), and we perform a simple, independent calculation using the associations' total UV and Hα luminosities. Both approaches employ single-age, single-metallicity models with a Salpeter IMF. While the Starburst99 model accounts for details of stellar evolution, it cannot account for anything but a scaled-down IMF over the full range of stellar initial masses. Our independent calculation is more quantized with regard to the stellar populations, but does not account for some of the details of stellar evolution. In section 3.3.3 we discuss the limited applicability of both models to our data given the low luminosities of the isolated associations, and masses below what is required for a fully-populated IMF.

3.3.1 Comparison with Starburst99 Model

To accurately designate a metallicity for the Starburst99 model, we used an optical spectrum of association 1, estimating its metallicity to be roughly $\sim 0.4Z_\odot$ (Werk et al., in preparation). Figure 3.7 plots various diagnostics from ages 1 - 16 Myr for a Starburst99 synthetic population for Z$= 0.4$Z$_\odot$, an instantaneous burst of 10^6M$_\odot$, and a Salpeter IMF with a lower limit of 0.5 M$_\odot$ and an upper limit of 100 M$_\odot$. It also shows the corresponding values calculated for associations 1, 2 and 5. The error bars indicate photometric errors.

In Figure 3.7a, we show the temporal evolution of the ratio Log $(F_{H\alpha}/F_{UV})$ for the Starburst99 model and the three associations. Hα and UV luminosities serve as reasonable star formation indicators (Kennicutt, 1998a). While Hα traces the ionizing radiation from stars more massive than $15M_\odot$, the UV luminosity originates

from stars more massive than $3M_\odot$. The ratio Log $(F_{H\alpha}/F_{UV})$ decreases steeply with time, as massive ionizing stars die out, and late-type O stars and B stars produce the majority of the UV flux. The best-match ages to the evolution of Log $(F_{H\alpha}/F_{UV})$ are 3.2 Myrs, 4.5 Myrs, and 3.0 Myrs for associations 1, 2, and 5 respectively. In this plot, the horizontal error bars represent the minimum possible error given the photometric errors.

The evolution of UV−V, UV−I, and V−I colors of the same Starburst99 population is plotted in three color-color diagrams for the same range in ages in Figure 3.7. The Starburst99 UV magnitudes in the HRC F250W bandpass were generated by the SYNPHOT package for the output Starburst99 spectra. Seen in Figure 3.7 associations 1, 2, and 5 are consistently bluer than the model colors, except for association 2 in V-I. Thus, we cannot constrain the ages using simply the colors of the associations. As we will discuss, the inability of the Starburst99 model to match the association colors most likely arises from small number sampling in which a few early-type stars dominate the output radiation. An incompletely-sampled IMF results in a significant scatter of colors at a given age (Chiosi et al., 1988), and would explain the discrepancies seen in figures 1.7b, 1.7c, and 1.7d.

From the Starburst99 model, we can also derive mass estimates based on the absolute V band magnitudes and ages of the associations. At a particular age, a 10^6 $M_\odot$ Starburst99 stellar population has a predicted absolute V band magnitude, $M_{V,S99}$. We then use a simple scaling relation between mass and absolute magnitude to derive the masses of the associations: $M = 10^{6+0.4(M_{V,S99}-M_V)}$, where M is the mass of the stellar population and M_V is the absolute magnitude of the association given in Table 3.2. The total stellar mass of each association is 1490, 1850, and 840 $M_\odot$ for associations 1, 2 and 5 respectively. We repeat this calculation for the I-band magnitudes. The total stellar mass from the I-band magnitude of each associations is 1240, 2030, and 610 $M_\odot$ for associations 1, 2 and 5, very similar to the results of the V-band calculation. We note that this particular way of estimating the mass assumes a scaled-down IMF containing the full-range of stellar masses from 0.5 $M_\odot$ to 100 $M_\odot$. Indeed, if we were to try to quantize the numbers of stars by their spectral type
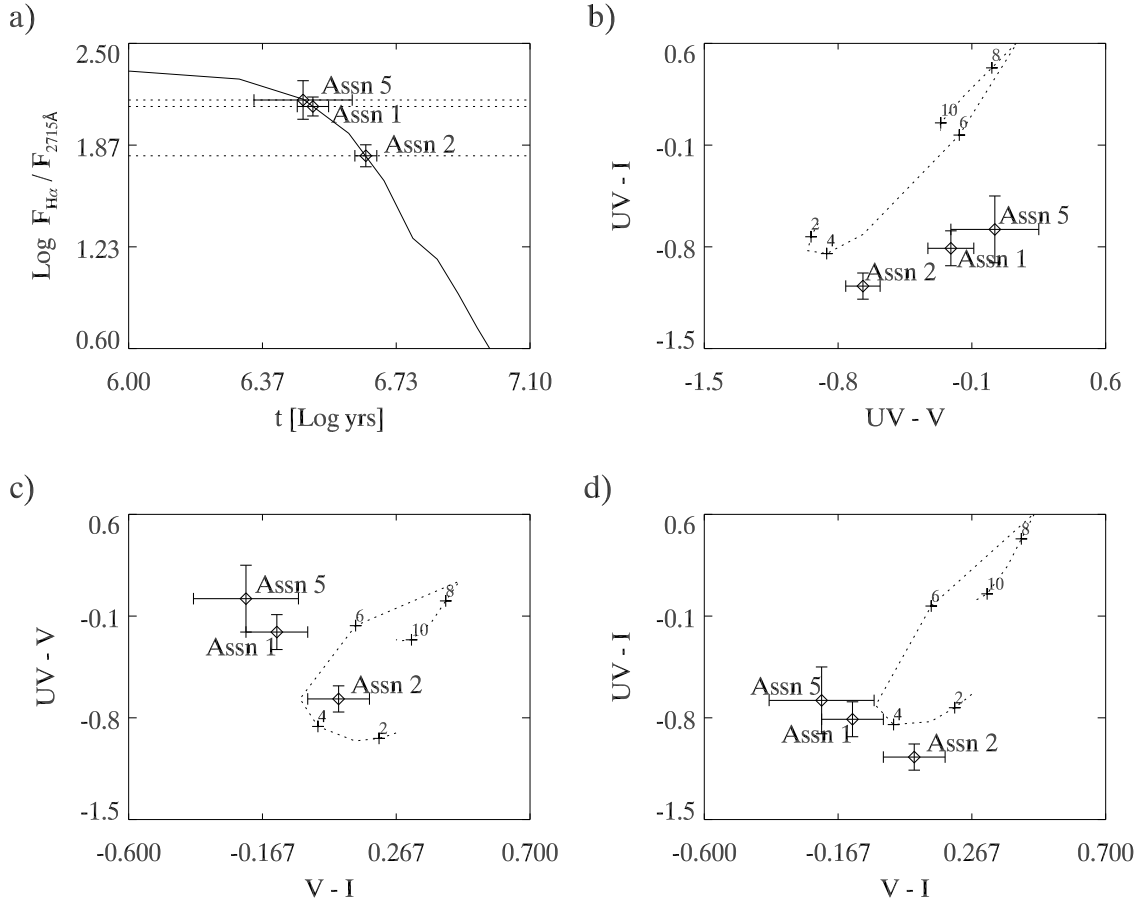
Figure 3.7. Color and flux evolution with time. Evolution with time of the Hα to UV ratio and relevant optical color-color diagrams for the Starburst99 stellar population synthesis model at Z= 0.4Z$_\odot$. The model was run for an instantaneous burst Salpeter IMF ($\alpha = 2.35$, $M_{up} = 100$), and employs Padova group isochrones. a) The Hα to UV ratio of each association with a symbol at the intersection point of the Starburst99 model. The inferred ages are 3.2 Myr, 4.5 Myr, and 3.0 Myr for associations 1, 2, and 5 respectively. The errors in the best-match ages correspond to the uncertainty due to the photometric errors alone, and do not include stochastic effects or model errors. b) UV−I versus UV−V; the dotted line shows Starburst99 values for ages between 2 − 10 Myrs c) UV−V versus V−I d) UV−I versus V−I

we would find only fractional stars for the highest masses. Table 3.5 includes columns for the ages and masses derived using the Starburst99 model.

Although these plots and derived parameters are instructive, they are limited by the low luminosities of the clusters. A very basic limit for the application of evolutionary synthesis data to observational data, termed the "lowest luminosity limit" (LLL) by Cerviño & Luridiana (2004), is that *the total luminosity of the cluster modeled must be larger than the individual contribution of any of the stars included in the model.* Using figure 2 from Cervino & Luridiana (2004) for Z= $0.4Z_\odot$, we compare the absolute magnitudes of the associations with the LLL in both the V and I bands. For young star clusters (~ 5 Myrs), the minimum V and I band luminosities for which population synthesis models are valid are -10.0 and -10.5, respectively. In the UV, the LLL would be fainter, and the effects of undersampling will be less. Since the associations have absolute V and I band magnitudes significantly fainter than the limits, it is unlikely we are completely sampling the stellar population. Stochastic effects then will impact the data interpretation, and we explore these effects more thoroughly in Section 3.3.3.

3.3.2 Independent Calculation of Cluster Ages and Masses

We further constrain the stellar populations of the associations by performing an independent estimate of the total number of ionizing stars present in each association. We extrapolate this calculation to determine total masses and ages of the associations. We begin by converting an Hα luminosity to an emission of ionizing photons, $Q_0 = 7.33 \times 10^{11}$ $L_{H\alpha}$ s^{-1} with $L_{H\alpha}$ in ergs s^{-1} cm^{-2} Å^{-1} (Osterbrock, 1989). Models then predict the number of ionizing photons released per unit time from a certain spectral type (ST) of a massive star, usually O7V. By dividing the two quantities, one arrives at the number of "equivalent" stars of the given subtype. This number of "equivalent" ionizing stars, while a simple characterization of the stellar population, does not represent the *total* number of ionizing stars. To determine the total number of ionizing stars, one must integrate over an initial mass function, and use models that predict how the output of ionizing photons varies with stellar mass. In this section,

we give the results of our calculation. In the appendix, we include a detailed, step-by-step description of the calculation, including all relevant equations and parameters. Essentially, our method follows the calculations outlined in Vacca (1994), but uses the recently updated T_{eff} - spectral type calibration of Martins et al. (2005).

For associations 1, 2, and 5 we determine the upper limits of the present-day mass function to be 35 $M_\odot$, 25 $M_\odot$, and 40 $M_\odot$, respectively. The method we use, as described in the appendix, compares the total UV and Hα fluxes of the associations and the relative contributions from O and B stars. Essentially, we are modeling the UV flux as the sum of the flux from both the O and B stars. We ultimately determine what value of stellar mass corresponds to a present-day mass function upper limit that can account for both the UV and Hα fluxes that are observed. We use these upper masses to calculate a limit on the lifetimes of the clusters. For initial stellar rotation velocities between 0 and 300 km s^{-1}, a 35 $M_\odot$ star burns hydrogen for 4.7 - 5.9 Myr, a 25 $M_\odot$ star burns hydrogen for 5.9 - 7.4 Myr, and a 40 $M_\odot$ star burns hydrogen for 4.2 - 5.1 Myr (Meynet & Maeder, 2000). We obtain the total masses of the associations by integrating the present-day mass function, and using the upper mass cut-offs given above and lower mass limit of 0.5 $M_\odot$. The masses of associations 1, 2, and 5 calculated by this method are 2700, 7200, and 970 $M_\odot$, respectively. We note that this method of calculating the masses does not assume a scaled-down full IMF, as the Starburst99 mass estimate does, but rather uses a present-day mass function. We integrate only to the present-day upper mass limit, resulting in a more physical calculation of mass, minimizing the number of fractional stars. The number of "equivalent" O7V stars, total number of ionizing O stars, the total mass, and the derived ages from both the Starburst99 model and this independent calculation are given in Table 3.5 for each isolated H II region. To abbreviate the names of the two methods, we refer to the Starburst99 derived parameters with S99, and the calculation using the method and models of Vacca (1994); Vacca et al. (1996); Martins et al. (2005) as VM05. The range in ages given in Table 3.5 for VM05 correspond to stellar lifetimes without rotation, and the minimum error contributed by the uncertainty in the photometry.

There is general qualitative agreement between the corresponding quantities, yet some differences are clear. The ages determined with the VM05 calculation are systematically larger than those determined from Starburst99. Neither model accounts for stochastic effects upon the stellar masses present, so the differences in ages and masses most likely reflect the difficulty of modelling the integrated properties of an undersampled stellar population. Association 2 is the most discrepant across the separate calculations, particularly in mass.

A comparison between the number of equivalent O7V stars and the total O star population is illustrative of the limited information gained from a simple representative population. While association 1 has the most "equivalent" O7V stars, association 2 actually has a greater total O star population. This can be understood as follows: association 1 is younger than association 2, and thus contains more massive O stars with stronger ionizing fluxes than association 2; association 2 has evolved more than association 1, its most massive O stars having died out, and it is left with a large late-type O and B star UV radiation-producing population. This result is also readily apparent in the masses of the two associations.

3.3.3 Stochastic Effects

As with the interpretation of results from the Starburst99 model, we caution that stochastic effects may play a large role, largely unaccounted for in the stellar population analysis of these associations. In the VM05 calculation we have again assumed a fully populated IMF, which is most likely not the case, given the limits discussed above and tabulated in Cerviño & Luridiana (2004). Still, we may probe the extent to which we are overestimating the stellar populations by examining the behavior of the Salpeter IMF we have assumed thus far. We assume that the IMF is a probability distribution function such that the mass of the largest star formed in an underpopulated cluster of N stars decreases as N decreases. The expression for this expectation value of the maximum mass star, $< m_{max} >$, derived by Oey and Clarke (2005) is:

$$< m_{max} >= M_{up} - \int_{10}^{M_{up}} \left[\int_{10}^{M} \Phi(m) \, dm \right]^N dM \tag{3.1}$$

HII Region	N$_{O7V}$	S99: M$_{tot}$	Age	VM05: N$_{OV}$	M$_{tot}$	Age
(1)	(2)	(3)	(4)	(5)	(6)	(7)
1	8.06	1.24-1.49	2.9 - 3.5	11	2.73	4.4 - 5.0
2	5.46	1.85-2.03	4.2 - 4.8	22	7.17	5.6 - 6.2
5	3.81	0.61-0.84	2.2 - 3.8	4	0.97	3.8 - 4.6

Table 3.5. Derived properties for NGC 1533's outlying stellar associations. (1) ID of HII Region/Association (2) N$_{O7V}$ is the number of *equivalent* O7V stars in each association, calculated using the SINGG Hα luminosity (3) and (6) Total mass in stars in units of 10^3 M$_\odot$ of the associations determined from Starburst99 and the independent calculation based on VM05, presented in Section 3.3.2. (5) N$_{OV}$ is the *total* number of O stars present in each association (see Section 3.3.2 and the appendix for details). (4) and (7) Age of HII regions, for each method, in units of Myrs

In this equation, $\Phi(m)$ is the IMF, integrated over mass, shown as two separate variables (m and M) for the two separate integrals. For a single power-law Salpeter IMF and M$_{up}$ of 120 M$_\odot$, the expected maximum mass star produced does not approach M$_{up}$ until N stars with masses above 10 M$_\odot$ reaches ~ 1000 (in actuality, the expectation value never reaches M$_{up}$ as the integrated function is asymptotic). Below this value of N stars, varying degrees of stochastic effects must be considered. Since we have already normalized the IMF for each association using the UV-flux from B stars, we perform another simple integration to calculate the number of stars with masses initially greater than 10 M$_\odot$ in each association. Association 1 contains 25 stars greater than 10 M$_\odot$, association 2 contains 60, and association 5 contains only 9. We numerically integrated equation 1 for N =25, 60, and 9, and for a Salpeter IMF to arrive at $< m_{max} >$ for each of the associations. These values are 80 M$_\odot$, 96 M$_\odot$, and 55 M$_\odot$ for associations 1, 2, and 5. These results indicate that our age estimates and total masses for association 5 may be over estimated – if the maximum mass star in a population of this size is initially 55 M$_\odot$, and we have calculated the present-day upper mass limit to be 40 M$_\odot$ as well, we could just as easily be witnessing a zero-age population forming in-situ. Stochastic effects are less dramatic for associations 1 and 2, but nonetheless important. The greater difference between the expected initial maximum mass and the present-day upper mass limit indicates directly that some evolution has occurred for associations 1 and 2. We stress that while our age estimates for association 5 are strict upper limits, we can have more confidence in our age estimates for associations 1 and 2.

3.4 Discussion

In this section we discuss the properties of the associations, clumps, and blue field objects, and compare and contrast them with those of stellar populations in the Galaxy and outlying H II regions of other systems. Do stellar clusters carry an imprint of the environment in which they form, or are their properties independent of their surroundings? We also examine the H I properties of the environment containing the isolated associations and comment on the conditions for their formation and potential evolution. Finally, the age and mass constraints, along with physical sizes and locations, provide additional clues as to their likely fates in light of the rapid cluster dissolution inferred in many systems.

3.4.1 Comparison With Galactic OB Associations, Open Clusters, and Other Intergalactic H II Regions

Associations

The associations span roughly 100 pc, and contain components separated by up to 10 pc, similar to the unbound OB associations of the Milky Way. In addition, their luminosities and masses match those of a sample of Milky Way associations within 1 kpc, and the Galactic phenomenon of similarly-sized association subgroups is directly comparable to the clumps seen here (Blaauw, 1964). The properties of the associations match those of the extragalactic OB associations in seven nearby spiral galaxies with distances ranging from 6.5 - 14.5 Mpc (Bresolin et al., 1998) equally as well. These extragalactic OB associations (diameters $\leq$ 200 pc) have median diameters between 70 - 100 pc, contain 6 -15 blue stars with $M_V \leq -4.76$, and contain cluster candidates with V-I colors between -0.07 and 1.53. By comparison, the associations discussed here contain 3 - 9 clumps with $M_V \leq -3.4$, and V-I colors between -0.90 and 0.2. Previous studies of spiral galaxy OB associations have noted a constant mean size of OB associations near 80 pc, a size that may represent the smallest step in the hierarchical structure of giant star-forming regions (Efremov et al., 1987; Efremov, 1995; Ivanov, 1996). The sizes of these outlying OB associations are consistent with the mean sizes of both Milky Way and extragalactic OB associations.

As noted in the Introduction, there is a growing number of objects in the literature termed "intergalactic H II regions," with photometric properties that span a wide range, and environments that range from compact groups of galaxies to tidal streams from interacting galaxy pairs. One population of four intergalactic H II regions lies in the H I tail to the east of NGC 7319, a member of Stephan's Quintet, a Hickson Compact Group composed of 3 interacting galaxies at 80 Mpc (Mendes de Oliveira et al., 2004). The four intergalactic H II regions in Stephan's Quintet appear to represent brighter, more massive, and larger versions of the outlying H II regions of NGC 1533. Their absolute B band magnitudes cluster near -12, at the level of a faint dwarf galaxy, their derived masses are near 3×10^4 M$_\odot$, their physical sizes (FWHMs) are between 400 - 600 pc, and their Hα luminosities are between 10^{38} and 10^{39} ergs s^{-1}. In contrast, the Hα luminosities of the NGC 1533 outlying H II regions are between 10^{37} and 10^{38} ergs s^{-1}, with physical sizes < 100 pc, and masses on the order of 10^3 M$_\odot$.

In the ring-like H I structure surrounding the galaxy NGC 5291 (d = 62 Mpc), 29 intergalactic H II regions have been discovered, and appear to be characterized by a "UV-excess" compared to their Hα emission (Boquien et al., 2007). The ratio of the Hα star formation rate (SFR) to the NUV SFR (SFR(Hα)/SFR(NUV) $\sim$ 0.5 for their entire sample) is considerably lower than typical ratios for Galactic H II regions (1 - 3). Here, we calculate SFR(Hα)/SFR(NUV) for our three outlying H II regions, transforming our F250W UV fluxes (2715Å) to NUV fluxes (2271Å) by assuming a UV spectral slope typical of starbursting systems, $F_\lambda \sim \lambda^{-2.5}$, thus multiplying the UV fluxes given in Table 3.2 by a factor of 1.56 (Meurer et al., 1999). We use the equations presented in Boquien et al. (2007) for the SFRs (converted to cgs): SFR(UV) = [NUV] = 2.41 $\times$ 10^{-40} L$_{NUV}$ [ergs s^{-1}Å^{-1}] M$_\odot$ yr^{-1}; and SFR(Hα) = [Hα] = 7.9 $\times$ 10^{-42} L$_{H\alpha}$ [ergs s^{-1}] M$_\odot$ yr^{-1}. Associations 1, 2 and 5 have [Hα]/[NUV] of 3.0, 1.3, and 3.1, respectively, and thus do not show any UV excess as observed for the intergalactic H II regions around NGC 5291. Boquien et al. (2007) explain the UV-excess in their sample as the result of a quasi-instantaneous burst of star formation, resulting in two populations of stars, one roughly 4 Myrs old, and the

other 10 Myrs. For comparison, their PSF in the NUV has a characteristic width of 5″, 75 times larger than our PSF. At 62 Mpc, 5″ covers 1.5 kpc, and would therefore encompass most of the HRC field of view at the distance to NGC 1533, and quite possibly all of the visible star formation around regions 1 and 2, which we show spans a range of possible ages (2-9 Myrs).

Clumps and Blue Field Objects

Aside from single O and B stars, the closest Galactic analogs to the clumps and blue field objects are young open clusters. For example, Bonatto et al. (2006) presents a detailed analysis of the properties of NGC 6611 (the Eagle Nebula) deriving an age of 1.3±0.3 Myr, a limiting radius of 6.5±0.5 pc, and an observed mass of 1600 $M_\odot$. Viewed from a distance of 19 Mpc, a young open cluster such as NGC 6611 would appear unresolved in the HRC and similar to one of the clumps or blue field objects. Moreover, the integrated photometric characteristics of Galactic open star clusters younger than 10 Myrs are fairly consistent with those of the clumps and field objects. Of the 140 open clusters (masses between 25 and 4×10^4 $M_\odot$) tabulated in Lata et al. (2002), 17 are younger than 10 Myrs, with absolute V band magnitudes between -4.5 and -9, and V-I colors (for only 6 of the 17) between 0 and -0.27. These colors are similar to those found for the clumps and blue field objects listed in tables 3.2, 3.3, and 3.4. However, the properties of the clumps and blue field objects are also in line with single O and B stars, seen in Figures 3.5 and 3.6. In the end, we cannot distinguish between single stars and young open clusters at the physical resolution limit of the HRC.

The clumps and blue field objects also have extragalactic analogs, and more extreme counterparts. The photometric properties and sizes of the clumps and blue field objects align with those of the faint 1-10 Myr clusters in the LMC and SMC studied by Hunter et al. (2003). Compared to the young clusters in the disk of M82, a violently starbursting system, the clumps and blue field objects have similar V-I colors (on the blue side) and absolute V-band magnitudes. The range of V-I colors for the M82 young clusters is -0.05 to 2.34, with absolute V-band magnitudes ranging

from -11.2 to -5.3, having a mean of -6.75 (Konstantopoulos et al., 2007). However, the young massive ($\sim 10^5$ M$_\odot$) clusters of the Antennae galaxies exhibit a range of properties nearly on a different scale from those of the stellar populations powering NGC 1533's outlying H II regions. The clumps lie on the faintest end of the Antennae cluster luminosity function constructed by Whitmore et al. (1999), contain far fewer stars (indeed, they may be single stars), and for the most part, occupy the bluest end of the V-I color distribution. Overall, the properties of the clumps and blue field objects show no deviation from the continuum of properties for known star clusters (if they are not single stars) in both our Galaxy and others.

3.4.2   Gas Properties

The H I distribution shown in Figure 3.1 reveals a ring around NGC 1533 with a total H I mass of 6×10^9 M$_\odot$ (Ryan-Weber et al., 2003b). The southeast cloud, the site of the star formation discussed throughout this Chapter, contains approximately 1/3 of this total H I mass (2.4×10^9 M$_\odot$), and has a maximum H I column density of 4×10^{20} cm^{-2}. The three associations do not lie in the densest regions of the SE H I cloud, but rather in regions well below the canonical neutral gas surface density cutoff for star formation on global scales (10^{21} cm^{-2}, Skillman 1987). Of course, the Q scenario predicts that this critical gas density threshold (Σ_{crit}) scales with velocity and radius (Kennicutt, 1989). For a flat rotation curve and parameters fitted in Kennicutt (1989), Σ_{crit} (M$_\odot$ pc^{-2}) $= 0.4 \frac{c}{6} \frac{V}{R}$, where c is velocity dispersion and V is the rotation velocity of the galaxy, both in km s^{-1}, and R is the projected distance from the galaxy nucleus in kpc. Given a fitted rotation velocity of the gas around NGC 1533 of 150 km s^{-1} and a velocity dispersion of 10-30 km s^{-1} (Ryan-Weber et al., 2003a), at the projected radii of the isolated H II regions (19 - 31 kpc), the threshold column densities of the H I would range between $4 - 20 \times 10^{20}$ cm^{-2}. The observed column densities at the positions of the outlying H II regions appear to fall below this range in critical surface density (see Table 3.1); although it is possible the true H I column densities are underestimated due to the 1 arcmin beam. It should also be noted that though the H I ring appears to be rotating around NGC 1533, it

is not part of a smoothly rotating disk as studied by Kennicutt (1989).

Across entire galaxies, star formation regions tend to align with H I peaks, but this global correlation breaks down on sub-kiloparsec scales (Kennicutt et al., 2007). On a local scale, low-levels of star formation can proceed despite lower than normal neutral gas column densities. Similar to the H II regions outside NGC 1533, the Stephan's Quintet outlying H II regions are not associated with H I peaks in the tidal tail (at levels below 10^{20} cm^{-2}) (Mendes de Oliveira et al., 2004). Additionally, the H II region found in the Virgo Cluster by Gerhard et al. (2002) lies in no detectable amount of H I gas (down to 10^{19}cm^{-2}; Oosterloo & Van Gorkom 2005). There must be a reservoir of yet undetected molecular material at the positions of these outlying H II regions. The Atacama Large Millimeter Array (ALMA) will shed light on the molecular conditions required to trigger star formation outside the disk of galaxies.

Though it may appear as though associations 1 and 2 lie near a relatively dense cloud of H I (just to the north of the associations), there are actually multiple clouds along the line of sight, and not a single, rotating cloud. Figure 3.8 shows the lack of a smooth velocity gradient at the position of this apparent H I concentration in a position velocity slice across the long diameter of the cloud. The total H I mass of the concentration of gas clouds in the vicinity of associations 1 and 2 is 3×10^8 M$_\odot$, similar to the amount of H I found in the vicinity of the potential tidal dwarf galaxies of the Antennae (Hibbard et al., 2001a) and NGC 5291 (Bournaud & Duc, 2006), but lower than what is typically found for tidal dwarf galaxies ($\geq 10^9$ M$_\odot$ e.g. Duc & Mirabel 1994, 1998; Hibbard & Barnes 2004;). The velocity dispersions in the vicinity of NGC 1533's outlying H II regions are near 30 km s^{-1}, with gradients in the range 7-50 km s^{-1} kpc^{-1} (Ryan-Weber et al., 2003a). The relatively high velocity dispersions may lend some clue to the conditions of their formation, as cloud-cloud collisions are known to trigger star formation. These velocity dispersions are much higher than the H I velocity dispersions measured in the vicinity of the tidal dwarf galaxy candidates in the Antennae (5-15 km s^{-1}; Hibbard et al. (2001a)), and the overall kinematic structure is much more irregular than that of both the Antennae and other potential tidal dwarf galaxies (e.g., Bournaud et al. 2007). We plan to
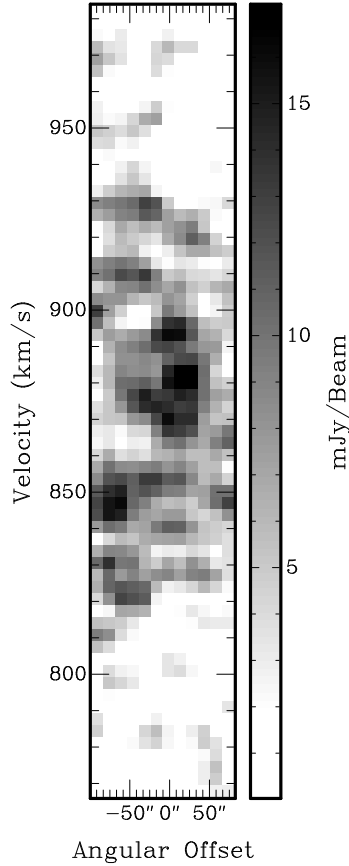
Figure 3.8. A slice in position-velocity space across the long diameter of the apparent H I concentration just to the north of associations 1 and 2. This figure shows that the concentration is made up of numerous clouds across a wide range of velocities. The noise level is at ~ 4 mJy/bm and the beam is 1 arcminute (Ryan-Weber et al., 2003b).

explore the relation between H I column densities and velocity dispersions for star formation in the far outskirts of galaxies in a future paper including a larger sample of outlying H II regions and high-resolution H I data.

While the stellar masses revealed here do not place the star formation in the HI ring in the category of tidal dwarf galaxy (TDG) candidates, the location of associations 1 and 2 in the tip of the SE H I tidal tail may actually be a prime one for survival. In a set of 96 N-body simulations, Bournaud & Duc (2006) found that of all structures formed during mergers, the only objects that are long-lived are those formed in the extremities of the tidal tails. The tips of tails are often sites of kinematical pilings-up of gas (Duc et al., 2004), contain populations less prone to fall back upon the progenitor galaxy, and lie far beyond the reach of disruptive galactic

tidal forces (Bournaud & Duc, 2006). However, these simulations were limited to stellar tidal structures with masses greater than 10^8 M$_\odot$, a criterion our associations surely do not meet. If one assumes the gas in the clump near associations 1 and 2 is part of a bound structure, the resulting dynamical mass is 20-25 times higher than the baryonic mass in this region. This abnormally high dynamical mass for a TDG, together with the structure of the clouds, indicate the stellar associations are unlikely to evolve into a relatively long-lived tidal dwarf galaxy.

3.4.3 Fate and Evolution

In the recent literature, there has been much focus on the age distribution of star clusters as a way of examining their rate and nature of dissolution. We cannot construct an age distribution of the 19 individual clumps and 18 field objects because they all have V-band absolute magnitudes considerably fainter than -9, a limit indicating that single stars dominate their output radiation. We can, however, comment on the associations and their relationship to the clumps and blue field objects in the context of cluster disassociation. In this section, we assess the survival of the associations by considering the locations of the objects in the HRC fields relative to each other, their relative sizes, and age and mass constraints from stellar evolution models.

Rapid Dissolution

Star clusters of a wide range of masses and in various environments are subject to a large number of possible internal and external evolutionary effects. In the Milky Way, embedded protoclusters less massive and more densely concentrated than the isolated associations discussed here are observed to dissolve on fast timescales ("infant mortality"), with less than 4-7% surviving as bound clusters (Lada & Lada, 2003). In the extreme environment of the colliding Antennae galaxies, the survival prospect is just as grim for more massive young "super star" clusters (Fall et al., 2005). In more quiescent systems like the SMC, "infant mortality" may play a much smaller role, if any; however, its role has not been fully investigated for clusters younger than $\sim$10 Myrs due to a detection bias against clusters having nebular emission in the SMC samples (Gieles et al., 2007; de Grijs & Goodwin, 2007). The fate of the stellar

systems powering outlying H II regions (ages < 10 Myrs; masses 10^3 - 10^4 $M_\odot$) has not yet been explored in the literature. On one hand, their fate may be similar to that of Galactic OB associations, thought to expand freely for tens of Myrs (Blaauw, 1964; de Bruijne, 1999). In this case, one of their most massive clumps (subgroups) on average ends up as a bound, open cluster such as the Pleiades (Lada & Lada, 2003). On the other hand, their location in an environment vastly different from that of the Galactic disk may result in a different fate. Furthermore, objects of similar masses and sizes to these isolated associations seem to be able to survive for hundreds of Myrs in the SMC (de Grijs & Goodwin, 2007), while the vast majority appear to dissolve on the order of tens of Myrs in the Antennae Galaxies (Fall et al., 2005). In this context, it is relevant to explore what will become of these isolated associations given our high-resolution photometric data.

The scenario of rapid cluster dispersion requires some disruptive effect other than the general stellar evolutionary processes and gravitational effects such as stellar evaporation driven by two-body relaxation considered in typical cluster fading laws. Most commonly proposed is that the energy and momentum input from massive stars (in the form of winds, jets, ionizing radiation, and supernovae) remove the cluster's ISM, leaving it unbound and freely expanding (Hills, 1980; Goodwin, 1997; Fall et al., 2005). These effects result in an average expansion rate of the stars in Galactic OB associations of 5 km s^{-1}, or 5 pc in 1 Myr, estimated analytically (Hills, 1980). Observationally, the direct measurement of an expansion speed will have to wait until the launch of Gaia. However, under realistic assumptions of expansion, the stars' proper motions and radial velocities (along with the best positions available from Hipparcos) are consistent with linear expansion coefficients of about 5 km s^{-1} per 100 pc (Blaauw, 1964; Bobylev & Bajkova, 2007). Thus, typical Galactic associations can expand for only tens of Myrs before dispersing into the general field population. If these outlying OB associations expand similarly, they eventually will not be recognizable as distinct groups of stars. The expansion of associations also implies that larger associations, will be, on average, older than more compact associations. Of the three studied here, Association 5 is the youngest (2 - 4.5 Myrs), and also has

the smallest visible physical extent of roughly 60 pc. On the other hand, association 2 is the oldest (4.5 - 6.5 Myrs), and has the largest physical extent of roughly 100 pc. This age-size sequence is consistent with a scenario of dispersion. Association 5 may still be recognizable as an association of massive stars for some time, whereas associations 1 and 2 likely have less time before they will be indistinguishable from the blue field objects.

Do the blue field objects then represent stars and/or star clusters that were once physically linked with the associations and have since dispersed into the field? Given the typical expansion rate of OB associations, if the blue field objects were once part of association 1 or 2, they would have to be 30 - 240 Myrs old to account for the observed separations of 150 - 1200 pc. The colors of the blue field objects are not consistent with this range of ages. The single stars dominating the radiation output of the blue field objects are roughly consistent with main sequence stars ranging from 8 $M_\odot$ to 40 $M_\odot$ (consistent with B2V - O5V stars; see Figures 3.5 and 3.6). Geneva stellar tracks (Lejeune & Schaerer, 2001) predict that an 8 $M_\odot$ star has a V-I color below zero as it burns hydrogen, and reddens by over 1 magnitude at an age of 27 Myrs, while a 40 $M_\odot$ star has a V-I color below zero as it burns hydrogen, and reddens by more than 1 magnitude near 6 Myrs. Since the blue field objects generally have V-I colors below zero, they are unlikely to be older than 6 - 27 Myrs, and therefore would not have had time to reach their current projected separations from the nearest association (1 or 2) at the assumed velocity of 5 km s^{-1}. There is also no indication that the field objects further from the association are redder (and, by inference, older) than those that are nearby. Some of the blue field objects may also represent single runaway O or B stars ejected from the associations at maximum speeds ranging from 200 - 350 km s^{-1} (Hoogerwerf et al., 2001; Leonard & Duncan, 1990). This speed would give the stars the ability to travel between 1200 - 9450 pc in their estimated lifetimes, but this phenomenon is highly unlikely to account for all 18 blue field objects, if any at all.

A more likely scenario for the blue field objects in the context of cluster dissolution is that some of them once formed their own association that is no longer easily

recognizable as such. In the Galaxy, the Cassiopeia-Taurus group may represent a similar grouping of objects with a common origin in a more advanced state of disintegration (Blaauw, 1964; de Zeeuw et al., 1999). Here, F5, F6, F8, F9, and F11 (and other tiny sources visible in the same locale, but undetected by SExtractor, see Figures 3.2 and 3.4) appear to be clustered together themselves, in an ostensibly young, diffusing complex with a total extent of about 150 pc and average object projected separations of 20 pc. The radius of this potential complex, given average association expansion velocities and assuming all its components formed at roughly the same position, is indicative of an age of ~ 20 Myrs, which is roughly consistent with the range of ages possible for the blue field objects (see above). In the SINGG Hα image (1.37″ resolution), we do not detect unresolved Hα emission at the location of this "complex" as we do for associations 1, 2, and 5. Assuming the H II region potentially associated with this diffusing complex is similarly unresolved in the SINGG image (likely, given the 1″ FWHM of the complex of objects), the upper limit to the Hα flux at the location of this "complex" is 9.96×10^{-17} ergs s^{-1} cm^{-2}, based on 5σ point source detection limits of the SINGG data. Dividing this upper limit by the sum of the UV flux of F5, F6, F8, F9 and F11, we derive an upper limit Log $(F_{H\alpha}/F_{2715\mathring{A}})$ of 1.44. The subsequent lower age limit of the diffusing "complex" based on Figure 3.7 is 5.6 Myrs, at least 1-2 Myrs older than the ages of associations 1, 2 and 5 based on this same plot, and consistent with the idea that these blue field objects represent an association in the process of dissolving while the other associations are comparably more intact.

One can also consider what should be observable in the field if we assume a continuous and homogeneous low rate of star formation in this region for the past 100 Myrs. In this scenario, if we see 2 associations of 2000 M$_\odot$ that are under 10 Myrs old, then it follows that we would expect 2 associations of 2000 M$_\odot$ every 10 Myrs for the last 100 Myrs, or twenty 2000 M$_\odot$ associations in this region. Independent of the processes responsible for rapid cluster dissolution, we should consider the effects of fading due to mass loss from stellar evolution and tidal effects, as this will decrease the number of clusters we expect to see. Because our detection limits are similar to those

of Hunter et al. (2003) in their study of the Large and Small Magellanic Clouds, we assume a cluster fading function similar to theirs, where $M_{fade} = 982(t/Gyr)^{0.69}$ $M_\odot$. Thus, without rapid cluster dissolution, we would be able to detect similar mass associations with ages up to $\sim$1 Gyr (approximately the age of the HI ring, Ryan-Weber et al. 2003a). That we do not detect associations independent of those directly associated with the H II regions indicates that the clusters are either rapidly dispersing or this is the first generation of star formation in the HI stream.

In the scenario of rapid dissolution, we may still expect to find background fluctuations in our images representative of previous star formation in the HI stream that has subsequently dispersed. In our HRC data, we see no evidence of an underlying older population after investigating the noise distributions in each band. The shape of the noise distribution is nearly perfectly Gaussian in all cases, and in UV, V, and I we probe down to 28.0, 28.9, and 29.0 AB magnitudes, respectively. While this does not rule out an older population of dispersed clusters (or a previous stellar component to the HI stream), if one exists, it is below the noise level. Considering an expansion rate of 5 km s^{-1}, we can estimate the expected cluster fading due to its dissociation alone. A linearly increasing cluster radius with time (Blaauw, 1964; Fall et al., 2005), results in the surface brightness decreasing with the square of time (in fact, the surface brightness will decrease faster because as stars age and die, the cluster becomes fainter). For areas the size of these associations ($\sim$186 pixels^2), our HRC images give a 5σ surface brightness limit of 24.3 mag arcsec^{-2} in the V band. We calculate the V-band surface brightnesses of the associations 1, 2, and 5 (using their half-light radii) to be 21.85, 22.26, and 22.0 mag arcsec^{-2}, respectively. Thus, in 14 Myrs, when the average radius of the associations has increased by a factor of 2.5 (from 47 pc to 117.5 pc), the surface brightness of the associations will fade below the detection limit of the HRC images. It is consistent with the idea of rapid cluster dissolution that we see one nearly dissolved association roughly 6 - 20 Myrs old, and several younger, more intact associations.

Alternative Scenario: A First Generation of Stars

Contrary to the above argument for rapid dissolution, the associations, clumps, and blue field objects may represent a distribution of a first-generation of star formation in which the stars and clusters have not strayed far from their location of formation. We emphasize that this scenario is self-consistent only if star formation in this region began less than 10 - 15 Myrs ago, otherwise we would see older, intact associations similar in mass to those observed. In this scenario, the blue field objects would occupy the low mass end of the initial cluster mass function (CMF) rather than represent the remnants of dissolved larger stellar associations. That the youngest association (association 5) is the most compact may simply indicate a lower initial mass of this association compared to the others, and not that it is part of an age-size sequence of cluster dissolution. If the observed associations comprise a first generation of stars, then we cannot use these HRC data to untangle their fates.

In this regard, the isolated and singular association 5 may be most likely to be an initial episode of star formation. For, if star formation has been continuous in this region for any period of time greater than 10 Myrs, the absence of any sign of dispersed cluster remnants in its vicinity may be inconsistent with cluster disintegration. That this youngest association remains isolated in comparison with its older counterparts offers some indication that it represents an initial episode of star formation in this northern region of NGC1533's H I ring. There are a few related caveats to consider: 1) even if association 5 represents a first generation of star formation, rapid dissolution may subsequently proceed 2) association 5 could simply represent the youngest, most compact component of the age-size sequence we expect for cluster dissolution 3) the star formation in this northern region may have begun later than that in the southeast, and so should simply be considered separately.

3.5 Summary and Conclusion

HST ACS/HRC images in UV, V and I bands resolve the three very young stellar associations powering the outlying H II regions that lie up to 30 kpc from the stellar

disk of the S0 galaxy NGC 1533. We have catalogued and performed circular aperture photometry on 48 individual sources in the HRC images, 27 of which appear to be associated with the ongoing star formation. From background galaxy statistics and broadband colors, we have determined that the other 21 sources are likely distant background galaxies. Furthermore, we have defined a range of sources in the images: the term "associations" refers to the total stellar populations powering the H II regions; the term "clumps" refers to the individual resolved sources composing the associations; and the term "field objects" refers to the individual sources detected separately from the associations. Using two different methods, (Starburst99; Leitherer et al. 1999, and an independent calculation derived from Vacca 1994 and Martins 2005, see appendix) in combination with our broadband colors and magnitudes, and Hα luminosities from SINGG (Meurer et al., 2006), we have placed upper limits on the the total numbers of stars, masses and ages of each association. The masses of the isolated associations range from 600 M$_\odot$ to 7000 M$_\odot$, and the ages range from 2 - 6 Myrs. Given the faint luminosities of the stellar associations, we have also considered the importance of stochastic effects upon our calculations. Colors and absolute magnitudes of many of the clumps within the associations and field objects are consistent with single O and B stars dominating the output radiation.

There are three results from our analysis that deserve emphasis:

- Despite their location in an environment that is vastly different from that of a Galactic spiral arm, the photometric properties and sizes of the associations, clumps, and blue field objects are consistent with those of Galactic stellar associations and clusters and/or stars. This result suggests something uniform about the star-formation process on scales of tens of parsecs, independent of environment.

- The level of star formation in the SE H I cloud of NGC 1533 is lower than that observed in other systems (e.g. NGC 5291; Boquien et al. 2007). Furthermore, low H I column densities (10^{20}cm^{-2}) and high H I velocity dispersions (~ 30km s^{-1}) characterize its environment. These data hint that there may be some

relation between SFR, H I column density and velocity dispersion that holds outside of massive gas disks, on local scales. These data are also consistent with the recent finding that H I surface density and star formation rate densities do not correlate on sub-kiloparsec scales (Kennicutt et al., 2007). The kinematics of the H I in the vicinity of the H II regions do not suggest the stellar associations will evolve into a larger tidal dwarf galaxy.

- The stellar associations detected here are either in the process of rapid dissolution or represent the first generation of stars in the gaseous ring around NGC 1533. If the star formation in the SE part of the H I ring has been continuous over the last 20 Myrs to 1 Gyr, we are directly witnessing the rapid dissolution of young clusters and associations. Not only do the associations display a range of ages and sizes consistent with cluster dissolution, but the age constraints and locations of several clustered blue field objects indicate they are the last visible remnants of an already dispersed association. If instead, these isolated associations and blue field objects represent a first generation of stars in the stripped H I of NGC 1533, we cannot determine the ultimate fate of the associations. This possibility of a first generation of stars is then uniquely suited for exploring star formation triggers and initial conditions without the influence of stellar feedback. Given that their Galactic OB association analogs are generally thought to be gravitationally unbound and freely expanding (Blaauw, 1964; Hills, 1980), along with evidence for star cluster "infant mortality" in various clustered stellar systems (e.g. Lada & Lada 2003; Fall et al. 2005), we find it most likely that the stellar populations of the outlying H II regions will soon (< 20 Myrs or so) no longer be detectable nor recognizable as associations of stars; rather, they will be building a background population of young objects in the halo of NGC 1533.

CHAPTER 4

Case Study: The Metal-Enriched Outer Disk of NGC 2915

4.1   Introduction

The mass fraction of heavy elements in a galaxy is a fundamental physical property: it contains a record of the star formation history and therefore serves as an indicator of its evolutionary state. Numerous observational studies of gas metal abundances in a wide variety of galaxies, spanning a large range in mass and morphological types, have established a now well-known, yet poorly understood global relation in which the mean metallicity and stellar mass are directly correlated (e.g. Lequeux et al. 1979, Tremonti et al. 2004, Geha et al. 2009). The physical processes that govern this mass-metallicity relation are under debate (see Introduction), yet there is some consensus that low-mass dwarf galaxies hold the key to understanding this relation. Using a sample of 53,400 star-forming Sloan Digital Sky Survey galaxies, Tremonti et al. (2004) argue that metal loss via galactic winds is most likely to be responsible for the steep decline in the "effective yield" (a parameterization of the metallicity divided by the galaxy total gas fraction) with galaxy baryonic mass. The physical basis for these outflows would be the cumulative effect of supernovae in disk OB associations which leads to low-mass galaxies with shallow gravitational potential wells selectively losing their metals (Mac Low & Ferrara, 1999; Strickland et al., 2004; Brooks et al., 2007). Nonetheless, there are several other possible mechanisms for explaining the correlation between low metal yields and galaxy mass, including metal mixing in extended gaseous disks (Tassis et al., 2008), and a lower effective stellar upper mass limit to the initial mass function in dwarf galaxies (Köppen et al., 2007; Meurer et al.,

2009).

The as-yet open question of whether the extended neutral gas disks of dwarf galaxies are metal-enriched is quite relevant to this discussion, since each proposed model makes a prediction for the metal distributions in galaxies. For instance, in the SN-blowout scenario, metals tend to get ejected into the IGM for galaxies less massive than 10^9 M$_\odot$ (Mac Low & Ferrara, 1999) or 10^{11} M$_\odot$ (Strickland et al., 2004), while in the metal-mixing scenario, the central regions and outermost regions of the dwarf galaxy should have the same metal abundance. Therefore, abundance gradients (or a lack thereof) in the extended gaseous disks of dwarf galaxies may help to untangle the physical origin of the mass-metallicity relation.

NGC 2915 is one of the most extreme examples of a blue compact dwarf galaxy with an extended gaseous disk (Meurer et al. 1996; hereafter M96). This nearby (4.1 Mpc, Meurer et al. 2003) dwarf galaxy has an HI disk that extends 5 times beyond the optical stellar component (12 kpc for the gas; 2.3 kpc for the stars; see Figure 4.1, and Table 4.1 for a list of its full properties). Its total baryonic mass (gas plus stars; $\sim 10^9$ M$_\odot$) puts it on the high-mass end of the spectrum of dwarf galaxies, and its total dynamical mass gives it one of the highest-known mass-to-light ratios for a gas-rich galaxy (M96). Recent Hα images of NGC 2915 have revealed several small pockets of star formation embedded in its extended gaseous disk at projected radii of $\sim$ 3kpc that otherwise contains few stars (see Figure 4.1). In addition, new, very deep (t$_{exp} = \sim 14$ ks) images from the *Galaxy Evolution Explorer* Satellite (*GALEX*) show very faint extended-UV (XUV) emission near the location of these HII regions. Because of their strong emission-line spectra, HII regions are relatively straightforward probes of the oxygen abundance of surrounding gas. In the most luminous cases, a direct measurement of the oxygen abundance can be made using the temperature sensitive, faint [OIII]$\lambda4363$ line, and in other cases, calibrated relations between strong lines (e.g. R23; Pagel et al. 1979; McGaugh 1991, hereafter M91) can provide reasonable estimates of the oxygen abundance. Dwarf galaxies have been observed to have spatially homogeneous oxygen abundances, although the most recent studies have so far been limited to well-within the Holmberg radius (Lee
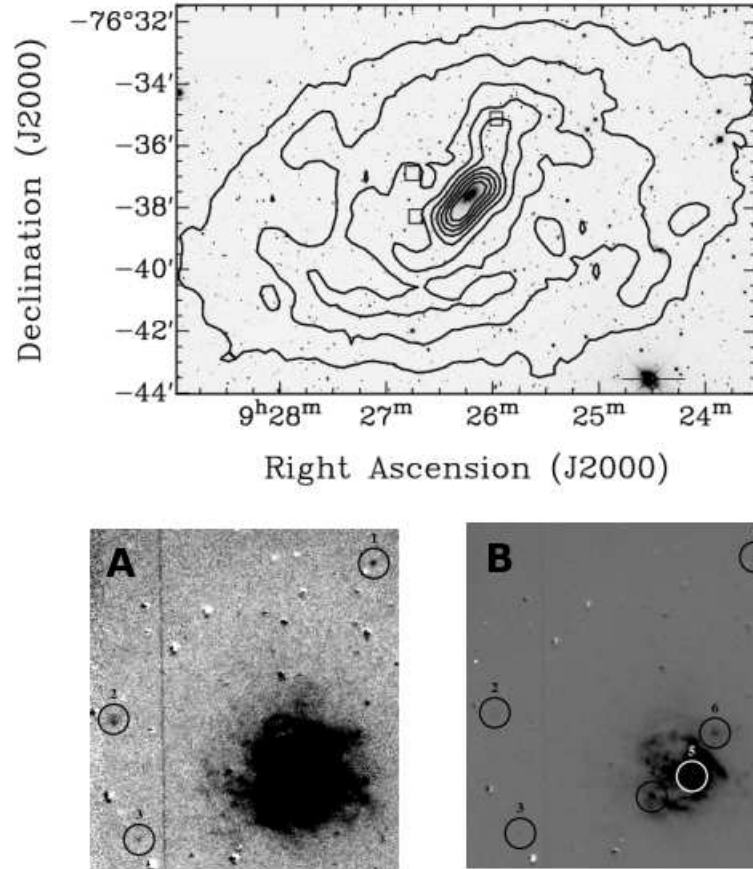
Figure 4.1. V−band and Hα images of NGC 2915 overlaid with ATCA HI contours. Top: A CTIO 1.5-m broadband optical V-Band image of NGC 2915 overlaid with ATCA HI contours. The HI contour levels are 5, 15, 25, 35, 45, 55, 65, 75, 85, and 95 percent of the peak HI column density, 1.71×10^{21} cm^{-2}. The outer gaseous disk of NGC 2915 mapped with the ATCA appears to extend 5 times beyond the optical component of the galaxy which has a 2.3 kpc extent. On the image, we have boxed the 3 outlying HII regions included in this study, and contained in the lower zoomed-in panels. Bottom: Hα continuum-subtracted images of the core of NGC 2915 shown in two stretches: (A) to highlight the outer HII regions included in this study, and (B) to highlight the inner HII regions included in this study.

Property	Value
RA (J2000)	09:26:11.5
dec (J2000)	-76:37:35
distance	4.1±0.3 Mpc
Holmberg Radius	2.3 kpc
$M_\star$	3.2×10^8 $M_\odot$
M_{gas}	7.4×10^8 $M_\odot$
E(B-V)	0.275±0.04
M_V	-16.42
M_{dyn}/L	62* (solar)
R_{HI}	11.9 kpc

Table 4.1. NGC 2915 optical and HI properties. Values are from M03 and M96, in some cases updated for a revised distance measurement. (*) New HI data from Elson et al. (2010) indicates that M_{dyn}/L may in fact be as high as 140 (solar units). Reddening comes from Schlegel et al. (1998)

et al., 2006; Croxall et al., 2009). By comparison, we report the oxygen abundances for HII regions out to 1.2 times the Holmberg radius (the isophotal radius at which the surface brightness is below 26.5 in the B-band) and discuss the implications of our results.

4.2 Observations and Data Reduction

4.2.1 Imaging

We selected HII regions in and around NGC 2915 from Hα images taken in February 1998 on the 3.9-m Anglo-Australian Telescope (AAT) with the Taurus Tunable Filter (TTF; Bland-Hawthorn & Jones 1998). The images consist of a total of four $600s$ exposures using an 11Å filter centered on Hα and two $90s$ exposures in the 11 Å continuum-band. These images were reduced using standard techniques for TTF images, aligned, and combined to make a single image spanning $7.2'$ (8.5 kpc) with $2.3''$

ID	RA	dec	R/R_{Ho}	Log $L_{H\alpha}$	Notes
(1)	(2)	(3)	(4)	(5)	(6)
1	09:26:00.3	-76:35:25.0	1.2	36.2	low ionization parameter; [OIII]$\lambda4959$ not detected
2	09:26:45.9	-76:37:01.1	1.1	36.5	diffuse, outer HII region; [OII]$\lambda\lambda3727$ detected at 3σ
3	09:26:41.7	-76:38:12.9	1.0	35.8	only Hα and [OIII]$\lambda5007$
4	09:26:19.8	-76:38:02.0	0.34	38.4	slit length $= 30''$, on edge of central star formation in NGC 2915
5	09:26:11.1	-76:37:39.0	0.04	39.2	central, luminous HII region; [OIII]$\lambda4363$ detected
6	09:26:07.3	-76:37:12.9	0.23	37.8	bright HII region within galaxy

Table 4.2. NGC 2915 HII region properties. (1) HII Region ID (2) and (3) RA and dec positions (J2000) (4) Location of HII region in terms of number of Holmberg radii, R/R_{Ho}. (5) Log of the total Hα luminosity, in ergs s^{-1}. Values of the total Hα luminosity are derived from the TTF image, and are corrected for internal extinction derived from Schlegel et al. (1998). Errors in the Hα luminosity are on the order of 10% dominated by the flux calibration errors.

(46 pc) seeing. The data were flux calibrated to $\sim 10\%$ accuracy using observations of two spectro-photometric standards. Figure 4.1 shows both a broadband optical image of NGC 2915 overlaid with HI contours (M96) and two continuum-subtracted Hα images of the galaxy that show the six HII regions presented in this study. The broadband optical data (V, R, I-bands) were obtained in February 2003 on the CTIO 1.5-m telescope. The I-band data used for calculations in Section 4.3 are the sum of 6 exposures totaling 720s. Table 4.2 presents the locations, Hα luminosities, and a brief description of the spectral properties of the HII regions.

The UV observations of NGC 2915 were obtained as part of the GALEX Deep Galaxy Survey (Thilker et al. in prep). FUV and NUV images were recorded over the course of 12 independent visits and subsequently co-added using the GALEX pipeline (release ops$-$v6_2_0). Total exposure time is 13.8 ks in both bands. The angular resolution of GALEX is 4.2"[5.3"] FWHM in FUV[NUV]. More details regarding the on-orbit performance of GALEX can be found in Morrissey et al. (2007). Foreground stars were manually masked within our region of interest prior to performing the UV photometry.

4.2.2   Spectroscopy

Multi-slit spectroscopy (0.7″ slitlets, 10″ long in most cases) was carried out on NGC 2915 over two clear nights in January 2008 with the Imamori Magellan Areal Camera and Spectrograph (IMACS) on the Baade 6.5-m telescope at Las Campanas Observatory. IMACS, in combination with the f/4 camera, provided a 15.4′ FOV that is well matched to the size of the field containing the extended HI envelope of NGC 2915 (R_{HI} = 10 arcmin; M96). In order to detect and resolve both [O II]$\lambda\lambda$3727 and [S II]$\lambda\lambda$6717,6731, we used two 600 l/mm gratings, one tuned to the blue portion of the optical spectrum, and the other tuned to the redder side. The red side spectra cover 5430 Å – 8590 Å , while the blue side spectra cover 3360 Å – 6470 Å, both with a dispersion of 0.382 Å per pixel. The blue-red overlap coverage contains the faint HeI λ5876 and [OI] λ6300 emission lines, allowing us to examine the agreement of the red and blue flux calibration for the brightest central HII region in our sample. For
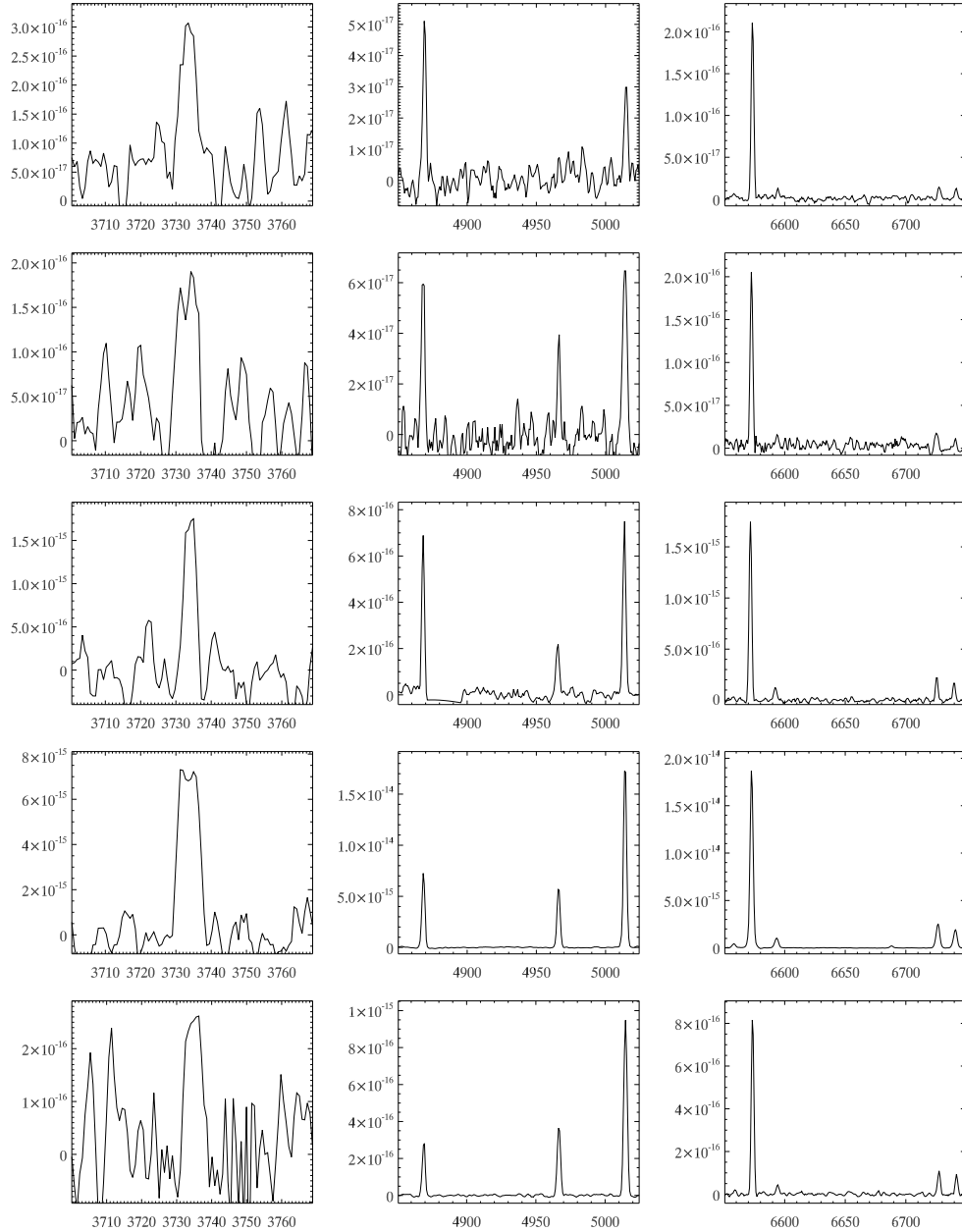
Figure 4.2. HII region multi-slit spectra. These spectra reveal the essential emission lines for abundance determination. Left: [OII] $\lambda\lambda3727$, Middle: Hβ, [OIII] $\lambda4959$ and $\lambda5007$, and Right: Hα, [NII] $\lambda6583$ and [SII]$\lambda\lambda6717,6731$. The spectra are arranged in descending order: outer HII Region 1 at the top, followed by outer HII Region 2, then central regions 4, 5, and 6 (bottom). Flux units are ergs s^{-1} cm^{-2} $\mathring{A}^{-1}$, and wavelength is in Angstroms. These one-dimensional calibrated spectra have been continuum-subtracted (inner regions), dereddened, and 3×3 boxcar-smoothed.

both of the emission lines, the line flux agreement is excellent and well-within the typical uncertainty of $\sim 7\%$ (see below; [OI], red (blue), is 2.97 ± 0.15 (3.05 ± 0.17)$\times10^{-15}$ ergs s^{-1} cm^{-2} Å^{-1} and HeI, red (blue), is 2.23 ± 0.12 (2.24 ± 0.14) $\times10^{-15}$ergs s^{-1} cm^{-2} Å^{-1}). Since the HII regions are very faint, we required numerous long exposures: 7 $\times$ 2000 seconds in the red, and 7 $\times$ 3000 seconds plus 10 $\times$ 2000 seconds in the blue.

For the reduction of our multi-slit data, we used the COSMOS package, a set of programs developed by Carnegie Observatories and based on a precise optical model of IMACS. The COSMOS process is one of alignment, production of an accurate spectral map, basic reduction steps (i.e. bias subtraction, flat-field corrections), night sky line subtraction, and spectral summing and extraction. Arc lamps taken before and after each exposure ensure an accurate wavelength calibration. We performed flux-calibration on 1-d extracted, summed spectra using two standard stars, LTT 1788 and LTT 4816, both observed multiple times over the course of the observing run. The short length of the mask slitlets resulted in some emission lines occupying the full-length of the slit, therefore complicating night sky line subtraction. A number of strategically-placed blank slitlets on the field of NGC 2915 allowed us to properly subtract the night sky by fitting and subtracting profiles (IRAF task fitprofs) for individual sky lines near emission-lines arising in NGC 2915. Finally, for the three HII regions more centrally-located, we corrected for absorption from underlying stellar populations by subtracting gaussian fits to the Balmer-line absorption.

4.3 Analysis

For two of the faint, outer HII regions, and all three of the more centrally located HII regions, we were able to measure the strong recombination emission lines of the Balmer series (Hα and Hβ), and forbidden metal lines of [OII] $\lambda\lambda3727$, [OIII] $\lambda4959$ and $\lambda5007$, [NII] $\lambda6583$ and [SII]$\lambda6717$ and $\lambda6731$. In the three central HII regions, we detect Hα, Hβ, Hγ and Hδ (only region5), in addition to several fainter lines of helium, neon, and argon. For example, in the spectrum of region 5, we detect fainter lines of helium (HeI $\lambda4026$, $\lambda4472$, $\lambda4922$, $\lambda5876$, $\lambda6678$, $\lambda7065$, and HeII $\lambda4687$), neon ([NeIII] $\lambda3869$, $\lambda3970$), and argon ([ArIII] $\lambda7135$). Also for Region 5, we detect

the very faint, temperature-sensitive [OIII] $\lambda 4363$ auroral emission line which provides a direct oxygen abundance measure (see below). We detect only Hα and [OIII] $\lambda 5007$ in the spectrum of region 3, and therefore exclude this region from our subsequent oxygen abundance analysis, as these two emission lines are not sufficient for our analysis. Final, reduced, one dimensional spectra for the 5 HII regions included in this study are shown in Figure 4.2. The Hβ emission line for Region 4 falls near, but luckily completely outside, one of the IMACS chip gaps (seen as a near straight line in the continuum of the center-most panel).

We apply a correction for interstellar reddening to all line measurements from the observed Hα to Hβ ratio for case B recombination where Hα/Hβ = 2.86 at an effective temperature of 10,000 K and electron density of 100 cm^{-3} (Hummer & Storey, 1987). We use a reddening function normalized at Hβ from the Galactic reddening law of Cardelli et al. (1989) assuming R$_v$ = A$_v$/E(B−V) = 3.1. Ratios of Hγ to Hβ were additionally examined in the three bright central HII regions (4, 5, and 6), and were found to give lower values of E(B-V): 0.14, 0.10, and 0.21 compared to 0.53, 0.35, and 0.26, respectively. Since we are directly comparing the measurements from the faintest HII regions with those of the more luminous central HII regions, we wished to use the same emission-line ratios for the analysis of the 5 HII regions included in this work. Therefore, in order to be consistent, we use only the Hα/Hβ Balmer decrement to correct for extinction, while acknowledging that the error in the reddening could be up to 0.2 magnitudes. Nonetheless, the reddening has very little impact on the calculated strong-line and direct abundances presented below. Table 4.3 presents the reddening-corrected strong line measurements for the 5 HII regions in this study. All listed line fluxes are relative to Hβ = 100. The errors given in the table account for the RMS of the line measurements, the flux calibration uncertainty, read noise, sky noise, and flat-fielding errors.

4.3.1 Strong Line Oxygen Abundances

We obtain the nebular oxygen abundances for four of the five regions presented in this study using the strong line R23 method originally presented by Pagel et al. (1979),

according to the calibration of M91. R23 is defined as log [([OII] $\lambda\lambda$3727 + [OIII] λ4959 + [OIII] λ5007)/Hβ]. We choose M91 over the many other calibrations of the R23 relation based mainly on the analysis presented in van Zee & Haynes (2006), which concludes that the photoionization grid of M91 is more physically-accurate than that of Pilyugin (2000). The drawbacks of the R23 method include a well known degeneracy and turnover at ~ 0.3Z$_\odot$ and systematic errors due to age effects and stellar distributions. These drawbacks have been discussed extensively in the scientific literature, and are not repeated here (Kewley & Ellison, 2008; Ercolano et al., 2007). We break the degeneracy using the [NII]/[OII] line ratio for our HII regions. Since all of the HII regions have log [NII]/[OII] < -1.0, all are assumed to lie on the lower metallicity branch of the R23 relation (M91). Errors in the R23 calibration are on the order of 0.2 dex in the turnover region (M91, Ercolano et al. 2007), but tend to be higher in regions that have low ionization parameters (van Zee & Haynes, 2006). Varying the reddening between 0.0 and 0.6 magnitudes randomly for all the HII regions results in values of 12 + Log(O/H) that differ from those quoted values by at most 0.1 dex.

4.3.2   Direct Oxygen Abundance for Region 5

Since we have detected [OIII] λ4363 in the spectrum of Region 5, we are able to make a direct measurement of its oxygen abundance. The line flux of the [OIII] λ4363 emission line is $7.8\pm0.54 \times 10^{-16}$ ergs s^{-1} cm^{-2} Å^{-1}. We use the IRAF package NEBULAR, based on the FIVEL program (De Robertis et al., 1987; Shaw & Dufour, 1995). We assume a 2-zone ionization model (high and low) in which the temperature of the O^{++} zone is derived from the line strengths of the [OIII] emission lines (Osterbrock, 1989), and the effective temperature, T$_e$, in the O$^+$ zone is given by T$_e$(O$^+$) = 2[(T$_e$(O^{++}))$^{-1}$ + 0.8]$^{-1}$ where T$_e$ is in units of 10^4 K (Stasińska, 1990; Pagel et al., 1992). We use the line ratio [SII] λ6717/λ6731 to determine the electron density, which is approximately 100 cm^{-3}. We obtain temperatures for the low and high ionization zones of 12900 K and 13400 K, respectively, which results in an intrinsic ratio Hα/Hβ = 2.80 (Hummer & Storey, 1987) for Region 5. Based

HII	[OII]	[OIII]	[NII]	[SII]	[SII]	Log R23	$f_{H\beta}$	E (B−V)	12 + Log(O/H)
reg	3727	5007	6583	6717	6731		10^{-15} cgs	mag	M91
1	480±55	40±3.9	18±2.8	34±3.4	25±2.7	0.721±0.06	0.20±0.02	0.450	8.26±0.25
2	500±55	130±10	16±2.9	29±2.7	18±1.9	0.830±0.07	0.22±0.02	0.309	8.26±0.25
4	430±36	120±9.3	24±1.9	34±3.1	28±2.3	0.765±0.04	1.68±0.13	0.533	8.14±0.20
5	240±18	250±19	18±1.1	41±1.6	31±1.4	0.757±0.05	21.1±1.6	0.350	7.94±0.05*
6	161±15	340±26	15±1.7	33±2.9	27±2.4	0.792±0.05	0.79±0.06	0.258	7.88±0.20

Table 4.3. Reddening-corrected line measurements for NGC 2915 HII regions. All line strengths are given in terms of Hβ=100. Reddening correction for case B recombination with T = 10000K and ne = 100 cm^{-3}, where Hα/Hβ = 2.86. E(B-V) values compare well with the Schlegel value of 0.275, but may have errors as high as 0.2 magnitudes (see Section 4.4). These large errors in E(B-V) contribute minimally to the error in the strong-line abundances. Region numbers match those in Figure 4.1. In the case of region 5, the central-most luminous HII region, we were able to determine the oxygen abundance via the direct method outlined in Section 4.3. Typical errors in the R23 method as defined by M91 are near 0.2 dex at the break in the R23 relation (at 12 + Log(O/H) $\sim$ 8.3), and are thus the largest contributors to the error in the oxygen abundance. The error in the R23 calibration increases for nebulae with very low ionization parameters. In this table, we have estimated the error of 12 + Log(O/H) to be between 0.20 and 0.25, except for region 5, which has a more accurate direct determination of its oxygen abundance. (*) A direct abundance value, with associated error. The M91 value for this region matches the direct abundance almost exactly, at 12 + Log(O/H) = 7.93.

on these values (which give emissivity coefficients) and the line strengths for Region 5, the IRAF package ABUND provides ionic abundances for oxygen from which we then compute the total oxygen abundance. Again, we note that the reddening has very little impact on the calculated oxygen abundance.

4.4 Results

Table 4.3 lists the derived strong-line R23 (M91) abundances for Regions 1, 2, 4, and 6, and the direct oxygen abundance obtained for Region 5. We compare the direct value for Region 5 with its R23 strong-line value, and find they are nearly identical: 12 + Log (O/H) direct = 7.94 ± 0.05 and 12 + Log (O/H) strong-line = 7.93 ± 0.20. Assuming 12 + Log (O/H)$_\odot$ = 8.66 (Asplund et al., 2005), we find that the 5 HII regions have oxygen abundances that range from 0.2 to 0.4 Z$_\odot$. These values are roughly consistent with several other strong-line abundance methods, including the N2 index obtained using the [NII] λ6583/Hα ratio (Pettini & Pagel, 2004) which gives an oxygen abundance of $\sim$ 0.4 Z$_\odot$ for all 5 HII regions. The inverse variance weighted mean of the 5 oxygen abundance measurements is 7.97 ± 0.05. We present the oxygen abundances as a function of galactocentric distance in Figure 4.3. The
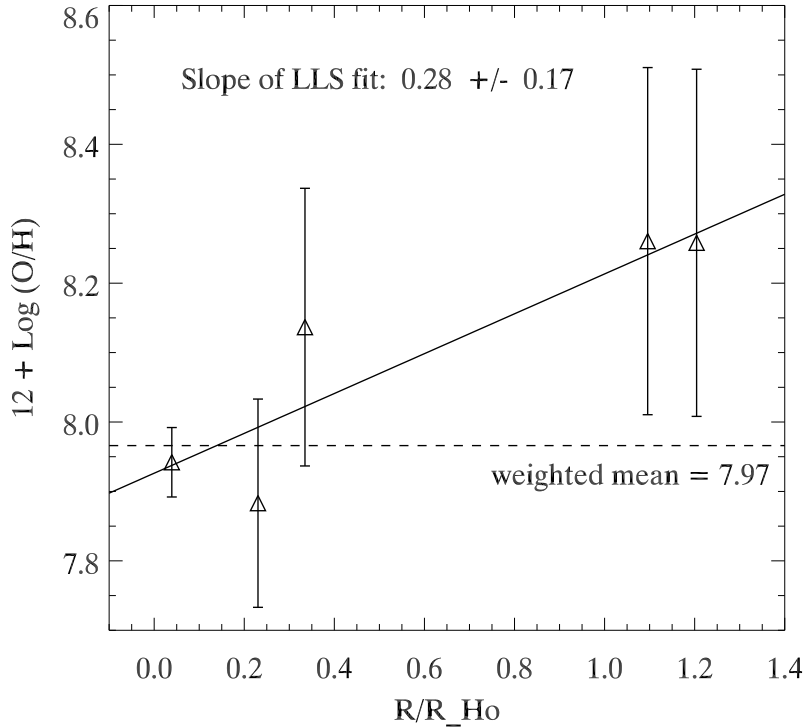
Figure 4.3. The oxygen abundance, $12 + Log\,(O/H)$, versus the galactocentric projected distances (in R/R_{Ho}). This plot includes 5 HII regions for which we could measure the necessary strong lines (5, 4, 6, 2, 1, in order of R/R_{Ho}). The errors are largest for the two outermost HII regions because they are both located on the turnover of the R23 relation, and because they have very low ionization parameters, which makes the R23 abundance determination more uncertain (van Zee & Haynes, 2006). The dashed line represents the mean $12 + Log\,(O/H)$ value, weighted by $1/\sigma^2$, for the 5 HII regions. The solid line represents a linear-least-squares fit to the data, the slope of which is consistent, within 2σ, with a flat radial oxygen abundance gradient in NGC 2915 out to 1.2 times its Holmberg radius.

linear-least-squares fit to these data, including their errors (performed with the IDL routine *fitexy*), shows that NGC 2915 has an increasing radial oxygen abundance gradient out to 1.2 Holmberg radii. However, due to the large errors inherent in the strong-line abundances, this slope (0.28 ± 0.17), within 2σ, is also consistent with a flat abundance gradient in NGC 2915. Nonetheless, the scatter of the five points about the best-fit line is much smaller than the error bars. For this reason, we consider that we may be overestimating the errors, and perform another inverse variance weighted linear least squares fit on the data (assuming the error values are now *relative*). The resultant slope is unchanged, although σ_{slope} is decreased from 0.17 to 0.07. This smaller σ_{slope} may be stronger evidence for an increasing abundance gradient, but only if we are overestimating the errors on the R23 oxygen abundances (as the small scatter about the best-fit line may indicate). We consider it quite unlikely, based on arguments by Ercolano et al. (2007) and others, that the errors in the strong line abundances are significantly less than 0.2 - 0.3 dex.

Figure 4.4 plots effective yield versus total baryonic mass for NGC 2915 (filled circle), assuming its total oxygen abundance is the weighted mean of our five measured HII regions, and shows the empirical relation of Tremonti et al. (2004). The total effective yield is computed from the observed metallicity, Z, and the galaxy total gas fraction (not including dark matter, 0.70 for NGC 2915), μ, such that $y_{eff} = Z/\ln(\mu^{-1})$. In this case, 12 + Log (O/H), an oxygen abundance by number, is converted to a metallicity by mass using the conversion factor 11.728, assuming that helium accounts for 36% of the total gas mass (Lee et al., 2003). The logarithm of the effective yield of NGC 2915 is -2.516, given its error-weighted mean oxygen abundance of 12 + Log (O/H) = 7.97. Along with total stellar and gaseous masses presented in Table 4.1, NGC 2915 falls exactly where it is expected to fall on this plot. The relation of Tremonti et al. (2004) seen in Figure 4.4 as a solid line is attributed to metal loss via galactic winds. NGC 2915 lies near its turnover, where winds are thought to start playing an important role in blowing out metals. In this context, NGC 2915 behaves just like other galaxies of its same mass, gas fraction, and metallicity.
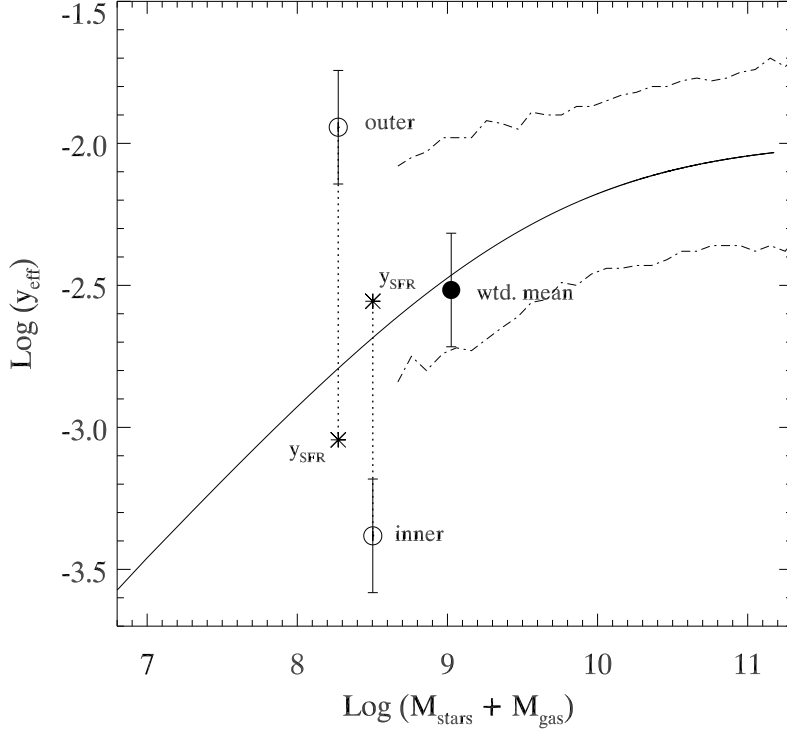
Figure 4.4. The effective yield versus the total baryonic (stellar plus gas) mass. The points include: the mean $12 + \text{Log (O/H)}$ of NGC 2915 (filled circle), the outer region of NGC 2915 defined in Section 4.3 (top open circle), and the central, inner region of NGC 2915 as defined in Section 4.3 (bottom open circle). The empirical relation in Tremonti et al. (2004), their equation 6, is shown for reference (solid line), along with contours (dashed-dotted line) that enclose 95% of the SDSS data presented in Tremonti et al. (2004). The vertical error bars (with hashes) for the points on this plot represent the error of 0.25 dex in the measured oxygen abundance, used here as a proxy for total metallicity. Assuming a 10% error in the stellar and gas mass estimates from M96, the radii of the NGC 2915 circles are the approximate size of the x-axis error. The dotted lines attached to each point extend to the effective yield values calculated from the current location-based FUV-derived SFRs (y_{SFR}) in Section 4.3. These values show the extent to which NGC 2915's outer disk is overabundant for its current gas-fraction and SFR, and to which the inner-disk is similarly under-abundant.

Considering the effective yields of the inner and outer components of NGC 2915 separately, however, gives a very different result. We present two simple cases in which we calculate the oxygen abundance we might expect to measure in the outer gaseous disk of NGC 2915 based solely on its stellar and neutral gas content. In the first case, we estimate the effective yield in the outer-disk of NGC 2915, and compare it to the Tremonti et al. (2004) relation between effective yield and total mass. We assume the I-band light best traces the stellar mass, and calculate a radius centered on the galaxy that contains 90% of the stellar mass (90% of the I-band luminosity), r_{90}, to be ~ 44". We then measure an approximate radius which contains all of the stellar light, including the outer HII regions and faint extended UV emission, r_{tot}, to be ~ 150". We note that ACS images presented in Meurer et al. (2003) show several globular clusters at radii similar to the outer HII regions. This population of older stars is included in our I-band measurements.

From the HI data presented in Meurer et al. (1996), we find that r_{90} contains 4.1% of the total HI mass, and the annular region between r_{90} and r_{tot} contains 20.9% of the total HI mass. Within this annular region, we measure an effective yield (log y_{eff}) of -1.94 and log $(M_* + M_{gas})$ of 8.3. Based on the empirical relation of Tremonti et al. (2004), we would expect log $y_{eff} \sim$ -2.8 in the outer annulus. Based on these crude expectations, the outer regions of NGC 2915 are therefore overabundant for their gas fraction. The central region within r_{90} has log $y_{eff} \sim$ -3.4, and log $(M_* + M_{gas})$ of 8.5, and is therefore concomitantly under-abundant for its gas fraction. We have chosen not to include the entire HI disk in our outer annulus, and instead truncate it at the edge of the detectable I-band emission. Including the entire HI disk in this measurement would only make the discrepancies between the calculated and expected effective yields more extreme.

In the second case, we derive the current star formation rate density (Σ_{SFR}) of the region between r_{90} and r_{tot} from the GALEX far-UV flux in this region, assume a constant SFR and net oxygen yield over some star-formation timescale (see next paragraph), and use neutral gas surface densities from Meurer et al. (1996) to approximate an expected O/H ratio in the outer region. After subtracting foreground

and background sources from the total flux, we measure the FUV AB magnitude (uncorrected for extinction) within r_{90} to be 15.59 ± 0.06 and that within r_{tot} to be 15.48 ± 0.16. The 1σ errors here account explicitly for the rather large background non-uniformity in this low galactic latitude field ($b = -18.4°$), and assume the outer disk contribution can never go negative. To correct these values for extinction, we use the average of the E(B-V) values computed from the Balmer decrement (E(B-V)$_{avg}$ = 0.380), shown in Table 4.3, and the ratio of $A(\lambda)/E(B-V)$ for the FUV to be 8.24 (Wyder et al., 2007). Using the UV SFR conversion of Salim et al. (2007) for sub-solar metallicity, a Salpeter IMF, and star formation averaged over timescales of 100 Myrs, where SFR ($M_\odot$ yr^{-1}) = 1.08×10^{-28} L_{FUV}, we find that $\Sigma_{SFR} = 3.4 \times 10^{-4}$ $M_\odot$ yr^{-1} kpc^{-2} in the outer annulus and $\Sigma_{SFR} = 3.5 \times 10^{-2}$ $M_\odot$ yr^{-1} kpc^{-2} in the central region. For reference, the values we derive for the entire disk of NGC 2915 are $\Sigma_{SFR} = 3.2 \times 10^{-2}$ $M_\odot$ yr^{-1} kpc^{-2}, which amounts to a total SFR of 0.09 $M_\odot$ yr^{-1}, similar to the value derived by Meurer et al. (1994) of 0.05 $M_\odot$ yr^{-1} using Hα luminosities.

In order to be consistent with our measurements of the mean galaxy-wide oxygen abundance in NGC 2915 (12 + Log (O/H) = 7.97), we find the length of time over which to average the star formation to be 1.6 Gyr, assuming a net oxygen yield of 0.01 (Maeder 1992; the mass of oxygen ejected by all stars per unit mass of matter locked up in stars). This timescale, along with an average gas density in NGC 2915 of 5.0 $M_\odot$ pc^{-2} and Σ_{SFR} given above, allows us to derive the galaxy-wide measured total oxygen abundance, 12 + Log (O/H), of 7.97. We then use this same timescale, along with measured SFRs, to calculate the oxygen generated in the outer annulus. Given $\Sigma(gas) \sim 3.2$ $M_\odot$ pc^{-2} at 100", a net oxygen yield of 0.01, and that star formation has been ongoing at the rate of $\Sigma_{SFR} = 3.4 \times 10^{-4}$ $M_\odot$ yr^{-1} kpc^{-2} for the last 1.6 Gyrs, the oxygen abundance in the outer annulus is expected to be 7.2 (0.04 $Z_\odot$). We have measured it to be 8.26 (0.4 $Z_\odot$), significantly higher than what is expected based on these crude assumptions. In order to reach our measured abundance in the outer disk of NGC 2915 at the current star formation rate, we would have to consider unrealistically-long timescales for ongoing star formation in the outer disk,

longer than the estimated age of the universe. We also note that, under these same assumptions, with a Σ(gas) $\sim$ 8.5 $M_\odot$ pc^{-2} at 25", the central region would be expected to have an oxygen abundance of 1.9 $Z_\odot$, 12 + Log (O/H) = 8.8, much higher than our measurement of 7.93 (0.2 $Z_\odot$).

4.5 Discussion

The flat, or possibly increasing oxygen abundance gradient in NGC 2915 leads us to conclude that one or more physical process(es) has distributed metals throughout its extended gaseous disk. The low-level of current star formation observed at large radii in NGC 2915 is not sufficient to have produced the measured oxygen abundances. In order for the star formation to be responsible for the oxygen enrichment at large radii, it would have to have been going on for longer than the age of the universe. Bresolin et al. (2009) come to a similar conclusion regarding metal-mixing after finding no gradient in the extended UV disk of M83. However, they do note that if star formation in the outer disk has been ongoing for the last 2-3 Gyrs, then it could potentially explain the flat oxygen abundance gradient in the outer disk.

The role of self-enrichment in the higher-than-expected oxygen abundances of the outer HII regions in NGC 2915 is most likely negligible. While the winds of massive stars can inject $\sim$ 0.5 $M_\odot$ of oxygen in *metal-enriched* HII regions over the course of their brief lives, their impact is minimal in HII regions with originally low metallicity (Z < 0.4 $Z_\odot$; Meynet & Maeder 2005). The metal lines are required for driving the winds efficiently. Along these lines, Wofford (2009) explores the impact of massive star winds on low-metallicity (Z$\sim$ 0.05 $Z_\odot$), massive HII regions (10^6 $M_\odot$) using starburst99 and CLOUDY codes, and finds that they contribute a maximum abundance enhancement of ΔLog (O/H) $\sim$ 0.025 dex. While the effect may be larger for the low-luminosity outer HII regions presented in this work due to their low gas mass and relative high fraction of O stars, it cannot account for the extent to which the outer HII regions are over-abundant. In this section, we consider 3 scenarios that may be responsible for the observed oxygen abundance trends in NGC 2915, and discuss the implications of our results.

4.5.1   Scenario 1: Metal Mixing Within the HI disk

The lower-than-expected central oxygen abundances and the higher-than expected outer-disk oxygen abundances may support a metal mixing scenario, in which metals generated by the central star-forming core are transported outward though the disk. The chemodynamical model of Ferguson & Clarke (2001) shows that viscous flows, perhaps resulting from cloud-cloud collisions or gravitational instabilities, can transport metals to large radii, resulting in flat abundance gradients. In simulations tailored to the Milky Way, Minchev & Famaey (2009) find that the interaction between spiral structure and a central bar is an effective and efficient (t < 3 Gyrs) mechanism for radial mixing in galactic disks, out to large radii. Yet, previous claims of a central massive HI bar in NGC 2915 have recently been discredited by the newer, better-resolution HI synthesis data of Elson et al. (2010), who instead find two elongated central HI concentrations separated by only 1.1 kpc in the core. Nonetheless, there is still a bar-like structure in its central HI morphology, which may be partially responsible for directing gas flow outward, and producing a diluting effect and a shallow abundance gradient (Friedli et al., 1994; Martinet & Friedli, 1997).

Tassis et al. (2008) present a cosmological model that does not include supernovae-driven metal ejection, yet reproduces the mass-metallicity relation for simulated galaxies. Their primary physical explanation for the decreasing metallicity with decreasing galaxy mass is that star formation is increasingly inefficient in low mass systems (see also Dalcanton 2007). To explain the low effective yields of dwarf galaxies, they propose metal-mixing, and suggest the transport of metals from the inner regions of the disk to its outer, unobservable regions of the halo. Detections of these metals in the warm/hot gas of the halo would be available only through absorption line studies using background quasars (e.g. Tripp et al. 2008). The high effective yield in the outermost gaseous disk of NGC 2915 is consistent with the picture of metal transport provided by Tassis et al. (2008), though does not confirm the presence of metals outside the HI-disk, in the ionized halo gas.

4.5.2 Scenario 2: Supernovae-Driven Blowout and Fallback

It has long been noted that feedback from supernovae in the shallow potential wells of dwarfs may serve to efficiently blow out the metals generated during the stellar evolution process (e.g. Larson 1974; Dekel & Silk 1986). Indeed, the low effective yields for dwarf galaxies are commonly attributed to strong galactic winds generated by supernovae (e.g. Tremonti et al. 2004), and dwarf galaxies may therefore be at least partially responsible for the enrichment of the IGM (Stocke et al., 2004). In order for this metal blowout scenario to fit the observed radial oxygen abundance trends in NGC 2915, a large percentage of the metals would have to fall back at large radii, at least a few kpc from where they were ejected. In a sense, then, this scenario has the overall effect of the metal-mixing scenario outlined above, though it is powered by a completely different source. Yet, most current models of supernovae-driven outflow tend to favor the ejection of metals into the IGM, rather than the fallback of metals on the galaxy's disk (Brooks et al., 2007). If these models do include the fallback of metals, this fallback generally occurs tens of parsecs from where the metals were originally ejected (Mac Low & Ferrara, 1999). Further complicating this interpretation, results from Summers et al. (2003) indicate that a large HI halo may prevent the escape of a wind.

The lack of a model for a scenario in which metals are entrained in galactic winds, and fall back down at large galactocentric radii does not make such a scenario impossible. Some observational evidence presented in Veilleux et al. (2005) for M82 suggests that such a scenario may indeed be possible. Moreover, our Hα images of NGC 2915 do show a bubbly Hα morphology (see Figure 4.1) that may be evidence for gas flows from the star-forming core. Additionally, Elson et al. (2010) find high central velocity dispersions (~ 30 km/s) in new, more highly-resolved HI data from the ATCA which could be indicating that the central gas dynamics of NGC 2915 are largely dominated by stellar winds from the central massive stars. Wind velocities derived from X-ray temperatures in several dwarfs can range from $500-900$ km/s (Martin et al., 2002). However, no such hot gas measurements exist specifically for NGC 2915. The Hα emission line widths of the central HII regions (regions 4, 5, and

6) do show some signs of line broadening, with a mean FWHM of 2.36 Å (~ 110 km/s). For reference, the mean Hα FWHM of the outer HII regions is 1.9 Å (~ 85 km/s), roughly consistent with the 2×2 binned spectral resolution of 1.7 Å (~ 75 km/s at Hα). We note that an estimate of the escape velocity from the inner parts of NGC 2915, based on its rotation speed of 80 km/s derived by M96, where $v_{esc} \sim 3 \times v_{circ}$ (Veilleux et al., 2005), is 240 km/s. Based on these rough calculations, we see no convincing evidence in the Hα line widths for the escape of ionized gas from the central starburst of NGC 2915.

4.5.3 Scenario 3: Past Interaction

NGC 2915 could have interacted with a low-surface-brightness neighbor and accreted its gas, potentially enriched from previous generations of star formation. In addition, the interaction may have triggered both the central star formation, and the faint outer-disk star formation in NGC 2915 (Hernquist & Mihos, 1995; Hopkins et al., 2009). Although it is not always the case, outer-disk, extended star formation does tend to be associated with previous or ongoing interactions (Thilker et al., 2007; Werk et al., 2010). Nonetheless, even if the metal-enriched gas from the accreted galaxy explains the high oxygen abundances in the outer regions of NGC 2915, we would still need an additional mechanism (one of the above) to explain the relatively low oxygen abundance in the central, dominant star-forming region. Along this line, recent numerical simulations by Rupke et al. (2010) predict that oxygen abundances in the central parts of interacting galaxies will be lower than expected based on the mass-metallicity relation due to radial inflow of low-metallicity gas from the outskirts of the merging galaxy. In this model, subsequent radial mixing (see Scenario 1) tends to flatten the observed metallicity gradients. If NGC 2915 has undergone a merger in its distant past, it appears to fit the model of Rupke et al. (2010) very well.

The relatively smooth kinematics and spiral structure of the extended HI disk requires that such an interaction happened at least 3 Gyr ago (Barnes & Hernquist, 1996; Hopkins et al., 2009). M96 do find signs of a warp in the HI-disk, a bar, and dark-matter regulated (strong) star formation in NGC 2915, all of which could be

attributed to an interaction with another galaxy (though such an interaction is not required). Although NGC 2915 is in a low density environment, M96 note that there is one possible interaction partner, the low-surface-brightness "object" SGC 0938.1-7623 (KK98-076; Corwin et al. 1985, Karachentseva & Karachentsev 1998). Based on observations with the 64-m Parkes Telescope, M96 note that SGC 0938.1-7623 is either not at the velocity of NGC 2915, or it is very gas poor. They give a 5σ upper limit on M_{HI} of the object to be 2.6×10^6 $M_\odot$. Also noted in the original discovery paper (Corwin et al., 1985) and in Karachentseva & Karachentsev (1998) is the possibility that this object is a reflection nebula. While there is no explicit evidence of an interaction, we cannot rule it out. We additionally note that if the abundance is actually increasing with radius (see Section 4.4), our results would probably favor an accretion scenario in which metal-rich gas is preferentially deposited into the outer parts of the galaxy (Peek, 2009) in conjunction with metals being transported out of the under-abundant central regions.

4.5.4   Implications for the Origin of the Mass-Metallicity Relation

The three scenarios discussed above are not necessarily mutually exclusive. For instance, the metal mixing scenario (1) could additionally include the SN-driven ejection of metals from the central parts to the IGM (scenario 2), given the under-abundance of the central regions, and that the global properties of NGC 2915 fit well with previously-determined trends relating metallicity, effective yield, and mass that have been attributed to metal loss via strong galactic winds. Or, the interaction scenario (3) could additionally include radial metal mixing (scenario 1), as does the model of Rupke et al. (2010). And finally, the interaction scenario (3), could include strong metal outflows from the central starburst (scenario 2), without the need for fallback.

Without further modeling the properties of the stars and gas in NGC 2915, we cannot say for certain which or what combination of these processes is contributing to the flat (possibly increasing) abundance gradient we observe. However, it is clear from the possibilities outlined that the radial redistribution of metals, whether driven by supernova-generated winds and fallback or viscous flows within the disk, is

required to reproduce the flat abundance gradient. Every scenario or combination of scenarios requires metal transport from the central to outer regions to some degree, with the exception of the interacting scenario (3) plus metal blow-out (2, without fallback) from the central regions. Our results, therefore, imply that metal-mixing is a significant process in the extended gas disk of NGC 2915. Furthermore, flat abundance gradients may not be uncommon in systems with low star formation efficiency and/or high HI content, perhaps owing to similar processes of metal-redistribution. In addition to the flat abundance gradient in the outer low surface brightness disk of M83 (Bresolin et al., 2009), de Blok & van der Hulst (1998) find no oxygen abundance gradient in a sample of 12 low surface brightness galaxies over the radial range of 3 scale lengths.

Our results indicate that a significant outflow of metals into the IGM may not be needed to reproduce the measured effective yields in NGC 2915. We have presented two plausible scenarios that explain the abundances in NGC 2915 that do not include supernova-generated galactic winds. Ours is not the first work to cast doubt on the universality of dramatic metal loss in dwarf galaxies. For example, a number of the dwarf galaxies in the sample of Lee et al. (2006) have yields far greater than expected from the empirical relation of Tremonti et al. (2004), leading the authors to conclude that some less energetic form of mass loss may be at work, or that star formation efficiencies are low in dwarf irregulars. Efficient metal mixing in extended gaseous disks is another physical mechanism that may be responsible for the observed low effective yields in dwarf galaxies.

4.6   Summary and Conclusions

We have derived oxygen abundances from optical emission-line spectra of 5 HII regions in the extended gaseous disk of NGC 2915, in locations ranging from the central starburst to 1.2 times the Holmberg radius. Outer-disk HII regions were originally found using deep AAT Hα images, and appear to lie in a very faint extended-UV disk visible in recent deep GALEX images. Out to these large galactocentric distances, we find no evidence of a decreasing metallicity gradient. The central HII regions

have a metallicity of 0.2 $Z_\odot$ ($\pm$ 0.15 dex), while the outer HI regions appear to be enriched at a level of 0.4 $Z_\odot$ ($\pm$ 0.25 dex). Based on calculations of metal yields and star formation rates in NGC 2915, we conclude that the outer disk is considerably more metal-rich than its "expected" value of $0.04 - 0.08$ $Z_\odot$, and that the central region is similarly under-abundant compared to its "expected" value of $1.7 - 1.9$ $Z_\odot$. These observations indicate that some process, other than ongoing star formation, has enriched the gas at large radii. We present 3 plausible (and non-exclusive) scenarios for the metal-enriched outer gas disk of NGC 2915: metal mixing, supernovae-driven winds entraining metals and falling back down at large radii, or a past interaction leading to the accretion of enriched gas. Measurements of metal abundances for the outer gaseous disks of additional galaxies will cast light on the processes that redistribute metals and their effect on the mass-metallicity relation for galaxies.

CHAPTER 5

The Distribution of Oxygen in HI Rogues

5.1 Introduction

Through nuclear fusion and well-understood stellar evolution processes, stars with $M_* > 8$ $M_\odot$ generate metals in their cores, and return them to the local interstellar medium (ISM) near the end of their lifetimes. The global processes that govern how those metals are subsequently distributed throughout a galaxy, however, are largely unknown and widely debated (see Introduction and Section 5.5). There is the added uncertainty of how and to what extent galaxies lose some of their metal content to the intergalactic medium (IGM). Metals (commonly: oxygen, nitrogen, magnesium, iron) are evenly distributed in some spiral galaxies, while others exhibit steeply declining radial abundance gradients (Vila-Costas & Edmunds, 1992; Oey & Kennicutt, 1993). Furthermore, the overall metal content of a galaxy is well-correlated with its total mass (mass-metallicity relation), yet the slopes of the radial abundance gradients in galaxies is not strongly correlated with any galaxy large-scale property (Zaritsky et al., 1994). A gradient of -0.07 dex/kpc is average for the inner regions of nearby spiral galaxies (van Zee et al., 1998), including the Milky Way (Shaver et al., 1983), though there is ongoing debate as to whether the gradients best fit by a single exponential profile or if there is a break such that the gradient flattens at large radii (Vilchez et al., 1988; Ferguson et al., 1998a; Pilyugin, 2003). There is an observed flattening of the radial abundance gradient at large radii in M83 (Bresolin et al., 2009), yet there are few other measurements of gas-phase abundances at large radii to help pin down the overall shape ($r > r_{25}$). Characterizing the metal distribution in galaxies of all morphological types and masses over a range of galactocentric distances is essential

for determining the processes largely responsible.

Here, we describe a search for outlying HII regions in the gaseous outskirts of a subsample of the HI Rogues catalog (Hibbard et al., 2001b), and subsequent Gemini Telescope multi-slit spectroscopy from which we obtain the nebular oxygen abundances of numerous outlying and centrally-located HII regions. The outlying HII regions provide an excellent laboratory in which to make straightforward measurements of gas metallicities outside the optical stellar components of gas-rich galaxies. We report abundance gradients out to as far as $2.5 \times r_{25}$ for 13 gas-rich galaxies that span a range of morphologies and masses in an effort to understand the physical processes that give rise to the observed metal distributions in galaxies.

The HI Rogues catalog consists of 189 HI synthesis maps of nearby galaxies with extended, unusual, or disturbed HI morphologies, including: galaxies with extended (many times the optical extent) or warped HI distributions, interacting groups, minor and major mergers, intergalactic debris with no optical counterparts, and early-type galaxies with HI inside and/or outside their optical bodies. As the host galaxies of outlying HII regions are strongly correlated with disturbances, companions, extended gas, and interactions (Chapter 2), this collection of "rogue" galaxies provides a potentially rich hunting ground for outlying, massive star formation. Another benefit of the HI rogues sample is that all galaxies have readily available HI synthesis maps, providing crucial information about the gaseous environments of the outlying stars. In cases of very extended gaseous disks around dwarf galaxies, the oxygen abundance of the outer-disk gas informs our picture of metal-mixing and/or gas blowout in dwarf galaxies (see Chapter 4). In these HI Rogue systems, the oxygen abundances of the extended and/or stripped outer gaseous material can place much-needed constraints on metal transport in gas-rich galaxies.

This chapter proceeds as follows: Section 5.2 describes imaging and spectroscopic data obtained at various telescopes over the course of several years; Section 5.3 reviews our methods for obtaining strong-line oxygen abundances from HII region emission-line spectra; Section 5.4 presents radial oxygen abundance gradients reaching beyond r_{25} for 13 HI rogues with outlying HII regions; Section 5.5 discusses these results

and comments on the physical mechanisms that could be responsible for the metal distributions; and Section 5.6 summaries and concludes the chapter. Our Gemini multi-slit data allow the largest to-date observational study of the metal content of outlying gas (beyond r_{25}), and how it compares to the metal content of gas within the galaxy.

5.2 Observations and Data Reduction

5.2.1 Hα Imaging

In April 2005, over the course of four clear nights, we imaged 27 galaxies from the HI Rogues Catalog (Hibbard et al., 2001b) in Hα and R$-$band continuum with the MDM 2.4-m Hiltner telescope. The MDM 2.4-m telescope direct images, with the Echelle CCD, have a field of view of $9.5'\times 9.5'$ and a plate scale of $0.275''$ per pixel. The average seeing over the course of these four nights was $1.2''$. These observations were made in a similar fashion to the Hα imaging of the SINGG survey (described in Chapter 2). We used four of the SINGG narrow$-$band filters with bandpasses that corresponded to the Hα emission line at the target galaxy's velocity. The central wavelengths, in angstroms, of the filters used are 6568, 6596, 6605, and 6628, each with a FWHM of $\sim$ 30 Å (Meurer et al. 2006 contains a full description of the SINGG filters). Exposure times were $3\times$ 600 s in Hα and $3\times$ 120 s in R. Targets were selected from the full HI Rogues catalog on the basis of their visibility from MDM observatory and their recessional velocities, such that the redshifted Hα emission line is encompassed by the SINGG Hα filters' narrow bandpasses. Galaxies were also selected to have angular optical extents such that they were fully contained in the $9.5'$ field of view. Observations of several different spectrophotometric standards were used to flux calibrate the data.

We performed a basic reduction of the data using IRAF CCD processing routines for bias subtraction and flat field division. Images were then combined and astrometry was performed using the SINGG IDL pipeline routines (see Meurer et al. 2006) modified specifically for the MDM 2.4-m telescope. Photometry was performed on

the images based on observations of spectrophotometric standards calibrated to the AB magnitude system. We followed the basic SINGG procedure detailed in Appendix A of Meurer et al. 2006. The average 5σ limiting Hα flux for a point source is $\sim 1 \times 10^{-16}$ ergs cm^{-2} s^{-1} and the average 5σ limiting R$-$band magnitude is ~ 24.

5.2.2 Searching Images for Outlying HII Regions

We searched the reduced, calibrated MDM Hα and R$-$band images for ELdots (emission-line dots; see Chapter 2) using the basic selection criteria outlined in Section 3 of Chapter 2, with the exception of the requirement that the ELdot lie beyond $2 \times r_{25}$. Instead, we selected by-eye sources that appeared to lie beyond the main R$-$band optical extents of the potential host galaxies. The reason for relaxing our projected distance requirement is that r_{25} is not well-defined for merging, interacting, and/or irregular, asymmetric galaxies. For comparison to the sample in Chapter 2, and an estimate of the ELdots' projected distances from the main optical extents of their host galaxies, we did calculate an approximate r_{25} at a later time. In order to obtain the approximate location of r_{25} in these messy systems, we used the IRAF task ELLIPSE found in the STSDAS package, fitting elliptical isophotes to the target rogue galaxies in the 2.4-m MDM R$-$band images. In one case (NGC 3227), two merging galaxies had to be fit with a single ellipse. In other cases, incidences of tails, plumes, and warps caused the fixed-center elliptical isophotes to be significantly larger than they otherwise would have been (see figures $5.1 - 5.13$). The laxness of the r_{25} fitting should be noted throughout this chapter, and the quantity itself should be treated as a simple radial reference point when discussing oxygen abundance gradients. All of the rogue ELdots, originally identified by-eye, lie beyond this crude r_{25}.

13 of the 27 HI rogues imaged with the MDM 2.4-m were found to have over 40 ELdots in total. We began the process of spectroscopic confirmation as outlined in Chapter 2, with longslit spectroscopy at the MDM 2.4-m telescope (see 5.2.4). Various difficulties with blind offsets and large observational overhead (see Chapter 2) forced us to discontinue the follow-up longslit spectroscopy before it was complete.

Yet, of the dozen ELdot spectra that were obtained, all were confirmed as outlying HII regions (the Hα emission line, instead of any of the redshifted strong blue emission lines, falls in the SINGG narrow bandpass). This high confirmation rate led us to pursue deeper multi-slit spectroscopy with the Gemini 8-m telescope, as described in the next Section, 5.2.3.

Figures 5.1 $-$ 5.13 show three-color Hα continuum-subtracted (red), R$-$band (blue), and Hα (green) images for the 13 HI rogue fields in which we found ELdots. The images do not show the full MDM field of view. Rather, they are centered and zoomed to highlight the inner and outer-galaxy star formation. We show r$_{25}$ on the images, in addition to all of the HII regions (outer + inner) for which we were able to obtain GMOS multi-slit spectra (see next section). Several of the outlying HII regions are not visible in these 3-color images because they are so faint. Table 5.1 lists optical, HI properties, and derived properties of the HI rogues with outlying HII regions. Column 8 provides an estimate of the total oxygen abundance for each galaxy from the literature. In most cases, the oxygen abundance measurement was made with various strong emission-line ratios for HII regions in the central parts (within r$_{25}$ in all cases) of each galaxy. Column 9 lists the HI morphology code from the HI rogues catalog for each target. The codes are defined in the caption of Table 5.1, and the HI morphology of each target is described in greater detail in Section 5.4. Table 5.2 lists the remaining 14 targets in which we did not find any ELdots, along with their HI morphologies, distance, and r25. Although their properties are not fundamentally different from those of the HI rogues with ELdots, we do note that the only three optical early-type elliptical galaxies with HI that we imaged with the MDM 2.4-m appear in this sample.
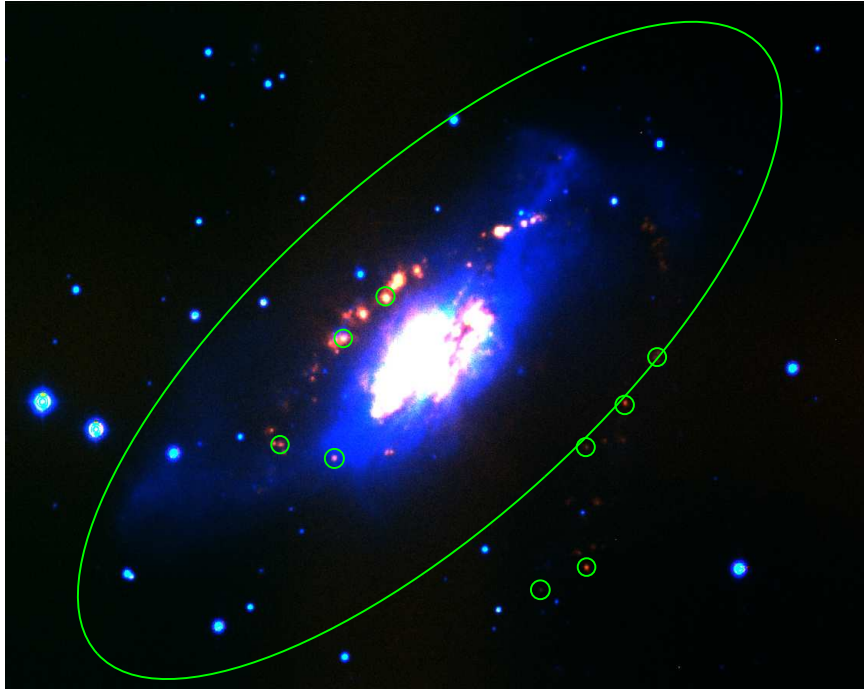
Figure 5.1. MDM continuum-subtracted Hα image: NGC 2146. A pseudo-three-color image of in which blue represents R−band continuum emission, green (mostly for blending purposes) is the Hα narrow−band image, and red represents the continuum-subtracted Hα emission. These images were taken at the MDM 2.4-m telescope, and are described in Section 5.2. The green ellipse shows the rough location of the elliptical 25th magnitude isophote (r_{25}) for the galaxy, while the smaller green circles point to the locations of the HII regions for which we obtained GMOS-N multi-slit spectra (see Figure 5.14). This image is aligned to a world-coordinate system such that north is upwards, and east is to the left. The field of view is roughly 30 kpc (N-S) × 40 kpc (E-W).

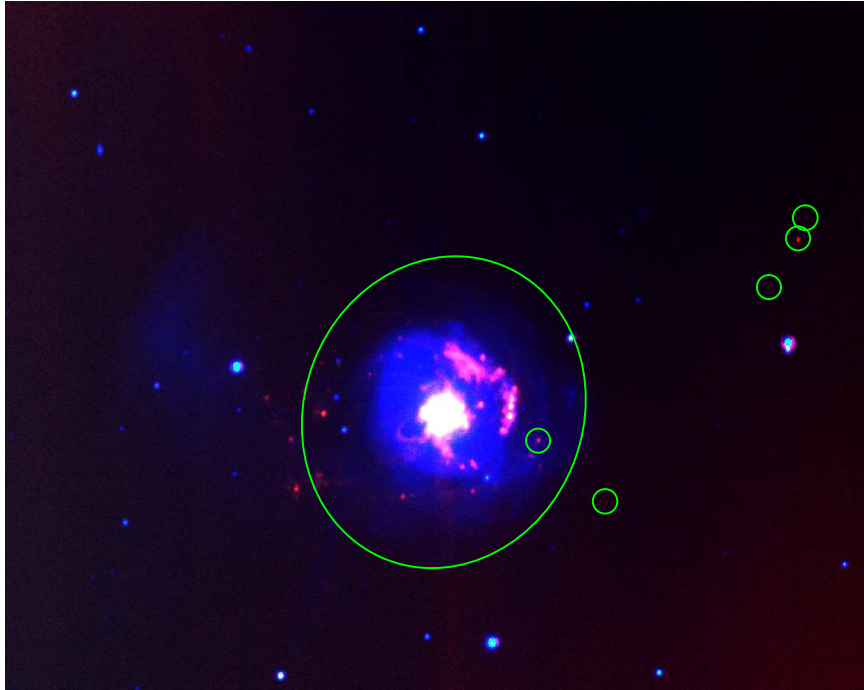**Figure 5.2.** MDM continuum-subtracted Hα image: NGC 2782. Same as Figure 5.1 for NGC 2782. The field of view is roughly 45 kpc (N-S) × 60 kpc (E-W).

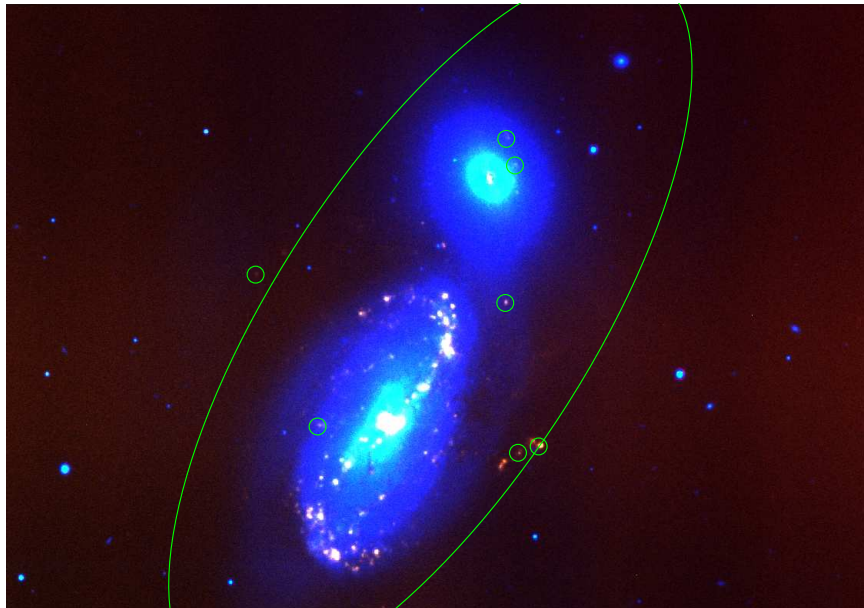**Figure 5.3.** MDM continuum-subtracted Hα image: NGC 3227. Same as Figure 5.1 for NGC 3227. The field of view is roughly 15 kpc (N-S) × 25 kpc (E-W).
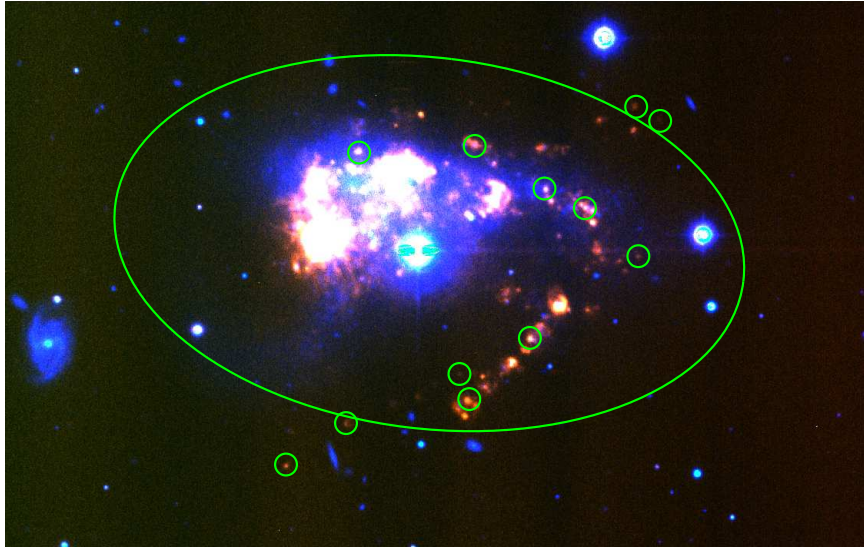
Figure 5.4. MDM continuum-subtracted Hα image: NGC 3239. Same as Figure 5.1 for NGC 3239. The field of view is roughly 10 kpc (N-S) × 17 kpc (E-W).
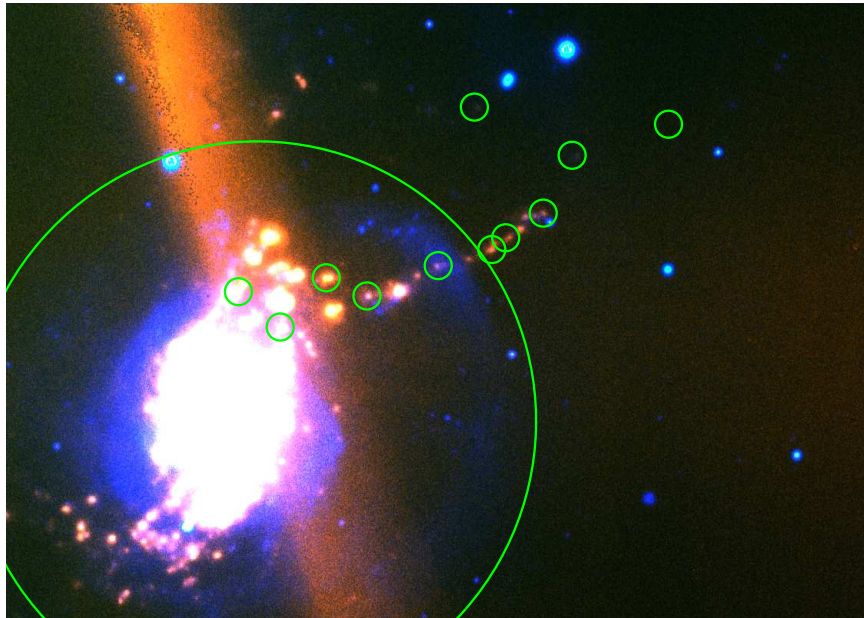

Figure 5.5. MDM continuum-subtracted Hα image: NGC 3310. Same as Figure 5.1 for NGC 3310. The field of view is roughly 16 kpc (N-S) × 24 kpc (E-W). The large orange stripe through the galaxy is a strong scattered light feature.
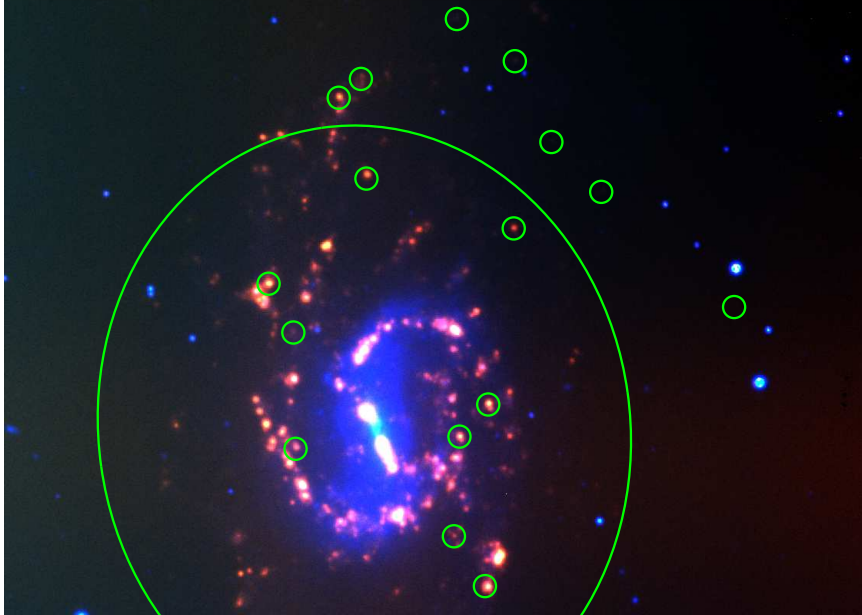
Figure 5.6. MDM continuum-subtracted Hα image: NGC 3359. Same as Figure 5.1 for NGC 3359. The field of view is roughly 30 kpc (N-S) × 40 kpc (E-W).
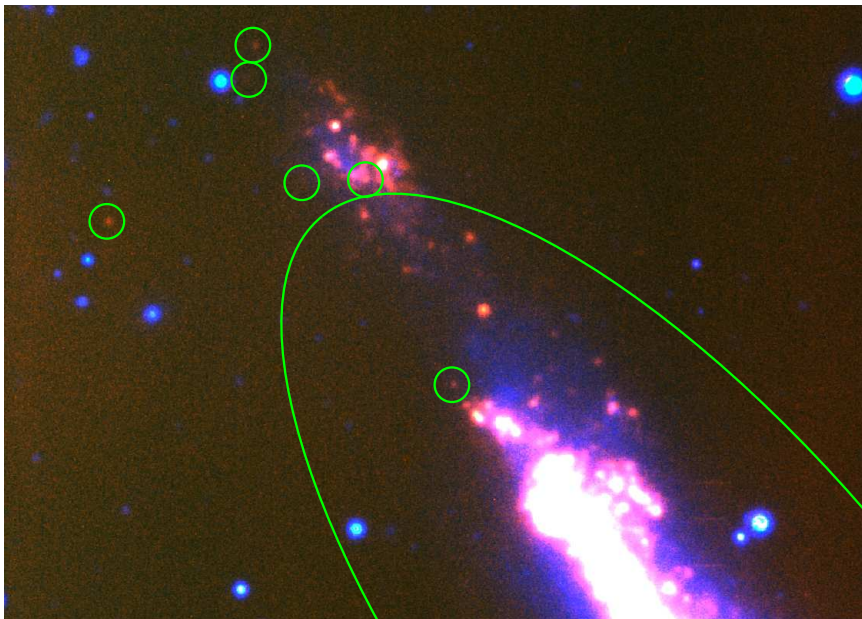

Figure 5.7. MDM continuum-subtracted Hα image: NGC 3432. Same as Figure 5.1 for NGC 3432. The field of view is roughly 15 kpc (N-S) × 25 kpc (E-W).
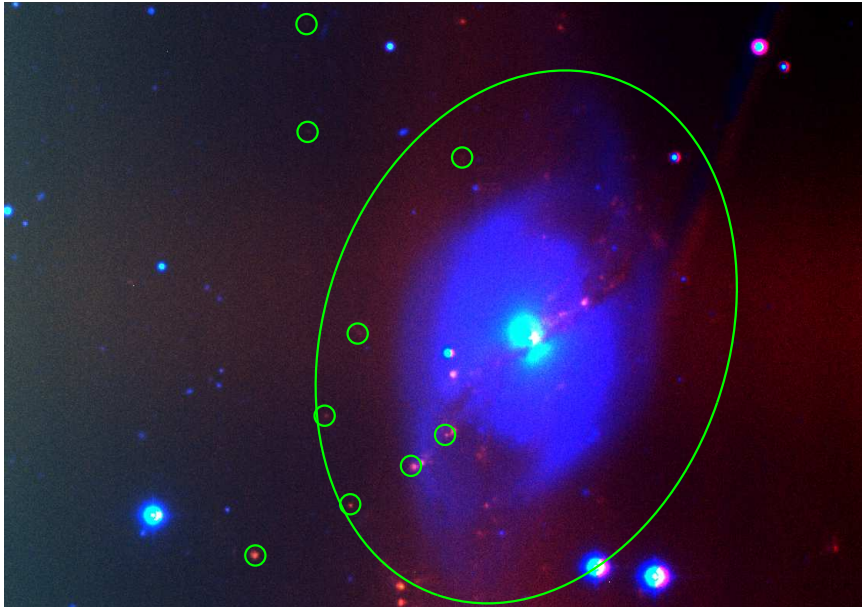
Figure 5.8. MDM continuum-subtracted Hα image: NGC 3718. Same as Figure 5.1 for NGC 3718. The field of view is roughly 30 kpc (N-S) × 40 kpc (E-W).
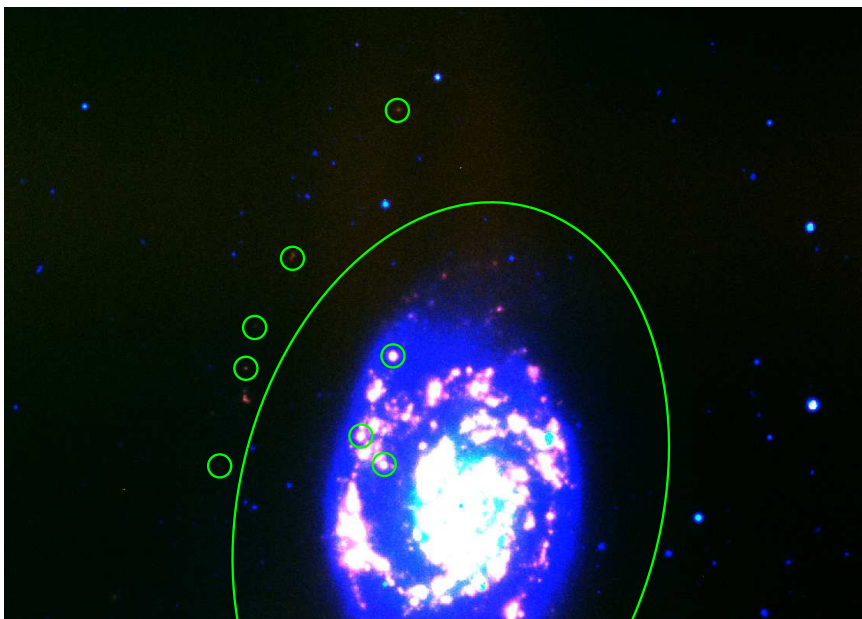

Figure 5.9. MDM continuum-subtracted Hα image: NGC 3893. Same as Figure 5.1 for NGC 3893. The field of view is roughly 25 kpc (N-S) × 35 kpc (E-W).

Figure 5.10. MDM continuum-subtracted Hα image: NGC 5774/5. Same as Figure 5.1 for NGC 5774 and NGC 5775. The field of view is roughly 45 kpc (N-S) × 50 kpc (E-W).

Figure 5.11. MDM continuum-subtracted Hα image: NGC 6239. Same as Figure 5.1 for NGC 6239. The field of view is roughly 8 kpc (N-S) × 10 kpc (E-W).

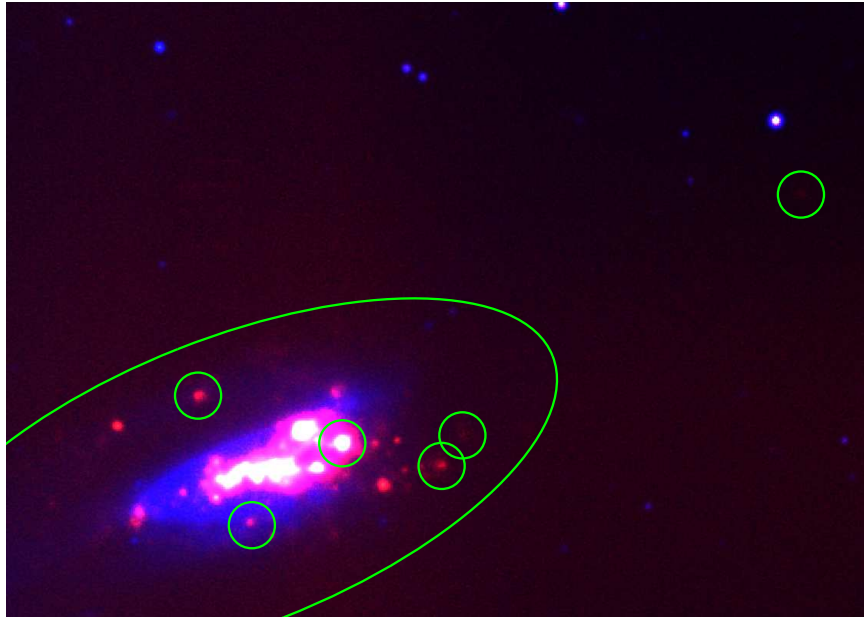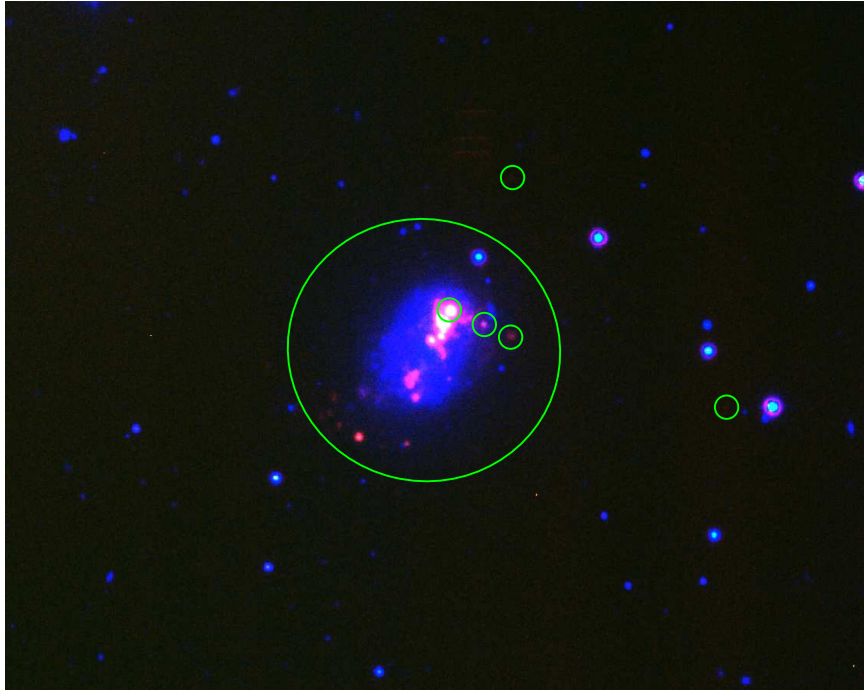**Figure 5.12.** MDM continuum-subtracted Hα image: UGC 5288. Same as Figure 5.1 for UGC 5288. The field of view is roughly 8 kpc (N-S) × 10 kpc (E-W).
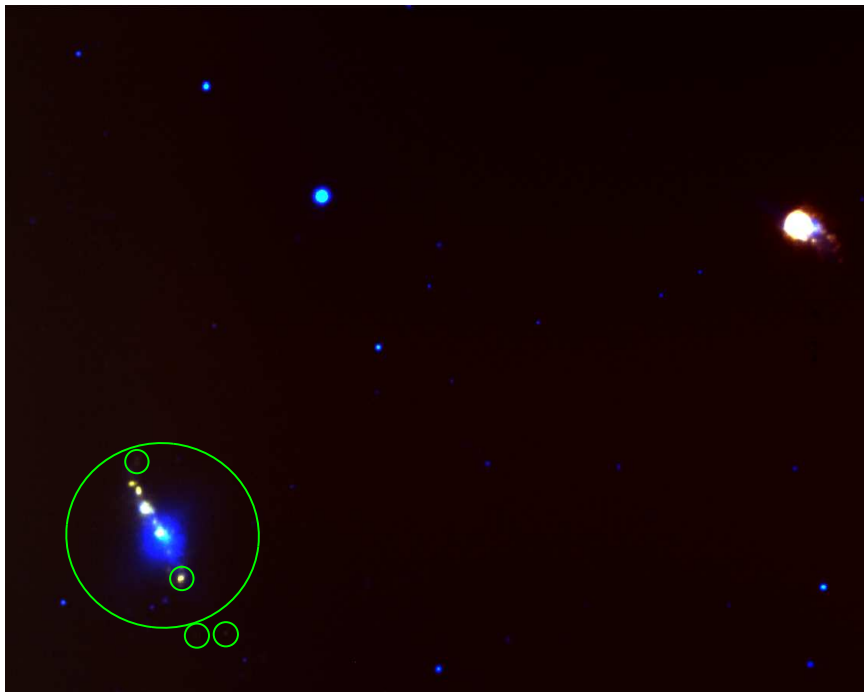

Figure 5.13. MDM continuum-subtracted Hα image: UGC 9562. Same as Figure 5.1 for UGC 9562.The field of view is roughly 18 kpc (N-S) × 25 kpc (E-W).

Name(s):		RA	dec	d	r_{25}	E(B$-$V)	Abun	HI morph	M$_*$	M$_{HI}$	SFR$_{total}$
(1)	(2)	(3)	(4)	(5)	(6)	(7)	(8)	(9)	(10)	(11)	(12)
NGC 2146	***	06 18 38.1	+78 21 26.3	22.45	22.15	0.096	8.68[1]	mMR	6.02	2.10	2.40
NGC 2782	Arp215	09 14 05.1	+40 06 48.9	37.30	12.93	0.016	8.80[2]	mMR	1.55	0.35	1.40
NGC 3227	Arp94	10 23 29.0	+19 52 42.3	20.85	20.57	0.023	8.60[3]	E$-$Sp	5.17	0.20	0.38
NGC 3239	Arp263	10 25 04.3	+17 09 11.5	8.10	6.26	0.032	8.54[2]	Sp$^+$$-Sp^+$	0.122	0.12	0.23
NGC 3310	Arp217	10 38 44.3	+53 30 07.9	18.10	9.17	0.022	8.40[4]	mMR	0.798	0.52	3.00
NGC 3359	***	10 46 37.7	+63 13 25.5	17.80	13.05	0.008	8.60[5]	HIc	1.31	0.45	0.67
NGC 3432	Arp206	10 52 31.2	+36 37 06.9	12.98	12.46	0.013	8.30[6]	mM	0.313	0.60	0.50
NGC 3718	Arp214	11 32 35.0	+53 04 05.2	17.00	12.24	0.014	8.48[2]	WARP	2.94	1.00	0.18
NGC 3893	Holm293a	11 48 38.6	+48 42 40.8	18.13	12.81	0.021	8.60[2]	mM	2.45	0.60	1.40
NGC 5774	***	14 53 42.5	+03 34 56.8	26.80	12.18	0.042	8.55[7]	Sp^0$-$Sp^0	1.10	0.54	0.45
NGC 5775	***	14 53 57.2	+03 32 48.5	–	20.04	–	8.70[7]	–	1.36	0.91	0.75
NGC 6239	***	16 50 05.9	+42 44 18.9	22.30	8.92	0.018	8.40[7]	mM	0.403	0.70	0.85
UGC 5288	***	09 51 17.2	+07 49 37.1	6.03	1.37	0.034	8.08[8]	ENVL	0.00852	0.023	0.0063
UGC 9562	IIZw71	14 51 14.4	+35 32 32.0	23.80	3.81	0.013	8.24[9]	Sp^0$-$Sp^0	0.095	0.082	0.11

Table 5.1. Properties of the galaxies in the HI Rogues sample. (1) and (2) common names of the galaxies. (3) RA (J2000) in hms. (4) dec (J2000) in dms. (5) Redshift-independent distances from NED, in Mpc. (6) Length of the 25th magnitude elliptical isophote (r_{25}) semi-major axis, in kpc. (7) Color excess E(B$-$V) from Schlegel et al. (1998). (8) Oxygen abundance (central or integrated) as $12 + \text{Log(O/H)}$ from various sources: 1. Engelbracht et al. (2008) $-$ direct measurement using [OIII]λ4363. 2. Moustakas & Kennicutt (2006) $-$ strong-line R23 abundances from nuclear SDSS spectra 3. Lisenfeld et al. (2008) $-$ strong-line R23 abundances. 4. Pastoriza et al. (1993) $-$ average of direct [OIII] λ4363 and R23 measurements for full optical disk out to r_{25}. 5. Martin & Roy (1995) $-$ average of R23 oxygen abundances for disk HII regions located between 4$-$9.5 kpc in projected distance from the optical center 6. Pilyugin & Thuan (2007) $-$ average of strong-line R23 oxygen abundances for central HII regions. 7. Márquez et al. (2002) $-$ average of strong-line [NII]/Hα abundances (Pettini & Pagel, 2004) for a number of central disk HII regions. 8. van Zee & Haynes (2006) $-$ average strong-line R23 oxygen abundance for central HII regions 9. Shi et al. (2005) $-$ average strong-line R23 oxygen abundances for central HII regions. (9) HI morphology code from the online HI Rogues Catalog: mMR $-$ minor merger remnants; E$-$Sp $-$ interacting doubles, only 1 with HI; Sp$^+$$-Sp^+$ $-$ interacting doubles, both with HI, both with tails; HIc $-$ detached HI clouds; mM $-$ minor mergers; WARP $-$ galaxies with two-sided warps; Sp^0$-$Sp^0 $-$ interacting doubles, both with HI, no tails; ENVL$-$ galaxies with extended HI envelopes. (10) Stellar masses derived from B, V, and sometimes R-band photometry and the luminosity/color and stellar mass functions of Bell et al. (2003) in units of 10^{10} M$_\odot$. (11) HI-masses for the galaxy in units of 10^{10} M$_\odot$, obtained from the literature (see text for the original sources) and corrected for the galaxy distances we use in column 5 of this table. (12) Derived SFRs in M$_\odot$ yr^{-1} from the total Hα luminosity obtained from the MDM 2.4-m images.

Galaxy	d	r_{25}	HI morph
(1)	(2)	(3)	(4)
NGC 2768	20.06	25.63	EpecH
NGC 2777	18.61	2.27	mM
NGC 3396	28.00*	15.18	Sp^+-Sp^+
NGC 3471	28.64	9.0	mM
NGC 3769	15.50	13.24	mM
NGC 3998	17.85	9.00	EpecH
NGC 4088	15.80	12.32	mM-3
NGC 4111	16.00	16.70	EpecH
NGC 4532	15.80	8.97	IGHI
NGC 4639	22.34	10.08	EXT
NGC 4789A	4.14	1.98	ENVL
NGC 5916	30.60	14.24	Trip+
UGC 8201	4.29	2.18	MISC
VIRGOHI 21	14.00*	–	IGHI

Table 5.2. Galaxies imaged at MDM found to have no outlying HII regions. (1) Common name for the galaxy. (2) Redshift-independent distances from NED, in Mpc. *no red-shift independent distances available, Hubble-flow distance. (3) Length of the 25th magnitude elliptical isophote (r_{25}) semi-major axis, in kpc. (4) HI morphology code from the online HI Rogues Catalog: EpecH− Normal early-type galaxies with peculiar HI; mM-3 − Minor mergers, 3 body-encounters; IGHI − intergalactic HI with no optical counterpart. To clarify, VIRGOHI 21 is one of these intergalactic clouds, while NGC 4532 is an optically-detected galaxy surrounded by such HI debris; Trip+ − Interacting triples; MISC − miscellaneous. The caption of Table 5.1 contains additional descriptions of morphology codes.

5.2.3 Multi-slit Spectroscopy

In the spring of 2008, we obtained multi-slit spectra of numerous HII regions in and around the 13 HI Rogues with ELdots using the Gemini-North Multi-Object Spectrograph (GMOS-N) in order to make metallicity measurements of outer-disk and/or stripped gas. We were somewhat limited by the $5\,'\times 5\,'$ field of view of GMOS, which restricted us to partial coverage of the rogue galaxies and their outskirts. The generation of the GMOS slit mask required that we obtain pre-imaging with GMOS-N in queue mode prior to our spectroscopic observations. We used a 90 Å-wide Hα filter for GMOS to image the 13 fields in our sample, and in concert with the R−band continuum-subtracted MDM images, were then able to pick out and obtain precise instrumental positions for outlying and galactic HII regions. Four to five alignment star holes per-field, and slitlet lengths of at least $10''$ allowed us to fit ~ 25 science slitlets per mask. In practice, however, we had an average of 8 usable science slitlets per mask (minimum = 4; maximum = 17) due to HII region position/alignment conflicts, very faint HII regions without multiple emission-line detections (discovered post-reduction), several blank "sky slitlets" (see Chapter 4, and below), constraints

134

on the instrument rotator angle due to available guide stars, and an increased slit-let length for the brightest central HII regions (for proper night-sky emission line subtraction). In Figures $5.14 - 5.26$ we show the GMOS narrow$-$band pre-images (aligned to the instrument rotator angle, and thus, the slit mask) with the circled slitlets that we end up using for the analysis in Section 5.3.

Our spectral observations were taken in queue mode under the following conditions: a grey lunar phase, an image quality of $1.5''$ (occurring 85% of the time), and some cloud cover (better than that occurring 50% of the time). We used the B600-G5303 600 l/mm grating with various grating angles optimized for each individual slit mask so that key emission lines would not fall in either of the 2 CCD chip gaps. Central wavelengths range between 4100 and 4800 Å. The above grating configuration results in a spectral coverage of 2760 Å, and was chosen so that we could detect emission lines between $\sim 3700 - 5007$ Å for the vast majority of the HII regions on our masks. Several HII regions falling close to the image edges did not achieve this range, and, for a few of those HII regions, we were able to detect the Hα and [NII] $\lambda6583$ emission lines. However, we generally did not obtain spectral data above 5500Å for two reasons: 1. The low-resolution grating (R150, which would have given a larger spectral coverage) is not sensitive enough in the blue to obtain a detection of [O II] for our faint objects, an emission line absolutely essential to nebular abundance estimates. 2. An additional grating configuration for red spectral coverage would have doubled our observing time, and therefore would have reduced the number of targets we could observe with Gemini. We opted for only blue spectral coverage (since we will be using the R23 method for obtaining abundances, see Section 5.3), and therefore sometimes had to use several unconventional methods to break the degeneracy of the R23 relation (see Section 5.3.2 for details). $1.0''$ wide slitlets and 4 (spatial) $\times$ 2 (spectral) binning yields a spectral resolution of 1.8 Å per pixel, and a spatial resolution of 0.28 arcsecond per pixel. Our science exposure times were $3\times$ 20 minutes for each field.

Arc-lamp (CuAr) and spectral flat field calibrations were done between and after each of the science observations. Baseline Gemini calibrations additionally include

the observation of one standard star per grating configuration, HZ-44 in our case, over the execution of the entire science program. The main dangers of using a single standard not taken on the same night as the targets are that seeing variability combined with differential refraction will alter the effective sensitivity function, and that the atmospheric extinction curve will change. Fortunately, in every case, our targets (and the standard star) were observed close to zenith, minimizing the effect of seeing variability with differential refraction. Additionally, I received assurances from the Gemini instrument scientists that variation in atmospheric extinction (or overall throughput) is minimal on Mauna Kea. Nonetheless, our single relative sensitivity function probably subjects our relative line fluxes to higher errors than if we had used at least one standard star on every night data were taken.

For the reduction of the GMOS multislit data, we used the IRAF Gemini/GMOS software package, specifically designed for GMOS multislit data reduction. Once the basic reduction is performed (GPREPARE, GSFLAT, GSREDUCE), we apply the wavelength solution from GSWAVELENGTH, using GSTRANSFORM, the fits to which had a typical RMS of $0.8-1.0$ Å. As was the case with our IMACS multislit spectra for NGC 2915 (Chapter 4), the short slit lengths complicated night-sky line subtraction for several of the bright or more extended HII regions in our sample. Again, several blank sky slitlets on every mask allowed us to properly subtract the sky for these bright/extended objects whose emission lines occupied the entire length of the slitlet. We therefore did two passes of sky subtraction for each mask dataset, one using GSSKYSUBTRACT, and the other using the manual sky subtraction method. Using GEMCOMBINE and GSEXTRACT, we obtained 1-dimensional reduced spectra, which we flux-calibrated using GSCALIBRATE based on our sensitivity function derived from HZ-44.

As a test of our manual sky-subtraction, we compared the two methods using calibrated 1-d spectra of the compact, fainter HII regions, and we found that line fluxes were identical. Typical RMS noise in the final, reduced spectra range from $\sim 9 \times 10^{-18}$ ergs s^{-1} cm^{-2} at 3730 Å, to $\sim 2 \times 10^{-18}$ ergs s^{-1} cm^{-2} at 5000 Å, to $\sim 7 \times 10^{-19}$ ergs s^{-1} cm^{-2} at 6500 Å (when data were redder due to objects being on images

edges). These values do vary somewhat for different slit masks/fields, and depend on the aperture size, and are noted only to illustrate that the emission-line Poisson noise is not a major contributor to the error. The RMS of the fitted sensitivity function was 6.5%, and we estimate that the addition of flux calibration uncertainty, read noise, sky noise, and flat-fielding errors bring our total errors in line flux measurements up to $\sim 10\%$.
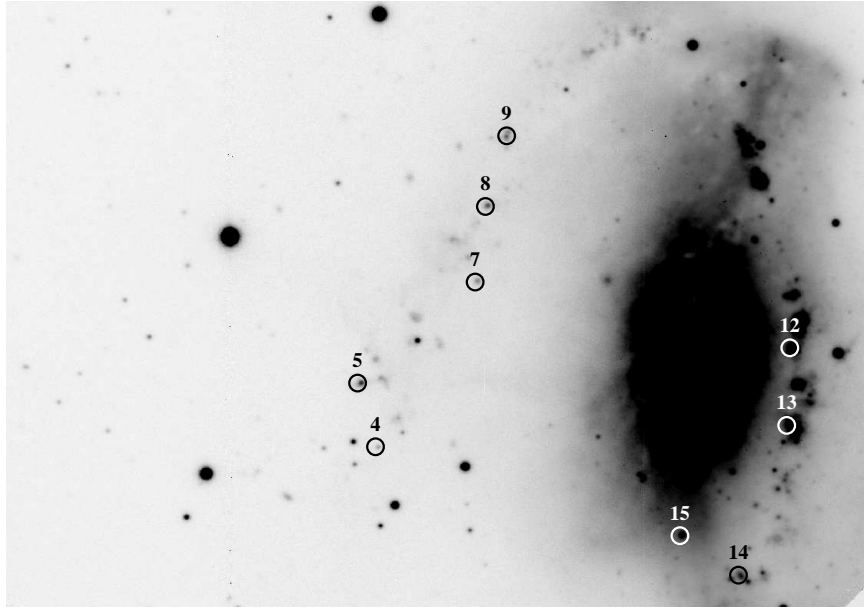

Figure 5.14. Gemini multi-slit mask: NGC 2146. A GMOS-N Hα pre-image, used in creating the multi-slit mask for spectroscopy. The HII regions included in this study are circled and labeled, according to their Gemini slit mask numbers. These slit mask numbers correspond to the HII region identifiers given in the tables, and referred to elsewhere in the text. This image is oriented in the same sense as the actual spectra were taken on the sky at Gemini-North, and does not have a world coordinate system.
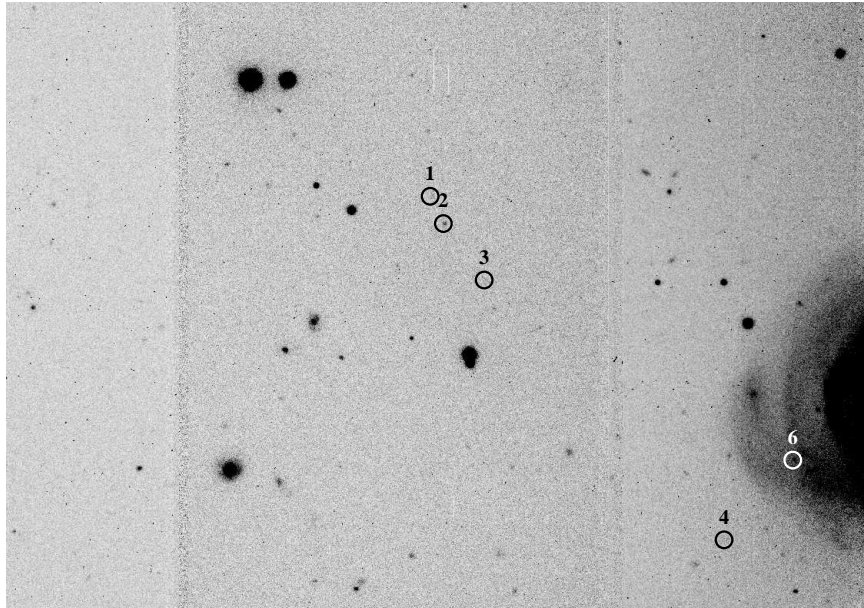
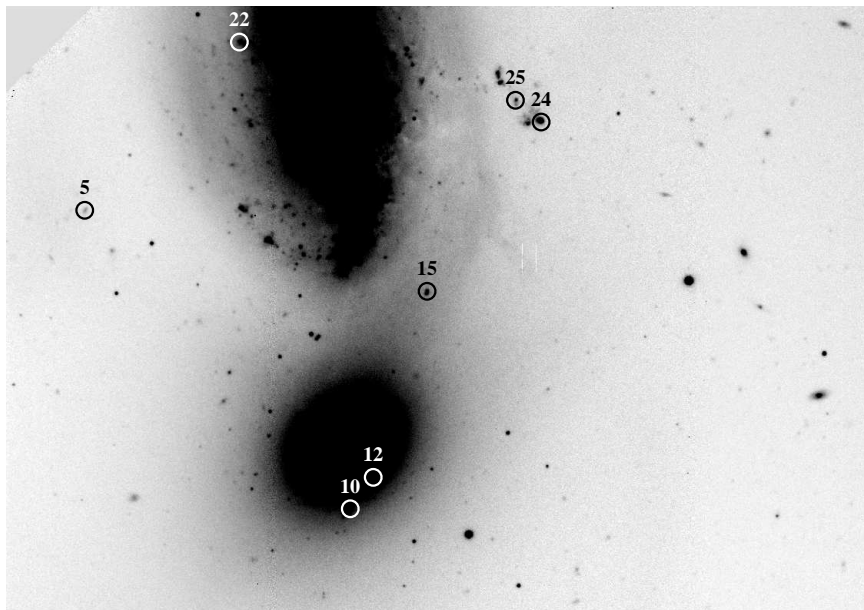**Figure 5.15.** Gemini multi-slit mask: NGC 2782. Same as Figure 5.14 for NGC 2782.

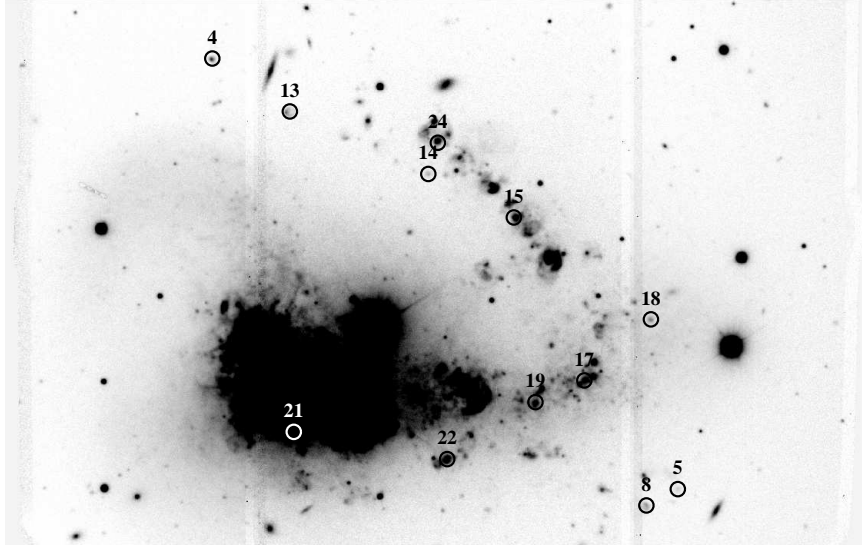**Figure 5.16.** Gemini multi-slit mask: NGC 3227. Same as Figure 5.14 for NGC 3227.

Figure 5.17. Gemini multi-slit mask: NGC 3239. Same as Figure 5.14 for NGC 3239.
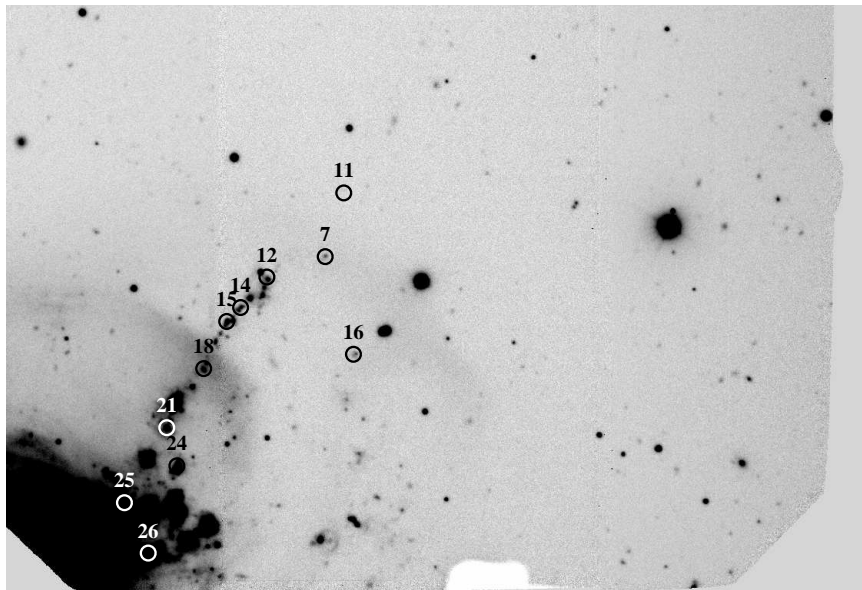

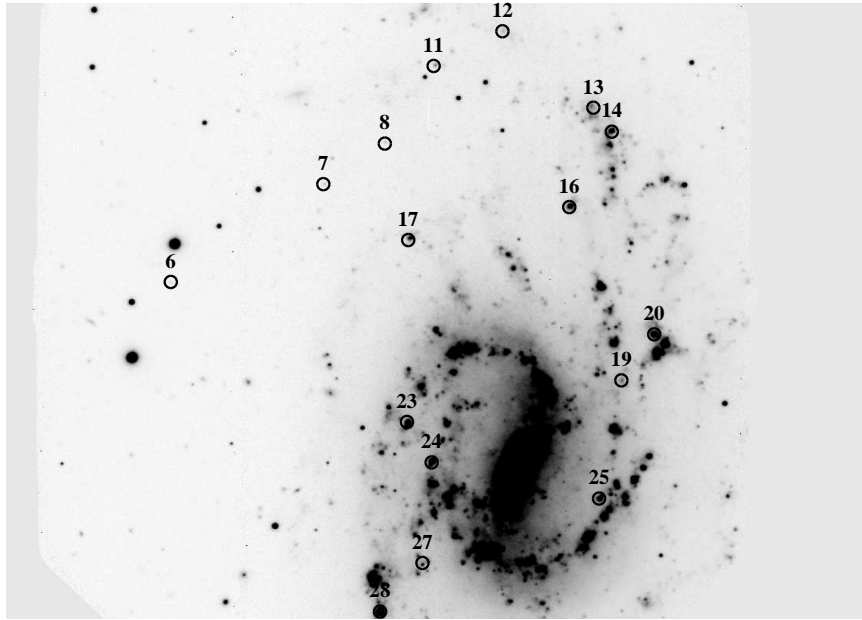**Figure 5.18.** Gemini multi-slit mask: NGC 3310. Same as Figure 5.14 for NGC 3310.

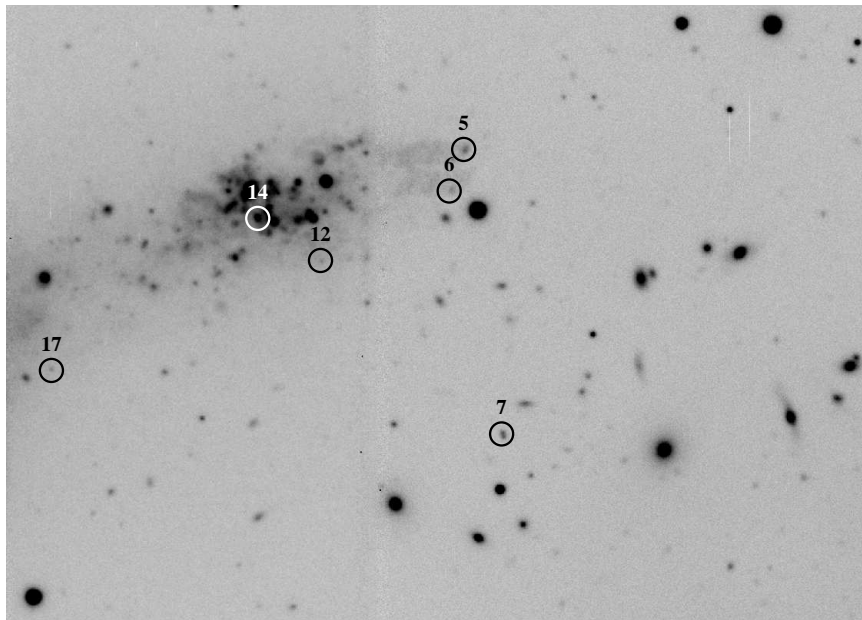**Figure 5.19.** Gemini multi-slit mask: NGC 3359. Same as Figure 5.14 for NGC 3359.

Figure 5.20. Gemini multi-slit mask: NGC 3432. Same as Figure 5.14 for NGC 3432.

Figure 5.21. Gemini multi-slit mask: NGC 3718. Same as Figure 5.14 for NGC 3718.

Figure 5.22. Gemini multi-slit mask: NGC 3893. Same as Figure 5.14 for NGC 3893.

Figure 5.23. Gemini multi-slit mask: NGC 5774/5. Same as Figure 5.14 for NGC 5774 and NGC 5775.

Figure 5.24. Gemini multi-slit mask: NGC 6239. Same as Figure 5.14 for NGC 6239.

Figure 5.25. Gemini multi-slit mask: UGC 5288. Same as Figure 5.14 for UGC 5288.
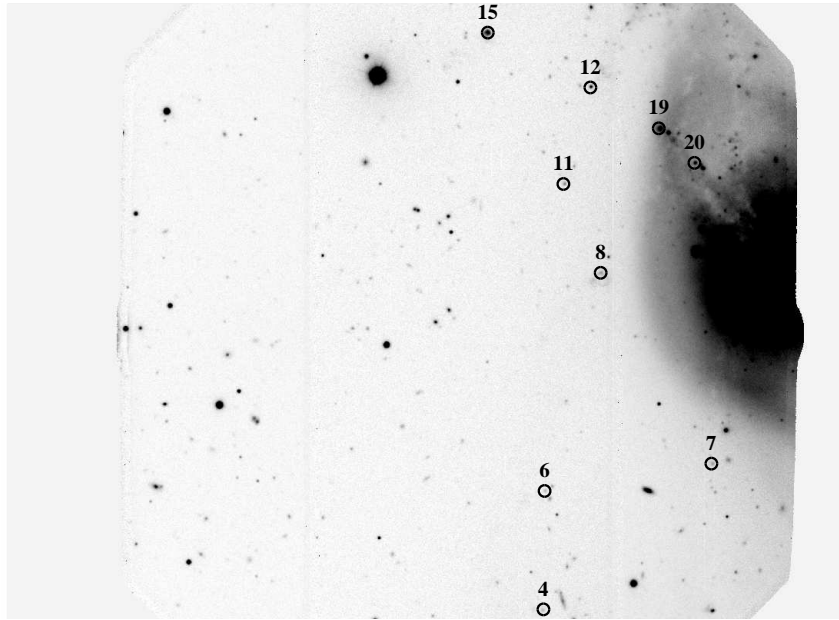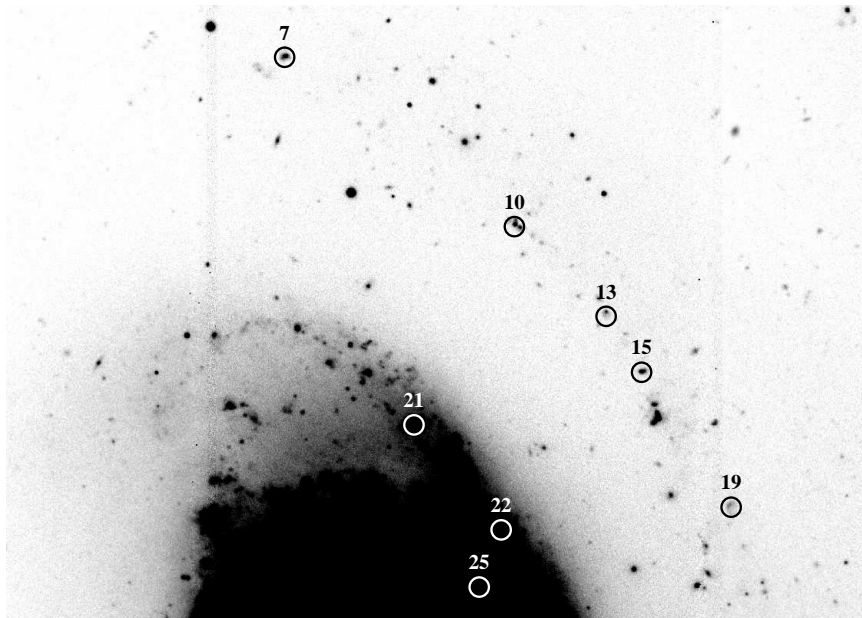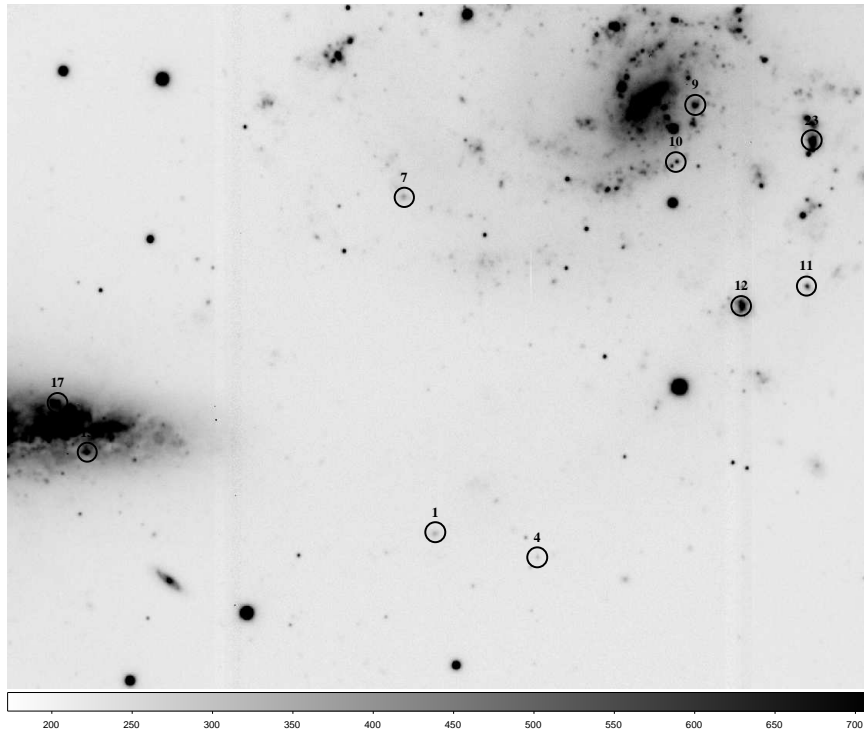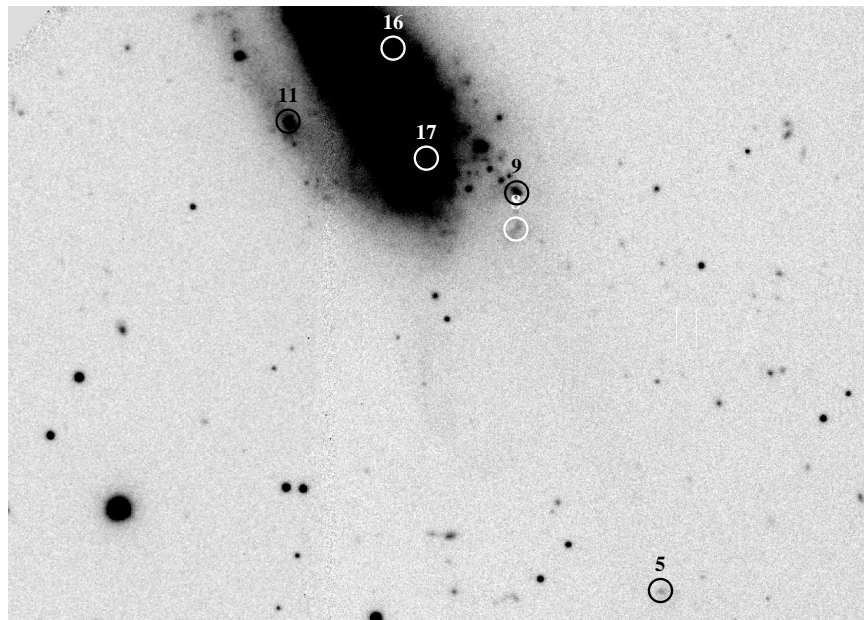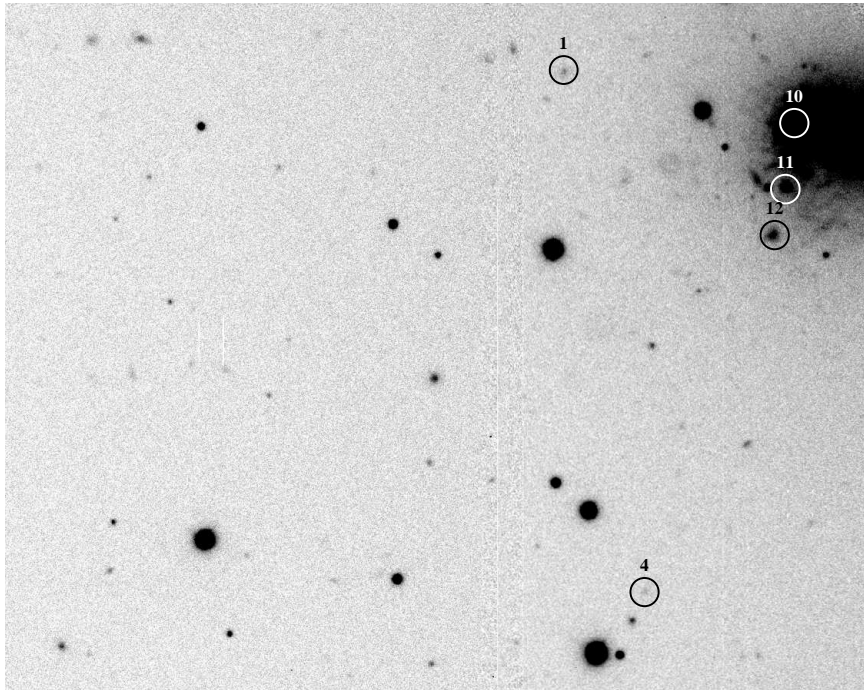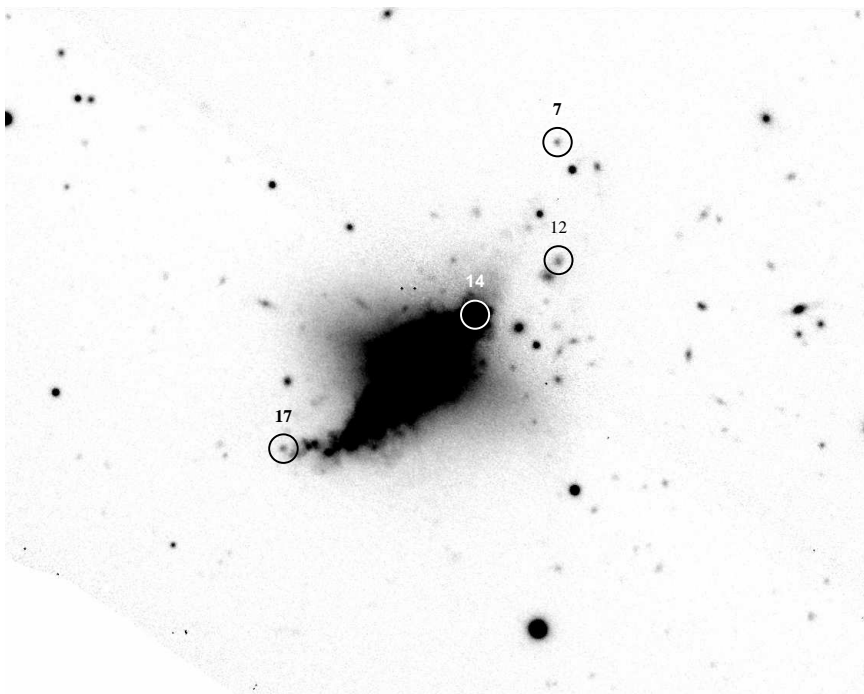

Figure 5.26. Gemini multi-slit mask: UGC 9562. Same as Figure 5.14 for UGC 9562.

5.2.4 Longslit Spectroscopy

Over the course of two observing runs, one at the MDM 2.4-m in the winter of 2007, and one at the Keck 10-m in the spring of 2010, we obtained longslit, low-resolution spectra for several HII regions in our sample of HI rogues with extended star formation. We use these spectra in the subsequent analysis to obtain [NII] $\lambda6583$ and Hα emission lines, since these lines were generally absent in the GMOS multislit data. At MDM, we used the low-resolution Mark III spectrograph with the Echelle CCD, employing the 300/5400 grating and a 0.824 arcsecond slit width. The 300/5400 grating centered at 6500 Å gives a spectral coverage of 3120 - 9879 Å, a range containing all of the optical emission lines we could hope to detect, and a resulting dispersion of 3.3 Å per pixel. Blind offsets from nearby stars were required for positioning the often very faint ELdots in the slit. As mentioned in Section 5.2.2, the run on the MDM 2.4-m telescope was intended as a spectroscopic confirmation run, and we obtained spectra for only a dozen ELdots. Exposure times ranged from 300 s to 2×600 s, depending on the narrow-band flux of the ELdot.

At Keck, we were able to use the low-resolution imaging spectrometer (LRIS) for longslit spectroscopy of 3 HI Rogues with ELdots, during an observing run for an entirely different project which had several target list "holes" at the very start and end of the nights. The data were taken with the 600 l/mm grism (blue-side) and 400 l/mm grating (red side) which gives a spectral coverage between 3000 and 9300 Å. Binning the data 2×2 resulted in a dispersion of 1.2 and 2.3 Å per pixel for the blue and red cameras, respectively. ELdots were positioned in the $1''$ slit precisely by aligning the offset position angle between it and a bright star with the slit angle. In one case, NGC 6239, we were able to align several other galactic HII regions with the slit position angle as well. A problem with an amplifier on the red camera results in an unusable lower CCD chip on the red side (each side has two chips). Exposure times were 2×600 s in the blue and 3×400 s in the red.

Basic reduction steps, which included bias-subtraction, flat-fielding, and flux calibration with a single spectrophotometric standard star (one for each telescope) were performed with the IRAF longslit package. We use these longslit data only to ob-

tain [NII]/Hα ratios in order to break the R23 degeneracy (as described in 5.3.2) for our blue GMOS multislit data. Because these two emission lines ([NII] λ6583 and Hα, at $\lambda = 6563$ Å) are so close in wavelength, we did not require an accurate flux (or wavelength) calibration or reddening correction. Table 5.3 lists the outlying HII regions for which we were able to observe the [NII]/Hα ratio using the longslit data from MDM (only 4/12 ELdot spectra in which we detect the fainter [NII] emission line) and Keck. Table 5.3 also lists the outlying HII regions so far to the edge of the CCD in the GMOS data for NGC 2146 and NGC 2782 that we were able to obtain [NII]/Hα ratios.

Galaxy	Region	r/r$_{25}$	Telescope	[NII]/Hα	Abun
(1)	(2)	(3)	(4)	(5)	(6)
NGC2146	14	0.5	GMOS	0.31±0.03	8.61
NGC2146	13	0.4	GMOS	0.31±0.03	8.61
NGC2146	12	0.4	GMOS	0.27±0.03	8.54
NGC 2782	2	2.5	MDM	0.24±0.02	8.52
NGC 2782	4	1.4	GMOS	0.27±0.02	8.55
NGC 2782	6	0.6	GMOS	0.21±0.02	8.47
NGC 3310	12	1.3	Keck	0.18±0.01	8.42
NGC 3718	15	1.4	MDM	0.20±0.03	8.46
NGC 3893	7	1.4	MDM	0.13±0.02	8.34
NGC 5774/5	4	1.5	MDM	0.18±0.02	8.42
NGC 6239	5	1.9	Keck	0.08±0.02	8.23
NGC 6239	**	0.6	Keck	0.11±0.02	8.24
NGC 6239	**	0.4	Keck	0.22±0.01	8.49
NGC 6239	17	0.3	Keck	0.12±0.01	8.30
NGC 6239	**	0.2	Keck	0.20±0.02	8.46
NGC 6239	**	0.1	Keck	0.10±0.01	8.28
UGC 5288	1	1.4	Keck	<0.08	<8.23
UGC 5288	10	0.4	Keck	0.07±0.01	8.15
UGC 9562	7	1.2	Keck	0.08±0.01	8.23
UGC 9562	14	0.5	Keck	0.08±0.01	8.23

Table 5.3. NII/Hα for selected HII regions from longslit spectra obtained at the MDM 2.4-m and Keck. Values are also tabulated for those HII regions with red lines in the GMOS multi-slit data. (1) Host galaxy name (2) Region name that corresponds to the GMOS multi-slit ID given in HII region properties tables, if applicable. (3) Projected distance from the 25th magnitude elliptical isophote. (4) The telescope at which the spectral data were obtained. (5) the ratio of [NII] λ6583 to Hα with associated errors. In one case, this value is an upper limit. (6) 12+ Log(O/H) abundance derived from the calibration of Pettini & Pagel (2004). The scatter is large, 0.35 dex on average, and therefore this value is used in most cases only to break the R23 degeneracy for the Gemini data.

5.3 Analysis

5.3.1 Emission-line Measurements

The HII regions in our final sample, and circled in figures 5.14 - 5.26, were included based on the presence of the relevant emission lines for R23 strong-line abundances (see Chapter 4). As a reminder, these emission lines are Hβ and forbidden metal lines of [OII] $\lambda\lambda$3727, [OIII] λ4959 and λ5007. R23 is then defined as log [([OII] $\lambda\lambda$3727 + [OIII] λ4959 + [OIII] λ5007)/Hβ]. The majority of the multi-slit spectra contained Hγ as well, which we used to correct for interstellar reddening (see below). The highest signal-to-noise spectra on every mask often contained additional emission lines, including Hδ, HeI λ4026 and HeII λ4687, occasionally [NeIII] λ3869 and λ3970, and rarely the very faint, temperature-sensitive [OIII] λ4363 auroral emission line which provides a direct oxygen abundance measure (see Chapter 4). Using the IRAF task *splot*, and fitting gaussian profiles we obtain integrated line fluxes. For the galactic HII regions, we corrected for absorption from underlying stellar populations by subtracting gaussian fits to the Balmer-line absorption.

We apply a correction for interstellar reddening to all line measurements from the observed Hγ to Hβ ratio for case B recombination where Hγ/Hβ = 0.459 at an effective temperature of 10,000 K and electron density of 100 cm^{-3} (Hummer & Storey, 1987). These lines have been corrected for underlying Balmer absorption (see above). We use a reddening function normalized at Hβ from the Galactic reddening law of Cardelli et al. (1989) assuming R$_v$ = A$_v$/E(B$-$V) = 3.1. In most cases, the measured E(B-V) from the Balmer decrement is similar to the value given in Table 5.1, or lower. We do note, as in Chapter 4, that the reddening has very little impact on the calculated strong-line abundances, which, as we have discussed, have very large errors. Tables 5.4 to 5.16 present the reddening-corrected strong line measurements for the HII regions in all 13 rogue galaxies. All listed line fluxes are relative to Hβ = 100.

5.3.2 Breaking the Degeneracy of the R23 Relation

We use the M91 (McGaugh, 1991) calibration of the R23 relation to obtain the oxygen abundances of all the HII regions in our sample of 13 rogue systems. The R23 relation exhibits a well-known degeneracy, with a turn-over in the relation at $Z \sim 0.3\ Z_{\odot}$ (12+Log(O/H) $\sim$ 8.35). Figures 5.27 - 5.39 show the model photoionization grid of M91 and the positions of the HII regions on that grid for every target in our sample. These figures also show that the derived oxygen-abudance (solid and dashed near-vertical lines) is double-valued for every HII region. For example, in Figure 5.27, HII Region 9 in NGC 2146 (see Figure 5.14 for its position in the galaxy) could have an oxygen abundance, $12 + \text{Log (O/H)}$, of either 8.8 or 7.9. The most robust way to place an HII region on the upper or lower branch of the R23 relation is to use the [NII] $\lambda 6583$ to [OII] $\lambda\lambda 3727$ ratio. When log [NII]/[OII] < -1.0, HII regions lie on the lower metallicity branch of the R23 relation (M91). Since our multislit data are bluer than 5500 Å in most cases, we cannot use this method. Instead, we use a combination of several methods described below. The errors for the strong-line abundances range between 0.25 and 0.35 dex, depending on the method used to break the degeneracy in the R23 relation (see below). We approximate the error in the R23 abundances at a constant value of at least 0.25 dex, which is consistent with values quoted in the literature (McGaugh, 1991; Ercolano et al., 2007, 2009). Although the errors may be slightly lower the farther the abundances are from the turnover of the relation, it has not been shown quantitatively, and significant systematics may persist (Ercolano et al., 2009).

- **[NII]/Hα** Kewley & Ellison (2008) discuss how to use the [NII]$\lambda 6583$/Hα ratio (N2 index) to break the degeneracy in the R23 relation. If Log N2 < -1.3, there is a high degree of certainty ($\sim$86%) that the oxygen abundance is on the lower-branch of the R23 relation. Whereas if Log N2 > -1.1, the oxygen abundance is on the upper branch. Between -1.1 and -1.3, Log N2 does not accurately discriminate between the upper and lower branches of R23 because the oxygen abundance is very close to the turnover at $12 + \text{Log (O/H)} = 8.3$. This method

of breaking the R23 degeneracy works because the N2 index is sensitive to the oxygen abundance to within 0.4 dex accuracy at a 95% confidence level up to $12 + \text{Log(O/H)} = 8.8$ (Pettini and Pagel 2004, henceforth PP04). The benefits of this strong-line abundance indicator are that it is monotonic with (O/H) and it does not require flux calibration or reddening correction due to the proximity in wavelength of [NII] $\lambda6583$ and Hα. The primary drawback is the large uncertainty in the calibration (0.4 dex), and the limited range over which it is useful.

For the abundance values tabulated in the last column of Table 5.3, we use the calibration of the N2 index by PP04 as a rough estimate of the HII region's oxygen abundance. It is apparent from the N2 indices given in this table that most of the HII regions, with the exception of those in UGC 5288, UGC 9562, and one in NGC 6239, lie on the upper branch of the R23 relation. Therefore, we are able to use the N2 index to break the M91 R23 degeneracy for the majority of the HII regions given in Table 5.3 such that the oxygen abundance is the upper branch value of the M91 R23 relation. For the few ambiguous cases in which Log N2 lies between -1.1 and -1.3, we adopt the M91 R23 oxygen abundance value closer to the PP04 calibration oxygen abundance. In these cases, the M91 values are also consistent with being very close to the turnover, and are therefore subject to large uncertainties of ~ 0.3 dex. We refer to this method in tables 5.4 to 5.16 as "M91/PP04."

- **Previously Published Values of 12 + Log (O/H)** Every single galaxy in our sample of HI rogues has a published value of $12 + \text{Log(O/H)}$ for its central HII regions, which we tabulate in Table 5.1. The methods used to obtain these values vary from direct T_{eff} measurements of the oxygen abundance with [OIII] $\lambda4363$ to the N2 index, and therefore also vary widely in accuracy. Furthermore, some of these values in the table reflect the average value of multiple central HII region measurements, and others come from integrated nebular SDSS spectra. In the table caption, we briefly describe the sources of these $12 + \text{Log (O/H)}$

148

values. We use these values from the literature *only* to break the degeneracy of the R23 relation for our multislit data of *central* HII regions in galaxies without a measured N2 index from our longslit (or GMOS) data. From the literature, ten of the 13 galaxies in this study have central oxygen abundances greater than the turnover value of 8.35. UGC 5288 appears to lie on the lower branch of the M91 R23 relation, consistent with the N2 indices (one of which is an upper limit) we measure with Keck longslit data. UGC 9562 (also consistent with N2 index) and NGC 3432 have oxygen abundances very close to the turnover value. In tables 5.4 to 5.16 we refer to this method as "M91/lit" for literature.

- **Iterative Method** Kewley & Dopita (2002) present what they call an "iterative" R23 oxygen abundance determination when only Hβ, [OIII] $\lambda\lambda$ 4959, 5007, and [OII] λ 3727 are available. We use this method for breaking the M91 R23 degeneracy *only* when neither of the two previous methods are available, and therefore only for cases of HII regions beyond R25 in 6 galaxies. This method uses an initial metallicity guess based on an R23 abundance value from the Zaritsky et al. (1994) calibration (Z94; generally only valid for 12 + Log (O/H) $>$ 8.5), the ionization parameter from [OIII]/[OII], and abundance coefficients from Kewley & Dopita (2002), and iterates until the abundance and ionization parameter converge. Once we obtain this iterative value of 12 + Log (O/H), we use the closer M91 R23 value for the oxygen abundance estimate. For the outlying HII regions of all 5 galaxies for which we had to use this method, all were found to lie on the upper branch. This iterative method is subject to the largest errors of all three of our methods of oxygen abundance determinations ($\sim$ 0.4 dex), especially in the range 8.5 $<$ 12 Log (O/H) $<$ 9.0, where most of our HII regions seem to lie. We refer to this method as "M91/KD02" after Kewley & Dopita (2002).

We checked whether these three methods were consistent with each other by examining the several cases in which all three methods are available for selected HII regions. It is reassuring that the different methods give the same branches in almost

all of these cases. The two cases in which these different methods give different results are those of UGC 5288 and UGC 9562, both of which lie near or below the R23 turnover in literature and N2 index measurements. For example, in the central regions of UGC 5288, we have a literature value from van Zee & Haynes (2006) which averages M91 R23 abundances for several HII regions (average 12 + Log (O/H) = 8.08), we have an N2 index from Keck longslit data that places it in the "ambiguous" turnover region, and has a PP04 abundance of 8.15 (which is lower branch), and the KD02 iterative method places it on the upper branch of the R23 relation. The problem here is that Z94, used for the initial estimate, is known to be unreliable at 12 + Log (O/H) < 8.5. We use the iterative method only as a last resort when no other method is available, because it appears to be biased toward the upper branch of the R23 relation. The 6 cases in which we do use this method are for outer HII regions of NGC 2146, NGC 3227, NGC 3239, NGC 3359, NGC 3432 and NGC 3718. We discuss these cases individually in Section 5.4, and note that only in the case of NGC 3432 is the initial Z94 estimate in the dubious zone. Otherwise, we are inclined to trust the results of the KD02 method. Both lower and upper branch values for these systems can be seen in figures 5.27 - 5.39.
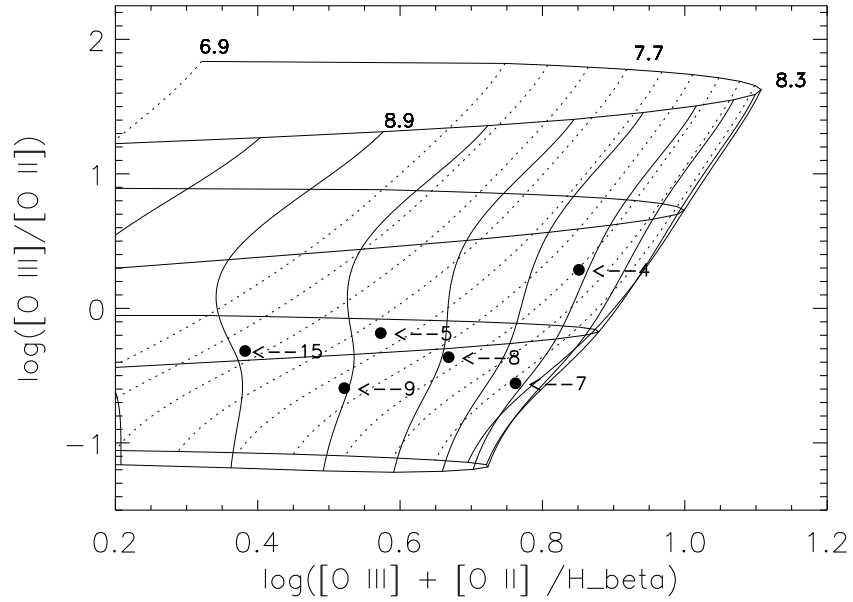
Figure 5.27. The theoretical model grid from M91 showing the R23 relation and positions of HII regions in NGC 2146. The roughly vertical lines represent lines of constant abundance. Dotted lines delineate the lower branch of the R23 relation, and solid lines show the upper branch. The turnover occurs at $12 + \mathrm{Log(O/H)} = 8.35$ ($\sim 0.3 Z_\odot$). Lines are drawn in increments of 0.1 dex, and several are marked for reference. The solid horizontal lines are lines of constant ionization parameter. The six HII regions from NGC 2146 with available blue lines are labeled in the plot with arrows and their GMOS ID numbers. The errors for the strong-line abundances range between 0.25 and 0.35 dex, depending on the method used to break the degeneracy in the R23 relation (see Section 5.3). All of these HII regions in NGC 2146 are determined to lie on the upper-branch of the R23 relation.

Figure 5.28. Model grid of the M91 R23 relation with upper and lower-branch values for NGC 2782. Same as Figure 5.27 for NGC 2782. All of these HII regions in NGC 2782 are determined to lie on the upper-branch of the R23 relation.

Figure 5.29. Model grid of the M91 R23 relation with upper and lower-branch values for NGC 3227. Same as Figure 5.27 for NGC 3227.All of these HII regions in NGC 3227 are determined to lie on the upper-branch of the R23 relation.

152

Figure 5.30. Model grid of the M91 R23 relation with upper and lower-branch values for NGC 3239. Same as Figure 5.27 for NGC 3239. All of these HII regions in NGC 3239 are determined to lie on the upper-branch of the R23 relation.
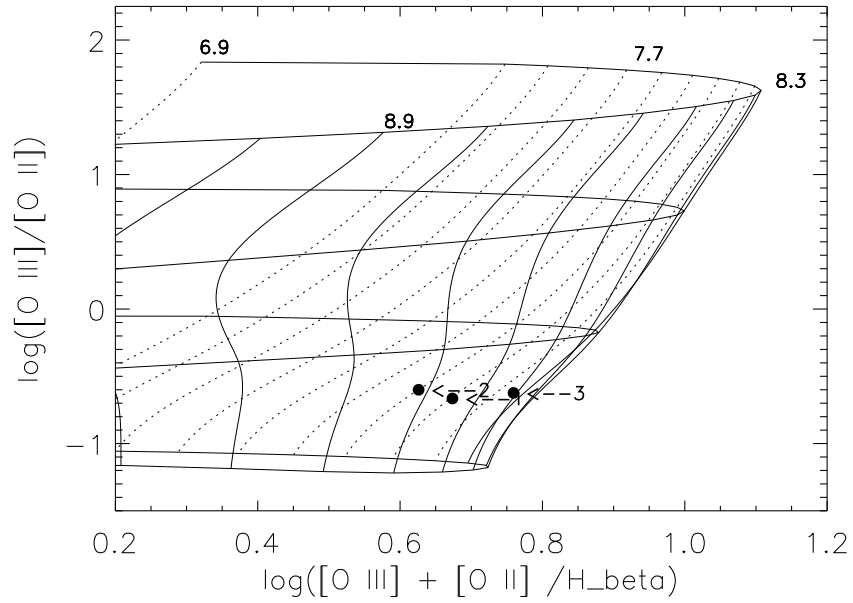

Figure 5.31. Model grid of the M91 R23 relation with upper and lower-branch values for NGC 3310. Same as Figure 5.27 for NGC 3310. All of these HII regions in NGC 3310 are determined to lie on the upper-branch of the R23 relation.

Figure 5.32. Model grid of the M91 R23 relation with upper and lower-branch values for NGC 3359. Same as Figure 5.27 for NGC 3359. With the exception of regions 20 and 28, all of these HII regions in NGC 3359 are determined to lie on the upper-branch of the R23 relation.

Figure 5.33. Model grid of the M91 R23 relation with upper and lower-branch values for NGC 3432. Same as Figure 5.27 for NGC 3432. With the exception of region 17, all of these HII regions in NGC 3432 are determined to lie on the upper-branch of the R23 relation.

Figure 5.34. Model grid of the M91 R23 relation with upper and lower-branch values for NGC 3718. Same as Figure 5.27 for NGC 3718. All of these HII regions in NGC 3718 are determined to lie on the upper-branch of the R23 relation.
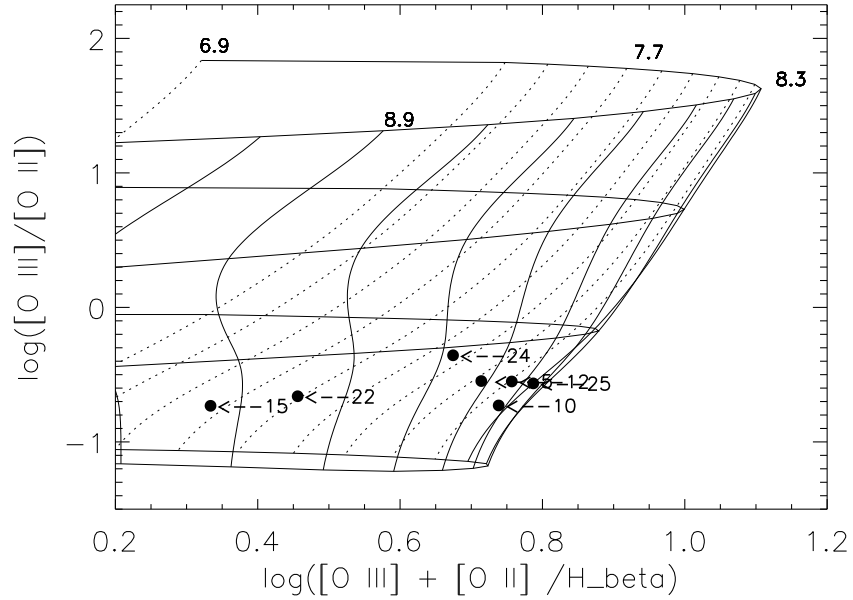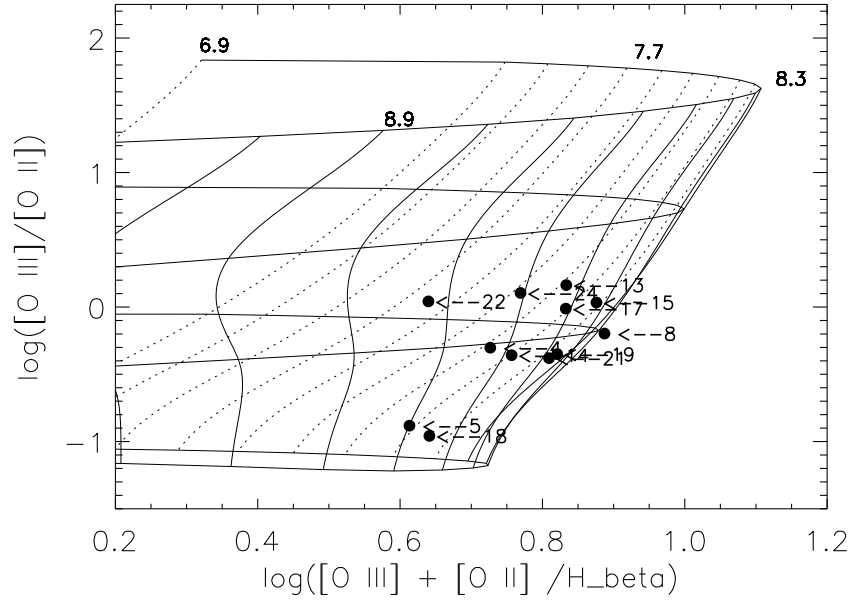

Figure 5.35. Model grid of the M91 R23 relation with upper and lower-branch values for NGC 3893. Same as Figure 5.27 for NGC 3893 All of these HII regions in NGC 3893 are determined to lie on the upper-branch of the R23 relation.
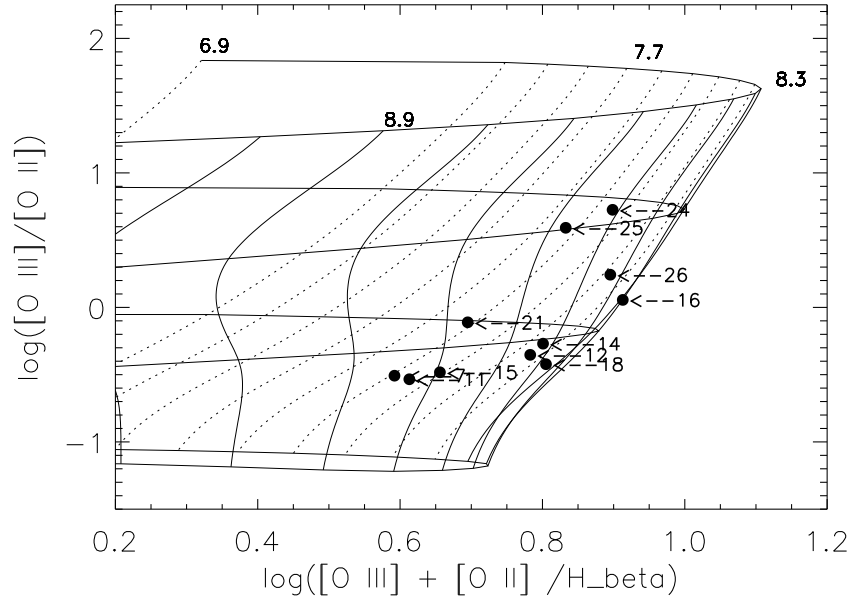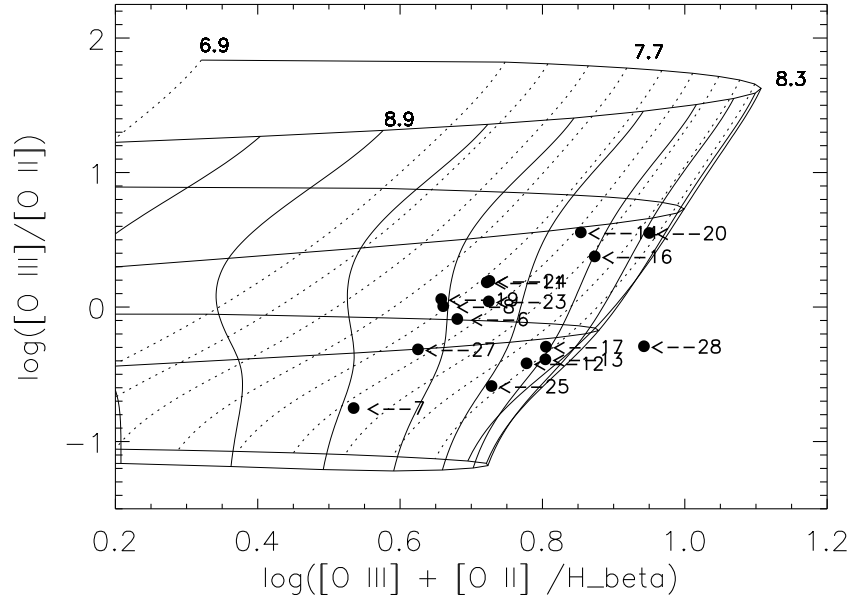
Figure 5.36. Model grid of the M91 R23 relation with upper and lower-branch values for NGC 5774/5. Same as Figure 5.27 for NGC 5774 and NGC 5775. All of these HII regions in NGC 5774/5 are determined to lie on the upper-branch of the R23 relation.
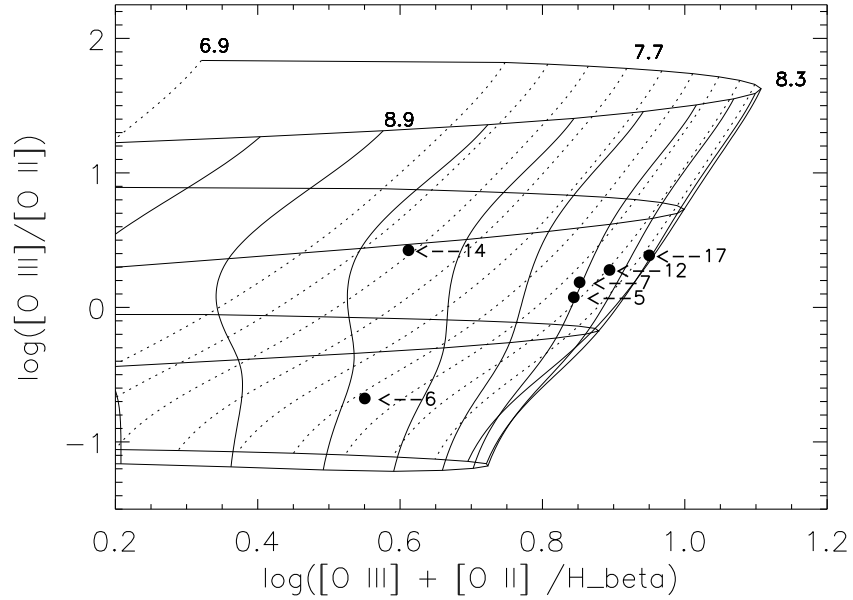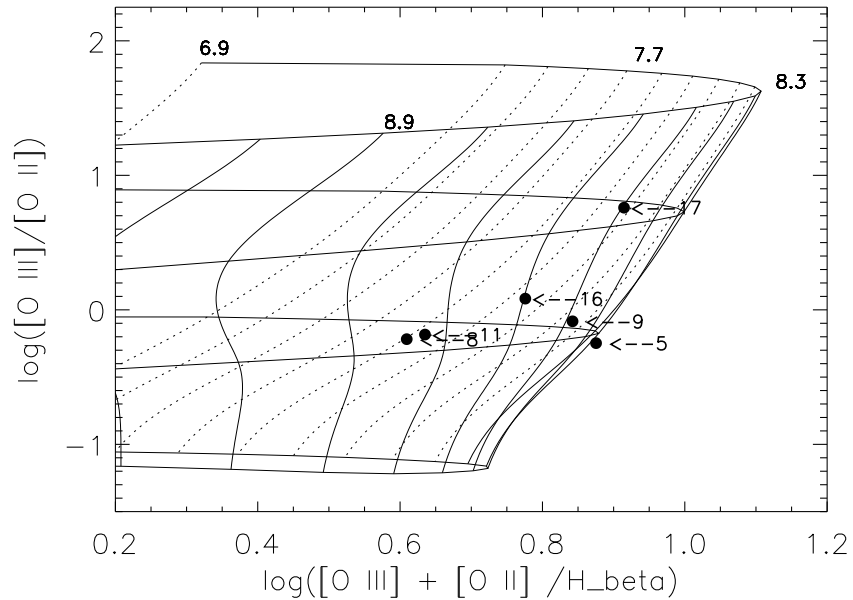

Figure 5.37. Model grid of the M91 R23 relation with upper and lower-branch values for NGC 6239. Same as Figure 5.27 for NGC 6239. With the exception of region 5 (which is right on the turnover), all of these HII regions in NGC 6329 are determined to lie on the upper-branch of the R23 relation.

156

Figure 5.38. Model grid of the M91 R23 relation with upper and lower-branch values for UGC 5288. Same as Figure 5.27 for UGC 5288. All of these HII regions in UGC 5288 are determined to lie on the lower-branch of the R23 relation.

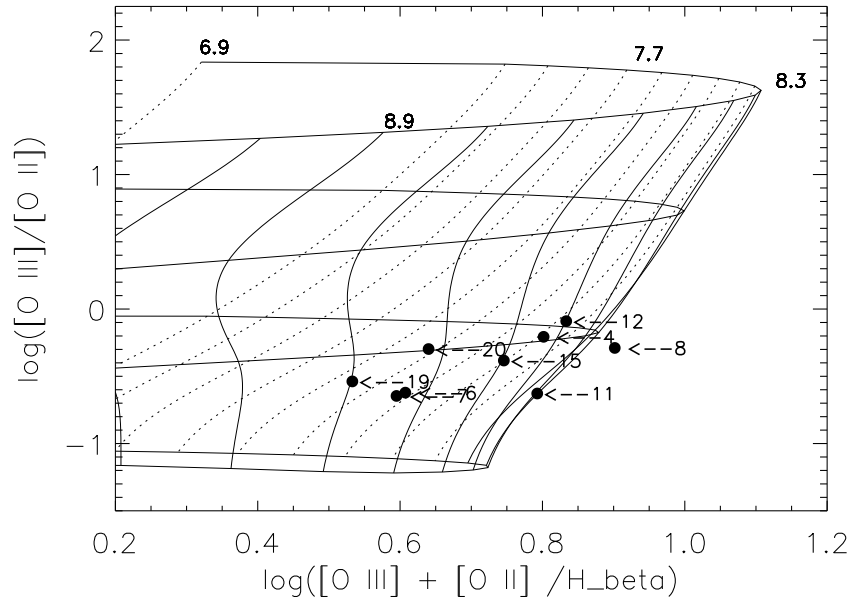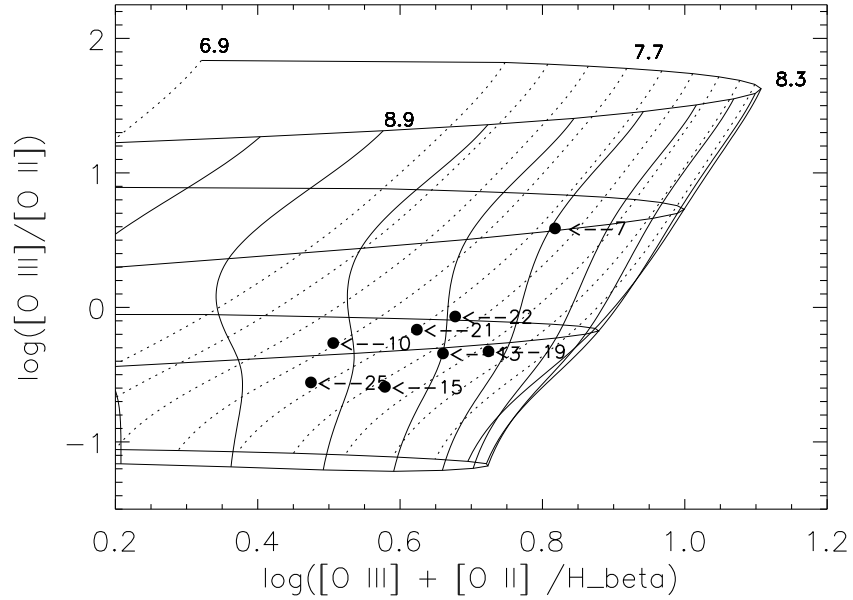**Figure 5.39.** Model grid of the M91 R23 relation with upper and lower-branch values for UGC 9562. Same as Figure 5.27 for UGC 9562. All of these HII regions in UGC 9562 a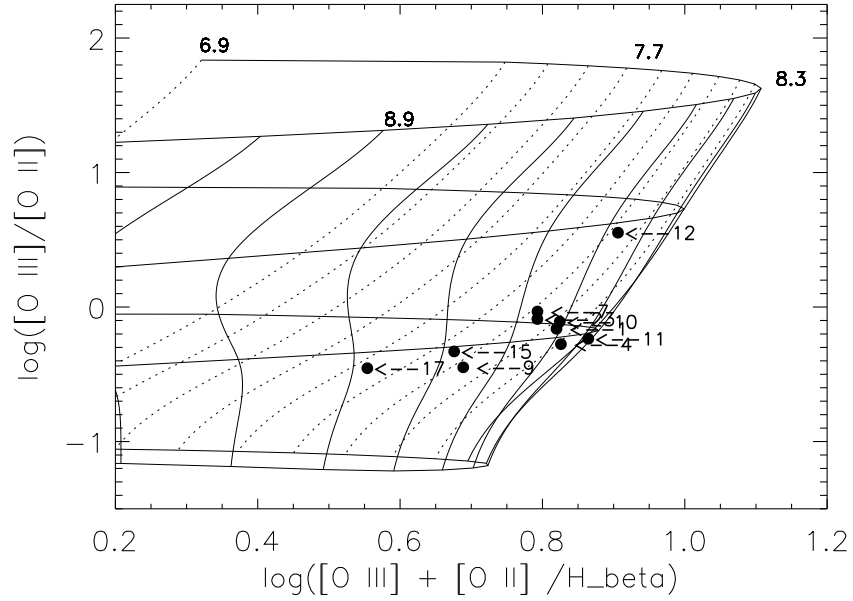re determined to lie on the lower-branch of the R23 relation (though all are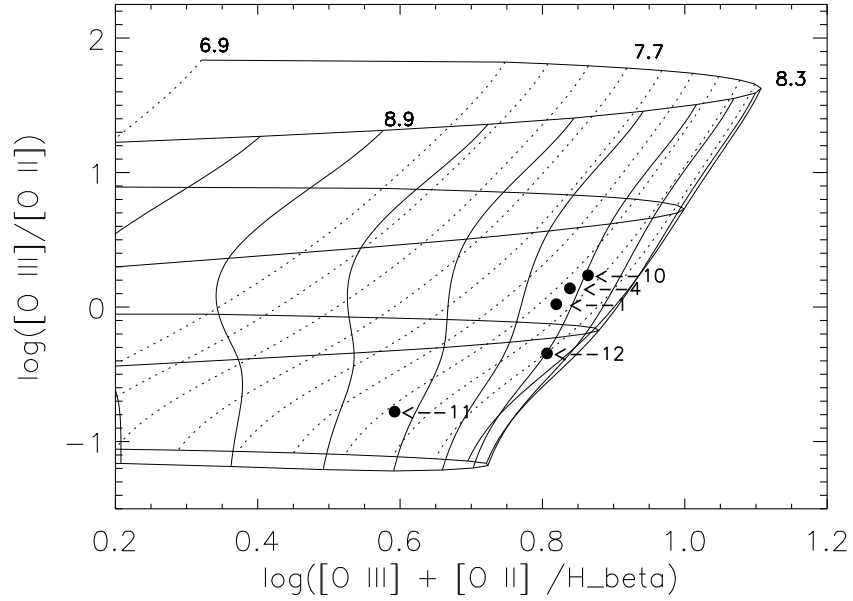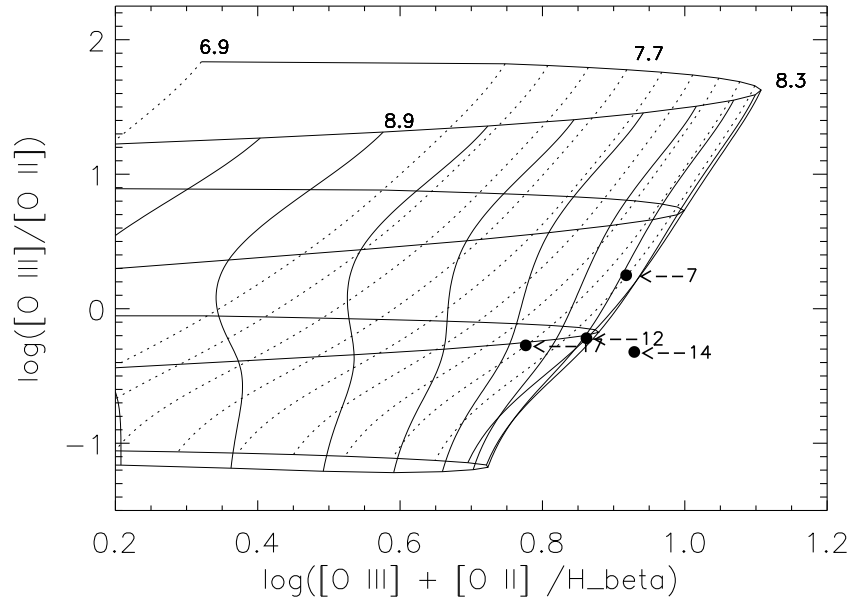 very close to the turnover), except for region 14, which lies off the grid, and is given a turnover value of $12 + \mathrm{Log}\,(\mathrm{O/H}) = 8.35$.

157

5.4 Results: The Distribution of Oxygen in 13 HI Rogues

Here, we report radial oxygen abundance distributions for our sample of 13 HI Rogues with Gemini GMOS-N spectral data. We consider each galaxy separately, and comment on its environment, HI morphology, and the distribution of star formation. Figures 5.40 to 5.76 show optical DSS images overlaid with HI column density contours for each galaxy from the HI Rogues Gallery (Hibbard et al., 2001b). Figures 5.41 to 5.77 show the oxygen abundance, 12 + Log (O/H), versus the galactocentric projected distances (in r/r_{25}) for the HII regions in each galaxy. The dash-dotted line on each plot represents an error-weighted linear-least-squares fit to the data. For reference, the solar oxygen abundance, in 12 + Log (O/H) is 8.66 (Asplund et al., 2005), and the turnover of the R23 relation occurs at 12 + Log (O/H) = 8.35 (McGaugh, 1991).

To help with the interpretation in the oxygen abundance gradients, we also show the radial dependence of the excitation diagnostic, Log ([OIII]/[OII]), in figures 5.42 to 5.78. This quantity is a direct observable, and is therefore not subject to the large systematic uncertainties that complicate the interpretation of oxygen abundances derived from the R23 relation. The excitation diagnostic, while sensitive to the ionization parameter, also strongly depends on metallicity, as shown in figure 1 of Kewley & Dopita (2002). The ionization parameter, q, is defined in Kewley & Dopita (2002) as the ionizing photon flux through unit area divided by the local number density of hydrogen atoms ($q = Q/4\pi R_S^2 n$; Q = ionizing photon emission rate, R_S is the Stromgren sphere radius, and n is the local number density of hydrogen atoms), and has units of cm/s. A unitless and more commonly-used definition of the ionization parameter is U $\equiv$ q/c, where c is the speed of light in cm/s. We consider the spectra of the HII regions to be dominated by three parameters: the stellar ionizing effective temperature, T_{eff}, U, and Z (Oey et al., 2000). These parameters are all related, both subtly and directly, and we consider in Section 5.5.4 the effects and implications of varying these parameters with radius.

Examining dispersion in measurements relative to sample size, Zaritsky et al.

(1994) find that 5 HII regions per galaxy should serve as a minimum on which to base reliable measurements of radial abundance gradients. For reference, we measure at least 5 HII regions per galaxy in all but UGC 9562. We measure the oxygen abundances of only 4 HII regions in UGC 9562. The range of radial distances over which we measure oxygen abundance gradients is generally between 0.4 and 1.5 r/r_{25}, though several gradients extend beyond 2 r/r_{25}. Tables 5.4 through 5.16 provide all of the relevant data on the HII regions for which we determine abundances in every galaxy: RA and declination, r/r_{25}, the projected distance from the nearest galaxy center in kpc, Hα fluxes and R$-$band magnitudes from MDM narrow-band images, oxygen emission-line fluxes relative to H$\beta = 100$, the oxygen abundance, and the method used to obtain the oxygen abundance.

5.4.1 NGC 2146

NGC 2146 is classified in the HI Rogues catalog as a minor merger and has HI streams extending to the north and south of the galaxy out to 6 Holmberg radii (Taramopoulos et al., 2001). These streams are thought to be due to tidal interaction between NGC 2146 and an unseen LSB companion approximately one Gyr ago. The outlying HII regions in this system are embedded within the HI of this system and are generally within the $3 - 10 \times 10^{19}$ cm^{-2} column density contours. NGC 2146's total HI mass is 2.1×10^{10} M$_\odot$, with 5.5×10^9 M$_\odot$ coming from the bright region around the galaxy and 1.6×10^{10} M$_\odot$ coming from the extended component.

We find that the outlying HII regions in this galaxy are oxygen-enriched at the same level as the central HII regions, $12 + \text{Log (O/H)} \sim 8.7$, within the uncertainties. All 9 HII regions in NGC 2146 appear to lie on a single extended spiral arm that begins just to the SE of the central burst of star formation, turns north, and then ends at the outlying HII regions to the SW of the galaxy center. Regions 12, 13, and 14, all centrally-located, lie at the edge of the CCD in the GMOS observations, and we therefore measure the oxygen abundance of these HII regions using only the PP04 N2 index calibration. The PP04 abundances for these three central HII regions indicate that Region 15, the centermost HII region in this sample, is also on the
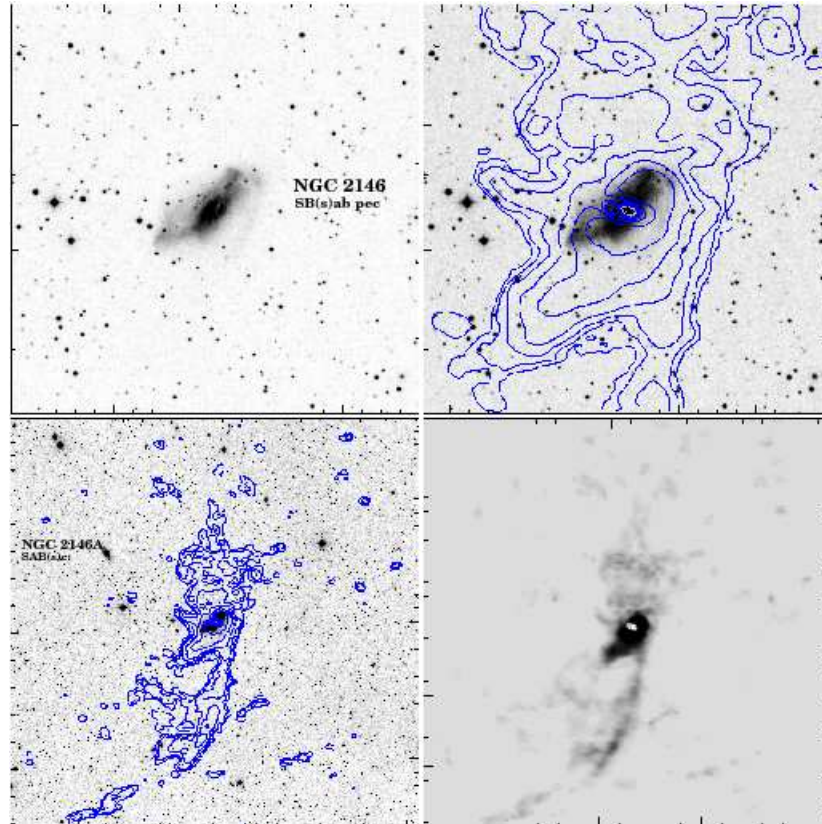
Figure 5.40. HI column density contours: NGC 2146. Neutral hydrogen column density contours taken directly from the HI Rogues catalog. Original VLA D-array data from Taramopoulos et al. (2001). The resolution of the HI synthesis map is $77'' \times 49''$ and the contours are 3.0×10^{18} cm^{-2} $\times 2^n$. Top left: DSS image of NGC 2146. Top right and bottom left: DSS image + HI contours. Bottom right: HI data for NGC 2146.

upper branch of the M91 R23 relation. Since we have neither longslit abundances nor literature values for the 5 outlying HII regions of this galaxy, we use the M91/KD02 iterative method for determining their oxygen abundances. The literature abundance value of 8.68 for this galaxy comes from Engelbracht et al. (2008), who use a direct abundance measurement with an [OIII] λ 4363 detection in a single spectrum from the center of NGC 2146.
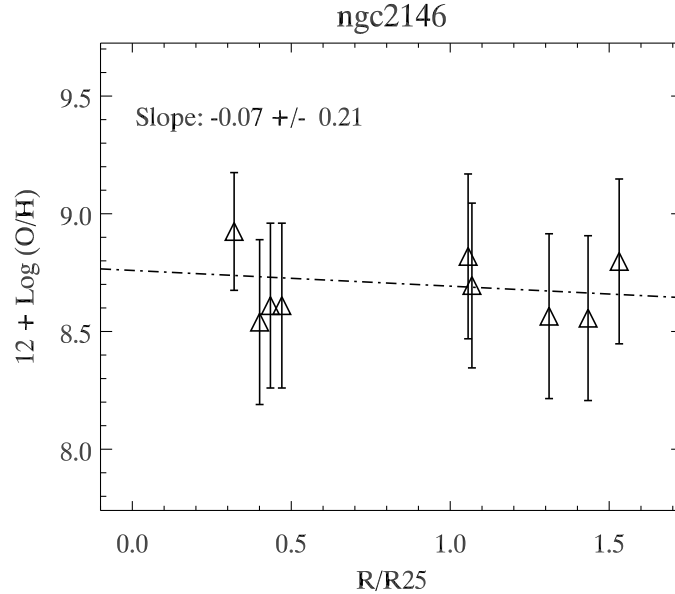
Figure 5.41. Radial oxygen abundance gradient: NGC 2146. The oxygen abundance, 12 + Log (O/H), versus the galactocentric projected distances (in r/r_{25}) for HII regions in NGC 2146. The errors for the strong-line abundances range between 0.25 and 0.35 dex, depending on the method used to break the degeneracy in the R23 relation (see Section 5.3). The dashed-dotted line represents a linear-least-squares fit to the data, the slope (and its associated σ) of which is given in the upper left corner of the plot.

The excitation plot for this galaxy shows a weak trend of increasing Log ([OIII]/[OII]) with radius, which is what we might expect for a decreasing oxygen abundance radial gradient. However T_{eff}, could also be increasing with radius. The excitation plots alone cannot distinguish between branch choice on the R23 relation, but may be instructive as a whole set for interpreting our results. We discuss these plots in Section 5.5.4.
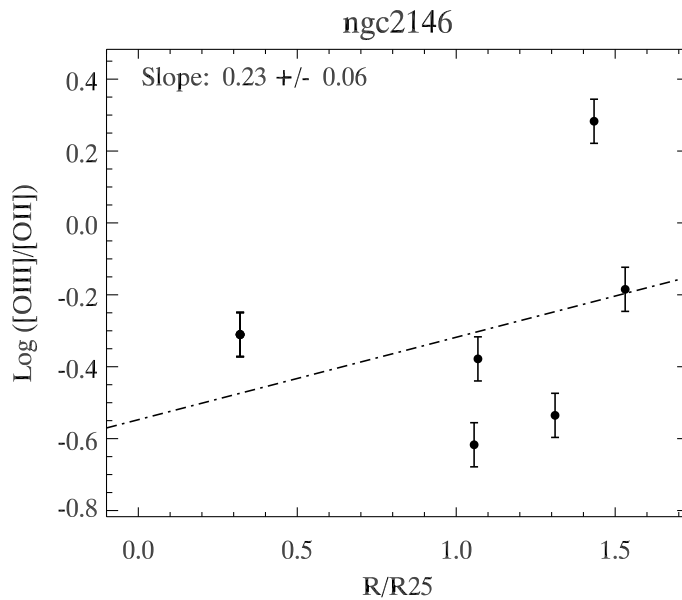
Figure 5.42. Radial dependence of the excitation diagnostic: NGC 2146. The excitation diagnostic, Log ([OIII]/[OII]), versus the galactocentric projected distances (in r/r_{25}) for HII regions in NGC 2146. The errors are propagated based on the line flux errors, which are $\sim 10\%$. Filled circles show HII regions that are determined to lie on the upper branch of the R23 relation, while open circles would indicate those HII regions that are determined to lie on the lower branch of the R23 relation (none, in this case). All of the HII regions in NGC 2146 are on the upper branch. The dashed-dotted line represents a linear-least-squares fit to the data, the slope (and its associated σ) of which is given in the upper left corner of the plot.

ID	RA	dec	r/r$_{25}$	R$_{proj}$	F$_{H\alpha}$	m$_R$	[OII]	[OIII]	O/H	Method
(1)	(2)	(3)	(4)	(5)	(6)	(7)	(8)	(9)	(10)	(11)
5	06 18 14.9	+78 19 48.4	1.5	13.12	4.13±.49	21.49±.08	226	147	8.80	M91/KD02
4	06 18 21.8	+78 19 38.2	1.4	12.94	1.11±.13	22.93±.19	243	466	8.56	M91/KD02
7	06 18 13.4	+78 20 18.1	1.3	11.02	1.94±.23	22.02±.10	447	130	8.57	M91/KD02
8	06 18 09.1	+78 21 02.4	1.1	9.91	2.98±.35	22.14±.11	328	137	8.70	M91/KD02
9	06 18 04.4	+78 21 23.3	1.1	11.13	1.66±.19	20.64±.07	267	64	8.82	M91/KD02
14	06 19 00.5	+78 20 44.1	0.5	8.68	3.57±.42	21.22±.08	***	***	8.61	PP04
13	06 18 51.0	+78 21 31.7	0.4	4.28	8.89±.06	19.48±.07	***	***	8.61	PP04
12	06 18 44.7	+78 21 50.4	0.4	3.40	28.14±.37	19.71±.07	***	***	8.54	PP04
15	06 18 52.5	+78 20 37.8	0.3	7.09	4.44±.53	22.94±.19	161	79	8.92	M91/PP04

Table 5.4. HII Region properties for NGC 2146, sorted by r/r$_{25}$. (1) The slit mask ID for the HII region. (2) Right Ascension (J2000) in hours, minutes, seconds. (3) Declination (J2000) in degrees, minutes, seconds. (4) Projected distance from the 25th magnitude elliptical isophote. (5) Projected distance in kpc from the center of the galaxy. (6) Hα flux and associated error from MDM 2.4-m images in units of 10^{-15}ergs s^{-1} cm^{-2} (7) R$-$band apparent magnitude and associated error from MDM 2.4-m images in AB magnitudes. We use the 5σ limiting magnitude for a point source in each image when an HII region is undetected in the R$-$band(8) and (9) The reddening-corrected [OII] $\lambda\lambda$3727 and [OIII] λ4959 and λ5007 summed emission line strengths, relative to Hβ of 100. Reddening correction was done for case B recombination with T = 10000 K and n$_e$ = 100 cm^{-3}, where Hα/Hβ = 2.86 and Hγ/Hβ = 0.459. (10) The strong-line oxygen abundance is in 12+Log(O/H). The error associated with strong-line abundances is notoriously large, ranging from 0.2 to 0.35 dex, as discussed in Section 5.3. (11) The method used to obtain the strong line abundance, in most cases from the M91 calibration of the R23 relation described in Section 5.3, along with another method for breaking the known R23 degeneracy (KD02's iterative method, PP04 [NII]/Hα calibration from longslit (or GMOS) spectra, and comparison with published values of the oxygen abundance, all of which we discuss in Section 5.3.2). In a few cases (for just NGC 2146 and NGC 2782 the GMOS multi-slit spectra were red enough to obtain Hα and [NII] λ6583, but not the blue lines) we used the [NII]/Hα method from PP04 on the Gemini spectra.
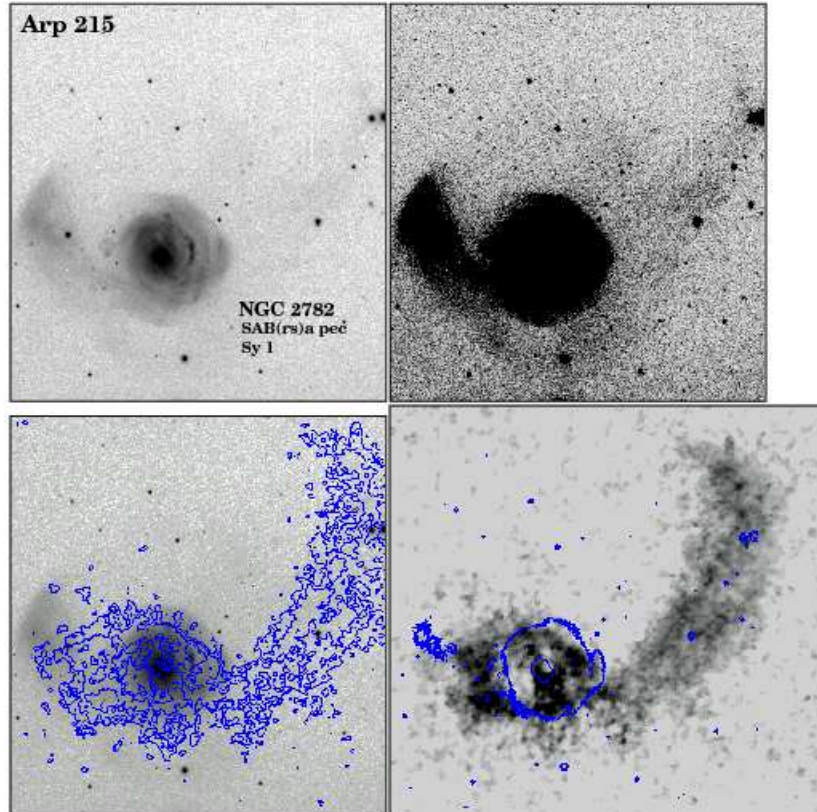
Figure 5.43. HI column density contours: NGC 2782. Neutral hydrogen column density contours taken directly from the HI Rogues catalog. Original VLA B+C+D-array data from Smith (1994). The resolution of the HI synthesis map is $9.4'' \times 8.7''$ and the contours are 4.0×10^{20} cm^{-2} $\times 2^n$. Top left and right: Optical B-band image of NGC 2782, with different stretches. Bottom left: B-band image + HI contours. Bottom right: HI data for NGC 2782 with optical contours.

5.4.2   NGC 2782

NGC 2782 is classified as a minor merger in the HI Rogues catalog, with a one-sided HI tail on the opposite side of an extension of optical emission. The HII regions are located within this HI tail, with column densities between 10^{19-20} cm^{-2} at the positions of the outermost HII regions. The tail contains 1.4×10^9 M$_\odot$ or $\sim 40\%$ of the galaxy's HI mass and is noted to consist of ~ 10 dwarf galaxy-sized clumps of $\sim 10^8$M$_\odot$. The basic properties of NGC2782 can be reproduced with the collision of two disk galaxies with a 1:4 mass ratio (Smith, 1994).

The three HII regions in the extended tidal tail of NGC 2782 (regions 1, 2, and 3) have the same oxygen abundance as the two HII regions closer to the center of the galaxy (regions 4 and 6), of 12 + Log (O/H) ~ 8.6. To break the degeneracy

ID	RA	dec	r/r_{25}	R_{proj}	$F_{H\alpha}$	m_R	[OII]	[OIII]	O/H	Method
(1)	(2)	(3)	(4)	(5)	(6)	(7)	(8)	(9)	(10)	(11)
1	09 13 50.9	+40 08 16.4	2.6	33.51	0.44±.05	23.07±.30	391	80	8.66	M91/PP04
2	09 13 51.2	+40 08 06.8	2.5	32.14	1.71±.20	22.46±.19	338	84	8.72	M91/PP04
3	09 13 52.3	+40 07 46.2	2.2	28.59	0.44±.05	>23.72±.36	462	112	8.56	M91/PP04
4	09 13 58.8	+40 06 08.8	1.2	15.00	0.28±.03	>23.72±.36	***	***	8.55	PP04
6	09 14 01.4	+40 06 36.3	0.6	7.99	1.40±.16	21.96±.13	***	***	8.47	PP04

Table 5.5. HII Region Properties: NGC2782. Same as Table 5.4, for NGC 2782

of the R23 relation for the outer HII regions, we use the M91/PP04 method which indicates that Region 2 is on the upper branch. Given the close proximity of regions 1 and 3, we assume that they also lie on the upper branch of the R23 calibration. Regions 4 and 6 lie on the edge of the GMOS CCD, and we are able to use only the N2 index of PP04 to get rough estimates of their oxygen abundances, which are roughly consistent with the values of Moustakas & Kennicutt (2006) from the central nebular SDSS spectrum that give 12 + Log (O/H) = 8.80. The excitation plot for the 3 outer HII regions of NGC 2782 shows no radial trend either way, since the HII regions are so close in proximity and values of r/r25.
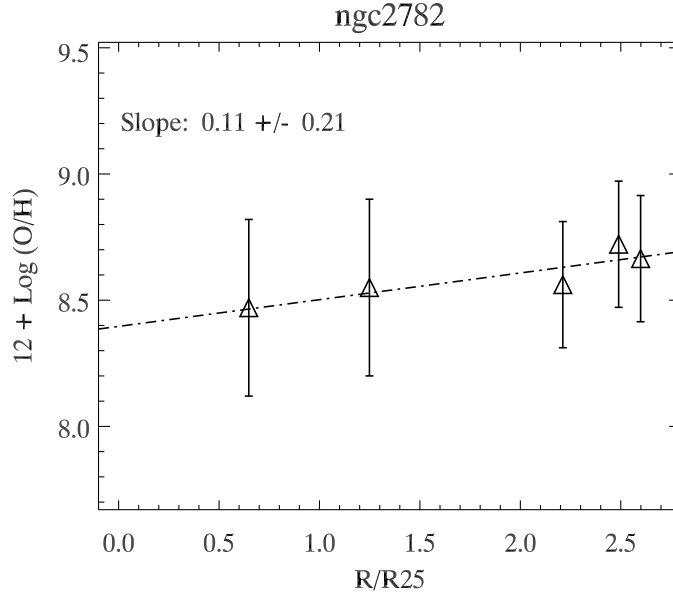

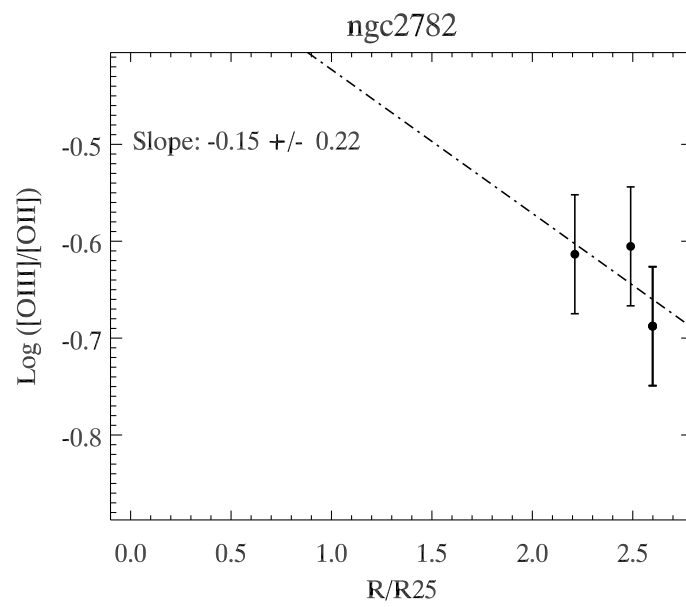**Figure 5.44.** Radial oxygen abundance gradient: NGC 2782. Same as Figure 5.41 for NGC 2782.

Figure 5.45. Radial dependence of the excitation diagnostic: NGC 2782. Same as Figure 5.42 for NGC 2782.

5.4.3 NGC 3227

The NGC 3226/7 system is classified as an interacting double system in which only one of the galaxies is gas-rich in the HI rogues catalog. NGC3227 is the gas-rich galaxy and also a nearby Seyfert (Mundell, 2001). HI tails extend 30 kpc to the south and 70 kpc to the north, beyond the region shown in our optical images. The total HI mass of the system is 2.0×10^9 $M_\odot$, with $\sim 5.5 \times 10^8$ $M_\odot$ of this mass located in the plumes. HII regions 24 and 25 are found within a cloud of HI that is thought to be a dwarf galaxy, while the outermost HII regions are found in outer lower density gas with column densities of a few $\times 10^{19}$ cm^{-2}.

HII regions 10 and 12 are associated with the early-type galaxy NGC 3226, while the rest of the HII regions in this system appear to be associated with NGC 3227. r_{25} for this particular system was very difficult to obtain, given the overlap of the isophotes of the two merging galaxies. Instead of fitting r_{25} for each galaxy, we fit r_{25} for both galaxies together, which somewhat downplays the extended star formation in this system. In a by-eye fit of r_{25} to NGC 3227 alone, Region 5 appears to lie at r/r_{25} closer to 1.5, and regions 24 and 25 are probably both further outside of r_{25}. Nonetheless, within the uncertainties, the outlying HII regions of this system appear to be about as oxygen-rich as those closer to the center of the system. We also note that the 2 HII regions in the gas-poor NGC 3226 appear to have roughly the same abundance as those within, and just outside of NGC 3227. Like NGC 2146, this galaxy shows an increasing trend of increasing Log ([OIII]/[OII]) with radius.

ID	RA	dec	r/r_{25}	R_{proj}	$F_{H\alpha}$	m_R	[OII]	[OIII]	O/H	Method
(1)	(2)	(3)	(4)	(5)	(6)	(7)	(8)	(9)	(10)	(11)
5	10 23 35.1	+19 53 07.9	1.1	9.08	0.57±.06	22.75±.16	402	115	8.63	M91/KD02
24	10 23 25.2	+19 51 44.4	1.0	7.95	7.21±.86	20.61±.07	330	141	8.69	M91/lit
25	10 23 26.0	+19 51 40.8	0.9	7.57	1.28±.15	22.13±.10	484	127	8.53	M91/lit
10	10 23 26.4	+19 54 14.5	0.5	10.04	0.87±.10	20.93±.07	461	85	8.58	M91/lit
12	10 23 26.1	+19 54 01.9	0.5	9.03	0.93±.11	19.45±.07	446	124	8.57	M91/lit
22	10 23 32.9	+19 51 54.3	0.4	7.39	1.42±.17	21.15±.07	234	50	8.87	M91/lit
15	10 23 26.4	+19 52 54.2	0.3	3.83	1.94±.23	22.12±.10	182	33	8.94	M91/lit

Table 5.6. HII Region Properties: NGC3227. Same as Table 5.4, for NGC 3227.

Figure 5.46. Neutral hydrogen column density contours for NGC 3227 taken directly from the HI Rogues catalog. Original VLA D-array data from Mundell (2001). The resolution of the HI synthesis map is $80'' \times 47''$ and the contours are 1.0×10^{19} cm^{-2} $\times 2^n$. Left: B-band images of NGC 3226/7. Right: B-band image + HI contours
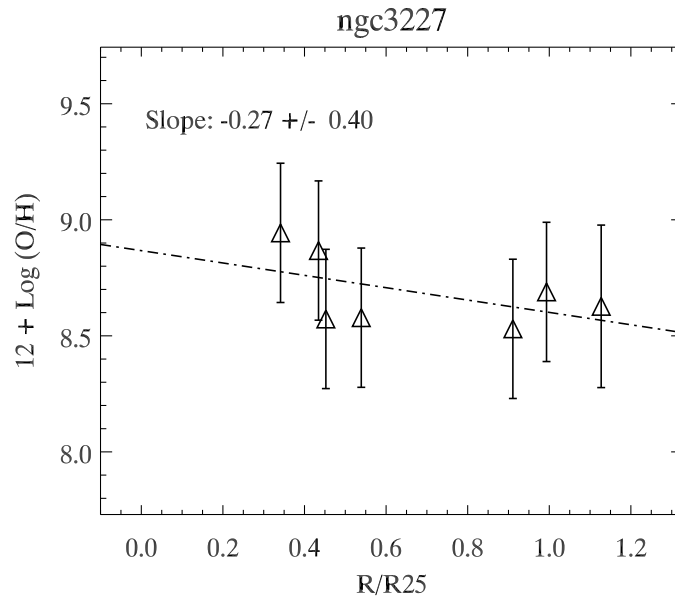
Figure 5.47. Radial oxygen abundance gradient: NGC 3227. Same as Figure 5.41 for NGC 3227.

Figure 5.48. Radial dependence of the excitation diagnostic: NGC 3227. Same as Figure 5.42 for NGC 3227.

Figure 5.49. Neutral hydrogen column density contours for NGC 3239, taken directly from the HI Rogues catalog. Original VLA D-array data from Iyer et al. (2001). The resolution of the HI synthesis map is $64.3'' \times 54.6''$ and the contours are 5.0×10^{18} cm^{-2} $\times 2^n$. Left: DSS image of NGC 3239. Right: DSS image + HI contours.

5.4.4 NGC 3239

NGC 3239 is classified as an interacting double in which both of the galaxies are HI rich with two HI tails according to the HI rogues catalog (Iyer et al., 2001). In the direction of the extended arm of HII regions shown in our optical images, the gas does not extend to a significantly larger radii, though there is a large HI feature on the opposite side of the galaxy. The outermost HII regions lie in gas that has a column density of 10^{20} cm^{-2}. The HI mass of this galaxy is 1.2×10^9 M$_\odot$ (Huchtmeier & Richter, 1989).

Within the uncertainties, the 12 HII regions of this galaxy have the same oxygen abundance, 12 + Log (O/H) $\sim$ 8.6. In the central parts of the galaxy we break the R23 degeneracy using integrated emission line strengths from the SDSS nebular spectrum published in the online catalog of Moustakas & Kennicutt (2006) which shows this galaxy to be on the upper branch. For Region 5, the furthest from the center, we resort to the KD02 iterative method to break the degeneracy, which places this HII region on the R23 upper branch as well. NGC 3239 shows no trend of Log ([OIII]/[OII]) with radius.
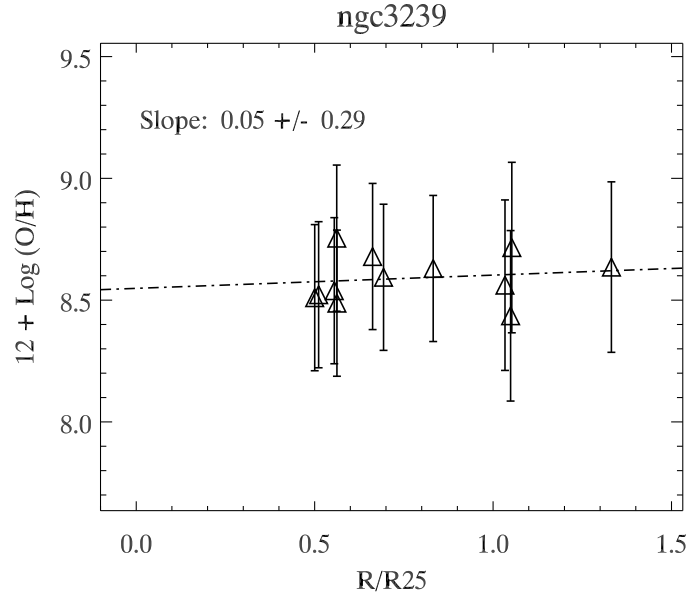
Figure 5.50. Radial oxygen abundance gradient: NGC 3239. Same as Figure 5.41 for NGC 3239.

ID	RA	dec	r/r$_{25}$	R$_{proj}$	F$_{H\alpha}$	m$_R$	[OII]	[OIII]	O/H	Method
(1)	(2)	(3)	(4)	(5)	(6)	(7)	(8)	(9)	(10)	(11)
4	10 25 09.4	+17 07 19.9	1.3	5.23	1.10±.13	21.69±.08	360	172	8.64	M91/KD02
5	10 24 56.2	+17 10 13.3	1.1	5.17	0.27±.03	23.54±.21	363	47	8.72	M91/KD02
8	10 24 57.1	+17 10 20.4	1.0	4.88	0.88±.10	23.20±.17	474	296	8.44	M91/KD02
13	10 25 07.3	+17 07 41.1	1.0	3.92	0.89±.10	22.48±.10	280	400	8.56	M91/KD02
24	10 25 03.0	+17 07 52.6	0.8	3.19	2.65±.31	21.77±.08	262	324	8.63	M91/lit
14	10 25 03.3	+17 08 05.8	0.7	2.65	0.35±.04	23.15±.16	404	166	8.59	M91/lit
18	10 24 57.0	+17 09 05.1	0.7	4.13	0.59±.07	22.97±.14	394	43	8.68	M91/lit
15	10 25 00.8	+17 08 23.9	0.6	2.73	3.58±.42	20.77±.07	361	389	8.49	M91/lit
22	10 25 02.7	+17 10 00.8	0.6	2.13	2.53±.30	21.07±.07	204	231	8.75	M91/lit
17	10 24 58.8	+17 09 29.3	0.6	3.15	2.63±.31	20.94±.07	348	331	8.54	M91/lit
21	10 25 06.8	+17 09 57.5	0.5	2.29	3.77±.45	20.84±.07	455	189	8.52	M91/lit
19	10 25 00.2	+17 09 38.7	0.5	2.53	3.01±.36	20.75±.07	446	215	8.51	M91/lit

Table 5.7. HII Region Properties: NGC3239. Same as Table 5.4, for NGC 3239

171
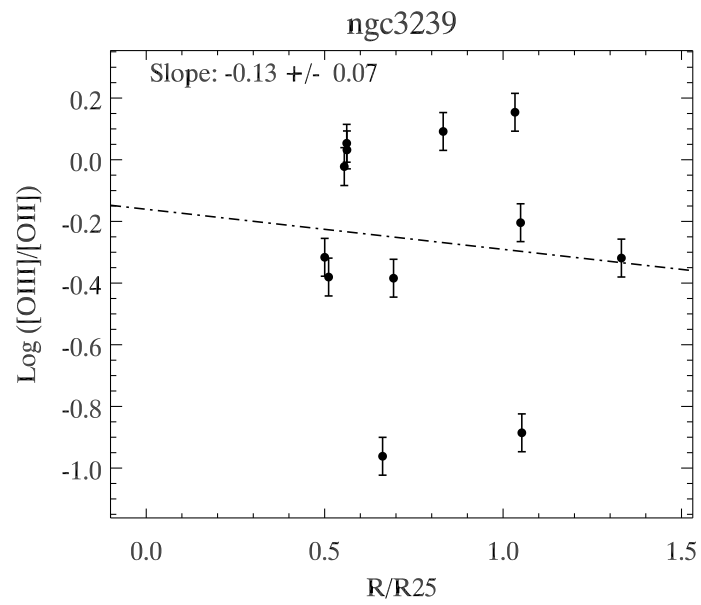
Figure 5.51. Radial dependence of the excitation diagnostic: NGC 3239. Same as Figure 5.42 for NGC 3239.

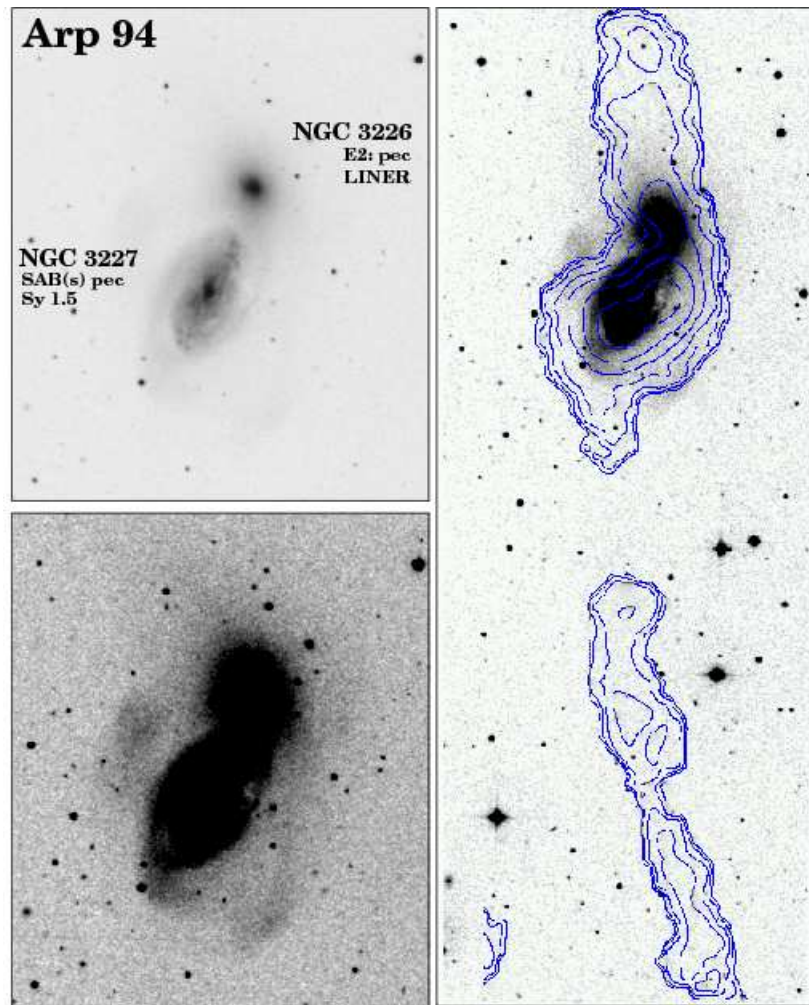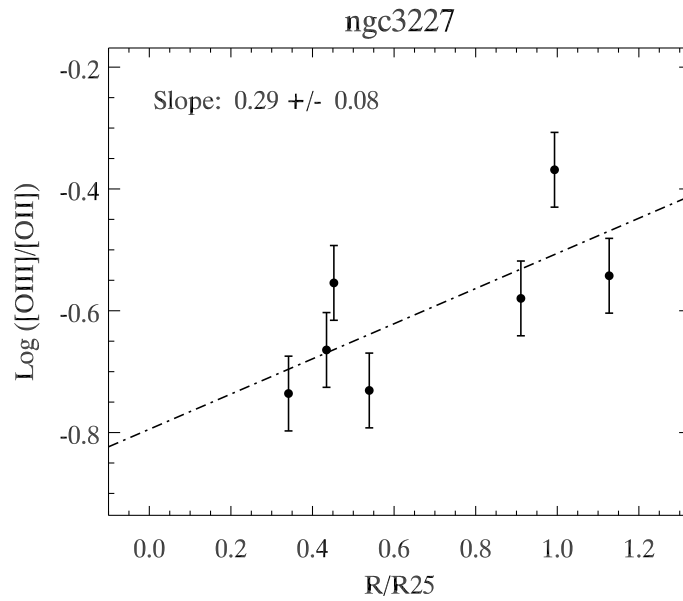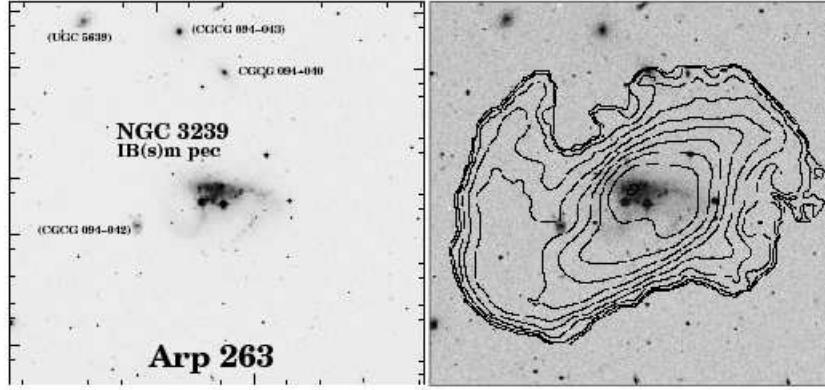**Figure 5.52.** Neutral hydrogen column density contours for NGC 3310, taken directly from the HI Rogues catalog. Original WSRT data from Iyer et al. (2001). The resolution of the HI synthesis map is $20'' \times 20''$ (upper panel) and $60'' \times 60''$ (lower panels). The contours are 2.0×10^{20} cm^{-2} $\times 2^n$ (upper panel) and 2.0×10^{19} cm^{-2} $\times 2^n$ (lower panels). Top left: DSS image of NGC 3310. Top right: Deeper B-band image of NGC 3310, with HI contours. Bottom left: DSS image + HI contours. Bottom right: HI data for NGC 3310.

5.4.5 NGC 3310

NGC 3310 is classified as a minor merger in the HI rogues catalog. The gas disk of the main galaxy shows signs of perturbation from its high velocity dispersion and tails that extend 23 kpc to the north and 51 kpc to the south of the galaxy (Kregel & Sancisi, 2001). The HI mass of the entire system is 5.2×10^9 M$_\odot$, with 4.2 and 5.0×10^8 M$_\odot$ in the northern and southern tails respectively. Only the northern tail was imaged in Hα and contains the HII regions presented here. The peak column densities in the northern tail are 10^{20-21} cm^{-2}.

Most of the 11 HII regions in this galaxy lie in an extended arm-like structure that extends to the northwest of NGC 3310, and all have the same oxygen enrichment of

12 + Log (O/H) ~ 8.6. According to the integrated emission line fluxes of Moustakas & Kennicutt (2006) for the central nebular spectrum of this galaxy, it is on the upper branch of the R23 relation. Additionally, we have measured the N2 index of Region 12 from its MDM 2.4-m longslit spectrum, and find that it is on the upper branch of the R23 relation as well. Because of their physical proximity, we assume the other outlying HII regions (11, 7, 16, and 14) are on the upper branch of the R23 relation. NGC 3310 shows a decreasing trend of Log ([OIII]/[OII]) with radius, which is counter to what we expect for declining oxygen abundance gradients. Our interpretation of this trend is that T_{eff} is decreasing with radius, while the abundance stays constant (consistent with the flat radial abundance gradient).
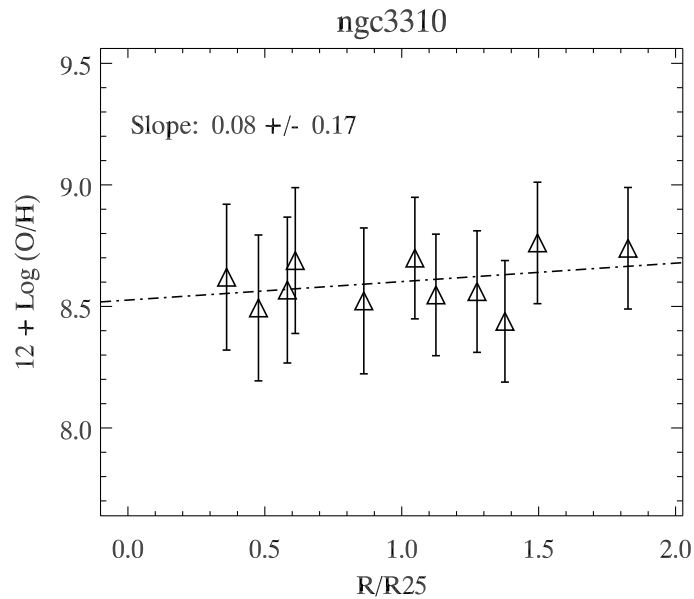
Figure 5.53. Radial oxygen abundance gradient: NGC 3310. Same as Figure 5.41 for NGC 3310.
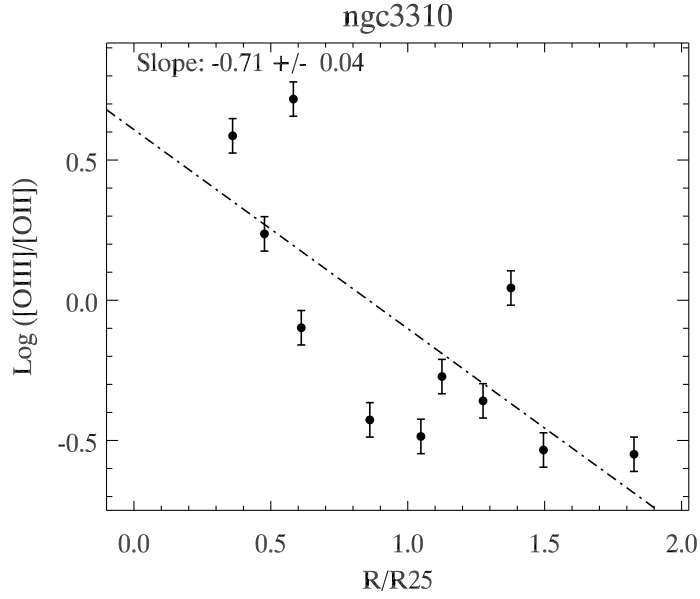
Figure 5.54. Radial dependence of the excitation diagnostic: NGC 3310. Same as Figure 5.42 for NGC 3310.

ID	RA	dec	r/r$_{25}$	R$_{proj}$	F$_{H\alpha}$	m$_R$	[OII]	[OIII]	O/H	Method
(1)	(2)	(3)	(4)	(5)	(6)	(7)	(8)	(9)	(10)	(11)
11	10 38 27.2	+53 31 58.6	1.8	16.54	0.06±.00	>23.79±.35	319	90	8.74	M91/PP04
7	10 38 31.0	+53 31 46.5	1.5	13.54	0.33±.03	23.01±.19	302	88	8.76	M91/PP04
16	10 38 35.1	+53 32 03.9	1.4	12.46	0.51±.06	22.83±.17	388	429	8.44	M91/PP04
12	10 38 32.4	+53 31 25.7	1.3	11.54	1.40±.16	21.54±.08	421	184	8.56	M91/PP04
14	10 38 33.8	+53 31 16.7	1.1	10.19	1.43±.17	22.39±.12	411	220	8.55	M91/PP04
15	10 38 34.6	+53 31 12.3	1.0	9.49	2.40±.28	21.74±.09	341	111	8.70	M91/PP04
18	10 38 36.8	+53 31 06.1	0.9	7.80	1.30±.15	21.90±.09	464	173	8.52	M91/lit
21	10 38 39.6	+53 30 55.4	0.6	5.53	2.18±.26	20.84±.07	275	219	8.69	M91/lit
24	10 38 41.3	+53 31 01.7	0.6	5.27	6.52±.78	21.06±.07	127	664	8.57	M91/lit
26	10 38 44.9	+53 30 57.2	0.5	4.34	5.85±.70	21.15±.07	288	497	8.49	M91/lit
25	10 38 43.1	+53 30 43.8	0.4	3.27	8.34±.00	20.75±.07	140	540	8.62	M91/lit

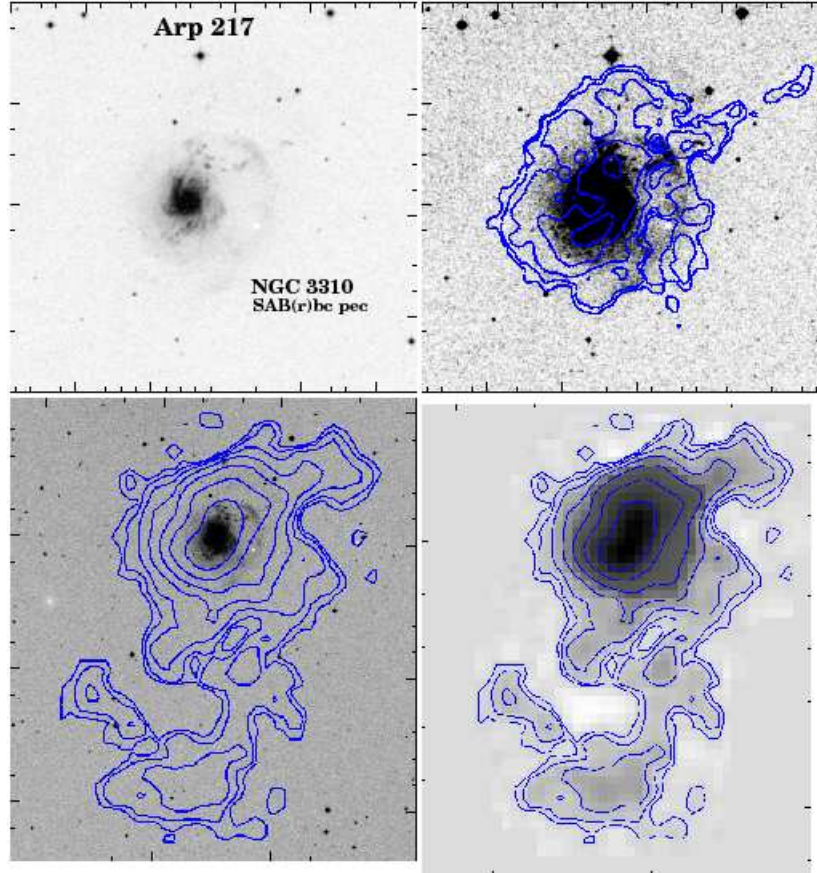**Table 5.8.** HII Region Properties: NGC3310. Same as Table 5.4, for NGC 3310
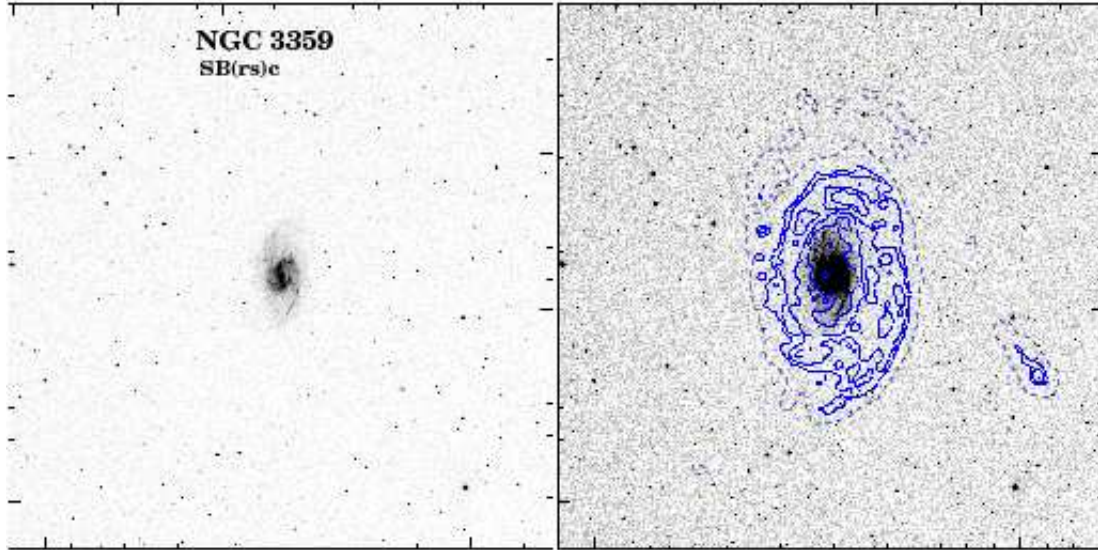
Figure 5.55. Neutral hydrogen column density contours for NGC 3359, taken directly from the HI Rogues catalog. Original WSRT data from Boonyasait et al. (2001). The resolution of the HI synthesis map is $30'' \times 30''$ and the contours are 3.0×10^{19} cm$^{-2} \times 2^n$. Left: DSS image of NGC 3359. Right: DSS + HI contours.

5.4.6 NGC 3359

NGC 3359 is categorized as a galaxy with a detached HI cloud in the HI rogues catalog, but from the deeper contours it appears that the cloud may be a further extension of the extended HI spiral arm to the north of the galaxy (Boonyasait et al., 2001). The HII regions we study here are located within the extended gaseous envelope of the galaxy, but not this far extended arm. NGC3359 contains 4.5×10^9 M$_\odot$ in neutral hydrogen gas.

The 16 HII regions we consider in NGC 3359 all have similar oxygen abundances near 12 + Log (O/H) $\sim$ 8.6. Martin & Roy (1995) report oxygen abundances for 77 HII regions within r$_{25}$ for this galaxy, and find a steeply decreasing oxygen gradient in the centermost part of the galaxy, out to $\sim$0.35 r$_{25}$, and then a flat oxygen abundance gradient that levels off at 12 + Log (O/H) = 8.6 from 0.35 to 0.9 r$_{25}$. Our results are consistent with this flat gradient, and indicate that it extends to even larger radii, out to 1.5 r$_{25}$. NGC 3359 shows no trend of Log ([OIII]/[OII]) with radius.
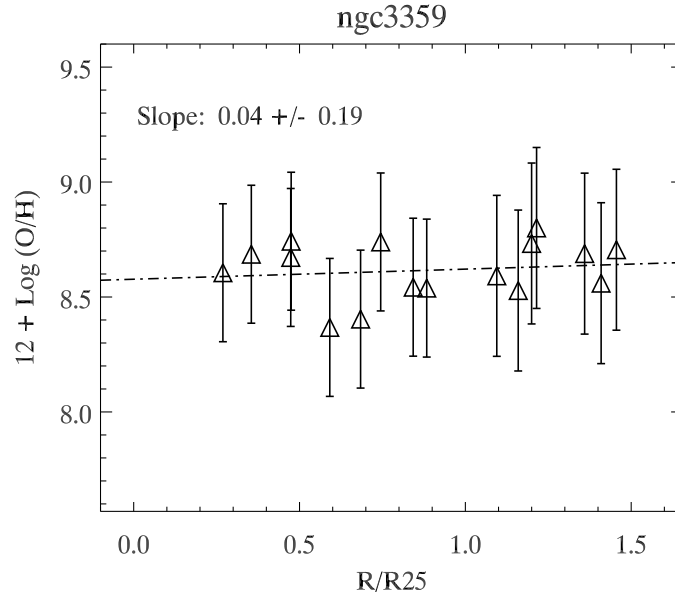
Figure 5.56. Radial oxygen abundance gradient: NGC 3359. Same as Figure 5.41 for NGC 3359.

ID	RA	dec	r/r$_{25}$	R$_{proj}$	F$_{H\alpha}$	m$_R$	[OII]	[OIII]	O/H	Method
(1)	(2)	(3)	(4)	(5)	(6)	(7)	(8)	(9)	(10)	(11)
6	10 46 10.6	+63 14 26.8	1.5	16.65	0.26±.02	>23.16±.36	269	209	8.71	M91/KD02
12	10 46 30.9	+63 16 49.3	1.4	18.05	0.55±.06	22.32±.19	434	164	8.56	M91/KD02
11	10 46 26.6	+63 16 28.4	1.4	17.08	0.95±.11	22.43±.21	206	320	8.69	M91/KD02
7	10 46 20.1	+63 15 24.0	1.2	14.48	0.45±.05	>23.16±.36	291	51	8.80	M91/KD02
8	10 46 24.0	+63 15 48.2	1.2	14.70	0.41±.04	>23.16±.36	230	227	8.73	M91/KD02
13	10 46 37.9	+63 16 20.2	1.2	15.09	1.85±.22	21.54±.11	454	182	8.53	M91/KD02
14	10 46 39.6	+63 16 10.3	1.1	14.28	7.59±.91	20.75±.08	158	555	8.59	M91/KD02
17	10 46 26.7	+63 15 05.4	0.9	10.74	3.99±.47	21.18±.09	425	213	8.54	M91/lit
16	10 46 37.6	+63 15 32.4	0.8	10.96	6.95±.83	20.94±.08	221	525	8.54	M91/lit
19	10 46 51.1	+63 14 13.9	0.7	8.86	0.78±0.08	>23.16±.36	210	244	8.74	M91/lit
28	10 46 28.6	+63 12 06.9	0.7	8.60	12.08±.44	19.74±.07	576	299	8.40	M91/lit
20	10 46 44.8	+63 14 38.1	0.6	7.51	13.90±.66	20.19±.07	247	867	8.37	M91/lit
27	10 46 31.1	+63 12 32.7	0.5	5.94	1.92±.22	>23.16±.36	276	145	8.74	M91/lit
23	10 46 28.6	+63 13 38.1	0.5	5.40	13.39±.60	20.27±.07	253	277	8.67	M91/lit
24	10 46 30.7	+63 13 22.2	0.4	4.06	9.76±.17	20.53±.07	207	323	8.69	M91/lit
25	10 46 42.8	+63 13 16.7	0.3	3.07	4.81±.57	20.78±.08	423	111	8.61	M91/lit

Table 5.9. HII Region Properties: NGC3359. Same as Table 5.4, for NGC 3359

**Figure 5.57.** Radial dependence of the excitation diagnostic: NGC 3359. Same as Figure 5.42 for NGC 3359.

Figure 5.58. Neutral hydrogen column density contours for NGC 3432, taken directly from the HI Rogues catalog. Original WSRT data from Swaters et al. (2002). The resolution of the HI synthesis map is $30'' \times 30''$ and the contours are 2.0×10^{20} cm^{-2} $\times$ 2^n. Left, center: DSS images of NGC 3432. Right: HI contours overlaid on DSS image.

5.4.7   NGC 3432

NGC 3432 is noted as a minor merger in the HI rogues catalog. It has a strong warp and a companion to the southwest corresponding to the side with the most dominant warp (Swaters et al., 2002). The total HI mass of the system is 6.0×10^9 M$_\odot$. The HII regions studied here are in the northern part of the galaxy's gaseous disk, with some of the outermost HII regions lying in gas at 4×10^{20} cm^{-2}.

The oxygen abundance of the central-disk HII region in NGC 3432 (Region 17) lies right on the turnover of the R23 relation, and is therefore uncertain at a level of 0.3 dex. Regions 7, 5, and 12 also lie near the turnover of the R23 relation, seen in Figure 5.33. Because we lack any additional information that would allow us to break the R23 degeneracy, we use the KD02 iterative method. Yet, the Z94 initial abundance estimates for 7, 5, and 12 lie in the dubious zone below $12 + \text{Log (O/H)}$ of 8.5. Therefore, it is possible that the KD02 method of breaking the degeneracy has failed in these cases. We tentatively adopt upper-branch values for regions 7, 5, and 12, and note that their lower-branch values, $12 + \text{Log (O/H)} \sim 8.1$, are also plausible despite adding significant scatter to the radial oxygen abundance gradient. Regions 6 and 14 lie more definitively on the upper branch of the R23 relation, according to the M91/KD02 method of breaking the degeneracy. Therefore, they are either slightly

offset from the other HII regions, or more significantly offset if the other HII regions (7, 5, and 12) instead lie on the lower branch. Assuming all HII regions in NGC 3432 are on the high-metallicity branch of R23, NGC 3432 appears to have a flat oxygen abundance gradient with a median value of 12 + Log (O/H) $\sim$ 8.5. Like NGC 3310, NGC 3432 shows a decreasing trend of Log ([OIII]/[OII]) with radius, we we interpret as being due to a constant abundance and a decreasing T_{eff} with radius.
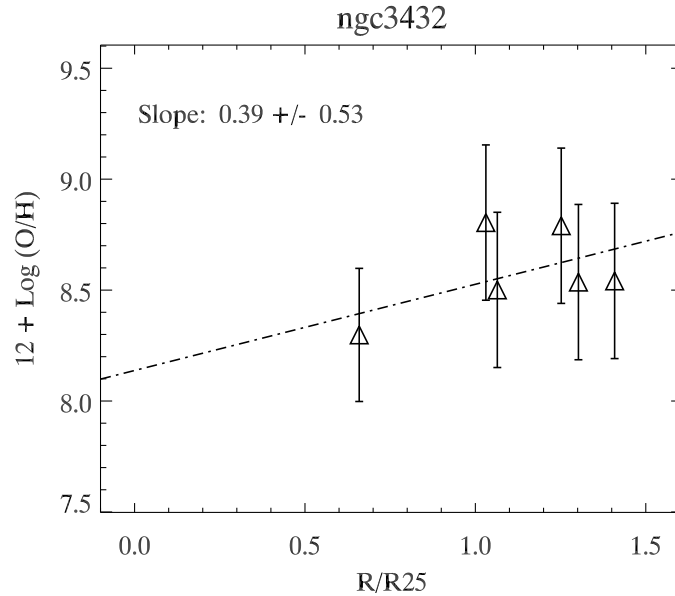
Figure 5.59. Radial oxygen abundance gradient: NGC 3432. Same as Figure 5.41 for NGC 3432.

ID	RA	dec	r/r$_{25}$	R$_{proj}$	F$_{H\alpha}$	m$_R$	[OII]	[OIII]	O/H	Method
(1)	(2)	(3)	(4)	(5)	(6)	(7)	(8)	(9)	(10)	(11)
7	10 52 47.2	+36 39 38.9	1.4	15.46	0.56±.06	23.77±.25	277	433	8.54	M91/KD02
5	10 52 43.4	+36 40 34.7	1.3	16.01	0.35±.04	23.47±.20	314	383	8.54	M91/KD02
6	10 52 43.6	+36 40 23.8	1.3	15.55	0.15±.02	23.81±.23	291	63	8.79	M91/KD02
12	10 52 42.1	+36 39 51.3	1.1	13.26	0.11±.01	>24.20±.36	269	514	8.50	M91/KD02
14	10 52 40.5	+36 39 52.2	1.0	12.56	0.78±.09	22.36±.10	111	297	8.80	M91/KD02
17	10 52 38.1	+36 38 46.9	0.7	8.21	0.36±.04	23.16±.16	288	695	8.30	M91/lit

Table 5.10. HII Region Properties: NGC3432. Same as Table 5.4, for NGC 3432
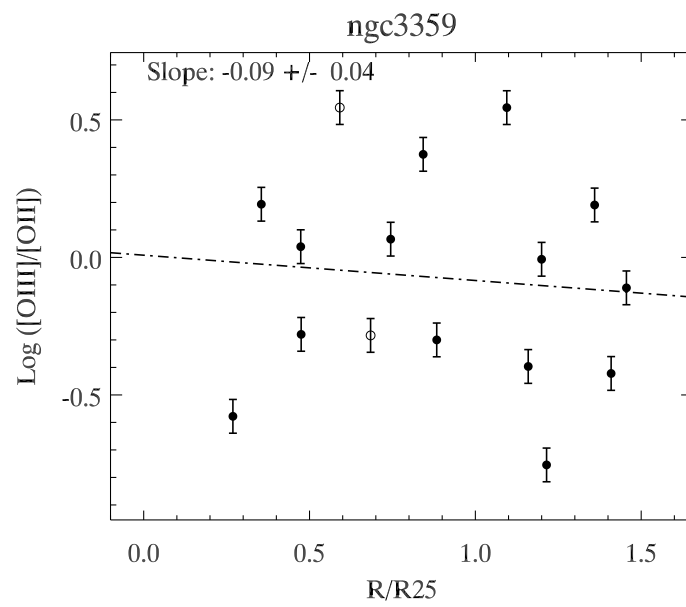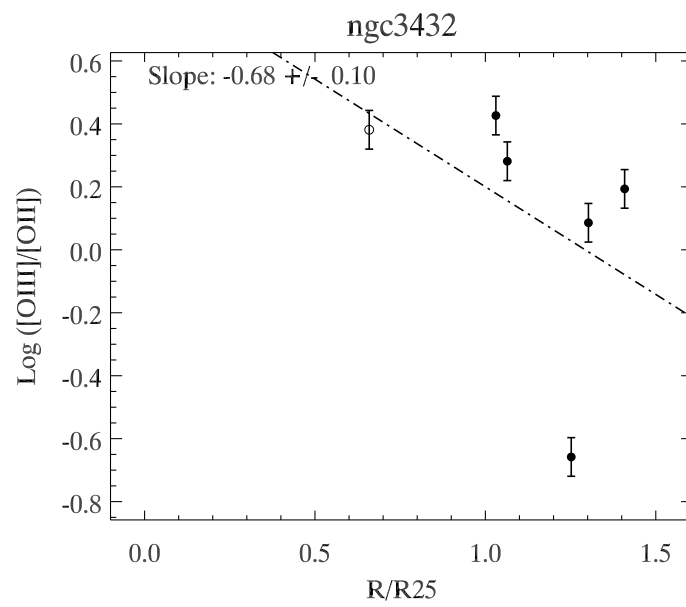
Figure 5.60. Radial dependence of the excitation diagnostic: NGC 3432. Same as Figure 5.42 for NGC 3432.
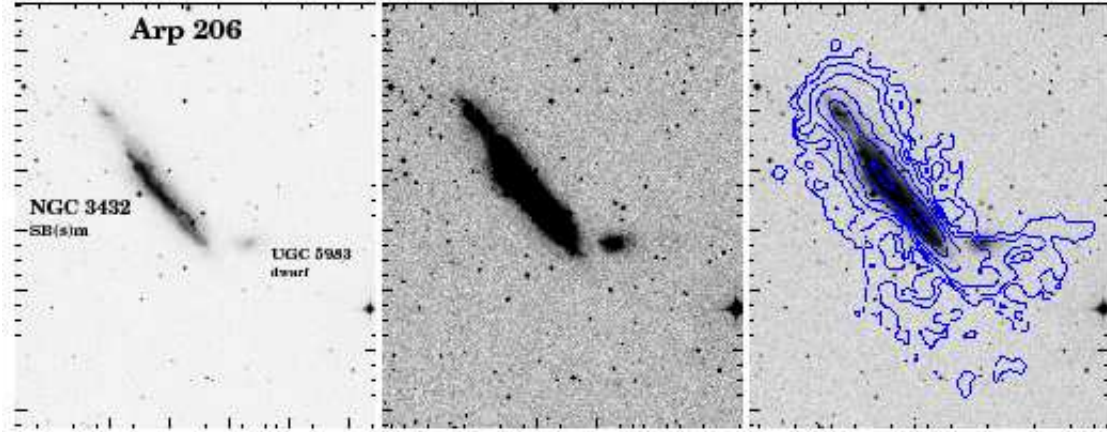
Figure 5.61. Neutral hydrogen column density contours for NGC 3718, taken directly from the HI Rogues catalog. Original WSRT data is from Verheijen & Sancisi (2001). The resolution of the HI synthesis map is $30'' \times 30''$ and the contours are 2.0×10^{20} cm$^{-2} \times 2^n$. Top: DSS images of NGC 3718. Bottom left: DSS image + HI contours. Bottom right: HI column density data.

5.4.8   NGC 3718

NGC 3718 is a galaxy located in the outer regions of the Ursa Major Cluster with a two-sided extreme HI warp (Verheijen & Sancisi, 2001). It has a total mass of 10^{10} M$_\odot$ in neutral hydrogen and a FWHM HI linewidth of 465 km s^{-1}. The HII regions studied here are generally not located in the highest column density gas along the warp, although that is where much of the new star formation appears to be concentrated.

All 9 HII regions presented here have abundances consistent with the mean of 12 + Log (O/H) $\sim$ 8.6. The central galactic HII regions are determined to lie on the upper branch of the R23 relation based on the integrated emission line fluxes from the nebular SDSS spectrum presented in the online catalog of Moustakas & Kennicutt (2006). We use the longslit spectrum of Region 15 and the PP04 method to place it

on the upper branch, and the KD02 method to place regions 4 and 6, which both lie at a projected distance of ~20 kpc from Region 15, on the upper branch. NGC 3718 shows no trend of Log ([OIII]/[OII]) with radius.
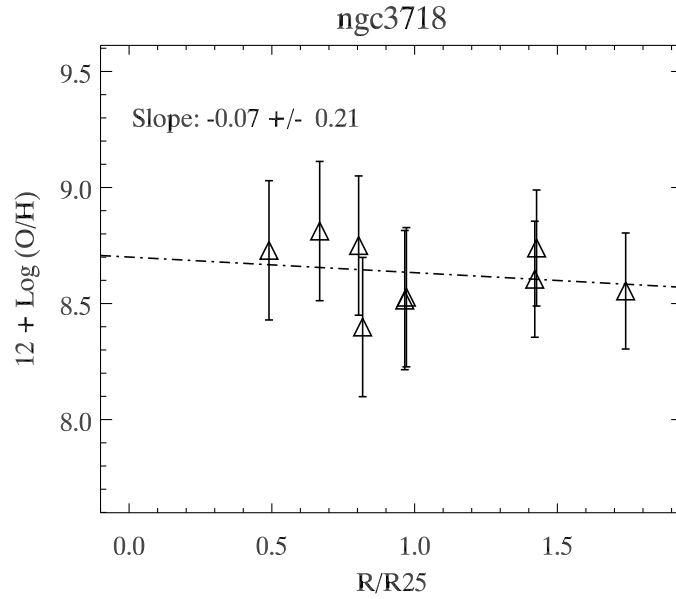
Figure 5.62. Radial oxygen abundance gradient: NGC 3718. Same as Figure 5.41 for NGC 3718.
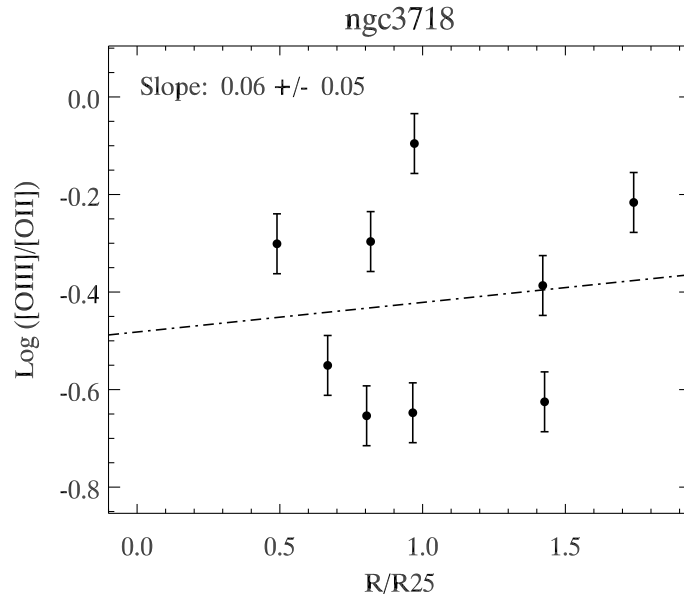
Figure 5.63. Radial dependence of the excitation diagnostic: NGC 3718. Same as Figure 5.42 for NGC 3718.

ID	RA	dec	r/r$_{25}$	R$_{proj}$	F$_{H\alpha}$	m$_R$	[OII]	[OIII]	O/H	Method
(1)	(2)	(3)	(4)	(5)	(6)	(7)	(8)	(9)	(10)	(11)
4	11 32 48.3	+53 06 55.5	1.7	17.16	0.17±.02	>23.60±.36	393	239	8.55	M91/KD02
6	11 32 48.3	+53 05 56.8	1.4	13.46	0.31±.03	>23.60±.36	327	77	8.74	M91/KD02
15	11 32 51.5	+53 02 06.3	1.4	15.65	2.50±.30	21.58±.11	394	162	8.60	M91/PP04
12	11 32 45.7	+53 02 33.7	1.0	10.96	1.16±.13	22.72±.25	378	303	8.53	M91/lit
11	11 32 47.2	+53 03 22.4	1.0	9.72	0.55±.06	>23.60±.36	506	114	8.51	M91/lit
8	11 32 45.2	+53 04 07.1	0.8	7.58	0.28±.03	23.01±.32	529	267	8.40	M91/lit
7	11 32 38.9	+53 05 43.0	0.8	8.56	0.29±.03	>23.60±.36	322	71	8.75	M91/lit
19	11 32 41.9	+53 02 54.6	0.7	7.73	1.81±.21	21.54±.11	266	74	8.81	M91/lit
20	11 32 40.0	+53 03 12.0	0.5	5.71	0.96±.11	>23.60±.36	291	145	8.73	M91/lit

Table 5.11. HII Region Properties: NGC3718. Same as Table 5.4, for NGC 3718
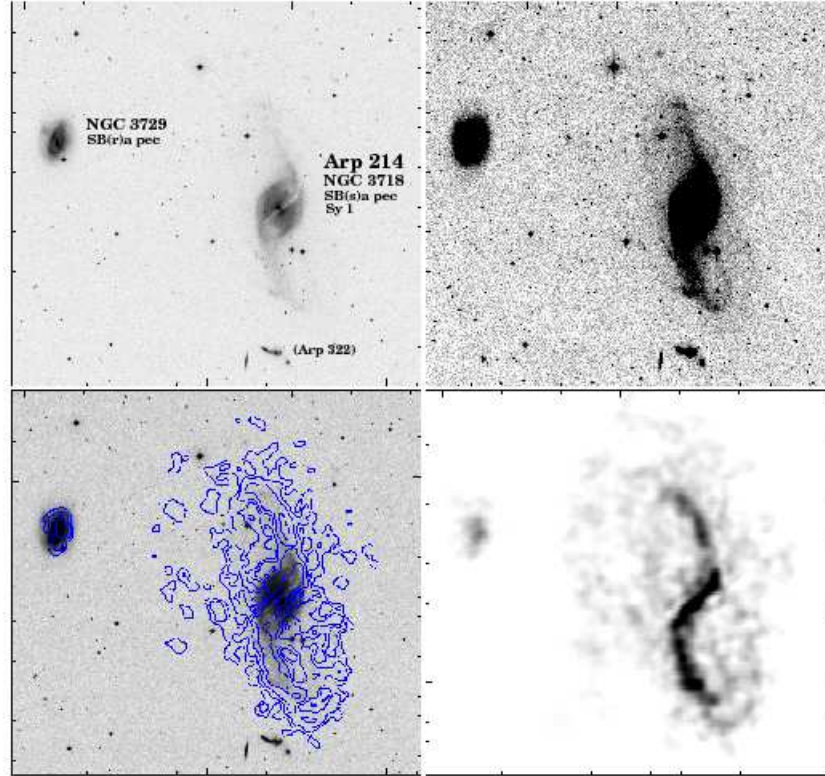
Figure 5.64. Neutral hydrogen column density contours for NGC 3893, taken directly from the HI Rogues catalog. Original WSRT data is from Verheijen & Sancisi (2001). The resolution of the HI synthesis map is $30'' \times 30''$ and the contours are 1.0×10^{20} cm$^{-2} \times 2^n$. Top: DSS images of NGC 3893. Bottom left: DSS image + HI contours. Bottom right: HI column density data with optical contours.

5.4.9 NGC 3893

NGC 3893 is classified as an M51-type minor merger and is located in the Ursa Major Cluster (Verheijen & Sancisi, 2001). The interacting companion (NGC3896) and NGC3893 appear to be embedded in a common envelope of HI. The HII regions studied here are embedded in high column density gas in the inner part of the large envelope and appear to trace an extended, low-surface brightness spiral arm. The HI mass of this system is 6×10^9 M$_\odot$.

All 8 of the HII regions we study in NGC 3893 have similar oxygen abundances, near the mean of ~ 8.75. We break the R23 degeneracy with the N2 index of PP04 for the outermost HII region (number 7), and then assume the other outlying HII regions are also on the upper branch, which is consistent with the results of the M91/KD02

iterative method as well. For the 3 inner HII regions in this galaxy, we use the integrated emission line fluxes from the central nebular spectrum of NGC 3893 as published in the online catalog ofMoustakas & Kennicutt (2006) to place them on the upper branch as well. NGC 3893 shows a weakly increasing Log ([OIII]/[OII]) with radius, mostly due to the most outlying HII region in this galaxy, region 7. Since we find that the abundance of this HII region is on the upper branch of the R23 relation, the ionization source for this HII region must be a very hot O star. If instead our upper branch choices for the outlying HII regions of this galaxy are incorrect, then the high excitation at large radius could indicate a decreasing radial abundance gradient.
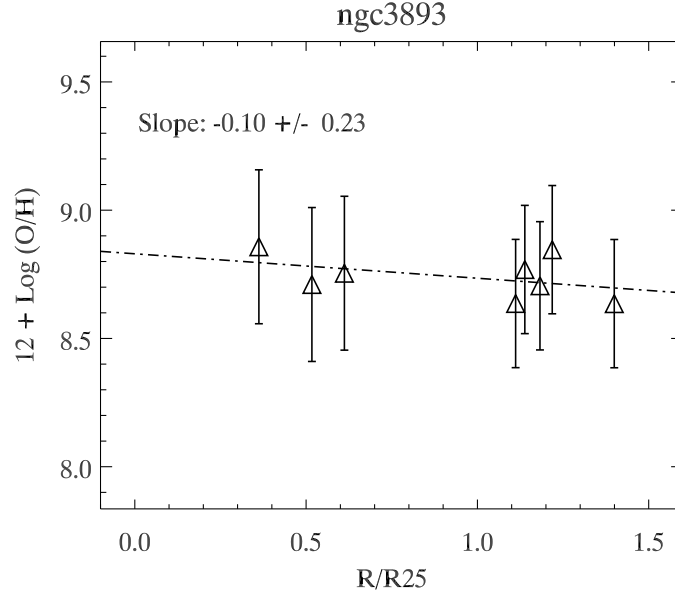
Figure 5.65. Radial oxygen abundance gradient: NGC 3893. Same as Figure 5.41 for NGC 3893.

ID	RA	dec	r/r$_{25}$	R$_{proj}$	F$_{H\alpha}$	m$_R$	[OII]	[OIII]	O/H	Method
(1)	(2)	(3)	(4)	(5)	(6)	(7)	(8)	(9)	(10)	(11)
7	11 48 41.2	+48 45 48.0	1.4	16.61	0.93±.11	22.73±.16	135	521	8.64	M91/PP04
10	11 48 46.3	+48 44 38.2	1.2	12.30	1.04±.12	22.65±.15	209	110	8.85	M91/PP04
13	11 48 48.1	+48 44 04.8	1.2	11.05	0.50±.06	23.30±.24	315	142	8.71	M91/PP04
15	11 48 48.5	+48 43 44.7	1.1	10.31	1.13±.13	22.72±.15	301	77	8.77	M91/PP04
19	11 48 49.8	+48 42 58.5	1.1	9.83	0.51±.06	23.68±.32	361	168	8.64	M91/PP04
21	11 48 41.5	+48 43 50.6	0.6	6.62	17.42±.09	19.79±.07	250	169	8.75	M91/lit
22	11 48 43.0	+48 43 12.4	0.5	4.73	11.47±.37	19.95±.07	260	214	8.71	M91/lit
25	11 48 41.9	+48 42 58.5	0.4	3.24	8.07±.96	20.10±.07	234	64	8.86	M91/lit

Table 5.12. HII Region Properties: NGC3893. Same as Table 5.4, for NGC 3893
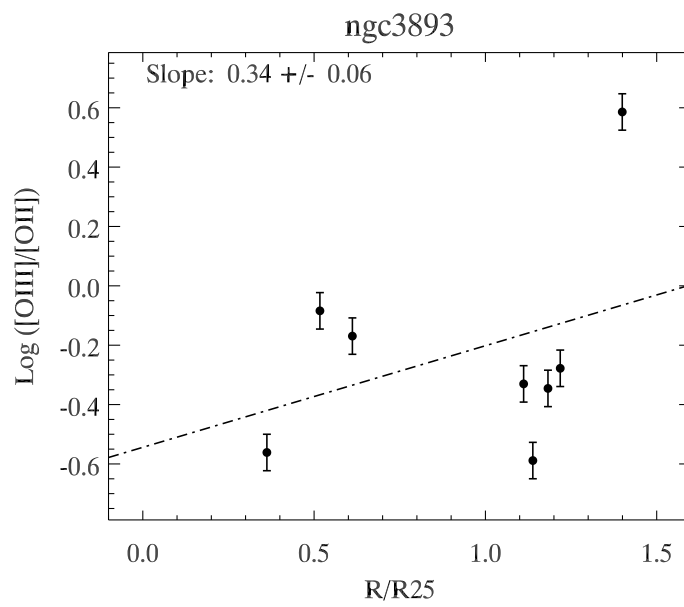
Figure 5.66. Radial dependence of the excitation diagnostic: NGC 3893. Same as Figure 5.42 for NGC 3893.
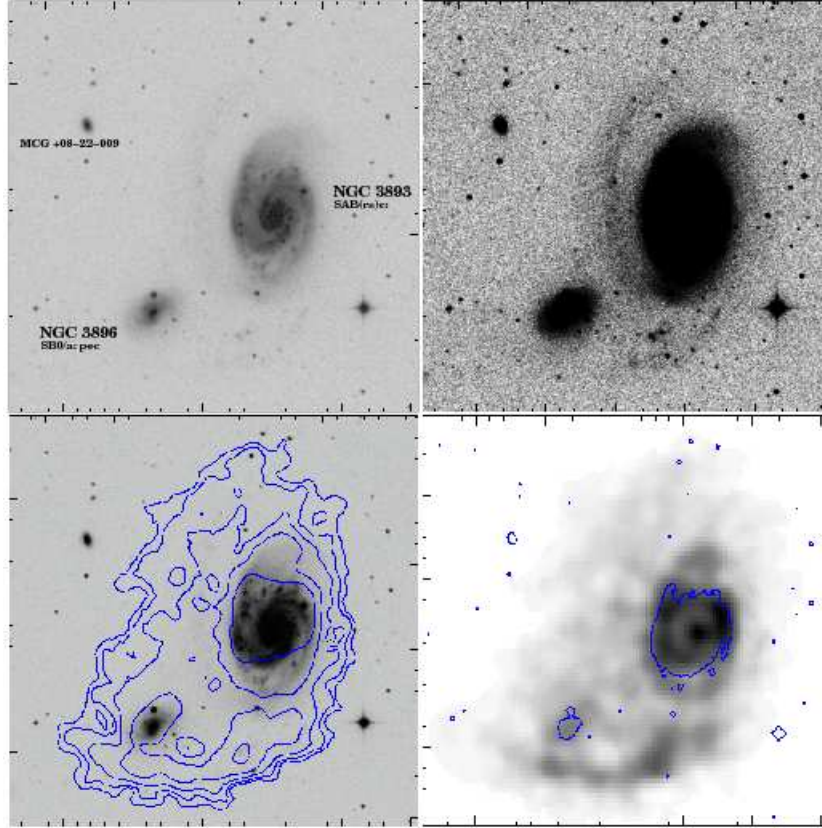
Figure 5.67. Neutral hydrogen column density contours for NGC 5774/5, taken directly from the HI Rogues catalog. Original VLA Cnb-Array data from Irwin (1994). The resolution of the HI synthesis map is $29'' \times 23''$ and the contours are 1.0×10^{20} cm$^{-2} \times 2^n$. Left: DSS image of NGC 5775 and NGC 5774. Right: DSS + HI contours.

5.4.10   NGC 5774/5

NGC 5774/5 is classified in the HI rogues catalog as an interacting double with no tails and an HI bridge joining the two gas-rich galaxies. HII regions in both galaxies and in the HI bridge were targeted in this study. The NGC 5774/5 system belongs to a small group of at least 6 galaxies and the gas in the bridge between the galaxies is thought to be transferring gas from NGC 5774 to NGC 5775 (Irwin, 1994). The HI masses of the galaxies are 5.4 and 9.1 $\times 10^9$ M$_\odot$ respectively.

The oxygen abundances of the HII regions in this system are all close to an average value of 12 + Log (O/H) $\sim$ 8.7. The central regions of NGC 5775 are perhaps slightly more oxygen-rich (though are roughly the same within the large errors) than the central regions of NGC 5774, and the gas between them (regions 1 and 4) lies at a level of $\sim$ 8.5. The oxygen abundances from the literature come from 10 HII regions in NGC 5774 (out to r_{25}) and 8 HII regions in 5775 that have measured N2 indices (Márquez et al., 2002). We place region 4 on the upper branch of the M91 R23 relation using its measured N2 index from our MDM longslit spectrum, and assume Region 1 also lies on the upper branch given its close proximity. Like NGC 2146, 3227, and 3893, NGC 5774 and NGC 5775 show a weakly increasing Log ([OIII]/[OII]) with radius.
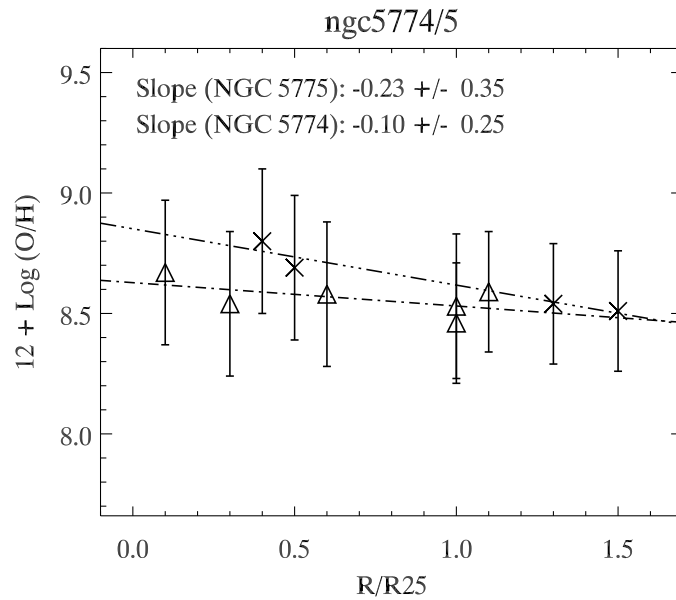
Figure 5.68. Radial oxygen abundance gradient: NGC 5774/5. Same as Figure 5.41 for NGC 5774 and NGC 5775.
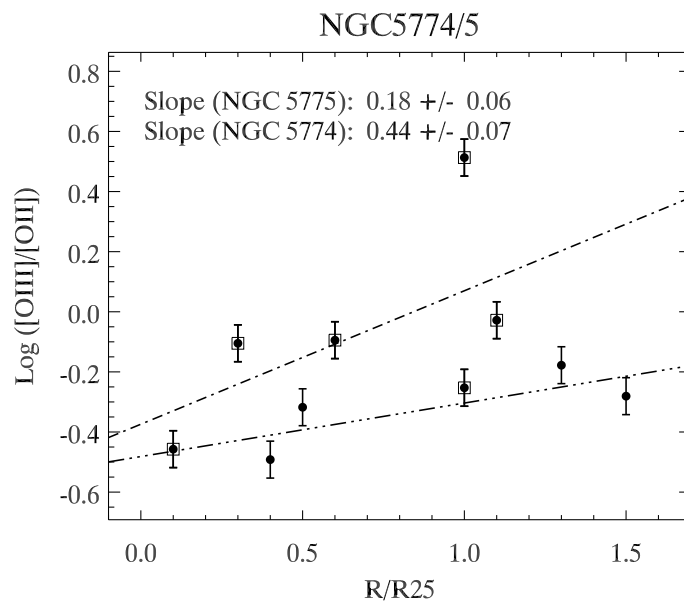
Figure 5.69. Radial dependence of the excitation diagnostic: NGC 5774/5. Same as Figure 5.42 for NGC 5774 and NGC 5775.

ID	RA	dec	r/r$_{25}$	R$_{proj}$	F$_{H\alpha}$	m$_R$	[OII]	[OIII]	O/H	Method
(1)	(2)	(3)	(4)	(5)	(6)	(7)	(8)	(9)	(10)	(11)
					NGC 5774					
7	14 53 48.6	+03 34 14.1	1.1	13.11	0.04±.00	20.20±.07	320	300	8.59	M91/lit
11	14 53 43.4	+03 36 09.6	1.0	9.66	2.11±.25	22.10±.15	469	262	8.46	M91/lit
12	14 53 44.6	+03 35 58.0	1.0	8.94	5.74±.68	19.85±.07	189	616	8.53	M91/lit
23	14 53 41.1	+03 35 43.7	0.6	6.65	10.10±.21	20.06±.07	343	276	8.58	M91/lit
10	14 53 43.1	+03 35 16.0	0.3	2.78	1.91±.22	21.92±.13	373	293	8.54	M91/lit
9	14 53 41.6	+03 35 03.2	0.1	1.79	2.30±.27	20.52±.07	361	126	8.67	M91/lit
					NGC 5775					
4	14 53 51.0	+03 35 55.9	1.5	27.20	0.40±.04	>23.19±.34	439	230	8.51	M91/PP04
1	14 53 51.9	+03 35 27.0	1.3	23.05	0.54±.06	21.67±.11	396	263	8.54	M91/PP04
15	14 53 54.8	+03 33 50.7	0.5	9.29	4.22±.50	22.42±.19	320	154	8.69	M91/lit
17	14 53 54.5	+03 33 34.4	0.4	7.98	4.80±.57	22.26±.17	270	87	8.80	M91/lit

Table 5.13. HII Region Properties: NGC5774/5. Same as Table 5.4, for NGC 5774 and NGC 5775
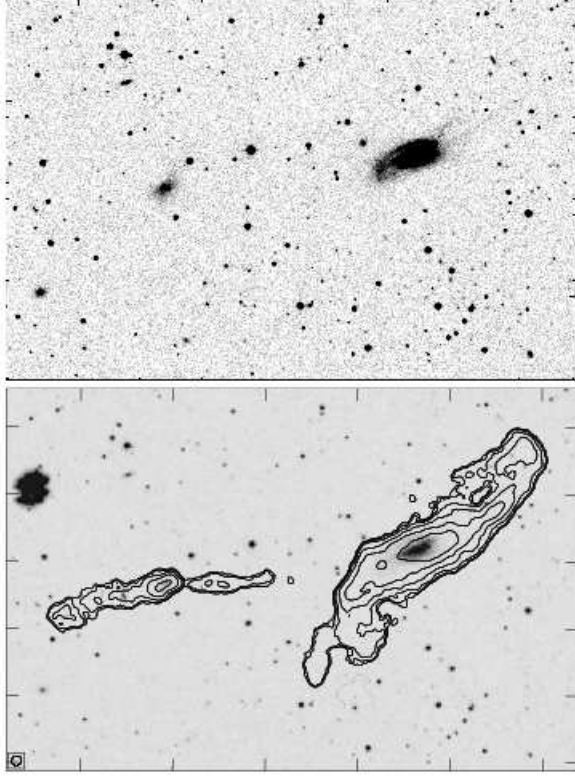
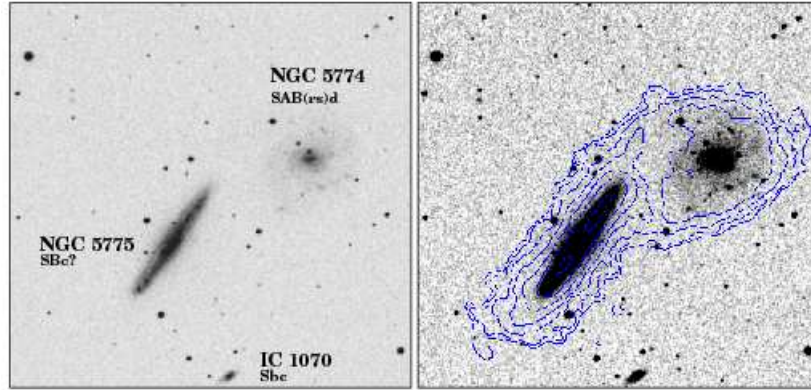**Figure 5.70.** Neutral hydrogen column density contours for NGC 6239, taken directly from the HI Rogues catalog. Original VLA D-Array data from Hogg & Roberts (2001). The resolution of the HI synthesis map is $18'' \times 17''$ and the contours are 8.0×10^{19} cm$^{-2} \times 2^n$. Top: DSS image of NGC 6239 and its HI-rich companion. Bottom: DSS + HI contours.

5.4.11 NGC 6239

NGC 6239 is a minor merger in the HI rogues catalog. Both galaxies appear to be gas rich, although we imaged only the primary galaxy NGC6239 in Hα and determined the metallicity of HII regions in that galaxy and one in its northern HI tail with an HI column density of 5×10^{19} cm^{-2}. The HI mass of this galaxy is 7×10^9 M$_\odot$ (Springob et al., 2005).

The oxygen abundance of the outermost HII region of NGC 6239 (Region 5), $12 + \text{Log (O/H)} = 8.27$, is lower than that of the inner HII regions which have an average $12 + \text{Log (O/H)}$ of 8.6. The longslit Keck data for this galaxy detect regions 5, 17, and three other HII regions that happened to fall within the $1''$ slit. Their measured N2 indices (see Table 5.3) are consistent with the N2 indices from several HII regions presented in Márquez et al. (2002) which place all the HII regions near,
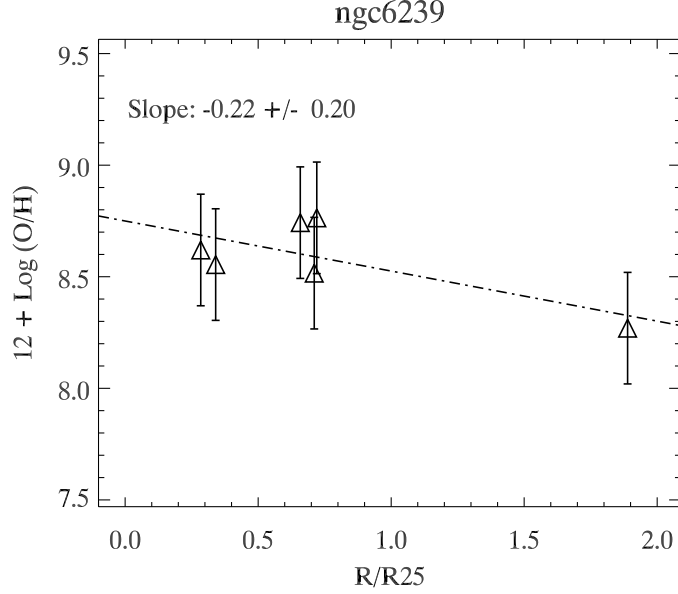
Figure 5.71. Radial oxygen abundance gradient: NGC 6239. Same as Figure 5.41 for NGC 6239.

ID	RA	dec	r/r$_{25}$	R$_{proj}$	F$_{H\alpha}$	m$_R$	[OII]	[OIII]	O/H	Method
(1)	(2)	(3)	(4)	(5)	(6)	(7)	(8)	(9)	(10)	(11)
5	16 49 53.6	+42 45 28.2	1.9	16.42	0.46±.05	>23.15±.35	480	269	8.27	M91/PP04
8	16 50 00.9	+42 44 30.6	0.7	6.07	0.53±.06	>23.15±.35	256	150	8.76	M91/PP04
9	16 50 01.3	+42 44 23.3	0.7	5.42	2.05±.24	21.80±.13	382	313	8.52	M91/PP04
11	16 50 06.6	+42 44 40.1	0.7	2.45	3.29±.39	21.01±.08	261	170	8.74	M91/PP04
17	16 50 03.5	+42 44 28.7	0.3	3.04	73.58±.82	18.36±.07	122	698	8.55	M91/PP04
16	16 50 05.5	+42 44 10.0	0.3	1.06	2.21±.26	21.62±.11	275	321	8.62	M91/PP04

Table 5.14. HII Region Properties: NGC6239. Same as Table 5.4, for NGC 6239

but slightly above the turnover of the M91 R23 relation $(12 + \text{Log(O/H)} = 8.3 - 8.4$ from the PP04 calibration). The M91 R23 calibration gives slightly higher (but consistent, within the large errors) values for $12 + \text{Log (O/H)}$ of the inner HII regions, with an average $12 + \text{Log (O/H)}$ of ~8.6. Therefore, the abundance gradient in this galaxy appears to decrease out to large radii, but is also consistent (within 1 σ) with being flat. A decreasing radial excitation gradient in this galaxy is probably further evidence of a flat oxygen abundance gradient, as opposed to a strongly declining one. The decreasing excitation with radius is then most likely indicative of a declining T_{eff} with radius.

**Figure 5.72.** Radial dependence of the excitation diagnostic: NGC 6239. Same as Figure 5.42 for NGC 6239.
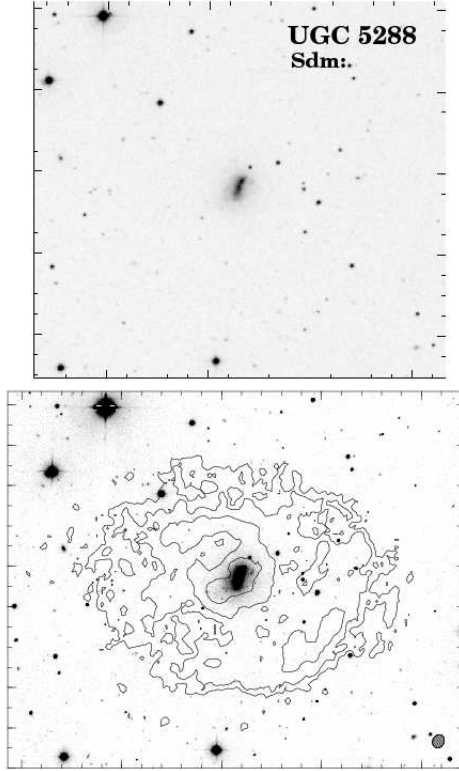
Figure 5.73. Neutral hydrogen column density contours for UGC 5288, taken directly from the HI Rogues catalog. Original VLA CS-Array data from van Zee & Haynes (2001). The resolution of the HI synthesis map is $20'' \times 17''$ and the contours are 8.0×10^{19} cm$^{-2} \times 2^n$. Top: DSS image of UGC 5288. Bottom: KPNO 0.9-m B-band image + HI contours.

5.4.12   UGC 5288

UGC 5288 is a blue compact dwarf galaxy with an extended HI envelope and no sign of interaction in the gas disk. Its optical and HI properties are qualitatively similar to those of NGC 2915 (see Chapter 4). The HII regions probed in the outer gaseous regions of this galaxy are found in gas with column densities as low as 2×10^{20} cm^{-2}. The total HI mass of this galaxy is 2×10^8 M$_\odot$ (Huchtmeier & Richter 1989).

We are able to break the R23 degeneracy for both outer and inner HII regions in UGC 5288 with the N2 index, and a comparison with the abundances calculated from the PP04 calibration. The faintness of [NII] compared to Hα in this galaxy (we do not detect [NII] in the longslit spectrum of Region 4 which allows us to place a 3σ upper limit on the N2 index) is probably indicative of its HII regions lying on the lower branch of the R23 relation (see Table 5.3). Still, the N2 index lies at or below

194

~-1.15, which is not quite low enough to definitively place it on the lower branch. Nonetheless, the literature abundance values for the central HII regions in this galaxy (van Zee & Haynes, 2006) indicate that they are on the lower branch, which leads us to adopt lower branch values as well. The radial oxygen abundance gradient for UGC 5288 is therefore flat. This galaxy's excitation diagnostic shows no strong radial trend.
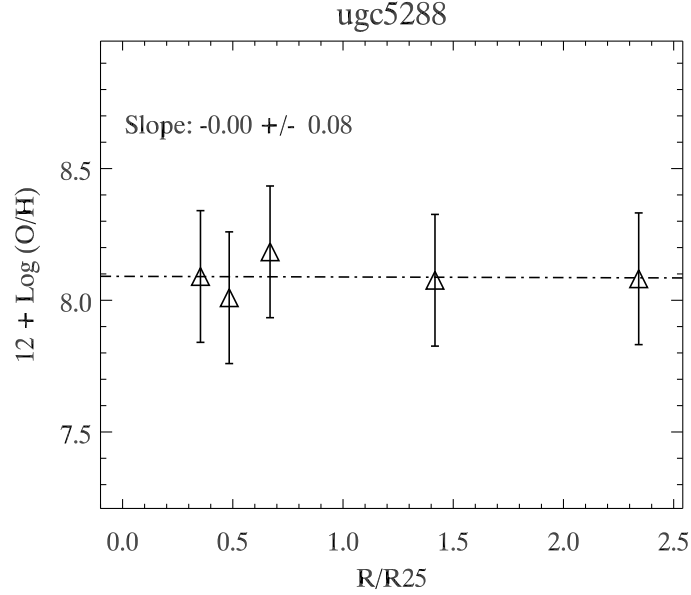
Figure 5.74. Radial oxygen abundance gradient: UGC 5288. Same as Figure 5.41 for UGC 5288.

ID	RA	dec	r/r$_{25}$	R$_{proj}$	F$_{H\alpha}$	m$_R$	[OII]	[OIII]	O/H	Method
(1)	(2)	(3)	(4)	(5)	(6)	(7)	(8)	(9)	(10)	(11)
4	09 51 10.3	+07 49 17.4	2.3	3.07	0.19±.02	>24.57±.34	323	336	8.08	M91/PP04
1	09 51 15.2	+07 50 35.9	1.4	1.93	0.22±.02	>24.57±.34	286	403	8.08	M91/PP04
12	09 51 15.2	+07 49 42.0	0.7	0.88	0.95±.11	23.41±.19	441	198	8.18	M91/PP04
11	09 51 15.9	+07 49 46.0	0.5	0.64	1.41±.16	21.93±.08	336	54	8.01	M91/PP04
10	09 51 16.6	+07 49 50.7	0.4	0.48	25.57±.06	19.31±.07	270	461	8.09	M91/PP04

Table 5.15. HII Region Properties: UGC5288. Same as Table 5.4, for UGC 5288
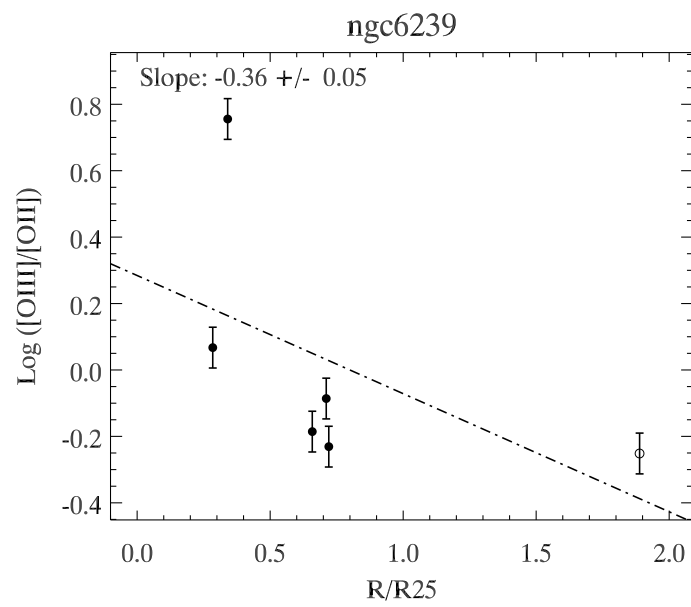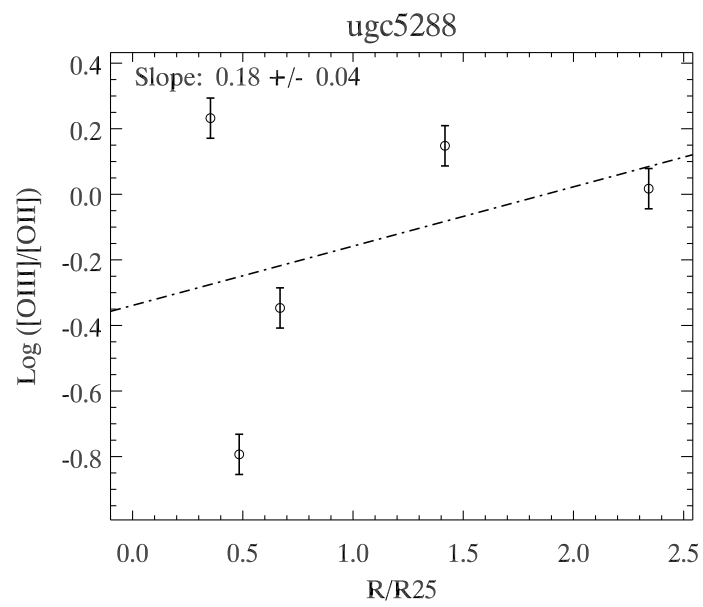
**Figure 5.75.** Radial dependence of the excitation diagnostic: UGC 5288. Same as Figure 5.42 for UGC 5288.
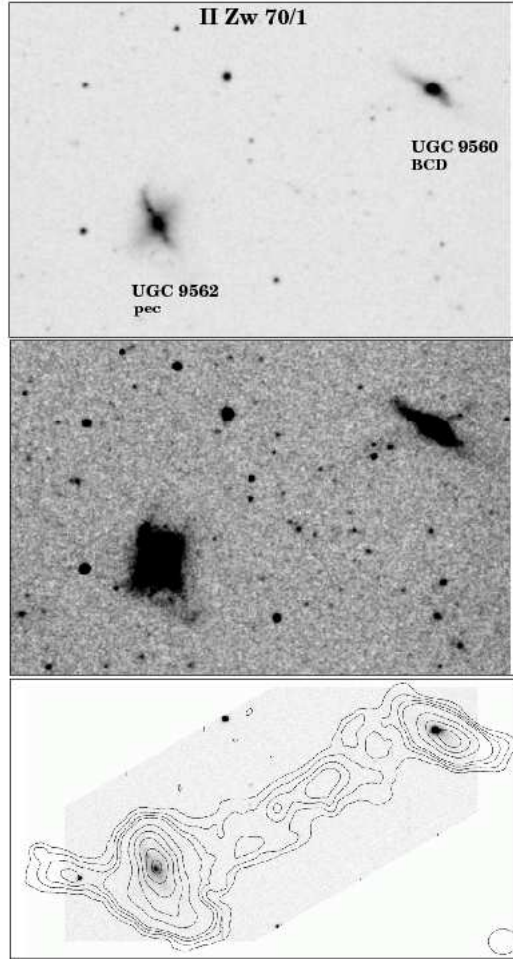
Figure 5.76. Neutral hydrogen column density contours for UGC 9562, taken directly from the HI Rogues catalog. Original VLA C+D-Array data from Cox et al. (2001). The resolution of the HI synthesis map is $22'' \times 20''$ and the contours are 2.0×10^{20} cm$^{-2} \times 2^n$. Top two panels: DSS images of II Zw 70/71 (UGC 9560/62) Bottom: B-band image from OSU Imaging Fabry-Perot Spectrometer + HI contours.

5.4.13 UGC 9562

UGC 9562 (also known as II Zw 71) is classified as an interacting double (the companion is UGC 9560/II Zw 70), or a polar ring galaxy. Both galaxies are gas rich, with a bridge joining the two galaxies and a tail on the opposite side of the bridge linked to UGC 9562 (Cox et al., 2001). All of the HII regions we study here are close to UGC 9562 which contains 8.2×10^8 M$_\odot$ in HI.

The N2 indices for one central (Region 14) and one outlying HII region (number 7) indicate that the oxygen abundance is near the turnover of the R23 relation.

The value from Shi et al. (2005), 8.24, determined from strong-line R23 abundance measurements of HII regions along the polar ring are also consistent with being near the turnover. Not surprisingly, then, the oxygen abundances from the M91 calibration lie near the turnover as well. The oxygen abundance gradient in UGC 9562 is flat, no matter which branch we choose for the R23 abundances. We tabulate lower branch values (due to their being slightly closer to the previously published abundances) in Table 5.16, but note that they are, on average, only 0.1 dex from the upper branch values, which can be seen in Figure 5.39. While the excitation may be increasing with radius for UGC 9562, there is basically no way to obtain a declining abundance gradient for this galaxy since we have already chosen lower-branch values for the outer HII regions. Therefore, this trend in Log ([OIII]/[OII]) is probably due to an increasing radial trend of T_{eff}.
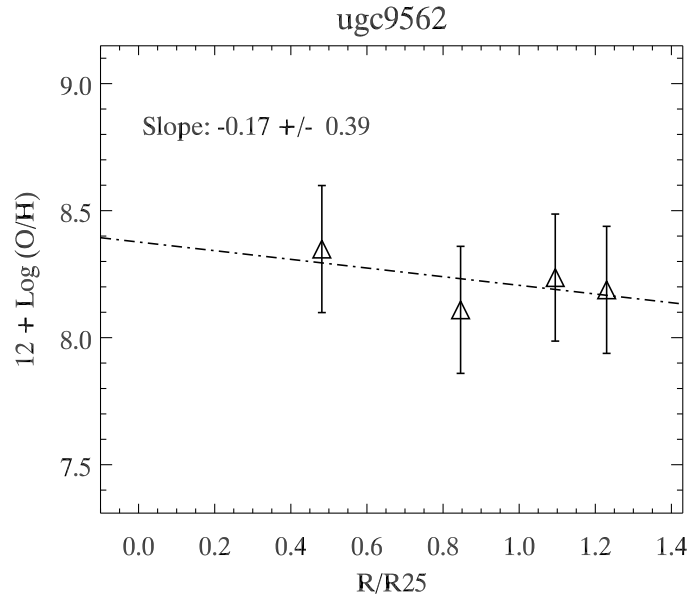
Figure 5.77. Radial oxygen abundance gradient: UGC 9562. Same as Figure 5.41 for UGC 9562.

ID	RA	dec	r/r_{25}	R_{proj}	$F_{H\alpha}$	m_R	[OII]	[OIII]	O/H	Method
(1)	(2)	(3)	(4)	(5)	(6)	(7)	(8)	(9)	(10)	(11)
7	14 51 12.7	+35 31 58.9	1.2	4.55	0.74±.08	22.97±.31	297	529	8.19	M91/PP04
12	14 51 13.5	+35 31 58.2	1.1	4.12	0.44±.05	>23.17±.36	448	278	8.24	M91/PP04
17	14 51 15.2	+35 32 58.0	0.8	3.18	1.24±.14	21.86±.13	396	200	8.11	M91/PP04
14	14 51 13.9	+35 32 17.5	0.5	1.80	9.13±.09	19.99±.07	572	276	8.35	M91/PP04

Table 5.16. HII Region Properties: UGC9562. Same as Table 5.4, for UGC 9562.
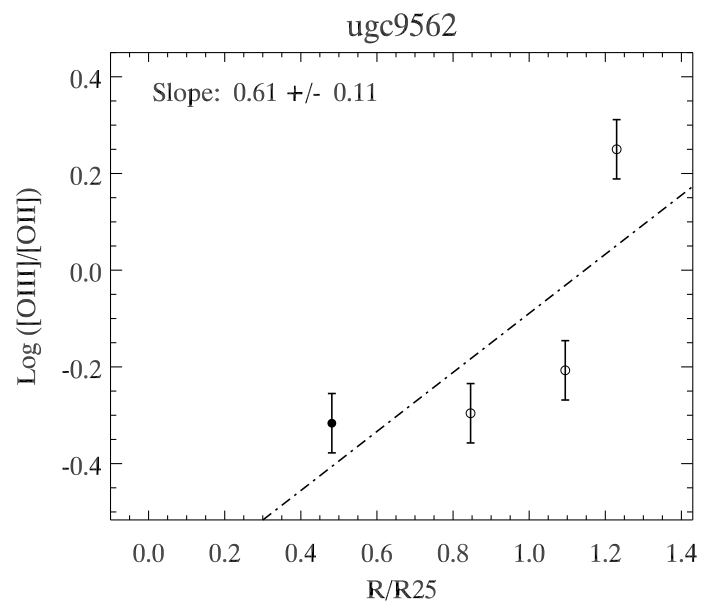
Figure 5.78. Radial dependence of the excitation diagnostic: UGC 9562. Same as Figure 5.42 for UGC 9562.

5.4.14 Gas Densities in the Outer Disks: Low-Density Star Formation

The HI gas densities at the locations of the outlying HII regions range from $3 - 500$ $\times$ 10^{19} HI atoms cm^{-2}, corresponding to a range in gas surface density of $0.25 - 80$ M$_\odot$ pc^{-2}. The median value, which is typical of most of the gas column densities at the outlying HII region locations, is 4×10^{20} cm^{-2}, or ~ 3 M$_\odot$ pc^{-2}. This gas surface density is at the typical "threshold" for star formation, usually cited between 2 and 8 M$_\odot$ pc^{-2} (Schaye, 2004). Thus, we are truly examining star formation at low average gas surface densities. The outlying HII regions presented in this Chapter cover a range of Hα luminosities, from $10^{35.5} - 10^{37.5}$ergs s^{-1}, corresponding to SFRs that range from 2×10^{-4} to 2×10^{-6} M$_\odot$ yr^{-1}. Most of the outlying HII regions are isolated within surface areas of roughly a kpc^2, so these SFRs can be viewed roughly as star formation rate surface densities in units of M$_\odot$ yr^{-1} kpc^{-2}. These values of SFRs and HI gas surface densities place the outlying HII regions in the same, or lower, "downturn" portion of the Kennicutt-Schmidt law (Section 1.1, Figure 1.1; Wyder et al. 2009), as expected. One caveat to keep in mind is that these stars may be forming in places where the local gas density is higher than the average surrounding gas densities, on a size scale which would be unresolved in the HI synthesis maps.

Several of the outlying HII regions presented in this Chapter lie in faint outer, spiral arms, which may explain why molecular clouds form at these large radii in low-density gas. Compression from gaseous and/or stellar spiral density waves may be the main mechanism at work in these cases: NGC 2146, NGC 3227, NGC 3359, NGC 3893, NGC 5775. In the other cases, there is no evidence of spiral structure at all within or outside the galaxies in the optical and HI data. Another source of compression could be minor mergers, which are known to trigger star formation. Indeed, many of our sample of HI rogues appear to have recently undergone, or are actively undergoing some form of interaction.

5.5 The Lack of Abundance Gradients at Large Galactocentric Radii

The 13 HI rogue galaxies in our sample are diverse, in terms of both their HI and optical properties. Their total baryonic masses range from dwarf galaxies with M < 10^9 M$_\odot$ (UGC 5288) to massive spiral galaxies with M $\sim 10^{11}$ M$_\odot$(NGC 2146). Their HI morphologies range from very extended, undisturbed HI envelopes, to warped HI distributions, to large tidal tails, representing an equally wide range of galaxy interactions. And, their SFRs range from 0.006 M$_\odot$ yr^{-1} to 3 M$_\odot$ yr^{-1}. Our results show that the outer gas of disturbed, interacting, or extended gas disk galaxies is as oxygen-enriched as that which is more centrally-located. Flat radial oxygen abundance gradients in this wide variety of galaxies with varying degrees of interaction and star formation provide compelling evidence of uniform metal distribution across extended gaseous features independent of large-scale galaxy properties and accretion histories.

In this section, we first describe the measurements we make and methods we use to determine stellar masses and SFRs. We then present an analysis of the oxygen yields of all the rogue galaxies, their positions on the mass-metallicity relation, and discuss the weak trends of Log ([OIII]/[OII]) with radius, and finally discuss the implications of flat oxygen abundance gradients out to large galactocentric radii.

5.5.1 Deriving Galaxy Masses and SFRs

For the calculations we perform in this section, we derive the total baryonic (stellar + gas) and global star-formation rate (SFR) for each galaxy in our sample. To obtain a value of the stellar mass, we use the published total integrated broad-band magnitudes in B and V−bands available on NED in conjunction with the stellar mass-luminosity/color relation from Bell et al. (2003). Most of the total B−band and V−band apparent magnitude estimates come from the 1991 De Vaucoleurs Catalog, using a combination of new and previously published data, and are corrected for internal and Milky Way extinction. UGC 5288 is an exception in this regard (not included in the catalog), and therefore we used the broadband optical B and R−band

photometry from van Zee (2000). To obtain the total stellar mass from the B$-$band luminosity and the B$-$V color (sometimes B$-$R), we use Table 7 of Bell et al. (2003) which gives coefficients for their derived stellar mass-luminosity/color relation for SDSS galaxies. These stellar masses are accurate to within 50%. In some cases, we are able to compare our B$-$V results with other calibrations of the Bell et al. (2003) mass-luminosity/color relations using different broadband filters, which give values that are consistent within the errors. The HI masses are obtained from the literature, as referenced in sections 5.4.1 to 5.4.13. We calculate SFRs using the relation SFR (M$_\odot$ yr^{-1}) = 5.3 $\times$ 10^{-42} L(Hα) (ergs s^{-1}) (Calzetti, 2008) and obtain total Hα luminosities from the MDM 2.4-m images within an elliptical aperture at 2 $\times$ r$_{25}$. These total Hα luminosities are corrected for the contribution of [NII]λ6583 using the implied N2 indices from the literature abundances (listed in column 8 of Table 5.1) and the PP04 relation. Considering errors in the continuum subtraction, occasionally strange Hα filter reflections/diffuse patterns, and uncertainties in the extinction correction, we estimate that these total Hα luminosities are accurate to within $\sim$20%. We provide stellar masses (M$_*$), neutral gas masses (M$_{HI}$), and total SFRs in Table 5.1.

5.5.2 Relationship to the Mass-Metallicity Relation

We calculate the effective oxygen yield for each galaxy, Z/ln(μ^{-1}), where μ is the gas fraction and Z is the metallicity by mass, using mean HII region oxygen abundance as a proxy for total metal content, the stellar masses listed in Table 5.1, and total gas masses computed from the HI masses given in Table 5.1 plus a 36% contribution from helium. For reference, Chapter 4 describes in greater detail how to convert from an oxygen abundance by number to a metallicity by mass. Figure 5.79 plots the effective oxygen yield versus total baryonic mass for the 14 galaxies (filled circles; NGC 5774 and NGC 5775 we consider separately, though they are technically part of the same HI envelope) along with the empirical relation of Tremonti et al. (2004). With the exception of NGC 3227, every galaxy in our sample appears to lie along the empirical Tremonti et al. (2004) relation, within the 95% contours (dashed-dotted

lines). Tremonti et al. (2004) explain the decrease in metal yields with decreasing galaxy baryonic mass by invoking metal-rich supernova-driven winds that preferentially escape from smaller potential wells of less-massive galaxies. Along this vein, it is interesting to note that two lower-mass systems ($M_{baryonic} < 10^{10}$ $M_{\odot}$) in our sample, UGC 5288 and NGC 3239, show no signs of metal-blowout, lying just above the Tremonti et al. (2004) relation.
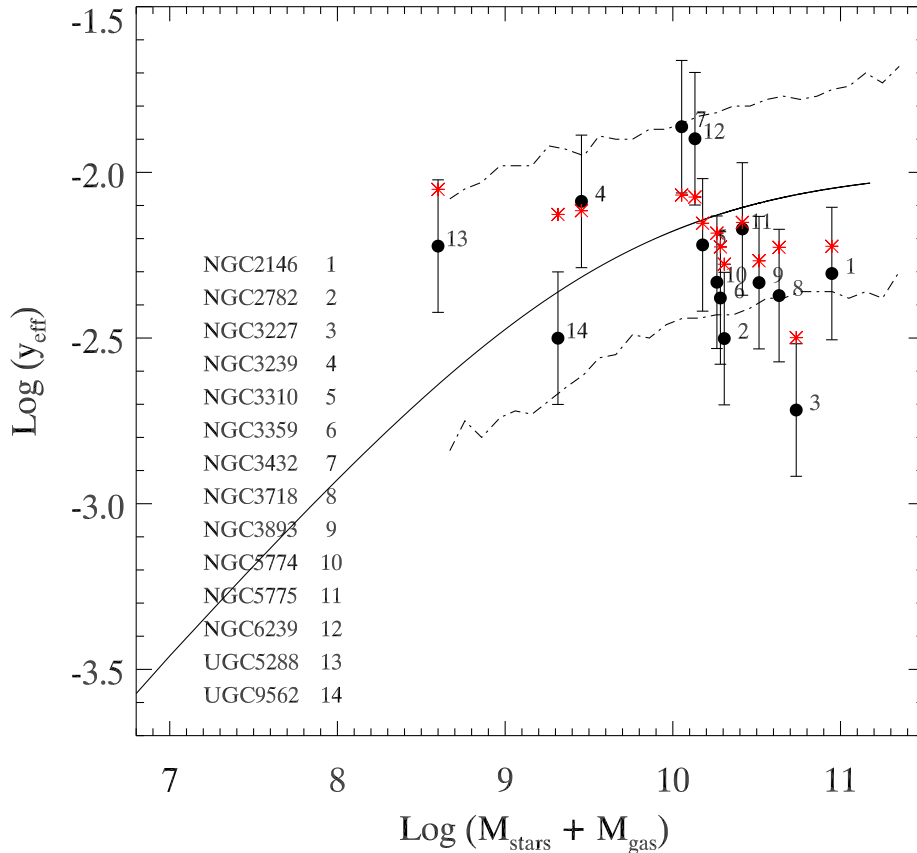
Figure 5.79. The effective yield versus the total baryonic (stellar plus gas) mass for the HII regions in every galaxy, shown as filled circles. Each point is marked with a number that corresponds to a galaxy listed in the key on the left hand side of the figure. We plot "expected" oxygen yields, determined from total stellar masses and a constant net oxygen yield, for each galaxy as red asterisks. The empirical relation in Tremonti et al. (2004), their equation 6, is shown for reference (solid line), along with contours (dashed-dotted lines) that enclose 95% of the SDSS data presented in Tremonti et al. (2004).

On the other hand, NGC 3227, one of the most massive galaxies in our sample, lies significantly below the relation. Peeples et al. (2009) explain 42 low-metallicity

outliers of the Tremonti et al. (2004) relation as the result of merger-induced gas inflow (Barnes & Hernquist, 1996; Hopkins et al., 2009; Rupke et al., 2010) that dilutes the metal content of the galaxy's nuclear ISM. This scenario is most likely irrelevant in the case of NGC 3227, because we find the outer gas, the very gas that would be responsible for the dilution, to be as enriched as gas more centrally located. We also note that several other strongly interacting/tidally disturbed galaxies in our sample, NGC 2146, NGC 2782, NGC 3310, NGC 3893, NGC 5774/5, and UGC 9562 lie slightly below (though within the 95% contours) of the Tremonti et al. (2004) relation. Three other merging galaxies in our sample, NGC 3239, NGC 3432, and NGC 6239, lie just above the Tremonti et al. (2004) relation. Thus, our results show no conclusive trend with regard to mergers and lower-than-expected central oxygen abundances.

The red asterisks on Figure 5.79 directly above or below the filled-circle galaxy points mark an "expected" oxygen yield determined by using the galaxy's total stellar mass and assuming a net oxygen yield of 0.01 (average value from Maeder 1992; the mass of oxygen ejected by all stars per unit mass of matter locked up in stars). All galaxies, with the exception of UGC 9562, have yields consistent with those predicted from a rough estimate that simply accounts for all metals using the existing stellar population. Interestingly, for UGC 9562, the "expected" $(12 + \text{Log (O/H)} = 8.59)$ and measured $(12 + \text{Log (O/H)} = 8.22)$ oxygen abundances (and yields) become consistent with each other if we instead choose upper-branch oxygen abundances in our R23 metallicity determination $(12 + \text{Log (O/H)} = 8.42)$. As UGC 9562 lies near the turnover of the R23 relation, the choice of lower-branch was only weakly motived by the lower oxygen abundances in Shi et al. (2005). However, that it has a lower measured effective yield than what is expected based on its total stellar mass could instead be evidence of metal loss in UGC 9562. Only a direct [OIII]$\lambda4363$ oxygen abundance determination, which is not available with our current data, would be able to settle this question. None of the other galaxies in Figure 5.79 shows evidence of having lost a significant fraction of metals.

As was the case with NGC 2915 (Chapter 4), there is only a low-level of ongoing

and previous star formation at the locations of the outermost HII regions. In this sense, the lack of radial oxygen abundance gradients beyond the optical "edges" of galaxy disks seems to necessarily imply some type of efficient metal transport. In the context of the mass-metallicity relationship, we can consider the yields for the outer and inner gaseous regions separately. First, keeping metallicity constant while lowering the stellar mass contribution to the effective yields relative to the gas mass contribution (outer HII regions) shifts the black points in Figure 5.79 to the left and up. In essence, the effective yields for the outer disk rise above their "closed-box" values. Conversely, the general trend of lowering the gas mass contribution relative to the stellar mass contribution while keeping metallicity constant (inner HII regions) has the effect of moving the points to the left and down. In essence, the effective yields for the inner disk fall below their "closed box" values. Although we do not present a detailed analysis of inner and outer disk abundances combined with their ongoing SFRs as we did in Chapter 4 for NGC 2915, the results in these 14 cases are similar. Outer-galaxy oxygen abundances are generally more metal-enriched than their gas fractions otherwise suggest, while inner-galaxy oxygen abundances lie below what is expected based on these simple stellar-population based assumptions. This duality appears to underlie the flat radial abundance gradients of gas-rich galaxies.

5.5.3   Comparison with Previous Work

Declining radial abundance gradients, often out to, and/or slightly beyond r_{25}, are well-observed in spiral galaxies (Oey & Kennicutt, 1993; Zaritsky et al., 1994; Kennicutt et al., 2003b). Here, we discuss previous work on the subject of radial abundance distributions and attempt to reconcile it with the flat gradients observed here. The broadest study to date is that of Zaritsky et al. (1994). They present metallicity gradients between 0.1 and 1.0 r/r_{25} using at least 5 HII regions in each of 39 local spiral galaxies with a wide range of morphologies (Sab - Sm; 7 galaxies have bars) and luminosities ($-21 < M_B < -17$). Because the scatter in oxygen abundance at a given galactic radius (0.4 dex at most) for each galaxy is much smaller the the mean abundance range for their entire sample (8.34 - 9.31), they conclude that these

gradients are determined globally, rather than set by local conditions (i.e. the local SFR and gas fraction). Given the duality of inner and outer oxygen yields in our sample of gas-rich galaxies, our results also strongly indicate that global phenomena are setting the radial oxygen abundance distribution.

Zaritsky et al. (1994) find a wide range of slopes in the 39 radial oxygen distributions, from flat to very steeply declining, at -1.45 dex/r_{25} corresponding to -0.231 dex/kpc. The average slope is -0.07 dex/kpc, or -0.59 dex/r_{25}. For comparison to the Zaritsky et al. (1994) sample, the slopes of our gradients range from $+0.4$ dex/r_{25} to -0.27 dex/r_{25}. Therefore, we do not see declining abundance gradients similar to those of Zaritsky et al. (1994). However, we note that our data generally do not apply to nuclear oxygen abundance gradients between 0 and ~ 0.4 r/r_{25}, which may very well be declining at similar rates. The error-weighted mean of the slopes of our radial abundance gradients, normalized to r/r_{25}, is -0.02 $\pm$ 0.27. Furthermore, our data rule out decreasing radial oxygen abundance gradients steeper than -0.30 dex over 15 kpc (-0.02 dex kpc^{-1}) in these outer regions. Put another way, all of our galaxies (beyond 0.4 r/r_{25}) have radial oxygen abundance gradients consistent with being flat within 1σ over an average of ~ 15 kpc, where typical $\sigma_{slope} = 0.3$ dex.

Several studies of metallicity gradients in the outer parts of relatively quiescent spiral galaxies have found a flattening beyond 0.5 r/r_{25} (Martin & Roy, 1995; Bresolin et al., 2009). Similarly, studies of low surface brightness disk galaxies (de Blok & van der Hulst, 1998) and dwarf galaxies (Croxall et al., 2009) are suggestive of flat oxygen abundance gradients out to r_{25}. Yet, this study is the first to measure radial oxygen abundance gradients in the outer regions of a large sample of gas-rich galaxies beyond r_{25}. A few of our galaxies are strongly interacting, which may partially explain a flattening in the abundance gradients (Rupke et al., 2010). Given the wide range of systems (including minor mergers, and warps) over which we measure flat gradients, our results suggest that galaxy interactions cannot be the sole explanation.

5.5.4 Possible Radial Trends of Log ([OIII]/[OII])

Six of the HI rogues we present in Section 5.4 show no radial trends of the excitation diagnostic, Log ([OIII]/[OII]). This excitation diagnostic is sensitive to HII region oxygen abundance (a proxy for Z), the ionization parameter (U, ionizing flux per unit area divided by the local number density of hydrogen atoms, full definition provided in Section 5.4), and the stellar ionizing effective temperature, T_{eff}. Therefore, a lack of any radial trend in the excitation parameter in a particular galaxy is consistent with a flat radial abundance gradient.

Three of our galaxies exhibit a declining Log ([OIII]/[OII]) with radius along with flat oxygen abundance gradient. If we assume that the nebular geometry and density (*not* the ambient HI gas density) do not vary systematically with galactocentric radius (there is no reason to expect they do), then the declining Log ([OIII]/[OII]) is due to a declining T_{eff} with radius. Such a trend might be expected if the stellar IMF changes at large radii such that there are fewer ionizing massive O stars produced as has been suggested by the IGIMF group (Pflamm-Altenburg et al., 2009). The only other explanation in these cases would be that the ionization parameter and T_{eff} are roughly constant, while the radial abundance gradient is increasing. We do not find evidence of significantly increasing abundance gradients for these galaxies, nor are such trends expected or observed elsewhere.

Four HI rogues, NGC 2146, 3227, 3893, and 5774/5, have radial excitation gradients that increase, as would be expected for declining radial oxygen abundance gradients. If these observable trends are indicative of declining abundance gradients in these four HI rogues, the flat radial abundance gradients that we present in Section 5.4 may not be correct. It is certainly possible that the upper branch choices for the outlying HII regions are incorrect or that the R23 relation is not in reality sensitive to the oxygen abundance near its turnover. There is indeed a notorious large margin of error in R23 oxygen abundance determinations. The alternative explanation is that the radial oxygen abundance gradients are flat, as we have measured them to be, and that in these systems the ionization parameter increases with radius, due to an increase in T_{eff}. An increase of T_{eff} with radius is unexpected, though possible, if

the few HII regions at large radii with large [OIII]/[OII] are ionized preferentially by very massive and hot ionizing O stars. If the latter is true, this trend runs counter to IGIMF claims that there are no very massive stars at large galactocentric radii where star clusters are on average less massive than their inner-galaxy counterparts.

NGC 2146, 3227, 3893, and 5774/5 are among the most massive galaxies in our sample of HI rogues, in terms of both their HI and stellar content. Two other massive galaxies in our sample, NGC 3359 and NGC 3718 show no trends in terms of the excitation diagnostic with galactocentric radius. Furthermore, the few inverted radial excitation gradients appear in galaxies at the low-mass end of our HI rogue sample, NGC 6239, 3310, and 3432. This potential trend, though weak, may indicate that we have made wrong branch choices for these four massive spiral galaxies in our HI rogues sample. In this interpretation, the higher mass spiral galaxies behave as expected, whereas the low-mass dwarf irregulars and interacting galaxies have flat radial oxygen abundance gradients and T_{eff} that sometimes declines with radius. The result here is inconclusive, and will only be resolved with data that can either more reliably break the R23 degeneracy or determine the metal abundance by another method.

5.5.5   The Implications of Flat Metallicity Gradients

As with the flat radial oxygen abundance gradient of NGC 2915, a number of physical mechanisms could be at work in various combinations to distribute metals in these HI rogue galaxies. Section 4.5 of Chapter 4 contains a discussion of these mechanisms, including 1. metal-mixing, 2. strong galactic winds with subsequent fallback, and 3. gas accretion resulting from a recent interaction. While our results for individual galaxies cannot discriminate between these scenarios, our results taken as a whole are highly suggestive that metal mixing is the dominant physical mechanism, sometimes enabled by a recent interaction. Galactic winds are thought to profoundly influence a galaxy's overall evolution (and the IGM's), but they cannot be entirely responsible for the redistribution of metals that takes place over such a broad range of galaxies since their strength and presence is highly dependent on the galaxy's star-forming properties and/or the presence of an AGN (Veilleux et al., 2005). Additionally, we

note that recent results from the simulations of Spitoni et al. (2009) indicate that galactic fountains have no impact on forming and/or erasing oxygen abundance radial gradients. The accretion of gas following a merger event or tidal interaction results in tidal torques that drive the gas to the system center (Barnes & Hernquist, 1996) and subsequently mix metals (Rupke et al., 2010). Nonetheless, several galaxies we discuss here show no evidence of a recent merger or interaction, yet are still well-mixed out to large radii.

Mixing itself can be driven by a number of processes: magnetorotational instabilities (Sellwood & Balbus, 1999), infall of gas clouds (Santillán et al., 2007), self-gravity in conjunction with differential rotation (Wada & Norman, 1999), quasi-stationary spiral structure interacting with a central bar (Minchev & Famaey, 2009), viscous flows generated by gravitational instability or cloud-cloud collisions (Ferguson & Clarke, 2001), thermal instability triggered self-gravitational angular momentum transport (McNally et al., 2009). Additionally, the presence of star formation in these outer-galaxy regions is evidence itself of local instability and a cool-phase medium, a required precondition for large-scale angular momentum transport (McNally et al., 2009). In general, the sound speed, ~ 10 km/s, is a robust upper limit to the speed at which mixing occurs in cold, neutral gas. Measurements of velocity dispersions in the outer HI disks of galaxies are roughly consistent with this number, generally no less than 8 km/s (Tamburro et al., 2009). A simple calculation of mixing timescales, assuming there is mixing at the sound speed over 15 kpc, yields 1.5 Gyr as the lower limit to the timescale over which mixing occurs in our extended HI features. Yet, the metals generated by massive stars are generally returned to the ISM on much shorter timescales, on the order of 10^8 years (Tenorio-Tagle, 1996). Thus, mixing may be occurring predominantly in a hot gas component (Tassis et al., 2008). The recent finding of OVI absorption over the entire Milky-Way disk, irrespective of circumstellar environments and spiral arms may provide some support for this idea(Bowen et al., 2008). Though the HI rogues we study here are quite different from Milky-Way-like spirals.

Efficient metal mixing has important implications for the origin of the mass-

metallicity relationship. Large-scale and universal metal-outflow may not be the dominant cause of the low effective yields in *gas-rich* dwarf galaxies as advanced by Tremonti et al. (2004) and others. Instead, these low-mass gas-rich galaxies on the whole would have fewer metals than expected from the simple nucleosynthetic yield because they are stirring those centrally-generated metals throughout their gaseous outskirts. Coupled with the idea that star formation is increasingly inefficient in these low-mass, gas-rich galaxies (Dalcanton, 2007), mixing could account for lower effective yields in lower mass galaxies with no real need for large-scale metal blow out.

5.6   Summary and Conclusions

Using narrow-band Hα and continuum R$-$band images from the MDM 2.4-m telescope, we have identified 13 "HI rogues" with massive star formation occurring beyond their optical radii. GMOS multi-slit optical spectroscopy targeting both inner and outlying HII regions in these 13 rogue galaxies allowed for the measurement of strong-line oxygen abundances of $\sim$100 HII regions with projected galactocentric distances ranging from $0.3 - 2.5$ r/r$_{25}$. Despite the diversity of these 13 systems in terms of their optical and HI morphologies, star-forming properties, and level of disruption, we find that all of them (with the possible exception of the four massive galaxies discussed in Section 5.5.4) have flat radial oxygen abundance gradients from their central optical bodies to their outermost regions. In addition to the interacting systems with flat abundance gradients, we find several non-interacting, gas-rich galaxies that have flat oxygen abundance gradients out to large projected radii.

There is a weak correlation of the excitation diagnostic, Log ([OIII]/[OII]), with radius and mass such that four of the most massive galaxies in our HI rogues sample exhibit excitations that increase with radius. Even if it is real, this trend is fairly inconclusive due to the multiple dependences of the excitation diagnostic on ionization parameter, T$_{eff}$, and metal abundance. However, we consider that we have made incorrect upper-branch choices for the R23 relation in these four cases and/or that the sensitivity of R23 to abundance is poor, especially near the knee. If this is the

case, the radial oxygen abundance gradients for these four galaxies may be declining, as expected for massive spiral galaxies. If the abundance gradients in these four cases truly are flat, then we must consider that the T_{eff} is high at large radii in some cases, counter to the IGIMF expectations. On the other hand, at least three of our less-massive galaxies exhibit a radially decreasing excitation diagnostic, Log([OIII]/[OII]). The most likely explanation for such a trend is that abundance is flat across the galaxy, while T_{eff} is systematically decreasing because of the decreasing presence of hot, massive O stars as ionization sources at large radii. This trend, combined with flat abundance gradients may support IGIMF theory in which the most massive star present in a star cluster is intrinsically related to the initial mass of the star cluster. Only more data that can place adequate constraints on the three defining parameters of HII regions, T_{eff}, U, and Z, will resolve these degeneracies and indicate what is responsible for the observed trends (or lack thereof).

We find that efficient metal-mixing or pre-enrichment and subsequent mixing from recent interactions are the two most likely potential causes for the enrichment of the gas beyond r_{25}. Large scale metal blowout then may not be the primary driver of the mass-metallicity relation for gas-rich or interacting galaxies. That metals are distributed throughout the extended gaseous regions of both interacting and non-interacting, strongly star-forming and quiescent, massive and dwarf galaxies has important implications for the origin of the mass-metallicity relation, and galaxy chemical evolution in general.

CHAPTER 6

Conclusions

Over the course of this thesis, I have described several studies that sought to answer fundamental questions related to star formation in the far, gaseous outskirts of galaxies. I conclude by summarizing each Chapter, reviewing those questions posed in the Introduction, discussing the progress I have made toward answering them, and finally, highlighting important work that remains to be done. The primary contribution of this thesis has been to set a foundation for future in-depth studies of outlying star formation.

6.1 Summary of Results from Individual Chapters

6.1.1 Chapter 2 Summary

Chapter 2 presents results from the first systematic search for outlying H II regions, as part of a sample of 96 emission-line point sources (referred to as ELdots – emission-line dots) derived from the NOAO Survey for Ionization in Neutral Gas Galaxies (SINGG). Our automated ELdot finder searches SINGG narrowband and continuum images for high equivalent width point sources outside the optical radius of the target galaxy ($> 2 \times r_{25}$ in the R−band). Follow-up long-slit spectroscopy and deep Galaxy Evolution Explorer (GALEX) images (exposure time >1000 s) distinguish outlying H II regions from background galaxies whose strong emission lines ([OIII], Hβ, or [OII]) have been red-shifted into the SINGG bandpass. We find that these deep GALEX images can serve as a substitute for spectroscopic follow-up because outlying H II regions separate cleanly from background galaxies in color-color space. We identify seven SINGG systems with outlying massive star formation that span a large range

in Hα luminosities corresponding to a few O stars in the most nearby cases, and likely unresolved dwarf satellite companion galaxies in the most distant cases. Six of these seven systems feature galaxies with nearby companions or are part of an interacting system. Furthermore, our results indicate that some outlying H II regions are linked to the extended-UV disks discovered by GALEX, representing emission from the most massive O stars among a more abundant population of lower-mass (or older) star clusters. The overall frequency of outlying H II regions in this sample of gas-rich galaxies is 8%−11% when we correct for background emission-line galaxy contamination (75% of ELdots).

6.1.2 Chapter 3 Summary

Chapter 3 presents HST ACS/HRC images in UV (F250W), V (F555W), and I (F814W) that resolve three isolated OB associations 30 kpc from the stellar disk of the S0 galaxy NGC 1533. SINGG narrow-band Hα imaging shows these objects as unresolved outlying HII regions having Hα luminosities consistent with being ionized by single early-type O stars. These young stars lie in stripped HI gas with column densities ranging from $1.5 - 2.5 \times 10^{20}$ cm^{-2} ($\sim$2 M$_\odot$ pc^{-2}, in the downturn region of the Kennicutt-Schmidt Law (Wyder et al., 2009) and velocity dispersions near 30 km s^{-1}. Using the HST broadband colors and magnitudes along with Hα luminosities, we place limits on the masses and ages of each association, considering the importance of stochastic effects for faint (M$_V > -8$) stellar populations. The upper limits to their stellar masses range from 600 M$_\odot$ to 7000 M$_\odot$, and ages range from $2 - 6$ Myrs. This analysis includes an updated calculation of the conversion factor between the ionizing luminosity and the total number of main sequence O stars contained within an HII region (see the Appendix). The photometric properties and sizes of the isolated associations and other objects in the HRC fields are consistent with those of Galactic stellar associations, open clusters and/or single O and B stars. We interpret the age-size sequence of associations and clustered field objects as an indication that these isolated associations are most likely rapidly dispersing. Furthermore, we consider the possibility that these isolated associations represent the first generation of

213

stars in the HI ring surrounding NGC 1533. This work suggests star formation in the unique environment of a galaxy's outermost gaseous regions proceeds similarly to that within the Galactic disk and that star formation in tidal debris may be responsible for building up a younger halo component.

6.1.3 Chapter 4 Summary

In Chapter 4, we present optical emission-line spectra for outlying HII regions in the extended, neutral gas disk surrounding the blue compact dwarf galaxy NGC 2915. Using a combination of strong-line R23 and direct oxygen abundance measurements, we report a flat, possibly increasing, metallicity gradient out to 1.2 times the Holmberg radius. We find the outer-disk of NGC 2915 to be enriched to a metallicity of 0.4 $Z_\odot$. An analysis of the metal yields shows that the outer disk of NGC 2915 is overabundant for its gas fraction, while the central star-forming core is similarly under-abundant for its gas fraction. Star formation rates derived from very deep $\sim$14 ks GALEX FUV exposures indicate that the low-level of star formation observed at large radii is not sufficient to have produced the measured oxygen abundances at these galactocentric distances. We consider 3 plausible mechanisms that may explain the metal-enriched outer gaseous disk of NGC 2915: radial redistribution of centrally generated metals, strong galactic winds with subsequent fallback, and galaxy accretion. Although we find NGC 2915 is not ejecting a significant fraction of its metals into the IGM, it falls along global correlations between galaxy mass and effective yield as a whole. This result implies that metal mixing may play a larger role than it is generally thought to in setting the mass-metallicity relation for gas-rich dwarf galaxies.

6.1.4 Chapter 5 Summary

In Chapter 5, we build upon the spectroscopic study of NGC 2915 with multi-slit spectroscopy of over 100 outlying and inner HII regions in 13 galaxies with extended or disturbed HI features. We catalogued HII regions using Hα and R-band continuum images obtained with the MDM 2.4-m telescope. Then, using the Gemini-North

Multi-Object Spectrograph, we obtained deep optical spectra of a number of inner- and outer-galaxy HII regions in our sample of 13 HI Rogues. We show that strong-line R23 oxygen abundances for the HII regions of each galaxy (or pair of interacting galaxies) are roughly constant over a large range of galactocentric radii extending to the outermost regions. The gas densities (~ 3 M$_\odot$ pc^{-2}) and low star formation rates ($\sim 2\times 10^{-4.5}$ M$_\odot$ yr^{-1}) at the locations of the outlying HII regions place them in the downturn region below the typical Kennicutt-Schmidt Law (Wyder et al., 2009). The low level of star formation in the general vicinity of the outlying HII regions cannot have generated enough metals over a Hubble time to produce the observed oxygen abundances. These results are consistent with previous work that finds metal distributions in galaxies must be governed by global processes (Zaritsky et al., 1994). The 13 HI rogues represent a wide range of galaxy HI morphologies, star-formation rates, and interaction stages, yet their oxygen abundance radial gradients are all flat in their outermost regions. This trend suggests that mixing processes in addition to pre-enriched gas accretion from mergers must be efficient at radially distributing metals throughout the full gaseous extents of nearby gas-rich galaxies. A potential consequence of these apparently efficient metal-mixing processes is that some gas-rich dwarf galaxies may not require significant metal-loss from galactic winds to reproduce the well-observed trends between effective metal yields and galaxy masses.

6.2   Questions: Posed and Answered

Q: How frequently does massive star formation occur beyond the main optical bodies of gas-rich galaxies?   **A:** It occurs in $\sim$10% of nearby, gas-rich galaxies. We approached this question systematically, using an automated algorithm on an unbiased sample of gas-rich galaxies from SINGG. Answering this question serves as an initial step toward understanding star formation in the low-density regime, and how it connects to the global star-forming properties of galaxies. Although a systematic search of nearby, spiral galaxies imaged with GALEX yields a much higher frequency for extended UV-bright star-formation, 30%, we caution against comparing the Hα and UV results directly. The GALEX Nearby Galaxy Survey and SINGG galaxies

215

are selected according to different criteria, and deep GALEX images are not available for many of the SINGG galaxies. Nonetheless, this frequency is consistent with limited previous studies that have calculated the approximate expected frequency of outlying Hα emission given the frequency of extended UV emission, and taking stochastic effects into account (Boissier et al., 2006). The return to Hα emission is timely, as questions of a variable upper mass end of the IMF at large radii appear with increasing frequency in the literature.

Q: Do OB associations at large projected radii carry a clear imprint of the environment in which they form?   **A:** No. The optical properties of the outlying OB associations of NGC 1533 show no divergence from Galactic and inner-galaxy OB associations at a resolution of 6.1pc and limiting apparent magnitudes of 28.0, 28.9, and 29.0 in the UV, V, and I bands, respectively. We based this analysis in part on the resolved properties of the OB associations, and in part on their integrated light properties determined from stellar population synthesis modeling, recognizing the uncertainties introduced by stochastic effects. We also found that these young stars are most likely in the process of rapidly dissolving, and will no longer be recognizable as associations of stars in the next 10 Myr. This result provides evidence that the stellar populations of clusters and associations are similar across a wide range of environments.

Q: Do the declining radial metallicity gradients observed for nearby, star-forming galaxies continue to decline at large radii? **A:** No. Radial abundance gradients for at least some gas-rich galaxies appear to flatten at large radii. Measurements of gas-phase oxygen abundances at projected galactic radii between 0.3 and 2.5 × r_{25} for 14 different galaxies (or pairs of galaxies) show no continuation of declining radial abundance gradients. The implications on metal-distibution processes in galaxies are that they must be efficient, and probably occur within a warm/hot gas component. It will be important to understand this result in combination with the declining gradients observed in the more central parts of galaxies. While gas-phase abundances determined from HII region spectra may be tracers of the global star formation history within a galaxy, they are not so useful for determining a more local star formation

history.

Q: What can the metal abundance in the outermost gas of galaxies tell us about the processes that govern the mass-metallicity relation for galaxies? **A:** The outermost gas of galaxies appears to be enriched at levels near and in excess of 0.4 $Z_\odot$, regardless of accretion history, star-formation rate, and total baryonic mass. In this context, we should then re-examine the assumption of large-scale metal loss for galaxies as the primary driver of the mass-metallicity relationship. If indeed metals are transported efficiently within a hot gas component, then it stands to reason that at least some metals are not lost, but rather optically unobservable in the hot gas while they are being mixed. Tassis et al. (2008) predicts such a phenomenon, and our results appear to be consistent with their theoretical model. There is more work that should be done to quantify what portion of the metals generated in the central galaxy are mixed, and what portion could still be lost to the IGM.

6.3 Future Prospects for Understanding Outlying Star Formation

There is much work that remains in terms of characterizing, in detail, the nature of star formation in the outskirts of galaxies. Here we summarize several planned projects.

6.3.1 Hα to UV Ratios

A statistical, uniform, and resolved photometric study of the UV and Hα emission in the far-outskirts of a large sample of galaxies will be able to directly address the one of the key questions regarding a variable upper mass limit to the stellar IMF raised by recent studies (Meurer et al., 2009; Lee et al., 2009; Köppen et al., 2007). Namely, is there a paucity of Hα emission in the far outskirts of XUV galaxies, compared to what is expected for a universal stellar IMF? Previous studies have used radial surface brightness profiles to address these questions, however, large uncertainties (especially in Hα measurements) due to background noise and variations, sample contaminants, and the tiny fraction of image pixels that contain point-source Hα emission at large

radii make their measurements less robust. Furthermore, the phenomenon of extended star formation should be addressed in a broader context for a large and varied sample of galaxies that show this type of emission beyond optical edges.

These shortcomings can be addressed with a large sample of outlying HII regions by performing photometry on the individual star forming complexes at large radii in both GALEX UV and Hα images, and summing their fluxes within radial bins. Taking into account stochastic effects, we can directly calculate whether we see less Hα emission than expected from stellar population synthesis models that assume a universal power-law IMF. Quantifying the properties of extended star formation in a wide variety of systems is essential for addressing questions about star formation thresholds and the potential suppression of massive star formation in the low-density outskirts of galaxies. Plans for this project are already underway using a subset of SINGG with available deep GALEX images (SUNGG) and some of the HI rogues with both Hα images (MDM) and deep GALEX images available from the archives.

6.3.2 Resolved Stellar Populations

By no means have we fully investigated the stellar populations in the low density gas of the outskirts of galaxies. Potential discrepancies between inner- and outer-star formation can be further investigated with additional deep, high-resolution *HST* images. The UVIS channel of WFC3 holds great promise for an examination of the resolved stellar populations of outlying HII regions, and a control sample of inner-disk HII regions. Additionally, the near-IR channel of WFC3 will be tremendously useful for investigating the presence of an older, underlying population. At distances < 10 Mpc, these instruments would achieve a resolution similar to that of the HRC data presented in Chapter 3, and would allow us to see down to $M_V \sim 0$, the equivalent of main sequence F stars up to 300 Myrs in age. Constructing color-magnitude diagrams for the young star clusters, and examining the detailed star formation histories from stellar evolution models would shed further light on the nature of the stellar populations at large radii. And, if there is an older, underlying population of evolved MS stars down to $1 M_\odot$ and 1-2 Gyrs in age, we will be able to see it, and perhaps resolve

it, with the near-IR images. These data have the potential to answer questions relating to the origin of the outer gas, and whether the outer star formation represents a first episode of star formation, or one of many episodes that have resulted in a faint underlying population of outlying field stars.

6.3.3 Gas-Phase Abundances at Large Radii

Metallicity gradients for a wider range of galaxies over the full range of galactocentric radii should be measured to confirm and expand upon our results. In particular, it would be interesting to determine if the radial oxygen distribution between 0 and 0.5 r/r_{25} shows a negative gradient. Although outlying star formation in both the UV and Hα is most often found in interacting systems, it would also be useful to perform this analysis for gas-rich galaxies that show no current sign of interaction or disturbance. In this sense, we probably need to examine gas-rich galaxies within 10 Mpc, since the faint, outlying HII regions like those in NGC 628 (Lelièvre & Roy, 2000) become more difficult to detect beyond this distance. Additionally, emphasis should be placed on lowering the systematic errors in the oxygen abundances and obtaining measurements for a larger number of HII regions per galaxy. To further define the radial abundance gradients, direct measurements of the oxygen abundance can lower the large dispersion. Deep, wide-field, multi-slit spectroscopy on 8-m class telescopes will be required to detect [OIII] λ4363 for a large number of HII regions over a wide range of galactocentric radii. Aside from detecting [OIII] λ4363, there are several other strong-line calibrations that improve upon the large systematic errors of the R23 method. Recently introduced by Pettini & Pagel (2004) is the ([OIII]/Hβ)/ ([NII]/Hα) diagnostic that lowers the overall error in abundance determinations to 0.2 dex. Although this method requires optical data in both the blue and the red, it does not hinge upon accurate flux calibration and reddening corrections (because the primary line ratios in the numerator and denominator are very close in wavelength), nor does it exhibit degenerate behavior.

These sorts of accurate abundance measurements for a large number of galaxies, interacting or not, will further inform us about the extent to which outlying gas is

enriched, and potentially well-mixed. An analysis of global star formation histories of the galaxies (star formation rates compared with gas measurements), combined with estimates of required mixing timescales will allow us to put constraints on both metal loss and metal mixing. Any dependence on the relative contributions of metal loss versus mixing on galaxy morphology and star formation history should be explored. It is essential that we parse out these physical mechanisms that distribute metals across galaxies and eject them into the IGM, as they critically influence our picture of galaxy evolution and star formation.

APPENDIX

APPENDIX A

Independent Calculation of Cluster Ages and Masses

Here we present the details of the estimate of the total number of ionizing stars present in each star-forming region derived from Vacca (1994). In Section 3.3, we use this method to determine association ages and masses, and compare the results with those of Starburst99. This method assumes no stellar evolution off the zero age main sequence, but is still provides reasonable estimates for the total number of main sequence O stars because the emission rate of ionizing photons does not vary substantially as massive stars evolve (Vacca, 1994). In A.1, we outline the calculations of the total number of O stars based on the observed ionizing flux of each association. In A.2, we use the observed UV fluxes to constrain the number of B stars, set the upper mass limit to the present-day mass function, and normalize the IMF for each isolated association.

A.1   The Number of O Stars

An Hα luminosity corresponds to an emission rate of ionizing photons, $Q_0 = 7.33 \times 10^{11}$ L$_{H\alpha}$ s^{-1} with L$_{H\alpha}$ in ergs s^{-1} cm^{-2} Å^{-1} (Osterbrock, 1989). Using this conversion factor, one can derive the number of "equivalent" stars of a given subtype powering an H II region. This number of "equivalent" ionizing stars, while a simple characterization of the stellar population, does not represent the *total* number of ionizing stars. With this notion in mind, Vacca (1994) present values for the conversion factor ($\eta_0 \equiv$ N$'_{O7V}$/N$_{OV}$) between the "equivalent" number of O stars of a given subtype and the full ionizing population, utilizing the most current stellar atmosphere and

stellar evolution models available in 1994. In this appendix, we describe our calculation of the total ionizing population of each H II region. Essentially, our method follows the calculations outlined in Vacca (1994), but uses the recently updated T_{eff} - spectral type calibration of Martins et al. (2005). Vacca (1994) thoroughly details the calculation of this conversion factor, η_0, and we refer the reader to that paper for a full description of the calculation.

The motivation for recalibrating η_0 using Martins et al. (2005) arose from the significant difference in their stellar parameters from previous results. Taking non-LTE, and wind and line-blanketing effects into account leads to effective temperature scales that are cooler than previously reported scales by 2000 to 8000K. Furthermore, the inclusion of metals in the model atmospheres of Martins et al. (2005) modifies the ionizing fluxes of the O stars. A true detailed recalculation of η_0 would have to include the new evolutionary tracks and regenerate stellar models, a task beyond the scope of this paper. Instead, we present a "re-estimation" of the conversion factor η_0 that hinges upon the number of ionizing photons produced as a function of stellar mass, $Q_o(M)$. Figure A.1 shows this function plotted versus stellar mass for two sets of stellar parameters taken from tables presented in Vacca et al. (1996) and Martins et al. (2005). Below 15.8 $M_\odot$, we used ionizing fluxes read from figure 1 in Vacca (1994) for both plots, making our two power-law fits identical in this regime. This approximation is valid since 1) the lower mass stars contribute very little to the ionizing radiation and 2) the two T_{eff} - spectral type calibrations are roughly the same below about 16 $M_\odot$. The solid lines represent the broken power-law fits (a series of linear fits in log-log space) to the data.

We begin our re-estimation of η_o by considering the equation for the conversion factor presented in Vacca (1994) and applying the values tabulated in Martins et al. (2005). From physical definitions, Vacca (1994) derives the following equation:

$$\eta_o = \frac{\int_{M_{low}}^{M_{up}} \Phi(M) Q_0^{ZAMS}(M)\,dM}{Q_0^{O7V} \int_{M_{OV}}^{M_{up}} \Phi(M)\,dM} \equiv N'_{O7V}/N_{OV} \tag{A.1}$$

Here, $\Phi(M)$ is the present day mass function with the form $AM^{-(1+x)}$, where A
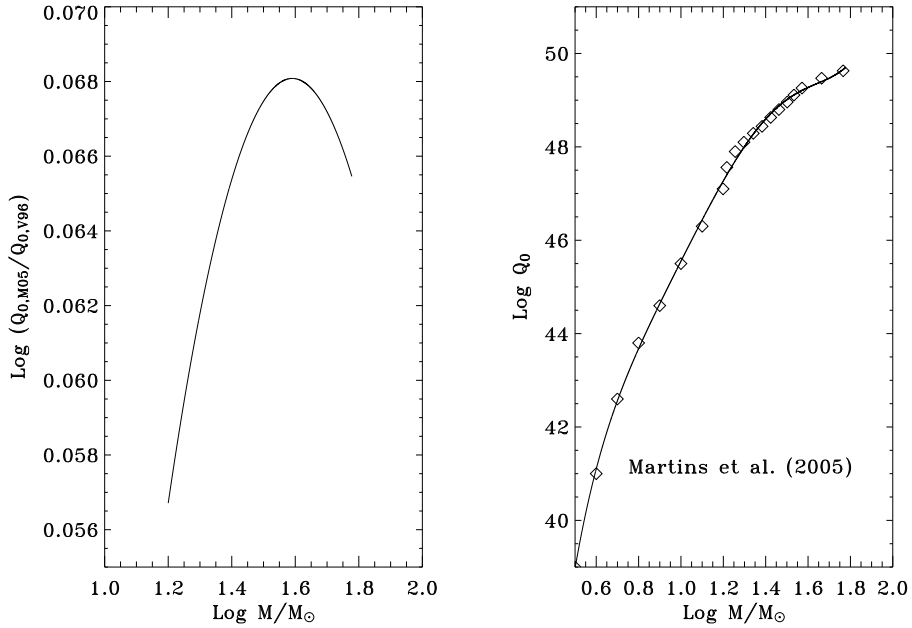
Figure A.1. On the left: The ratio of the ionizing photon emission rates in photons s^{-1} as a function of stellar mass between two sets of stellar parameters, those presented in Vacca et al. (1996) and Martins et al. (2005). The separate functions $Q_0(M)$ are quite similar, yet the differences produce significant changes in the conversion factors used to determine the total ionizing stellar populations (see Table 3.4 and this appendix for values and a detailed description). Below 16 M$_\odot$, the two functions are exactly the same. On the right: The polynomial fits to the data points of Martins et al. (2005) are plotted. The masses used to generate $Q_0(M)$ from Vacca et al. (1996) were the evolutionary masses, while the masses used to generate $Q_0(M)$ from Martins et al. (2005) were the spectroscopic masses (the only masses tabulated). Using the spectroscopic masses does introduce some error to our calculation, though slightly tempered by our use of only those masses below 60 M$_\odot$, and the lower effective temperature scales of Martins et al. (2005).

is the normalization constant and x is the power law index (x=1.35 for a Salpeter mass function). $Q_0^{ZAMS}(M)$ is the Lyman-continuum emission rate in photons s^{-1} as a function of stellar mass for stars on the main sequence. Using the relation $Q_0 = 7.33 \times 10^{11} L_{H\alpha}$ s^{-1} (Osterbrock, 1989), the Hα luminosities given in Table 3.1, and the fiducial $Q_0^{O7V} = 48.63$ (Martins et al., 2005), we calculate the number of equivalent O7V stars (N'_{O7V}) in associations 1, 2 and 5 to be 8.06, 5.46, and 3.81, respectively. We then evaluate Equation A1 to calculate η_0. From the definition $\eta_0 \equiv N'_{O7V}/N_{OV}$, we calculate the total ionizing main sequence O star population (N_{OV}) for a range of upper mass limits (M_{up}) given $Q_o^{ZAMS}(M)$ from Figure A.1b. The lower mass (M_{low}) is taken to be 3 M$_\odot$ (Schmidt-Kaler, 1982), and the lower mass limit to O stars (M_{OV}) is taken to be 15.8 M$_\odot$ (Martins et al., 2005). The total numbers of main

sequence O stars in each association are estimated at 11, 22, and 4 for associations 1, 2 and 5 using the present-day mass function upper mass limits we determine in the following section.

Table A.1 gives three different calculations of η_0 for solar metallicity, a Salpeter IMF, and various values of M_{up}. The first column of η_0 is taken directly from Vacca (1994), in which η_0 was calculated at larger mass intervals. For comparison, we also give η_0' for the $Q_o(M)$ of Vacca (1994) calculated by our method of function fitting, integrating, and our choice of a lower mass for O stars of 15.8 $M_\odot$. η_0'' is this re-estimation of Vacca's original conversion factor using the recent stellar models of Martins et al. (2005). Our values of η_0' for the model of Vacca (1994) agree well with the values of η_0 given directly in Vacca (1994). Furthermore, it is readily apparent that the most recent T_{eff}-spectral type calibration of Martins et al. (2005) has impacted the values of η_0 quite significantly.

We caution that these values of η_o should not be used as more than estimates, because of the assumptions and approximations used in the calculations. Still, these are the most up-to-date estimates of their kind. Martins et al. (2005) quote errors in their masses between 35 and 50%, which results in η_0 having 15-20% errors. While this calculation technically requires the use of an evolutionary (model dependent) mass, Martins et al. give only the theoretical spectroscopic ($M_{spec} = \frac{gR^2}{G}$) masses for each O star spectral type. Finally, the lower mass limit to O stars is quite poorly defined, which adds at least 10% to the error in the calculation of η_0. The discrepancy between evolutionary and spectroscopic masses is a known issue with stellar models, but is somewhat alleviated by the decrease in the effective temperature scale of Martins et al. (2005). We also stress that we have done this analysis for only main sequence solar-metallicity O stars. Varying the metallicities of the modeled stars will also have a small effect on the outcome.

A.2   The Number of B Stars

We calculate the total non-ionizing B star population expected from the UV luminosity of each association taking a path similar to that taken above. If the total UV

luminosity is produced by only O and B spectral types (to a good approximation), and we can quantify the ionizing population by the Hα luminosity, then we can also quantify the population of stars that contributes exclusively to the UV luminosity. Given the number of *equivalent* O7V stars from the Hα luminosity, we calculate the number of *equivalent* B9V stars from the UV luminosity as follows:

$$F_{UV} = N_{O7V} \times F_{UV}^{O7V} + N_{B9V} \times F_{UV}^{B9V} \tag{A.2}$$

In this equation, F_{UV}^{O7V} is F_λ of an O7V star in the F250W bandpass calculated using SYNPHOT (6.64×10^{-19} ergs s^{-1} cm^{-2} Å^{-1} at the distance of NGC 1533 from Kurucz 1993 spectral atlas in the SYNPHOT database), F_{UV}^{B9V} is F_λ of an B9V star in the F250W bandpass (9.20×10^{-22} ergs s^{-1} cm-2 Å^{-1} at the distance to NGC 1533), and F_{UV} is the total F_λ of the object measured in the HRC F250W image. For associations 1, 2, and 5 we calculate 3000, 8200, and 1100 equivalent B9V stars respectively.

Given the number of equivalent B9V stars for each association, an analysis similar to what we described above was undertaken to determine the *total* number of B stars that contribute to the UV luminosity of the intergalactic H II regions. In the same sense as for O stars, a conversion factor between a number of "equivalent" B stars of a certain spectral type and the full population of B stars can be determined: $\eta_o(B) \equiv N'_{B9V} / N_{BV}$. In this case, N'_{B9V} is the number of equivalent B9V stars (see above), and N_{BV} is the total B star population. The corresponding integral for the calculation of the conversion factor is simply:

$$\eta_o(B) = \frac{\int_{M_{B9V}}^{M_{up}} \Phi(M) F_\lambda^{ZAMS}(M) \, dM}{F_\lambda^{B9V} \int_{M_{BV}}^{M_{up}} \Phi(M) \, dM} \equiv N'_{B9V}/N_{BV} \tag{A.3}$$

We generate $F_\lambda^{ZAMS}(M)$ for all B spectral types using the masses and temperatures of Schmidt-Kaler (1982) and calculating the flux in the F250W bandpass of each spectral type using SYNPHOT and the Kurucz spectral type models. $\Phi(M)$ is the same present-day mass function used previously. Next, we calculate the *total number*

M_{up}	η_0	η_0'	η_0''
(1)	(2)	(3)	(4)
18	–	0.045	0.091
20	–	0.061	0.139
23	–	0.093	0.209
25	–	0.121	0.262
28	–	0.169	0.354
30	0.186	0.200	0.424
33	–	0.246	0.544
35	–	0.278	0.635
40	–	0.359	0.892
45	0.393	0.445	1.130
50	–	0.527	1.347
60	0.598	0.674	1.739

Table A.1. New Estimates of the conversion factor η_0 for Z=Z$_\odot$ and $\Phi(M) \propto M^{-2.35}$. (1) The upper mass limit to the IMF, in units of M$_\odot$. (2) η_0 is taken directly from Vacca (1994), we calculate (3) η_0' using the models presented in Vacca (1994), and we calculate (4) η_0'' based on the model presented in Martins et al. (2005). In our calculations, we cannot accurately report η_0 for upper masses above 60 M$_\odot$ due to the lack of data above this mass in Martins et al. (2005).

of non-ionizing B stars by integrating Equation A2 for masses between 3 and 15.8 M$_\odot$. We estimate a total B star population of 150, 400, and 50 in associations 1, 2, and 5, respectively.

Finally, for comparison with our original calculation, we use the normalization of the present day mass function from this calculation, and integrate $\Phi(M)$ between 15.8 M$_\odot$ and various values of M_{up} to determine the total number of main sequence O stars. The total number of O stars calculated using the Hα luminosity should match the total number of O stars calculated using the UV flux at some upper mass limit, interpreted as the maximum mass of the PDMF. For isolated associations 1, 2, and 5 these upper masses are 35 M$_\odot$, 25 M$_\odot$, and 40 M$_\odot$. Using the values of η_0 presented in Vacca (1994) gives slightly higher upper masses of 40 M$_\odot$, 28 M$_\odot$, and 50 M$_\odot$ for associations 1, 2, and 5, respectively.

BIBLIOGRAPHY

Arnaboldi, M., Aguerri, J. A. L., Napolitano, N. R., Gerhard, O., Freeman, K. C., Feldmeier, J., Capaccioli, M., Kudritzki, R. P., & Méndez, R. H. 2002, AJ, 123, 760

Asplund, M., Grevesse, N., & Sauval, A. J. 2005, in ASP Conf. Ser. 336: Cosmic Abundances as Records of Stellar Evolution and Nucleosynthesis, ed. T. G. Barnes, III & F. N. Bash, 25–+

Barber DeGraaff, R., Blakeslee, J. P., Meurer, G. R., & Putman, M. E. 2007, ArXiv e-prints, 710

Barnes, D. G., et al. 2001, MNRAS, 322, 486

Barnes, J. E. & Hernquist, L. 1996, ApJ, 471, 115

Bastian, N., Covey, K. R., & Meyer, M. R. 2010, ArXiv e-prints

Bastian, N., Gieles, M., Efremov, Y. N., & Lamers, H. J. G. L. M. 2005, A&A, 443, 79

Bell, E. F., McIntosh, D. H., Katz, N., & Weinberg, M. D. 2003, ApJS, 149, 289

Bertin, E. & Arnouts, S. 1996, A&AS, 117, 393

Bigiel, F., Leroy, A., Walter, F., Brinks, E., de Blok, W. J. G., Madore, B., & Thornley, M. D. 2008, AJ, 136, 2846

Blaauw, A. 1964, ARA&A, 2, 213

Blakeslee, J. P., Anderson, K. R., Meurer, G. R., Benítez, N., & Magee, D. 2003, in ASP Conf. Ser. 295: Astronomical Data Analysis Software and Systems XII, ed. H. E. Payne, R. I. Jedrzejewski, & R. N. Hook, 257–+

Bland-Hawthorn, J. & Jones, D. H. 1998, Publications of the Astronomical Society of Australia, 15, 44

Bland-Hawthorn, J., Vlajić, M., Freeman, K. C., & Draine, B. T. 2005, ApJ, 629, 239

Bobylev, V. V. & Bajkova, A. T. 2007, ArXiv e-prints, 708

Boissier, S., et al. 2006, ArXiv Astrophysics e-prints

Bonatto, C., Santos, J. F. C., & Bica, E. 2006, A&A, 445, 567

Boonyasait, V., Gottesman, S. T., & Broeils, A. H. 2001, in Astronomical Society of the Pacific Conference Series, Vol. 240, Gas and Galaxy Evolution, ed. J. E. Hibbard, M. Rupen, & J. H. van Gorkom, 857–+

Boquien, M., Duc, P. ., Braine, J., Brinks, E., Lisenfeld, U., & Charmandaris, V. 2007, ArXiv Astrophysics e-prints

Bournaud, F. & Duc, P.-A. 2006, A&A, 456, 481

Bowen, D. V., et al. 2008, ApJS, 176, 59

Bresolin, F. 2010, in IAU Symposium, Vol. 265, IAU Symposium, ed. K. Cunha, M. Spite, & B. Barbuy, 233–236

Bresolin, F. & Kennicutt, R. C. 1997, AJ, 113, 975

Bresolin, F., et al. 1998, AJ, 116, 119

Bresolin, F., Kennicutt, R. C., & Garnett, D. R. 1999, ApJ, 510, 104

Bresolin, F., Ryan-Weber, E., Kennicutt, R. C., & Goddard, Q. 2009, ApJ, 695, 580

Brooks, A. M., Governato, F., Booth, C. M., Willman, B., Gardner, J. P., Wadsley, J., Stinson, G., & Quinn, T. 2007, ApJ, 655, L17

Bruzual A., G. & Charlot, S. 1993, ApJ, 405, 538

Calzetti, D. 2008, in Astronomical Society of the Pacific Conference Series, Vol. 390, Pathways Through an Eclectic Universe, ed. J. H. Knapen, T. J. Mahoney, & A. Vazdekis, 121–+

Cardelli, J. A., Clayton, G. C., & Mathis, J. S. 1989, ApJ, 345, 245

Casertano, S., et al. 2000, AJ, 120, 2747

Cerviño, M. & Luridiana, V. 2004, A&A, 413, 145

Chandar, R., Fall, S. M., & Whitmore, B. C. 2006, ApJ, 650, L111

Chandar, R., Fall, S. M., & Whitmore, B. C. 2010, ApJ, 711, 1263

Chiosi, C., Bertelli, G., & Bressan, A. 1988, A&A, 196, 84

Cortese, L., Gavazzi, G., Boselli, A., & Iglesias-Paramo, J. 2004, A&A, 416, 119

Corwin, H. G., de Vaucouleurs, A., & de Vaucouleurs, G. 1985, Southern galaxy catalogue. A catalogue of 5481 galaxies south of declination -17 grad. found on 1.2m UK Schmidt IIIa J plates, ed. Corwin, H. G., de Vaucouleurs, A., & de Vaucouleurs, G.

Cox, A. L., Sparke, L. S., Watson, A. M., & van Moorsel, G. 2001, AJ, 121, 692

Croxall, K. V., van Zee, L., Lee, H., Skillman, E. D., Lee, J. C., Côté, S., Kennicutt, R. C., & Miller, B. W. 2009, ApJ, 705, 723

Dalcanton, J. J. 2007, ApJ, 658, 941

de Blok, W. J. G. & van der Hulst, J. M. 1998, A&A, 335, 421

de Bruijne, J. H. J. 1999, MNRAS, 310, 585

de Grijs, R. & Goodwin, S. P. 2007, ArXiv e-prints, 709

De Robertis, M. M., Dufour, R. J., & Hunt, R. W. 1987, JRASC, 81, 195

de Zeeuw, P. T., Hoogerwerf, R., de Bruijne, J. H. J., Brown, A. G. A., & Blaauw, A. 1999, AJ, 117, 354

Dekel, A. & Silk, J. 1986, ApJ, 303, 39

Drinkwater, M. J., Gregg, M. D., Holman, B. A., & Brown, M. J. I. 2001, MNRAS, 326, 1076

Duc, P.-A., Bournaud, F., & Masset, F. 2004, A&A, 427, 803

Duc, P.-A. & Mirabel, I. F. 1994, A&A, 289, 83

Duc, P.-A. & Mirabel, I. F. 1998, A&A, 333, 813

Efremov, I. N., Ivanov, G. R., & Nikolov, N. S. 1987, ApJ&SS, 135, 119

Efremov, Y. N. 1995, AJ, 110, 2757

Elmegreen, B. G. & Hunter, D. A. 2010, ApJ, 712, 604

Elson, E. C., de Blok, W. J. G., & Kraan-Korteweg, R. C. 2010, ArXiv e-prints

Engelbracht, C. W., Rieke, G. H., Gordon, K. D., Smith, J., Werner, M. W., Moustakas, J., Willmer, C. N. A., & Vanzi, L. 2008, ApJ, 678, 804

Ercolano, B., Bastian, N., & Stasińska, G. 2007, MNRAS, 379, 945

Ercolano, B., Wesson, R., & Bastian, N. 2009, MNRAS, 1583

Fall, S. M., Chandar, R., & Whitmore, B. C. 2005, ApJ, 631, L133

Ferguson, A. M. N. & Clarke, C. J. 2001, MNRAS, 325, 781

Ferguson, A. M. N., Gallagher, J. S., & Wyse, R. F. G. 1998a, AJ, 116, 673

Ferguson, A. M. N., Wyse, R. F. G., Gallagher, J. S., & Hunter, D. A. 1998b, ApJ, 506, L19

Friedli, D., Benz, W., & Kennicutt, R. 1994, ApJ, 430, L105

Fu, J., Hou, J. L., Yin, J., & Chang, R. X. 2009, ApJ, 696, 668

Garnett, D. R. 2002, ApJ, 581, 1019

Geha, M., Willman, B., Simon, J. D., Strigari, L. E., Kirby, E. N., Law, D. R., & Strader, J. 2009, ApJ, 692, 1464

Gerhard, O., Arnaboldi, M., Freeman, K. C., & Okamura, S. 2002, ApJ, 580, L121

Gieles, M., Lamers, H. J. G. L. M., & Portegies Zwart, S. F. 2007, ArXiv e-prints, 706

Gil de Paz, A., et al. 2005, ApJ, 627, L29

Gil de Paz, A., et al. 2007, ApJ, 661, 115

Goddard, Q. E., Kennicutt, R. C., & Ryan-Weber, E. V. 2010, MNRAS, 644

Goodwin, S. P. 1997, MNRAS, 284, 785

Hanish, D. J., et al. 2006, ApJ, 649, 150

Harris, W. E. 1996, AJ, 112, 1487

Heitsch, F. & Hartmann, L. 2008, ApJ, 689, 290

Hernquist, L. & Mihos, J. C. 1995, ApJ, 448, 41

Hibbard, J. E. & Barnes, J. E. 2004, in IAU Symposium, Vol. 217, Recycling Intergalactic and Interstellar Matter, ed. P.-A. Duc, J. Braine, & E. Brinks, 510–+

Hibbard, J. E., van der Hulst, J. M., Barnes, J. E., & Rich, R. M. 2001a, AJ, 122, 2969

Hibbard, J. E., van Gorkom, J. H., Rupen, M. P., & Schiminovich, D. 2001b, in Astronomical Society of the Pacific Conference Series, Vol. 240, Gas and Galaxy Evolution, ed. J. E. Hibbard, M. Rupen, & J. H. van Gorkom, 657–+

Hillenbrand, L. A. 1997, AJ, 113, 1733

Hills, J. G. 1980, ApJ, 235, 986

Hogg, D. & Roberts, M. 2001, in Astronomical Society of the Pacific Conference Series, Vol. 240, Gas and Galaxy Evolution, ed. J. E. Hibbard, M. Rupen, & J. H. van Gorkom, 859–+

Hoogerwerf, R., de Bruijne, J. H. J., & de Zeeuw, P. T. 2001, A&A, 365, 49

Hopkins, P. F., Cox, T. J., Younger, J. D., & Hernquist, L. 2009, ApJ, 691, 1168

Hubble, E. 1925, Contributions from the Mount Wilson Observatory / Carnegie Institution of Washington, 304, 1

Huchtmeier, W. K. & Richter, O. G. 1989, A General Catalog of HI Observations of Galaxies - the Reference Catalog (Springer-Verlag, New York, NY)

Hummer, D. G. & Storey, P. J. 1987, MNRAS, 224, 801

Hunter, D. A., Elmegreen, B. G., & Baker, A. L. 1998, ApJ, 493, 595

Hunter, D. A., Elmegreen, B. G., Dupuy, T. J., & Mortonson, M. 2003, AJ, 126, 1836

Hunter, D. A., Elmegreen, B. G., & Ludka, B. C. 2010, AJ, 139, 447

Irwin, J. A. 1994, ApJ, 429, 618

Irwin, M. J., Ferguson, A. M. N., Ibata, R. A., Lewis, G. F., & Tanvir, N. R. 2005, ApJ, 628, L105

Ivanov, G. R. 1996, A&A, 305, 708

Iyer, M., Simpson, C. E., Gottesman, S. T., Harsgis, J. R., & Malphrus, B. K. 2001, in Astronomical Society of the Pacific Conference Series, Vol. 240, Gas and Galaxy Evolution, ed. J. E. Hibbard, M. Rupen, & J. H. van Gorkom, 861–+

Kahn, F. D. 1974, A&A, 37, 149

Karachentsev, I. D., et al. 2002, A&A, 385, 21

Karachentseva, V. E. & Karachentsev, I. D. 1998, A&AS, 127, 409

Kay, S. T., Pearce, F. R., Frenk, C. S., & Jenkins, A. 2002, MNRAS, 330, 113

Kennicutt, R. C. 1983, ApJ, 272, 54

Kennicutt, R. C. 1989, ApJ, 344, 685

Kennicutt, R. C. 1998a, ARA&A, 36, 189

Kennicutt, R. C. 1998b, ApJ, 498, 541

Kennicutt, R. C., et al. 2003a, PASP, 115, 928

Kennicutt, R. C., Bresolin, F., & Garnett, D. R. 2003b, ApJ, 591, 801

Kennicutt, R. C., et al. 2007, ArXiv e-prints, 708

Kennicutt, R. C. & Garnett, D. R. 1996, ApJ, 456, 504

Kewley, L. J. & Dopita, M. A. 2002, ApJS, 142, 35

Kewley, L. J. & Ellison, S. L. 2008, ApJ, 681, 1183

Kobulnicky, H. A. 1999, in IAU Symposium, Vol. 193, Wolf-Rayet Phenomena in Massive Stars and Starburst Galaxies, ed. K. A. van der Hucht, G. Koenigsberger, & P. R. J. Eenens, 670–+

Konstantopoulos, I. S., Bastien, N., Smith, L. J., & Westmoquette, M. S. 2007, in preparation

Köppen, J., Weidner, C., & Kroupa, P. 2007, MNRAS, 375, 673

Kregel, M. & Sancisi, R. 2001, A&A, 376, 59

Krumholz, M. R., Cunningham, A. J., Klein, R. I., & McKee, C. F. 2010, ApJ, 713, 1120

Krumholz, M. R. & McKee, C. F. 2005, ApJ, 630, 250

Lada, C. J. & Lada, E. A. 2003, ARA&A, 41, 57

Larson, R. B. 1974, MNRAS, 169, 229

Lata, S., Pandey, A. K., Sagar, R., & Mohan, V. 2002, A&A, 388, 158

Lee, H., McCall, M. L., Kingsburgh, R. L., Ross, R., & Stevenson, C. C. 2003, AJ, 125, 146

Lee, H., Skillman, E. D., & Venn, K. A. 2006, ApJ, 642, 813

Lee, J. C., et al. 2009, ApJ, 706, 599

Leitherer, C., Schaerer, D., Goldader, J. D., Delgado, R. M. G., Robert, C., Kune, D. F., de Mello, D. F., Devost, D., & Heckman, T. M. 1999, ApJS, 123, 3

Lejeune, T. & Schaerer, D. 2001, VizieR Online Data Catalog, 6102, 0

Lelièvre, M. & Roy, J. 2000, AJ, 120, 1306

Leonard, P. J. T. & Duncan, M. J. 1990, AJ, 99, 608

Lequeux, J., Peimbert, M., Rayo, J. F., Serrano, A., & Torres-Peimbert, S. 1979, A&A, 80, 155

Lin, D. N. C. & Pringle, J. E. 1987, ApJ, 320, L87

Lisenfeld, U., Mundell, C. G., Schinnerer, E., Appleton, P. N., & Allsopp, J. 2008, ApJ, 685, 181

Mac Low, M. 2009, in Revista Mexicana de Astronomia y Astrofisica Conference Series, Vol. 36, Revista Mexicana de Astronomia y Astrofisica Conference Series, 121–127

Mac Low, M. & Ferrara, A. 1999, ApJ, 513, 142

Maeder, A. 1992, A&A, 264, 105

Márquez, I., Masegosa, J., Moles, M., Varela, J., Bettoni, D., & Galletta, G. 2002, A&A, 393, 389

Martin, C. L. & Kennicutt, R. C. 2001, ApJ, 555, 301

Martin, C. L., Kobulnicky, H. A., & Heckman, T. M. 2002, ApJ, 574, 663

Martin, P. & Roy, J. 1995, ApJ, 445, 161

Martinet, L. & Friedli, D. 1997, A&A, 323, 363

Martins, F., Schaerer, D., & Hillier, D. J. 2005, A&A, 436, 1049

McGaugh, S. S. 1991, ApJ, 380, 140

McNally, C. P., Wadsley, J., & Couchman, H. M. P. 2009, ApJ, 697, L162

Mendes de Oliveira, C., Cypriano, E. S., Sodré, L., & Balkowski, C. 2004, ApJ, 605, L17

Mengel, S., Lehnert, M. D., Thatte, N. A., Vacca, W. D., Whitmore, B., & Chandar, R. 2008, A&A, 489, 1091

Meurer, G. R., et al. 2003, ApJ, 599, L83

Meurer, G. R., Carignan, C., Beaulieu, S. F., & Freeman, K. C. 1996, AJ, 111, 1551

Meurer, G. R., et al. 2006, ApJS, 165, 307

Meurer, G. R., Heckman, T. M., & Calzetti, D. 1999, ApJ, 521, 64

Meurer, G. R., Mackie, G., & Carignan, C. 1994, AJ, 107, 2021

Meurer, G. R., et al. 2009, ApJ, 695, 765

Meynet, G. & Maeder, A. 2000, A&A, 361, 101

Meynet, G. & Maeder, A. 2005, A&A, 429, 581

Minchev, I. & Famaey, B. 2009, ArXiv e-prints

Morrissey, P., et al. 2007, ApJS, 173, 682

Mould, J. R., et al. 2000, ApJ, 528, 655

Moustakas, J. & Kennicutt, R. C. 2006, ApJS, 164, 81

Mundell, C. G. 2001, in Astronomical Society of the Pacific Conference Series, Vol. 240, Gas and Galaxy Evolution, ed. J. E. Hibbard, M. Rupen, & J. H. van Gorkom, 411–+

Mutchler, M., et al. 2005, in Bulletin of the American Astronomical Society, Vol. 37, Bulletin of the American Astronomical Society, 452–+

O'Donnell, J. E. 1994, ApJ, 422, 158

Oey, M. S., Dopita, M. A., Shields, J. C., & Smith, R. C. 2000, ApJS, 128, 511

Oey, M. S. & Kennicutt, R. C. 1993, ApJ, 411, 137

Oey, M. S., Parker, J. S., Mikles, V. J., & Zhang, X. 2003, AJ, 126, 2317

Oosterloo, T., Morganti, R., Sadler, E. M., Ferguson, A., van der Hulst, T., & Jerjen, H. 2004, in IAU Symposium, ed. P.-A. Duc, J. Braine, & E. Brinks, 486–+

Oosterloo, T. & van Gorkom, J. 2005, A&A, 437, L19

Osterbrock, D. E. 1989, Astrophysics of gaseous nebulae and active galactic nuclei, ed. D. E. Osterbrock (Mill Valley, CA, University Science Books)

Pagel, B. E. J., Edmunds, M. G., Blackwell, D. E., Chun, M. S., & Smith, G. 1979, MNRAS, 189, 95

Pagel, B. E. J., Simonson, E. A., Terlevich, R. J., & Edmunds, M. G. 1992, MNRAS, 255, 325

Pastoriza, M. G., Dottori, H. A., Terlevich, E., Terlevich, R., & Diaz, A. I. 1993, MNRAS, 260, 177

Peek, J. E. G. 2009, ApJ, 698, 1429

Peeples, M. S., Pogge, R. W., & Stanek, K. Z. 2009, ApJ, 695, 259

Pettini, M. & Pagel, B. E. J. 2004, MNRAS, 348, L59

Pflamm-Altenburg, J., Weidner, C., & Kroupa, P. 2009, MNRAS, 395, 394

Phillipps, S. & Edmunds, M. G. 1991, MNRAS, 251, 84

Pilyugin, L. S. 2000, A&A, 362, 325

Pilyugin, L. S. 2003, A&A, 397, 109

Pilyugin, L. S. & Thuan, T. X. 2007, ApJ, 669, 299

Rafelski, M. & Zaritsky, D. 2005, AJ, 129, 2701

Rupke, D. S. N., Kewley, L. J., & Barnes, J. E. 2010, ArXiv e-prints

Ryan-Weber, E., Webster, R., & Bekki, K. 2003a, in Astrophysics and Space Science Library, Vol. 281, The IGM/Galaxy Connection. The Distribution of Baryons at z=0, ed. J. L. Rosenberg & M. E. Putman, 223–+

Ryan-Weber, E. V., et al. 2004, AJ, 127, 1431

Ryan-Weber, E. V., Webster, R. L., & Staveley-Smith, L. 2003b, MNRAS, 343, 1195

Sakai, S., Kennicutt, R. C., van der Hulst, J. M., & Moss, C. 2002, ApJ, 578, 842

Salim, S., et al. 2007, ApJS, 173, 267

Salpeter, E. E. 1955, ApJ, 121, 161

Santiago-Figueroa, N., Putman, M., Werk, J., Ryan-Weber, E., & Meurer, G. 2009, ArXiv e-prints

Santillán, A., Sánchez-Salcedo, F. J., & Franco, J. 2007, ApJ, 662, L19

Schaye, J. 2004, ApJ, 609, 667

Schlegel, D. J., Finkbeiner, D. P., & Davis, M. 1998, ApJ, 500, 525

Schmidt, M. 1959, ApJ, 129, 243

Schmidt-Kaler, T. 1982, in Landolt-Bornstein, New Series, Group VI, Vol. 2, ed. K. Shaifers & H. H. Voigt, 1–+

Searle, L. 1971, ApJ, 168, 327

Sellwood, J. A. & Balbus, S. A. 1999, ApJ, 511, 660

Shaver, P. A., McGee, R. X., Newton, L. M., Danks, A. C., & Pottasch, S. R. 1983, MNRAS, 204, 53

Shaw, R. A. & Dufour, R. J. 1995, PASP, 107, 896

Shi, F., Kong, X., Li, C., & Cheng, F. Z. 2005, A&A, 437, 849

Shields, G. A. 1990, ARA&A, 28, 525

Shields, G. A. & Tinsley, B. M. 1976, ApJ, 203, 66

Shu, F. H., Allen, R. J., Lizano, S., & Galli, D. 2007, ApJ, 662, L75

Silk, J. 1997, ApJ, 481, 703

Sirianni, M., et al. 2005, PASP, 117, 1049

Skillman, E. D. 1987, in Star Formation in Galaxies, 263–266

Skillman, E. D., Kennicutt, R. C., & Hodge, P. W. 1989, ApJ, 347, 875

Smith, B. J. 1994, AJ, 107, 1695

Sommer-Larsen, J. & Yoshii, Y. 1990, MNRAS, 243, 468

Spitoni, E., Matteucci, F., Recchi, S., Cescutti, G., & Pipino, A. 2009, A&A, 504, 87

Springob, C. M., Haynes, M. P., Giovanelli, R., & Kent, B. R. 2005, ApJS, 160, 149

Stasińska, G. 1990, A&AS, 83, 501

Stocke, J. T., Keeney, B. A., McLin, K. M., Rosenberg, J. L., Weymann, R. J., & Giroux, M. L. 2004, ApJ, 609, 94

Strickland, D. K., Heckman, T. M., Colbert, E. J. M., Hoopes, C. G., & Weaver, K. A. 2004, ApJ, 606, 829

Summers, L. K., Stevens, I. R., Strickland, D. K., & Heckman, T. M. 2003, MNRAS, 342, 690

Swaters, R. A., van Albada, T. S., van der Hulst, J. M., & Sancisi, R. 2002, A&A, 390, 829

Tamburro, D., Rix, H., Leroy, A. K., Low, M., Walter, F., Kennicutt, R. C., Brinks, E., & de Blok, W. J. G. 2009, AJ, 137, 4424

Taramopoulos, A., Payne, H., & Briggs, F. H. 2001, A&A, 365, 360

Tasker, E. J. & Tan, J. C. 2009, ApJ, 700, 358

Tassis, K., Kravtsov, A. V., & Gnedin, N. Y. 2008, ApJ, 672, 888

Tenorio-Tagle, G. 1996, AJ, 111, 1641

Teplitz, H. I., et al. 2006, AJ, 132, 853

Thackeray, A. D. 1948, The Observatory, 68, 22

Thilker, D. A., et al. 2005, ApJ, 619, L79

Thilker, D. A., et al. 2007, ApJS, 173, 538

Thornley, M. D. & Wilson, C. D. 1995, ApJ, 447, 616

Tinsley, B. M. 1968, ApJ, 151, 547

Toomre, A. 1964, ApJ, 139, 1217

Tremonti, C. A., et al. 2004, ApJ, 613, 898

Tripp, T. M., Sembach, K. R., Bowen, D. V., Savage, B. D., Jenkins, E. B., Lehner, N., & Richter, P. 2008, ApJS, 177, 39

Vacca, W. D. 1994, ApJ, 421, 140

Vacca, W. D., Garmany, C. D., & Shull, J. M. 1996, ApJ, 460, 914

van den Bergh, S. 1976, AJ, 81, 797

van der Kruit, P. C. & Freeman, K. C. 1986, ApJ, 303, 556

van Zee, L. 2000, AJ, 119, 2757

van Zee, L. & Haynes, M. P. 2001, in Astronomical Society of the Pacific Conference Series, Vol. 240, Gas and Galaxy Evolution, ed. J. E. Hibbard, M. Rupen, & J. H. van Gorkom, 866–+

van Zee, L. & Haynes, M. P. 2006, ApJ, 636, 214

van Zee, L., Salzer, J. J., Haynes, M. P., O'Donoghue, A. A., & Balonek, T. J. 1998, AJ, 116, 2805

Veilleux, S., Cecil, G., & Bland-Hawthorn, J. 2005, ARA&A, 43, 769

Verdes-Montenegro, L., Yun, M. S., Williams, B. A., Huchtmeier, W. K., Del Olmo, A., & Perea, J. 2001, A&A, 377, 812

Verheijen, M. A. W. & Sancisi, R. 2001, A&A, 370, 765

Vila-Costas, M. B. & Edmunds, M. G. 1992, MNRAS, 259, 121

Vilchez, J. M., Pagel, B. E. J., Diaz, A. I., Terlevich, E., & Edmunds, M. G. 1988, MNRAS, 235, 633

Wada, K. & Norman, C. A. 1999, ApJ, 516, L13

Walter, F., Brinks, E., de Blok, W. J. G., Bigiel, F., Kennicutt, R. C., Thornley, M. D., & Leroy, A. 2008, AJ, 136, 2563

Walter, F., Martin, C. L., & Ott, J. 2006, AJ, 132, 2289

Weidner, C. & Kroupa, P. 2005, ApJ, 625, 754

Werk, J. K., Putman, M. E., Meurer, G. R., Oey, M. S., Ryan-Weber, E. V., Kennicutt, R. C., & Freeman, K. C. 2008, ApJ, 678, 888

Werk, J. K., et al. 2010, AJ, 139, 279

White, S. D. M. & Rees, M. J. 1978, MNRAS, 183, 341

Whitmore, B. C., Zhang, Q., Leitherer, C., Fall, S. M., Schweizer, F., & Miller, B. W. 1999, AJ, 118, 1551

Wofford, A. 2009, MNRAS, 395, 1043

Wyder, T. K., et al. 2009, ApJ, 696, 1834

Wyder, T. K., et al. 2007, ApJS, 173, 293

Zaritsky, D. 1992, ApJ, 390, L73

Zaritsky, D. & Christlein, D. 2007, AJ, 134, 135

Zaritsky, D., Kennicutt, R. C., & Huchra, J. P. 1994, ApJ, 420, 87